Visualisation and quantification of microstructural evolution in all solid state batteries

Patrice Perrenot

THÈSE

Pour obtenir le grade de

DOCTEUR DE L'UNIVERSITÉ GRENOBLE ALPES

École doctorale : PHYS - Physique
Spécialité : Physique des matériaux
Unité de recherche : Laboratoire d'Innovation pour les Technologies des Energies Nouvelles (LITEN - CEA)

Visualisation et quantification des évolutions microstructurales dans les batteries tout solide

Visualisation and quantification of microstructural evolution in all solid state batteries

Présentée par :

Patrice PERRENOT

Direction de thèse :

Pascale BAYLE-GUILLEMAUD — Directrice de thèse
DIRECTRICE DE RECHERCHE, CEA CENTRE DE GRENOBLE

Rapporteurs :

NELLA MARIE VARGAS BARBOSA
PROFESSEURE, UNIVERSITÄT BAYREUTH
ERIC MAIRE
DIRECTEUR DE RECHERCHE, CNRS DELEGATION RHONE AUVERGNE

Thèse soutenue publiquement le **19 janvier 2024**, devant le jury composé de :

NELLA MARIE VARGAS BARBOSA PROFESSEURE, UNIVERSITÄT BAYREUTH	Rapporteure
ERIC MAIRE DIRECTEUR DE RECHERCHE, CNRS DELEGATION RHONE AUVERGNE	Rapporteur
LUC SALVO PROFESSEUR DES UNIVERSITES, GRENOBLE INP	Président
VIRGINIE VIALLET MAITRESSE DE CONFERENCES, UNIVERSITE D'AMIENS - PICARDIE J VERNE	Examinatrice
NATHALIE BOZZOLO PROFESSEURE, MINES PARIS PSL	Examinatrice

Invités :

CLAIRE VILLEVIEILLE
DIRECTRICE DE RECHERCHE, CNRS DELEGATION ALPES

Acknowledgement

I had the chance to do my PhD in an excellent and dynamic environment. The PhD project stood at the crossroad between different CEA institutes, the LITEN and the IRIG, and gave me opportunities to meet and work with incredible people in various labs such as ESRF and LEPMI.

So first of all, this endeavour would not have been possible without Pascale Bayle-Guillemaud for directing this project, Jessica Thery for welcoming me to the LCAE team and Vincent Delaye for welcoming me to the PFNC. Many thanks to the project leaders of the FOCUS battery group, Didier Jamet and Xavier Averty, in which this PhD belonged.

Many thanks to the LCAE team for the shared moments and knowledge in the various fields of the laboratory. Thanks to Yves, Thomas, Camille, Raphael, Johannes, Lucile, Eric, Anass, Olivier, Nathalie, Gauthier, Nathalie, François, Laure, Adrien, Claire and Corinne. Thanks should also go to all the students this lab hosted, Thomas, Roberto, Julia, Julien, Nieves, Khawla, Abir, Adem, Zakariae, Samuel, Nicolas, Marie-Reine, Chloé, Théodore and without forgetting Alessandra, Paul and Julie.

Working mostly at the PFNC, I have met an incredible community emerging from different fields, I must thank David, Zineb, Audrey, Constantin, Theo, Alexandra, Marie-Christine, Matthew, David, and Bérangère. I would like to extend my deepest gratitude to Patrick for his help and his tremendous work on programming. I am deeply indebted to the students with whom I share our day-to-day experience on the platform, Kshipra, Benjamin, Lou, Vita, Vitomir, Cécile, Cathy, Ioanna, Trevor, Mei-Lin, Léa, Antonin, Serge, Claire, and more, Younes, Yousr, Florian, Lucas, Gwenael, Dorde, Claire and Andrea.

Then, I would also like to extend my sincere thanks to the people I worked with in the FOCUS group, Martine, Alexia, Joel, Antoine, Thibault, Guilhem, Sylvie, and Marion.

Acknowledgement

Special thanks to my colleagues in other LITEN departments, Juliette, Eric, Guillaume, Victor, Marc, Valentin, Marine and Xavier. I am extremely grateful to Lise for her help and the countless opportunities she gave me.

Many thanks to my colleagues in the IRIG institute for those fruitful experiences Pierre-Henri, Hanako, Ove, Etienne, Quentin & Quentin, Camille, Nino, Stéphanie, Zijie, Oscar, Alice, Samuel and Guillaume, and specifically, Caroline, Pascale and Sandrine who gave me great opportunities for my professional and personal enrichments.

I would like to express my deepest appreciation to the OpInSolid and LEPMI team with whom we accomplished great work in the friendly environment, Adrien, Lauréline, Sergio, Benjamin, Corentin, Maxime, Magda, Fannie and, last but not least, Oskar.

I am thankful for accessing ESRF to perform experiments that I never thought I would do and for the people I met there Valentin, Federico, Ludovic and, especially Marta.

A great thanks to my CSI jury which followed my project throughout the years, Nathalie and Maxime.

There are these people from outside of the aforementioned institutes/departments who participated in a plain and full experience of this PhD, Smail, Eric, Michel, Jean-Michel, Florence, Fréderic, Nicolas, Pierre-Xavier, Magalie and Céline.

Of course, all my friends and family who pushed me to surpass myself.

And at last, the success and the completion of this PhD would not have been possible without the support and nurturing of Claire. You gave me sight when I had broken focus, clarity when doubts, hope when despaired, and solution when troubled. Thank you for your devotion and your help, I will never forget about it.

Table of contents

Introduction

The global imperative to mitigate climate change and accelerate the transition to sustainable energy sources has galvanized research and innovation across numerous scientific disciplines[1]. At the forefront of this effort is the pursuit of efficient, safe, and environmentally friendly energy storage systems to support renewable energy generation, electric mobility, and grid stability. Amidst this landscape, lithium-ion batteries have emerged as promising candidates since they have reached a level of maturity that has made their use possible in multiple areas despite reaching their limitations in terms of safety, energy density and fast charge.

Conventional lithium-ion batteries have undeniably revolutionized portable electronics and entered smoothly the electric vehicles market, marking a significant step towards reducing our reliance on fossil fuels[2]. By utilizing a highly reducing negative electrode and consequently an organic liquid electrolyte, once combined with a suitable positive electrode, lithium-ion batteries deliver an electromotive force of approximately 3.8 V. The development of novel electroactive materials coupled with optimization of material selection and their engineering (particle size, specific surface coating, etc.) and the progress in manufacturing techniques achieved since the introduction of the first Li-ion batteries in 1991 now allow for energy densities approaching 250 $Wh \cdot kg^{-1}$ and 600 $Wh \cdot L^{-1}$, by far the highest energy densities achieved among rechargeable systems operating at room temperature[3]. However, the limitations of conventional battery technologies are becoming increasingly apparent. The use of metal lithium, the most energetic electrode, cannot be applied to liquid electrolytes as it induces the formation of dendrite between electrodes and subsequently, a short-circuit, often coupled with thermal runaway. This process, coupled with safety concerns associated with the use of organic liquid electrolytes causing thermal runaway events, has prompted a shift towards more innovative and sustainable solutions.

Founded on the principles of enhanced safety, higher energy densities and wider operating temperature, solid-state batteries, in which a solid electrolyte (SE) replaces a liquid electrolyte, have risen to the forefront as the enablers for a low-carbon future. The switch from liquid to the solid electrolyte is shown in **Figure 1**.

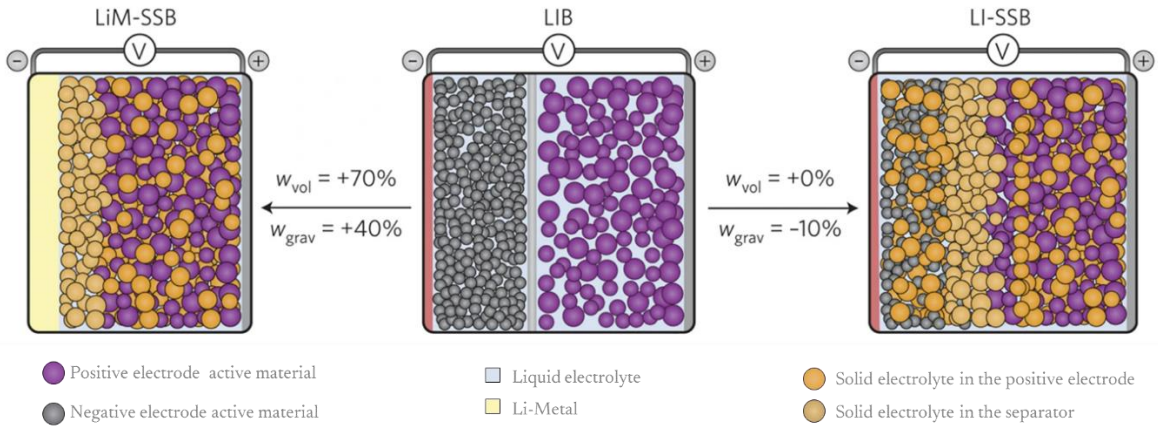

Figure 1: Conventional lithium-ion batteries (middle, LIB) contain a porous negative and positive electrode. In a lithium-ion solid-state battery with a conventional anode (right, LI-SSB) the liquid electrolyte in the electrodes is completely replaced by a solid electrolyte. Changes in energy density are estimated based on the density increase from liquid to solid, considering the high specific capacity of lithium metal (left, LiM-SSB) and the complete replacement of the graphite and anode electrolyte. Adapted from Ref. [4].

However, replacing a liquid electrolyte with a solid state one is far from trivial and the basic principle of cell assembly, engineering etc. should be thoroughly investigated as the know-how acquired in conventional Li-ion batteries cannot be applied directly in solid-state batteries. Among the solid electrolytes existing, sulfide-based solid electrolytes are promising candidates as they offer advantages such as i) enhanced safety due to their non-flammable nature ii), unlike other solid electrolytes, an excellent ion conductivity at room temperature, iii) low cost compared to expensive Li-ion salt and iv) easy manufacturing and synthesis. Nonetheless, despite these advantages, challenges persist especially driven by the solid/solid interfaces very difficult to control. This choice of moving away from organic liquid electrolytes fundamentally alters the battery dynamics, especially in terms of microstructure and morphologies of both the components at the macroscopic scale and the microscopic scale. Challenges such as establishing stable electrode-electrolyte interfaces, mitigating dendrite growth, and addressing the compatibility between sulfide electrolytes and electrode materials continue to be areas of concern[5].

The cell engineering and in particular the engineering of each component as well as the processing of each layer (separator, composite electrode, etc.) needs to be fully investigated keeping in mind that the battery together needs to ensure an ionic and electronic pathway in a solid matrix. As an example, sulfide electrolytes have the advantage of being densified at room temperature by only applying

pressure (referred to as room temperature sintering) but their full densification is seldom obtained which might impact their electrochemical properties. The challenges become even more complex when ductile sulfide electrolyte is densified alongside hard active material, like in composite electrodes, considering their disparate mechanical properties[6].

The inherent complexity in the interplay of materials, interfaces, and dynamic processes within these batteries has incited the use of advanced characterization techniques and in particular, imaging techniques. Over the past decades, various advanced imaging techniques have been extended to track and elucidate microstructure processes. Sulfide electrolytes investigation was restrained by their reactivity under the electronic beam, which to this day, remains a challenge. Nonetheless, due to intensive efforts, high-resolution imaging techniques have been customized for *operando* analysis giving information about the morphological changes dynamic during cycling[7]. In this perspective, FIB-SEM (focus ion beam–scanning electron microscopy) combines some of the aforementioned capabilities. It presents a notable high resolution through the SEM, simultaneously delving into buried interfaces through the FIB and offering volumetric analysis, crucial for determining morphological parameters such as tortuosity or percolation. In addition, the range of resolution is highly adapted to the investigation of microstructures and morphologies of the materials used in batteries[8].

This thesis is structured around four chapters. The first chapter introduces the context by presenting the lithium-ion battery working principle, encompassing its diverse characteristics, and subsequently delving into the challenges of solid-state battery development. Special attention will be directed towards sulfide electrolytes, differentiating amorphous from crystalline electrolytes. From the fixed nature of solid-state batteries, the chapter will highlight the pivotal role of morphologies in the different battery components. Furthermore, the chapter will introduce imaging techniques employed to examine these morphologies, elucidating the insights that can be derived from such analyses. The focus of this state-of-the-art lies in comprehending the profound importance of microstructures in each component of solid-state batteries within evolving materials in a fixed system.

Through this state-of-the-art, there are still three questions standing out which remain unanswered:

- **What is the impact of the electrolyte morphology on its subsequent electrochemical properties?**

- **Could the materials developed for liquid electrolytes could be directly applied in solid-state systems?**

- **How can push the limits of laboratory imaging techniques with high resolution?**

We will try in the following three chapters to answer those questions and explore the link between processing – morphologies – electrochemical properties. The second chapter focuses on investigating the separator within a solid-state battery, using exclusively the amorphous LPS solid electrolyte. Firstly, the methodology employed for SEM observations (later extended to FIB-SEM) will be controlled while the effect of the beam on the LPS will be assessed. Then, a comparative study between commercial versus homemade LPS will be conducted to ascertain the best electrolyte for subsequent phases of this PhD. Supplementary experiments will be presented, emphasizing the necessary precautions when investigating LPS with the homemade solid-state cell. Finally, an in-depth study on LPS will be presented, elucidating the intricate interplay between processing, morphology, and electrochemical performance against lithium metal.

In the third chapter, the LPS previously studied will be mixed with NMC622 to create composite positive electrodes. These composite positive electrodes will be electrochemically characterized while their morphologies will be assessed. The evolution of the morphology both dependent on the processing and the cycling will be presented, elucidating the main morphological obstacle to tackle in solid-state batteries.

The fourth chapter will be focused on the development of a novel *operando* technique within a FIB-SEM. After presenting the setup in detail as well as the challenges to overcome, the evolution of morphologies inside a composite positive electrode previously identified in chapter three will again be investigated but with the *operando* technique.

1

State-of-the-art

This first chapter is dedicated to the state-of-the-art in the battery field, screening the genesis of lithium-ion batteries, in particular, the way they operate and, consequently, the way they could be improved. The focus will then be set on solid-state batteries, the promises they bring in terms of energy density and safety while highlighting the challenges that still need to be overcome. Finally, we will focus on the impact of the electrode microstructures on the electrochemical performance of the batteries and, therefore, the benefit of imaging techniques at the nanoscale to properly characterize them in 2D and also in 3D. Due to the challenges imposed by microstructural investigation, imaging techniques will be discussed, along with their benefits and limitations.

1.1 Lithium-ion batteries

1.1.1 Generalities

A rechargeable battery is an ensemble of electrochemical cells connected either in series or in parallel that generate electricity through a chemical reaction. An electrochemical cell consists of a set of two electrodes, one positive and one negative, separated by a separator (either a polymer, or a paper soaked with a liquid, or a solid) through which ions can move, and a so-called electrolyte. As a secondary electrochemical system, they can be charged/discharged leading the researcher to call them the "rocking chair" batteries, as the Li-ions moved reversibly back and forth from one electrode to the other one. At the core of these motions is the cell potential, or electromotive force: electrons will flow spontaneously from one electrode to another. As lithium can lose an electron, the oxidation state of the electrode will change accompanied by the deintercalation of lithium-ion in the structure. To preserve the balance of charge in the system, the Li-ion will migrate to the other electrode to recombine with an electron. At the other electrode, the Li-ion will intercalate within the structure and the oxidation state of the electrode will decrease. This entire process leads to the discharge of the battery. By reversing the flow of electrons, the opposite reactions take place, this is the charge. Thus, the working processes of a Li-ion battery rely on a mechanism of reduction-oxidation reaction (so-called redox reaction).

Equation 1 and **Equation 2** give the electrochemical reactions at the positive electrode ($LiCoO_2$) and the negative electrode (graphite) of the first commercialized materials.

Equation 1: $LiCoO_2$ redox reaction

$$LiCoO_2 \leftrightharpoons Li_{1-x}CoO_2 + x\,Li^+ + x\,e^- \quad (1)$$

Equation 2: graphite redox reaction.

$$C_6 + xLi^+ + xe^- \leftrightharpoons Li_xC_6 \quad (2)$$

A scheme of the working principle of a lithium-ion battery is shown in **Figure 2**.

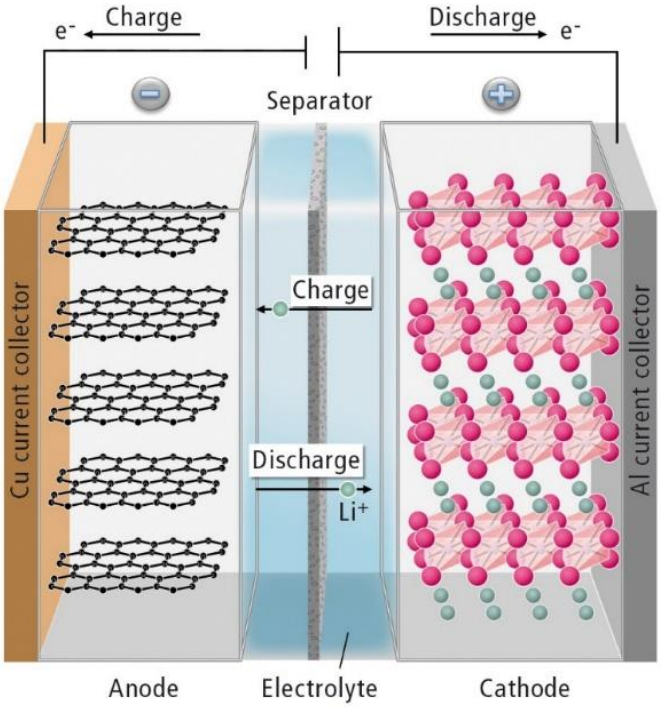

Figure 2: Scheme of a lithium-ion battery reprinted from Ref. [9].

Each electroactive material (AM) is characterized by a redox potential. Standardisation of these potentials has been made according to the standard hydrogen electrode (SHE) from which other redox potentials are measured. However, by convention and convenience, the redox potential of the Li^+/Li couple is taken as a reference (-3.04 V vs. SHE).

Another parameter that characterizes the battery is its specific capacity which fully relies on the electroactive materials selected. Commonly, we used the specific capacity ($mAh \cdot g^{-1}$) of the limiting electrode to determine the capacity a full cell can reach. The capacity (measured in Ah or Coulomb C) is the amount of electrical charge a cell can deliver within its electrochemical potential windows. For portable applications, specific or volumetric capacity is preferred where the capacity is normalised by the mass or the volume respectively of the active material.

In 1991, the first lithium-ion was commercialised based on the working principle above mentioned, with $LiCoO_2$ used as the positive electrode and graphite as the negative electrode and with an organic liquid-based electrolyte. Since then, the search for greater energy density coupled with enhanced safety has been the target of worldwide research to fit with new demanding applications. To reach this objective, there are two fundamental approaches: the first is to increase the potential difference between the two electrodes; the second is to increase the specific (or volumetric) capacity of one or both electrodes. The ideal is to combine the two approaches. As a consequence of this gigantic effort, hundreds of novel positive electrodes and negative electrodes were discovered and investigated to deliver better-performing batteries. The electrolyte has also been drastically improved over the years,

despite limitations caused by its flammable nature, prompting the use of a solid electrolyte, in theory, safer.

1.1.2 Electrode materials

1.1.2.1 Materials used as positive electrode

At the positive electrode, since 1991, the principle stayed the same: Li-ions can be intercalated in a vacant site available in a crystal lattice. Different structures have been found such as the spinel (e.g. lithium manganese oxide $LiMnO_2$ or $LiNi_{0.5}Mn_{1.5}O_4$) or olivine structure (e.g. lithium iron phosphate $LiFePO_4$), although the layered oxide remains the most employed nowadays. It is due to their high specific capacity[10] (< 150 mAh·g^{-1}) and their reasonable redox potential[11] (< 4.0 V vs Li^+/Li) that layered transition-metal oxides have asserted their position. More precisely, mixed transition-metal layered oxides have taken over as a result of a common effort to reduce the consumption of cobalt, a scarce and sensitive element[12], and boost specific capacity by increasing nickel content[13]. We can cite here Ni-rich NMC ($LiNi_xMn_yCo_zO_2$, with x > 0.5, x + y + z = 1) and NCA ($LiNi_xCo_yAl_zO_2$ with x + y + z = 1) materials. Unfortunately, most of the positive electrode materials are tricky to cycle at a potential higher than 4.2 V vs. Li^+/Li due to the decomposition of the organic liquid-based electrolyte, calling for better electrolytes and among them the solid-state are promising candidates. An overview of the specific capacity and average working potential of different materials with their electrochemical properties is presented in **Figure 3**.

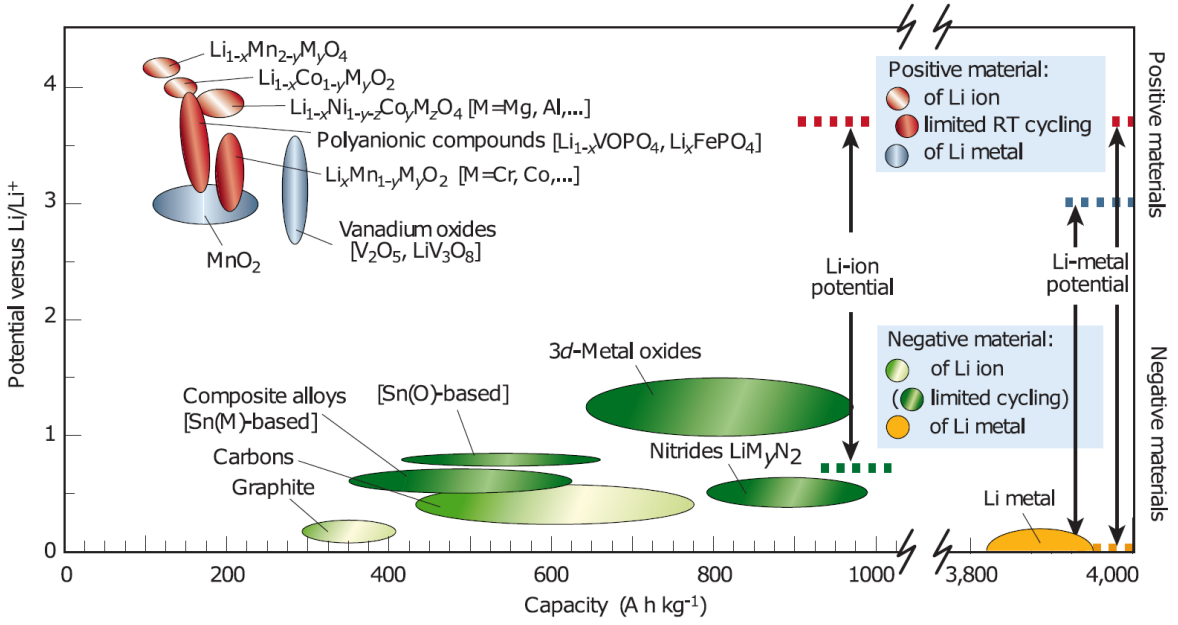

Figure 3: Electrochemical potentials of different positive and negative electrode materials for Li-ion batteries as a function of their specific capacity from Ref. [11].

1.1.2.2 Materials used as negative electrode

At the negative electrode, similar research is being carried out to increase the overall specific capacity of the most used electrode, graphite. Graphite has been widely used in commercial lithium-ion batteries due to its abundance, low cost and remarkable electronic conductivity. Its theoretical specific capacity of 372 $mAh \cdot g^{-1}$ could be reached at full lithiation where one lithium atom is intercalated amid six carbon atoms (**Equation 2**). In addition, the lithiation potential of the last lithiated graphite product (LiC_6) close to 0.01 V vs Li^+/Li, makes it an ideal material to maximize the potential difference in a battery[14]. Still, graphite reached its limitation and, due to its low working potential, it has some issues with fast charging as the lithium plating process is already observed. Thus, alternatives are currently under intense investigation. By changing the reaction mechanism from insertion-type to alloy/conversion reaction[15], the specific capacity of graphite electrodes could be multiplied by a factor of 10, the silicon being the best candidate. Silicon has a theoretical capacity of ca. 3578 $mAh \cdot g^{-1}$ which brought a lot of attention to this material[16]. Nevertheless, the process of alloying lithium with silicon creates a volume expansion of ca. 300 % which generates fractures during cycles leading to interfacial issues that drastically reduced its use up to now. Still, fine engineering of silicon particle size and content in a carbon matrix enhances the specific capacity while keeping the negative electrode's integrity[17–19].

1.1.2.3 Li metal used as negative electrode

Li metal is the ideal candidate for negative electrode material as shown in **Figure 3**. It possesses both the lowest negative electrochemical potential (-3.04 V vs. SHE) and the highest theoretical specific capacity (3860 $mAh \cdot g^{-1}$), far ahead of any other material[20]. However, the uncontrolled deposition of lithium metal poses safety issues. During cycling, lithium metal exhibits irregular platting and subsequently creates dendrite structures[21]. These dendrites have the potential to pierce the separator, creating a short circuit, where the two electrodes are in direct contact. A neutron imaging experiment allowed showing the dendrite propagation in the organic liquid-based electrolyte (**Figure 4**) meaning that the safety of the cell is compromised when Li metal is used in a liquid electrolyte[22].

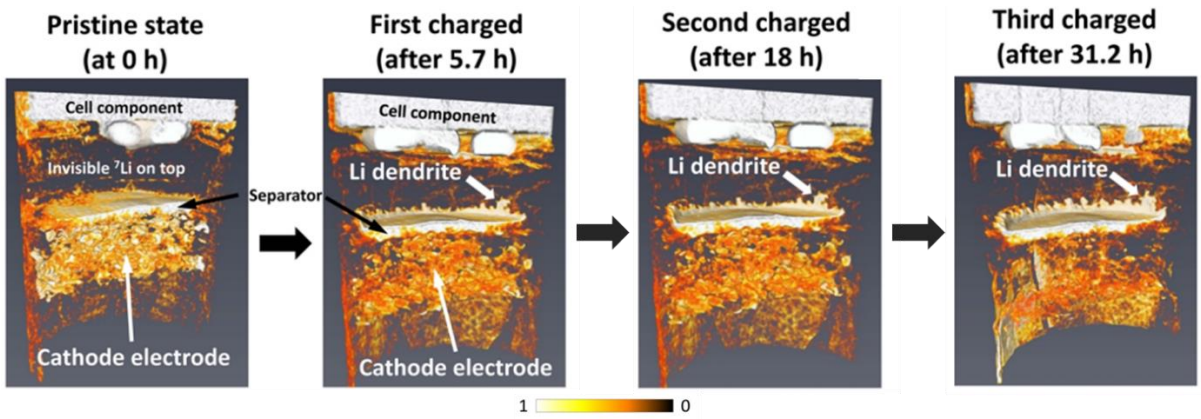

Figure 4: 3D evolution of the Li distribution in the battery cell (Li negative electrode and $LiMn_2O_4$ positive electrode and organic liquid electrolyte with $LiPF_6$ salt) at different stages of charging and discharging, contrast from the trend of absorption of neutrons. Adapted from Ref. [22].

Finally, for the massive development of electric vehicles, fast charging capability is needed and will induce high polarization, enhancing Li plating processes. Even though this process could be drastically minimized by careful engineering and smart designs, punctures (or physical damage in general) are harder to solve and require electrolyte alternatives and better separators.

1.1.2.4 Engineering of the electrode

While the positive and negative electrodes deliver the energy density to the batteries, the materials need to be embedded in an electronic conductive matrix to ensure fast charging and surrounded by a binder to maintain the electrode integrity. Notably, the binder, mainly polyvinylidene fluoride (PVDF), is chosen to maintain the electrode cohesion and adhesion to the current collector. The addition of a conductive agent (usually carbon black or CB) is needed to preserve an electron pathway from each electroactive material particle to the current collector. As this electronic/ionic matrix of PVDF/CB does not participate in the electrochemical reaction, it is considered a dead weight, and thus their ratio should be as low as possible in commercial applications. However, it was demonstrated that both participate actively in the ageing processes recorded in the batteries (solid electrolyte interphase, etc.). Finally, in conventional electrochemical batteries using a liquid-based electrolyte, porosity is a key player as it ensures both the wettability of the element and the ionic pathway. On the contrary, in solid-state batteries, the ionic path is ensured by the proper contact between the solid electrolyte (the ion carrier) and the electroactive materials, thus the porosity will drastically reduce the Li-ion transport.

1.1.2.5 Electrolyte

When high energy density batteries are targeted, two main obstacles stand in the way, i) the first obstacle is linked to the electrochemical stability windows of the electrolyte along with the

electroactive material and, ii) the second one is the fire (and/or explosive) hazards. Nowadays, the organic liquid-based electrolyte in commercial batteries consists of a mixture of lithium salt (commonly $LiPF_6$) and organic solvents (ethyl carbonate, dimethyl carbonate, propylene carbonate etc...). The former will ensure the ionic conduction in the electrolyte while the latter will enhance both the solubility of the salt and the mobility of ions simultaneously[23]. Arising from the use of high potential electrodes, the electrolyte will decompose at the electrolyte/active materials interfaces when the potential is out of its electrochemical stability window. Typically, this window ranges from 0.8 V to 4.2 V vs Li^+/Li for $LiPF_6$ in EC/DMC[24–26]. Outside of this electrochemical window, the electrolyte will decompose during reduction (below 0.8 V vs. Li^+/Li) generating the so-called solid electrolyte interphase (SEI) and in oxidation (> 4.2 V vs. Li^+/Li) leading to the development of the cathode electrolyte interphase (CEI). Both layers will negatively impact the battery's performance, lifespan and/or safety. This stability window could be overlaid on a cycling curve in **Figure 5**[3].

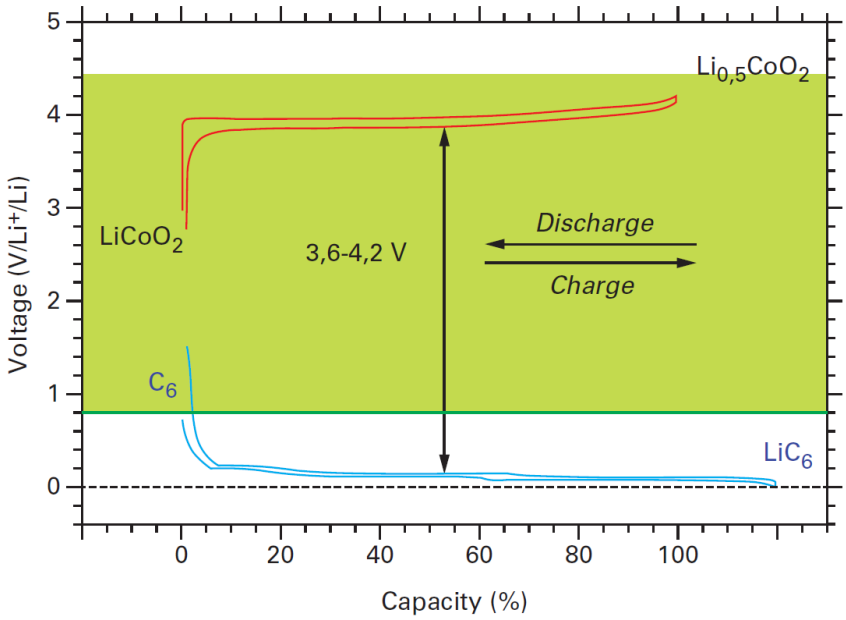

Figure 5: Galvanostatic curves of $LiCoO_2$ and graphite in PC:DEC 1:1, 1 M $LiPF_6$ electrolyte. Adapted from Ref. [3]. The green overlay represents the electrochemical stability of the organic liquid electrolyte.

The second impediment of organic liquid electrolytes is their fire hazard. Indeed, organic liquid electrolytes show poor thermal stability and violent reactivity towards air and moisture. Failures such as short circuits or punctures could cause thermal runaways of battery packs, corresponding to fierce fires and high risks for user safety[27,28].

As depicted through the several aforementioned sections, an alternative to the flammable organic liquid electrolyte could be solid, ion-conducting but allegedly more thermally stable and thus safer[29]. However, replacing a liquid electrolyte with a solid-state one is far from trivial, as numerous

challenges such as management of the electronic/ionic path and the interfacial contact deserve proper investigation. Finally, in solid-state batteries, the electrode microstructure will play a key role as by definition a solid cannot "wet" the several elements a battery is composed of.

1.2 Solid-state batteries

Solid-state batteries (SSBs) are lithium-ion batteries in which the liquid electrolyte has been replaced by solid electrolytes (SEs). A scheme of solid-state battery is presented in **Figure 6a** comparing SSB conduction pathways to the liquid electrolyte (**Figure 6b**)[30]. As can be seen, changing from liquid to solid electrolyte imposed drastic changes, i) the positive electrode is made of a composite electrode (mixture of solid elements, the solid electrolyte, the electroactive materials, the conductive agent), thus the volume occupied by the electrode is larger compared to conventional batteries; ii) the solid electrolyte could play the role of a binder which might not be necessary for solid-state batteries*, iii) the composite electrode needs to be sintered to enhance the contact between the solid element, thus the porosity should be reduced to the minimal value, iv) the negative electrode (supposed to be Li metal) occupies little space compared to the composite electrode and v) the separator relies on the densification of solid electrolyte powder to be as thin as possible with no porosity.

* Binder is not participating in either electronic or ionic conduction but it could improve the mechanical resistance[31]

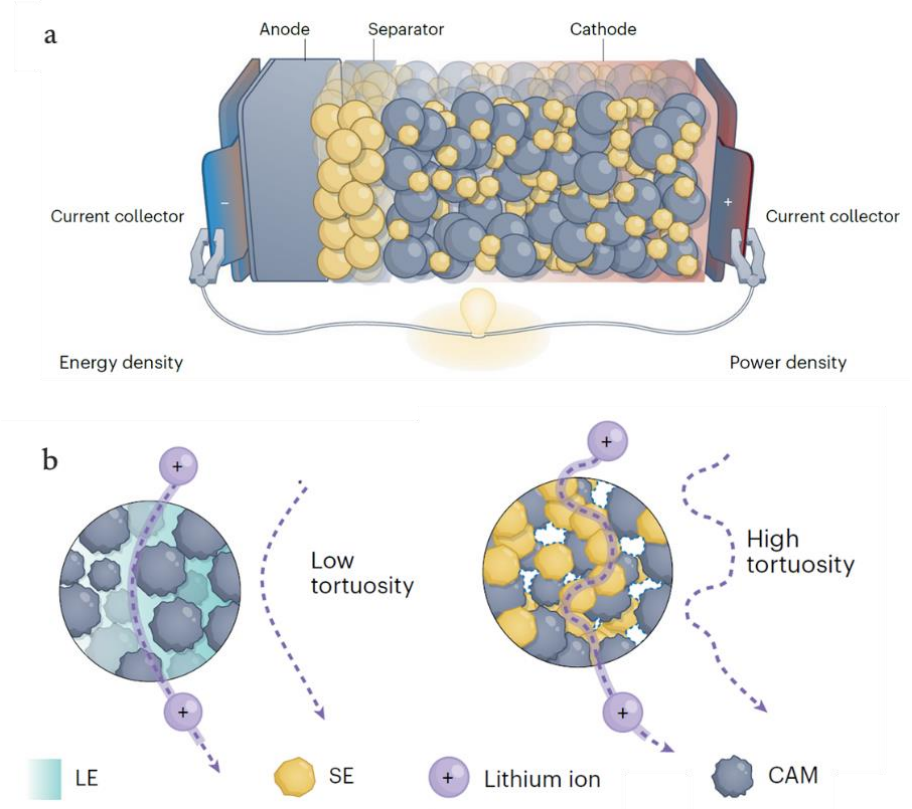

Figure 6: a) Scheme of a solid-state battery and b) its conduction difference compared to liquid electrolyte. Adapted from Ref. [30].

Different families of SSBs emerge from the nature of solid electrolytes employed, including inorganic solid electrolytes (ISEs), solid polymer electrolytes (SPEs), hybrid electrolytes (combining ISE and SPE) and other notable like metal-organic frameworks[32,33]. Each family possesses its own properties leading to certain cycling capabilities (temperature, potential windows, etc.). For example, while SPEs have the advantages of being lightweight and easy to produce, their low ionic conductivity at room temperature (10^{-4} - 10^{-2} mS·cm^{-1}) limits their practical use[34]. On the other hand, the ISE family, mainly consisting of oxide and sulfide groups, has reasonable or good ionic conductivity, respectively. The former, the oxides, have good thermal stability but both the high-temperature synthesis and the difficulty in maintaining contact at the interface of the electrode restrict their use[35]. Sulfides, however, compromise some of the aforementioned difficulties. They offer the advantage of having low density, which contributes to the overall lightness of the battery system. Combined with a low-cost synthesis, they have favourable mechanical properties that allow them to be shaped at room temperature[36]. In addition, they show high ionic conductivities[37–39], almost comparable to liquid organic electrolytes. Nonetheless, sulfides continue to present challenges, particularly in terms of electrochemical stability and mechanical fragility[40].

1.2.1 Amorphous vs. crystalline sulfide electrolytes

Li_6PS_5Cl (LPSCl) and amorphous LPS ($xLi_2S - yP_2S_5$) are major candidates in the sulfide family. Similar to other sulfide-based materials, they exhibit limited electrochemical stability windows (less than 1 V vs. Li^+/Li) but have the advantage of being sintered at room temperature[40]. LPSCl has one of the highest ionic conductivities reported for a solid (> 1 $mS \cdot cm^{-1}$) but requires an additional heat treatment for its synthesis to increase the amount of crystalline phase. On the other hand, amorphous LPS, especially the stoichiometry of 75% Li_2S – 25% P_2S_5, has only a twofold lower ionic conductivity (ca. 0.4 $mS \cdot cm^{-1}$) and possesses the advantage of being easily obtained by ball milling[41]. The microstructures of these electrolytes, the source of the wide range of ionic conductivities, are also influencing their densification, emphasizing the ambivalence of ionic conductivity and mechanical properties. Indeed, LPSCl will exhibit superior ionic conductivity but a tougher behaviour, making its densification exempt from defects very challenging. Due to its crystalline state and incomplete room temperature sintering[42], LPSCl possesses grain boundaries and defects, sites of vulnerability where lithium dendrites could propagate as shown in **Figure 7**[43].

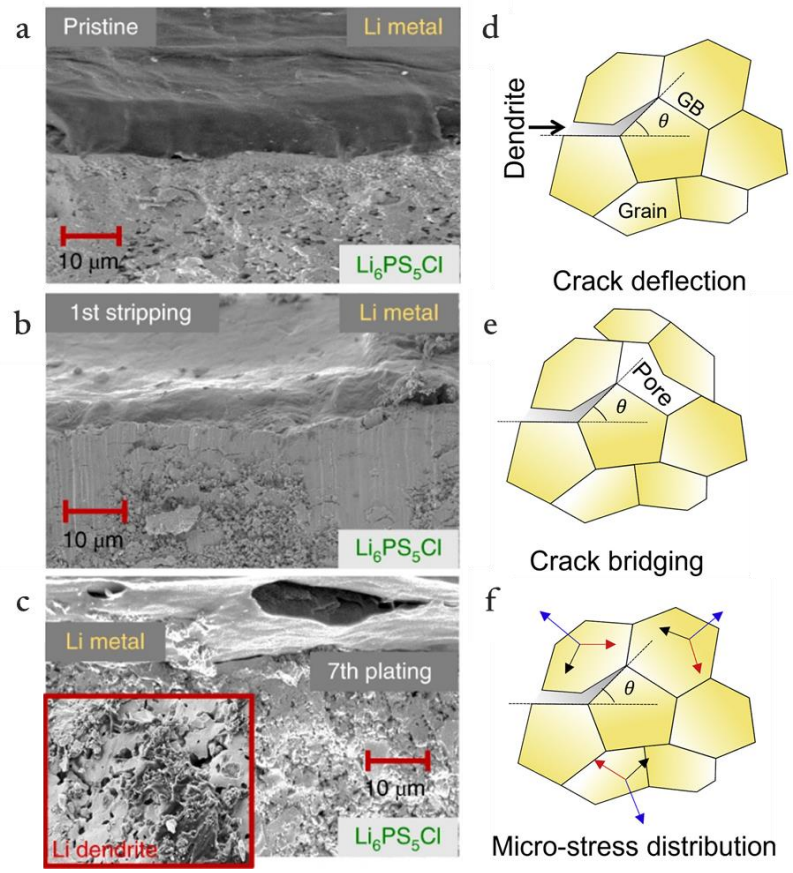

Figure 7: (a-c) SEM cross-section of Li | LPSCl interface at a) pristine and (b-c) after plating/stripping at 1.0 $mA \cdot cm^{-2}$ adapted from Ref. [44]. (d-f) Stress-shielding mechanisms in LPSCl: a function of bulk microstructural characteristics adapted from Ref. [43].

Kasemchainan *et al.* showed that the lithium deposition initiates at the triple contact point between the SE, Li and voids, in other words, where the densification is not complete. As a result, it further propagates along the free surface of the void to form a dendrite through the electrolyte (**Figure 7a-c**) after less than ten cycles. This was later confirmed and refined by Singh *et al.* that dendrites propagate along grain boundaries, with the propagation being closely linked to the microstructure of the SE (**Figure 7d-f**). Additionally, Cao *et al.* reported the dynamic formation of "soft short" in LPSCl, where the battery voltage remains constant (i.e. still delivering capacity) but cannot be increased[45]. However, under certain circumstances, these dendrites are not fatal and the battery is capable of recovering.

As LPS exhibits a lower elastic modulus than LPSCl (10.5 vs. 18.5 GPa respectively obtained by mechanical tests[46,47]), it appears that LPS full densification could be achieved with less pressure than the LPSCl. Yet, it has favourable mechanical properties towards lithium metal, which would reduce lithium dendrite penetration (**Table 1**). Moreover, LPS has an elastic domain that could adapt to the morphological evolution of electroactive materials during cycling[48].

Table 1: 75% Li_2S – 25% P_2S_5 (LPS) and lithium metal mechanical properties adapted from Ref. [49,50].

Mechanical properties †	**LPS** ††	**Li-metal**
Shear modulus (GPa)	5.9	2.8
Elastic Modulus (GPa)	15	7.8

† Determined by acoustic techniques, †† RT sintering at 360 MPa

Another appealing aspect of amorphous LPS lies in its crystallographic structure: in contrast to LPSCl, it possesses an amorphous structure that, upon room temperature sintering, effectively eliminates grain boundaries. Amorphous oxide electrolytes have already been shown to increase robustness against lithium dendrite growth[51]. Moreover, when comparing the densification of LPS vs LPSCl at room temperature[42,52], LPS complete densification can be achieved with reasonable pressure (**Figure 8**).

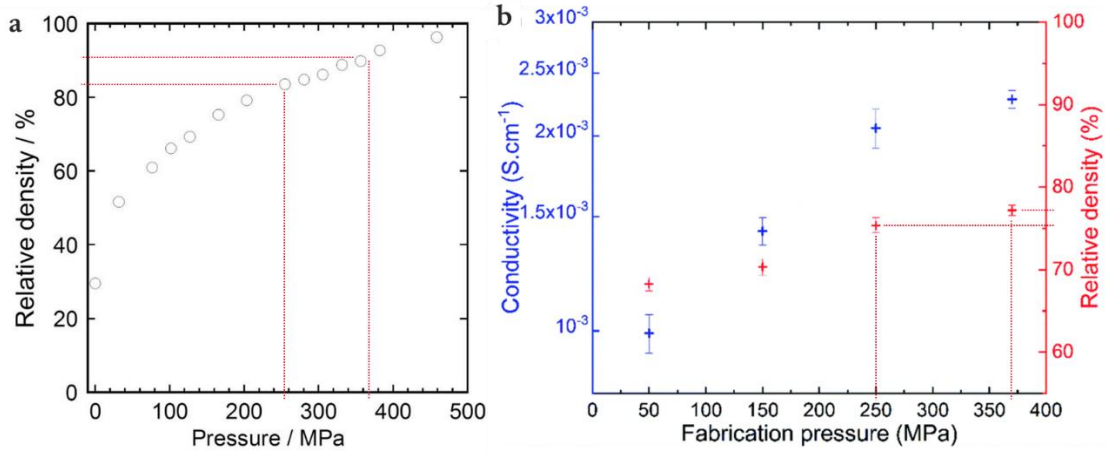

Figure 8: Room-temperature densification of a) amorphous LPS and b) crystalline LPSCl (adapted from Ref. [52] and Ref. [42]). Dotted lines help compare the densification at ca. 250 MPa and ca. 375 MPa.

As can be seen in **Figure 8**, LPSCl full densification seems not attainable with reasonable pressure since it reaches ca. 77 % densification at 370 MPa while LPS has ca. 92 % at the same pressure. The optimum pellet pressure is different for amorphous or crystalline sulfide electrolytes and has an impact on the stacking pressure later required to achieve high ionic conductivity[53]. Indeed, as seen in **Figure 9**, the energy needed to fully merge crystalline particles is greater than amorphous and high-pressure room-temperature sintering alone is insufficient to create a network for Li-ion conduction. In that case, contacts between grains are only maintained by pressure and annealing is needed to effectively merge grains.

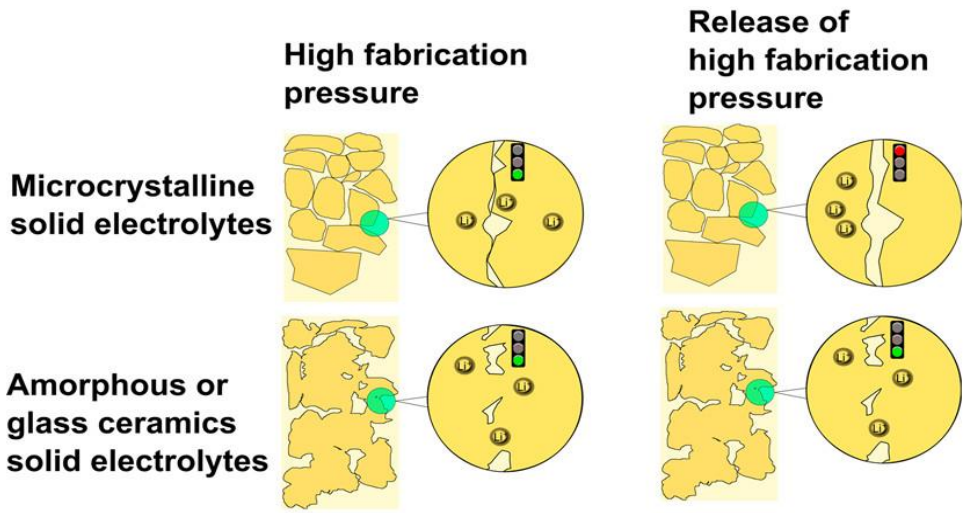

Figure 9: Fabrication-pressure-dependent morphology of microcrystalline solid electrolytes in contrast to amorphous or glass-ceramic solid electrolytes. While the particles in amorphous or glass-ceramic materials undergo a pressure-induced sintering process, the microcrystalline particles are only densified by the fabrication pressure, but not sintered together. Adapted from Ref. [53].

Considering the aforementioned problem, LPS appears to be an ideal candidate. Indeed, due to its favourable mechanical properties (**Table 1**) and its ease of being sintered at room temperature (**Figure 8a**), macroscopic defects can be reduced (**Figure 9**) as well as the grain boundaries contribution due to its amorphous structure. For the above reasons, amorphous 75% Li_2S – 25% P_2S_5 solid electrolyte will be thoroughly investigated during this thesis.

Even if, amorphous LPS theoretically addresses the majority of the preceding concerns, considerable conundrums still prevail, inherent to the SSB system: i) the full densification of SE and fine control of its morphology and ii) the optimisation and the persistence of the interfaces between the electroactive materials and the solid electrolytes. Indeed, "separator" morphologies are often overlooked and described mostly by their relative density. Moreover, battery electrodes undergo dynamic movements due to the lithiation/delithiation of the active material. As we have previously shown, LPS has interesting mechanical properties with Young's modulus around 15-20 GPa[50,52] and is generally able to manage little volume change, especially true for amorphous electrolytes since the stress/strain cannot propagate along grain boundaries[46,48,54].

As can be seen through this chapter, the challenges faced in developing solid-state batteries are numerous and different from those encountered in conventional batteries. Liquid electrolyte has the main advantage of wetting every single surface, which is not the case with a solid one, thus electrode engineering plays a key role. Additionally, as can be seen, the solid-solid interfaces are "controlled" by the pressure applied during the sintering and during cycling (called stack pressure). One can question the electrode microstructure and, in particular, the active materials microstructure as it will be at the centre of research and engineering to improve and preserve the effective battery performance of solid-state batteries.

1.2.2 Microstructure in batteries

1.2.2.1 LPS densification

The separator in SSB is made through the densification of the solid electrolyte powder, and, in our case, we exclusively consider room temperature sintering of the SE. In other terms, the electrolyte powder is shaped only under uniaxial pressure. The sintering process or densification needs to be optimised to reduce micro/macro defects (**Figure 9**, **Figure 10c-d, Figure 12**) as this will impact the achievable ionic conductivity of the electrolyte (**Figure 10a-b**) and as well as mechanical integrity (lithium metal penetration for example).

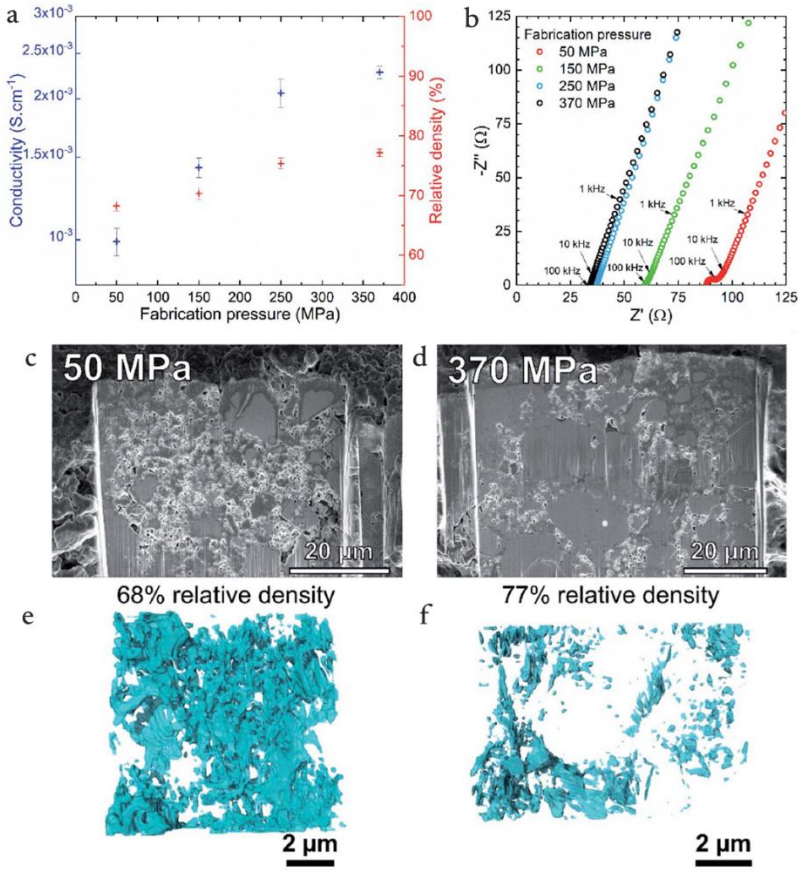

Figure 10: a) Conductivity and relative density of the Li_6PS_5Cl electrolyte as a function of the fabrication pressure and b) corresponding Nyquist diagrams under a stack pressure of 25 MPa. c) and d) SEM images of FIB cross-sections of the prepared pellets at c) 50 MPa and d) 370 MPa respectively, with their corresponding FIB reconstructions e) and f) showing respectively the porosity in blue. Reprinted from Ref. [42].

In order to attain optimal ionic and mechanical properties, the SE must be exempt from porosity. It is well known that Li-ion transport is optimal in solid-state batteries if the tortuosity is reduced to unity in the full multi-material 3D system. As shown in **Figure 10a** for LPSCl, the ionic conductivity increases with the relative density of the pellet but a sevenfold increase in pressure only improves the relative density by 9 % while doubling the ionic conductivity to 2.5 $mS \cdot cm^{-1}$. The study of the 3D morphology and/or microstructure could bring crucial information to improve their overall electrochemical performance. The main issue with those investigations is the lack of proper methodology. Commonly, cross-section observations[53,55] or a simple FIB-SEM tomography are used to determine the relative density (**Figure 10e-f**). These methods give results on the overall porosity, often assuming an isotropic microstructure. However, this approach has clear limitations because i) uniaxial sintering could give rise to anisotropy in the microstructure and ii) basic 2D or 3D analyses tend to omit key information when considering 3D complex microstructure such as tortuosity or extended pore network description.

To improve densification, coupling pressure and temperature for sintering have been proven to increase the rate at which current can pass through the cell before short circuiting[56]. However, amorphous LPS starts to degrade and crystallize at 180 °C[37,57] while the densification is still not complete at 300 °C. This gives rise to grain boundaries and remaining porosity, lastly identified as deleterious for the integrity of the separator (**Figure 9**). In general, as depicted in **Figure 10**, achieving complete densification without degradations is far from straightforward and is seldom accomplished.

1.2.2.2 Composite electrode

As mentioned before, the choice of electroactive materials and electrolytes will guide the overall electrochemical performance of the battery. However, the electrochemical performance is only reachable with a very precise electrode engineering. In the context of composite electrodes, the task of minimizing defects is even more challenging since it involves the sintering of at least two materials with significantly disparate mechanical properties. The complexity of composite positive electrode is greater as its functions are manifold. Like the separator, the SE transports the ions around the active material and the pores to the counter electrode: this later will be called the ionic network. As seen in the previous section, an ionic network exempt of pores is difficult to obtain but necessary for the performance and integrity of the separator. Furthermore, every single active material particle needs to be electronically connected to the current collector (CC) to participate in electrochemical reactions: this will be called the electronic network. In organic liquid electrolytes, the electronic network was ensured by the incorporation of carbon additives. Nonetheless, these additives have a detrimental impact on the stability of the electrolyte, leading to a progressive decline in the specific capacity of such systems[58]. The intertwining of both the ionic and electronic networks is essential, as the process of lithiation/delithiation involves the simultaneous participation of ions and electrons.

Neumann *et al.* showed the intricacy of the electronic (provided by NMC particles only as no conductive additives are added) and the ionic networks during the delithiation of NMC622 by the competing processes of the two networks with the lithiation front shown in **Figure 11**[59].

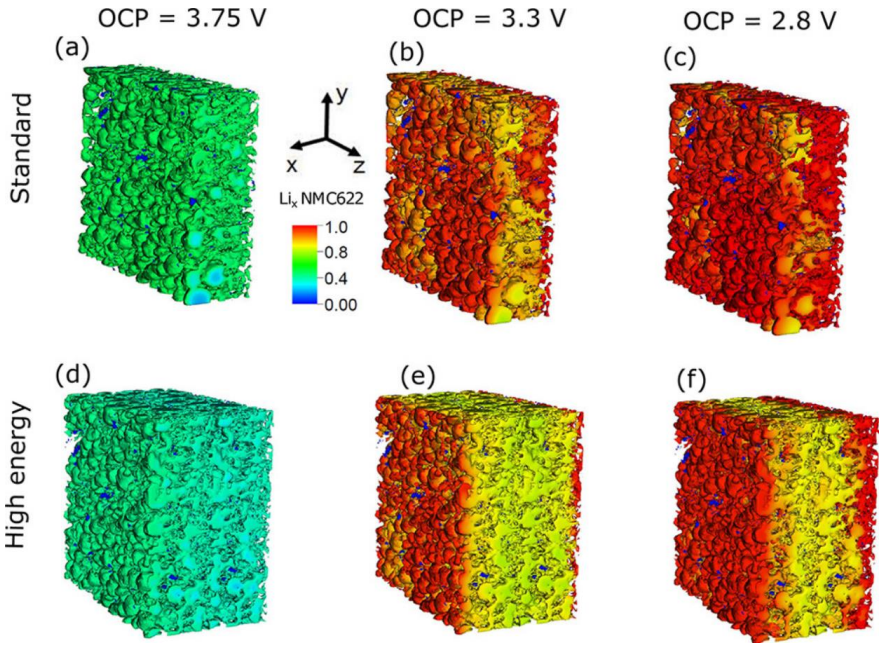

Figure 11: (a–c) Lithium distribution in the active material of the standard composite cathode (40 μm) at cell voltages of 3.75, 3.3, and 2.8 V during a 0.1C discharge. (d–f) Concentration distributions in the high-energy cathode (80 μm) under the same conditions. Adapted from Ref. [59].

During the initial stages of discharge of NMC-type material, the lithiation of NMC particles primarily takes place near the separator as a consequence of the low ionic conductivity of the SE (ionic network). As the lithiation process progresses, the electronic conductivity of NMC622 decreases, impacting the electronic network, which becomes the limiting factor. In order to maintain good performance, both the electronic and the ionic networks need to be optimised (positive electrode thickness, particle size, etc.) and preserved over numerous cycles.

Moreover, during cycling, the electroactive materials' breathing[60] can contribute to mechanical stresses leading to additional irreversible degradation[61–65]. As an example, the unit cell volume change of $LiNi_{0.6}Mn_{0.2}Co_{0.2}O_2$ (NMC 622) is reported to be 4.4 % at 4.5 V vs Li^+/Li[66] as the lattice parameters will undergo anisotropic evolution[67,68]. The main morphological consequence arising from this volume change is the cracking of polycrystalline NMC along the grain boundaries during cycling[68–71] as shown in **Figure 12a** and most probably the mechanical damage of the solid/solid interfaces.

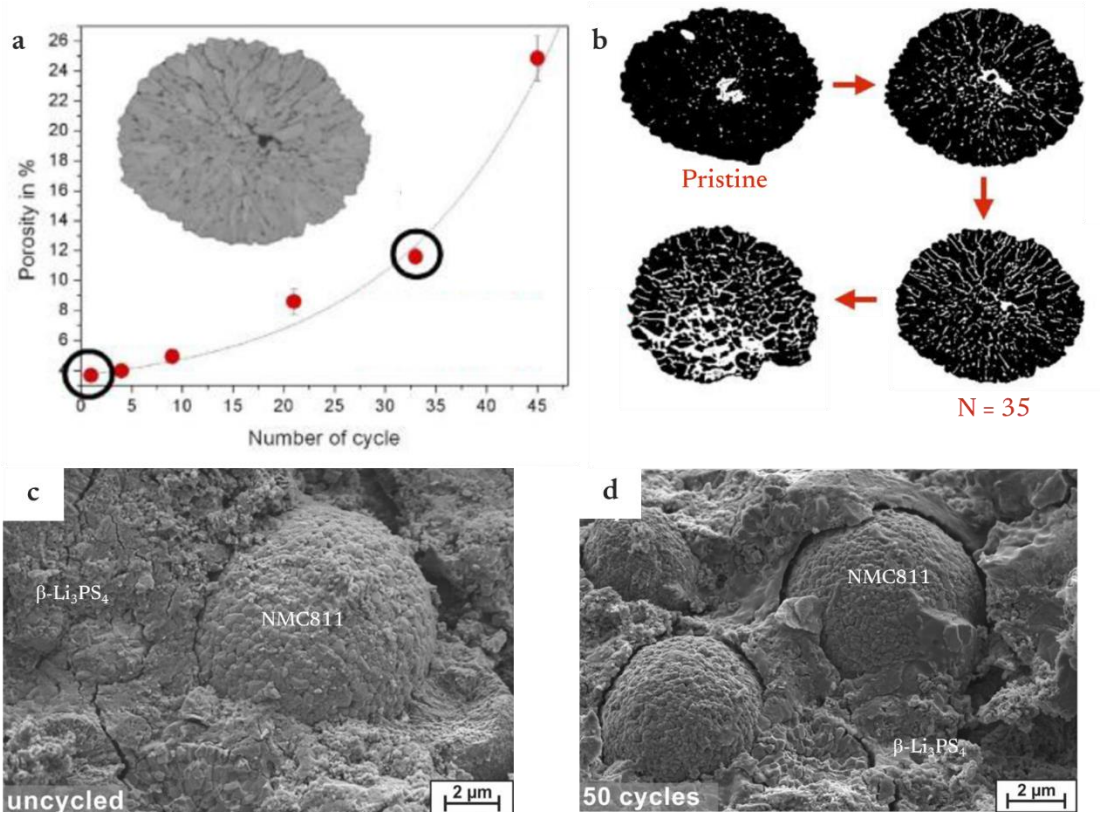

Figure 12: (a-b) Evolution of the fracturing of secondary NMC particles with the number of cycles, a) the porosity evolution and b) the crack structure evolution during particle ageing (white is porosity and black is NMC). Circles indicate the pristine and 35th cycle. Adapted from Ref. [69], (c-d highlighting the decohesion of NMC 811 in crystalline β-Li_3PS_4. Reprinted from Ref.[72].

The fracturing of NMC is mainly reported with a liquid electrolyte[69,73] as in Cadiou *et al.* in **Figure 12a-b** with an *in-situ* FIB-SEM technique. This effect has moderate consequences in a conventional lithium-ion battery such as small internal resistance increase[74] as the liquid electrolyte adjusts to those morphological changes if NMC particles remain connected to both the electronic and ionic network. However, it is problematic in the fixed nature of SSB, yet to be highlighted in solid-state composite positive electrodes. In addition, the strains from the active material breathing will be transferred to the surrounding matrix (active material, porosity and SE) that will subsequently need to adapt to the local change (**Figure 12c-d**). The latter study highlighted the decohesion of the NMC811 from β-Li_3PS_4, coupled to a highly resistive interphase in the positive electrode leading to an irreversible loss of the capacity. However, it is hard to quantify and obtain a representative morphological evolution from *ex-situ* 2D SEM images as fractography can bring artefacts (fractures on the uncycled state in **Figure 12c**).

Through these evolutions and degradations, the integrity of the ionic and electronic networks needs to be maintained to preserve performance. Unfortunately, sulfide electrolytes tend to fracture under stress as they possess low fracture toughnesses[75]. Coupling the volume and morphological changes of active materials with the nature of solid-solid interfaces in SSB, the microstructures of these systems

and their evolution are crucial. In this direction, imaging techniques are the best approach to assess the microstructures of materials.

1.2.3 Investigation of microstructures

1.2.3.1 Imaging techniques

There is a plethora of imaging techniques[76–79] but the ones used to characterize and describe microstructures and morphologies in the field of materials science are less abundant[80–82]. **Table 2** summarizes imaging techniques exclusively used in the microstructure/morphology analysis, divided based on the information they provide in terms of dimensionality and resolution.

Table 2: Advantages and drawbacks of imaging techniques to investigate battery microstructures.

Technique	Limit of resolution	Pros	Cons
Optical Microscopy[83,84]	**µm**	- Easy, fast, no/less sample preparation - 2D *operando*	- Limited resolution - Requires transparency
Scanning electron microscopy (SEM)[85,86]	**few nm**	- Easy, fast - Versatility - Quantity and quality of information (chemical/topographic contrast) - 2D *operando*	- High vacuum - Beam damage (e^- damaging)
Focus Ion Beam-SEM[87–90]	**few nm**	- Expert Versatility - Quantity and quality of information (chemical/topographic contrast) - 3D visualization - 2D *operando*	- High vacuum - Destructive (3D) - Beam damage (e^- damaging, Ga^+ implementation, surface amorphisation) - Time-consuming
X-Ray computed tomography (XCT)[91–93]	**tens of nm**	- Chemical mapping (density map) - 3D *operando*	- Beam damage - Accessibility (synchrotron) - Time-consuming

From **Table 2**, it is evident that each imaging technique can provide specific information, but none alone can give complete information on microstructure and chemical distribution. Optical microscopes and SEM will provide fast observations of a sample with limited sample preparation. Contrary to the aforementioned techniques, FIB-SEM or XCT gives 3D metrics of the sample but

with tedious acquisition and sample preparation. **Figure 13** provides images of different stoichiometry NMC particles at different scales with multiple imaging techniques for morphological investigation.

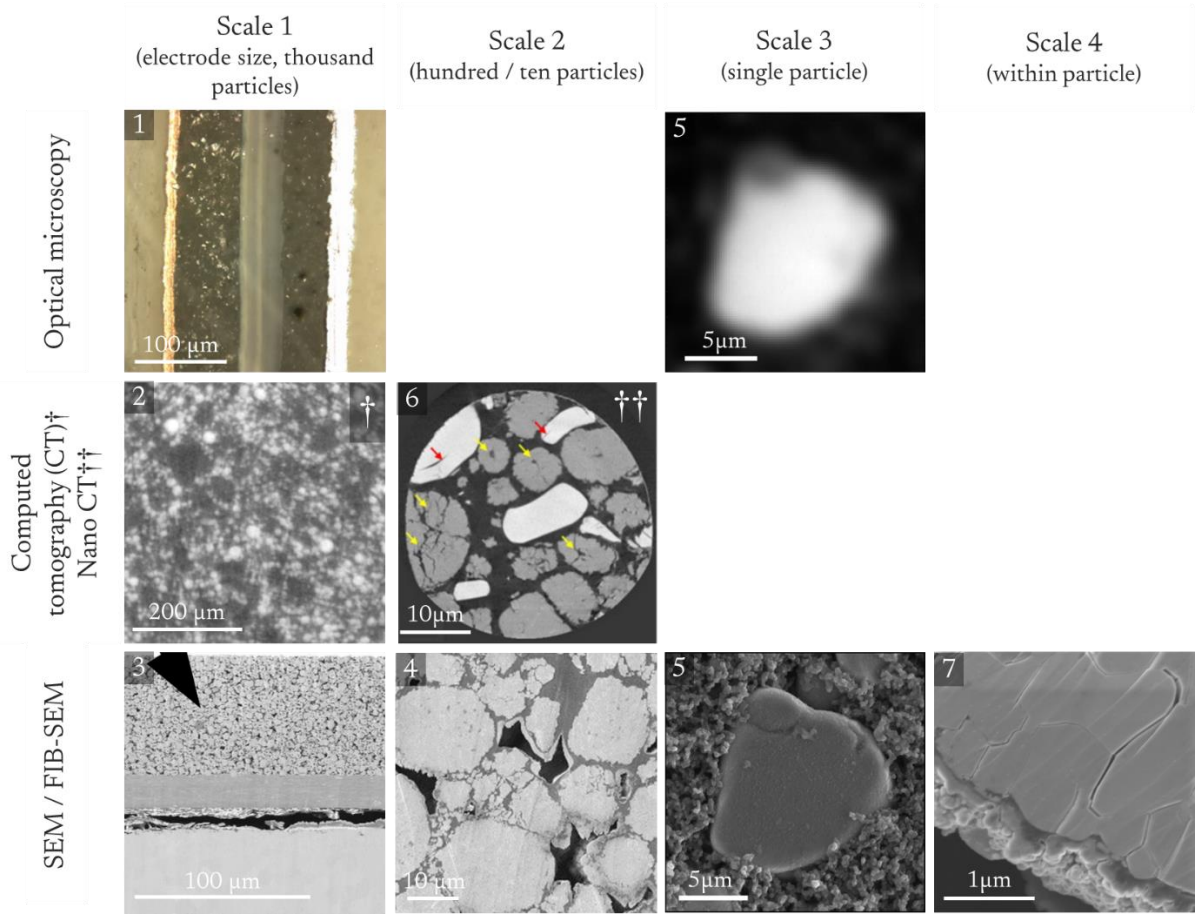

Figure 13: NMC particles observed at different scales with multiple imaging techniques. 1) Optical micrograph of an NMC622 (right side)-Graphite (left side) battery adapted from Ref. [94]. 3) SEM image of a positive electrode made from NMC111 adapted from Ref. [95]. 5) Ni-rich NMC particle ($LiNi_{0.87}Mn_{0.05}Co_{0.08}O_2$) observed by an optical microscope (top) and by an SEM (bottom) adapted from Ref. [96]. 6) Composite cathode made with LCO (white) and NMC111 (grey) adapted from Ref. [97]. 2) Composite cathode with LPS (grey) and NMC (white). 4) Cross-section of NMC811 infused with resin. 7) Cross-section of a cycled NMC highlighting cracks.

It becomes clear that optical microscopy and CT scans can only provide macroscopic information at the scale of an electrode or a battery (**Figure 13**, scale 1). Nano CT gives a better resolution helping to address very local processes (spatial resolution down to 25 nm). At the nanoscale resolution, large cracks (≈ µm) can be seen in the active materials (**Figure 13**, scale 3). Since the contrast and resolution are based on X-ray absorption difference, some phases unfortunately cannot be distinguished from each other in CT such as the carbon, binder and voids. In the study of Wu *et al.*, tin active material (Sn) was selected, in part (i) because of the difference in X-ray attenuation coefficient of the different phases enabling the identification of Sn, the lithiated Sn (Li-Sn), the solid electrolyte (LPS), and the

cracks and (ii) for its size relative to the beamline resolution capabilities[98]. Among these imaging techniques, FIB-SEM stands out more and more in recent years as it exhibits excellent contrast owing to the SEM imaging and, being coupled with a FIB, allows 3D reconstruction. As seen in **Figure 13**, SEM is the perfect imaging technique for battery morphologies investigation as it provides a continuous resolution from the scale of an electrode (hundreds of μm, scale 1) down to nano-sized cracks inside the active material (scale 4), resolutions impossible to achieve in other imaging techniques. Despite being destructive with the ion beam etching, the FIB-SEM has the advantage of digging in trenches, revealing possible buried interfaces. However, the beam damage due to Ga ions remains a challenge and involves very specific protocols to ensure surface integrity. In general, the higher the resolution of the observation, the more localized the incident beam is (X-rays or electrons), and the higher the potential for beam damage†. Moreover, on *operando* techniques where high fluxes and repeated doses are brought on a cycling battery, some artefacts can appear and bias the comprehension of the mechanisms[99]. Jousseaume *et al.* showed that large X-ray doses can result in an NMC appearing inactive or with a noticeable delayed charging. The alteration of the sample by the incident beam (integrate dose, use of the charged beam) and in particular during *operando* measurements, have an impact on the actual electrochemical response causing a delay in the processes and could lead to biased interpretation. Beam damage is fairly known on standard imaging techniques such as SEM and limiting the exposition or the dose leads to pertinent results[100,101]. Again, precautions should be taken to avoid any modifications leading to artefacts.

Commonly, 2D observations give fast and reliable information for extracting trends from numerous samples. Besides, by formulating a few hypotheses, surface observations could be extrapolated to obtain grain size distribution[102]. Despite providing trustworthy trends, 2D cannot provide extensive microstructure description and important metrics in batteries such as tortuosity, percolation or connectivity can only be determined with 3D techniques[103,104].

1.2.3.2 Battery component microstructures

Numerous studies have focused on the electrochemical properties and only primitive image analyses were employed. The volume fraction and particle size distribution were calculated, the first by the simple ratio of a voxel of each phase on the acquired volume, and the second by classifying each particle by its number of voxels. On *ex-situ* 3D FIB-SEM tomography coupled with electrochemical

† Beam damage (or radiation damage) refers to the deleterious effect of the beam on proper phenomenon observations. With X-ray beams, it could manifest as a delayed electrochemical process for example. With electron beams, it could manifest as the melting and structural rearrangement of the materials.

impedance spectroscopy (EIS), Shi *et al.* suggest that cycling-induced decohesion (**Figure 14a-b**) as indicated by higher bulk resistance (**Figure 14c-d**) and higher porosity volume fraction[64].

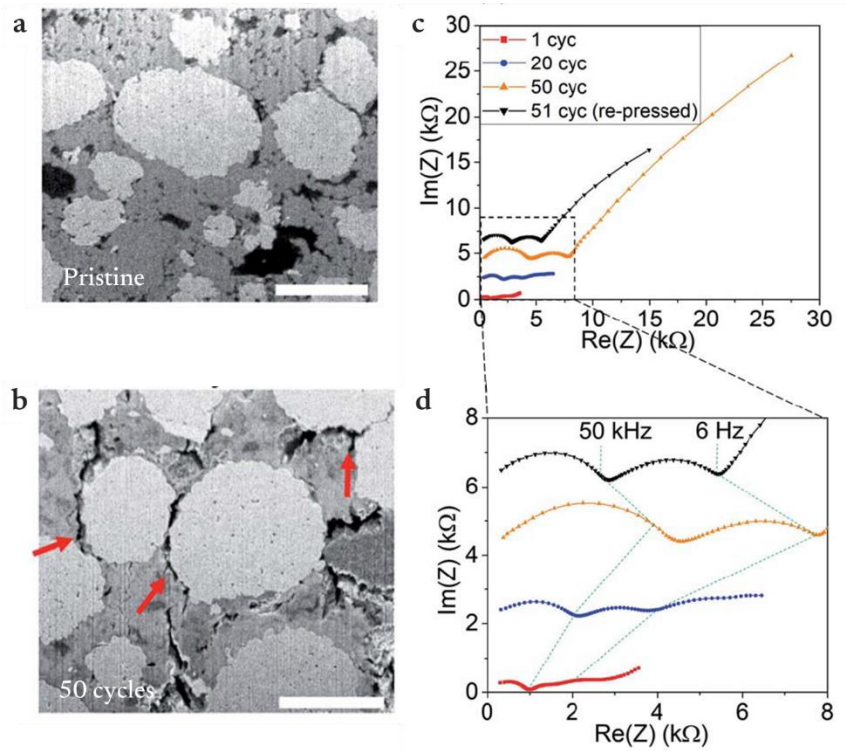

Figure 14: (a-b) cross-sectional SEM images of composite cathode a) before cycling and (b) after 50 cycles and (c-d) EIS measurement after 1, 20, 50, and 51 cycles (repressed pellet). Adapted from Ref.[64].

Still, several systematic quantifications have not been deployed such as the tortuosity of the SE or the percentage of connected particles, exposing the ambiguity of comparing *ex-situ* samples with each other to find a guideline for proper sintering. These parameters are essential for a comprehensive understanding of microstructural effects on effective properties and for the optimization of materials and processes in solid-state battery technology. These quantifications necessarily stem from the acquisition and analysis of 3D images with the help of advanced algorithms. Even if qualitative observation can be done by direct visual inspection, 3D explicit metrics, however, are automatically obtained by algorithms. This level of image quantification, particularly for tortuosity or percolation, needs to be systematically applied to gain insights into microstructural impacts on effective properties. Geometric tortuosity, for instance, is a crucial parameter mimicking the lithium-ion paths inside the electrolyte. However, it can lead to confusion due to its multiple definitions and calculation methods. It can be calculated geometrically in imaging in various ways (multiple path average or convolutions of the flow paths[105,106]) or empirically by Bruggeman's formula linking tortuosity to the porosity volume fraction. This latter formula has faced criticism as it does not describe extensively the lithium-ion pathways in all proportions[107]. Although multiphysic

simulations on 3D microstructures give the most accurate results for tortuosity[108], simpler approaches such as ImageJ plugin[105] or TauFactor[106] are often preferred. These methods yield similar trends in tortuosity while being less resource-intensive in terms of computational power and time.

Kroll *et al* had a more systematic approach to quantification[65] as they included the percentage of active material connected to the current collector, the active surface of AM (the area where SE and AM are in direct contact) and more detailed pores analysis. With complementary simulations, they proved that a twofold higher ion transport tortuosity due to porosity in an SE was compensated by a fourfold higher bulk ionic conductivity. Such a study highlights the importance of quantitative morphological data to understand kinetic limitations. Nevertheless, such studies that thoroughly characterize the reconstruction of a cathode are still scarce. The necessity to introduce a comprehensive, accessible and extensive methodology for characterizing lithium-ion battery morphologies and their essential metrics linked to battery performance becomes imperative.

1.2.3.3 *Operando*-based techniques to understand dynamic processes

In the previous section, 3D FIB-SEM analyses of the microstructure were presented. However, as this technique is destructive, the microstructure evolution can only be performed on *ex-situ* samples, while manipulation/sample preparation of a solid-state battery might initiate artefacts such as fractures. Novel imaging techniques are emerging where an entire cell is cycled while being observed: this is *operando* (or *in-situ*) imaging[109]. This class of techniques has experienced significant growth in popularity in recent years as it i) gives dynamic morphological evolution of the same region, ii) removes artefacts from multiple sample preparations[69,98,110,111]. Pertinent studies have highlighted dynamic phenomena in SSB as presented in **Figure 15**.

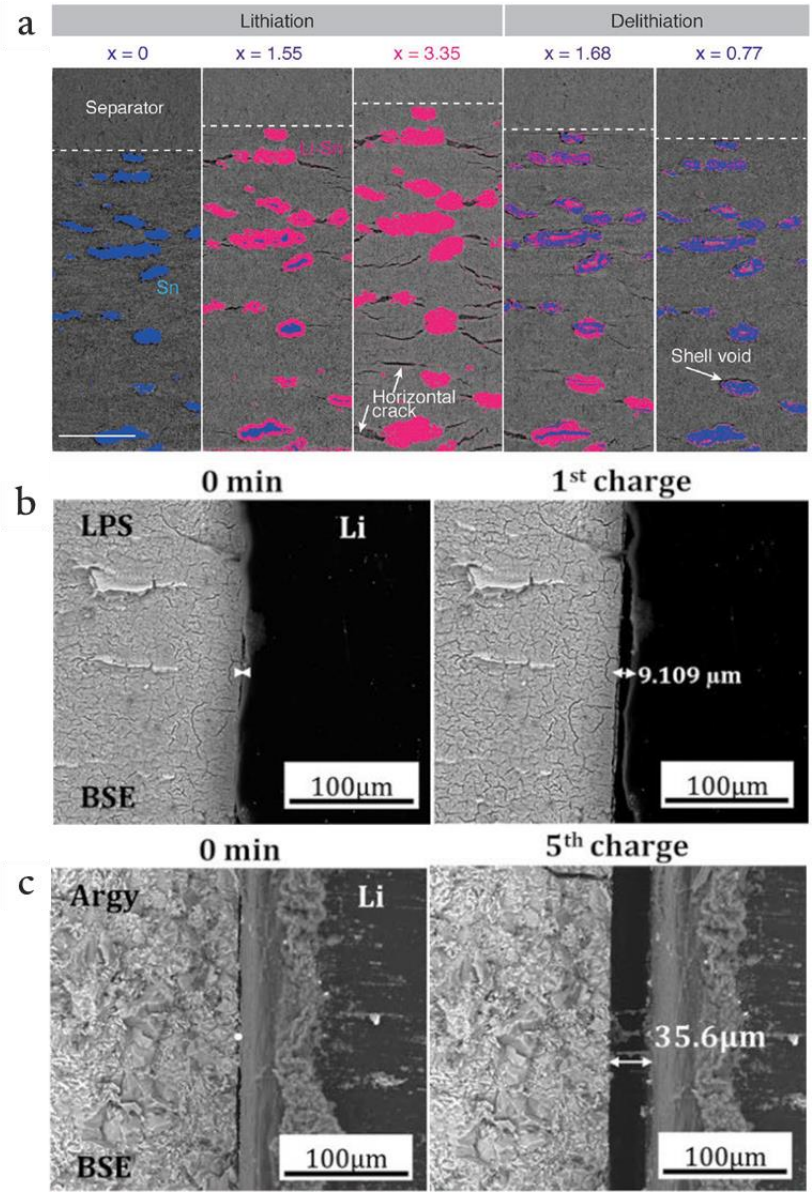

Figure 15: a) Cross-sectional image of working electrode at various states of charges (SOCs). The Sn and Li-Sn phases are coloured blue and pink respectively. The dashed line represents the border between the WE and the separator. Scale bar = 100 µm. Adapted from Ref.[98]. b) Anode interface: (b) and (c) images at the lithium interface for LPS and LPSCl solid electrolytes respectively. Adapted from Ref. [110].

Wu *et al.* provided a dynamic quantitative study of Sn particles in LPS composite negative electrode and separator that highlighted i) the densification of the solid electrolyte (separator) during the dynamic lithiation of the composite electrode and ii) the composite electrolyte tends to fracture drastically when the alloying lithiation mechanisms of Sn starts (**Figure 15a**)[98]. Thanks to the good Young's modulus of amorphous LPS material, the fractures could be partially closed along the delithiation. However, the low resolution of synchrotron radiation (≈ 1 µm) requires the study of material with high-density contrast (Sn versus LPS) and limits the fine observation at the nanoscale of the electrolyte and interfaces, as the porosity below 1 µm could not be explored. At a finer

resolution, Yadav *et al.* studied the Li interface with LPSCl and β-Li_3PS_4 qualitatively highlighting dendrite growth at the interfaces[110]. Nevertheless, the pristine morphology of LPS suggests an air exposure that mitigates the pertinence of the observation and the initial gap between LPSCl and Li suggests that the observations are hard to link to electrochemical processes. Another interesting *operando* study decoupled the initiation from the propagation of lithium dendrite with the help of the XRCT technique (**Figure 16**).

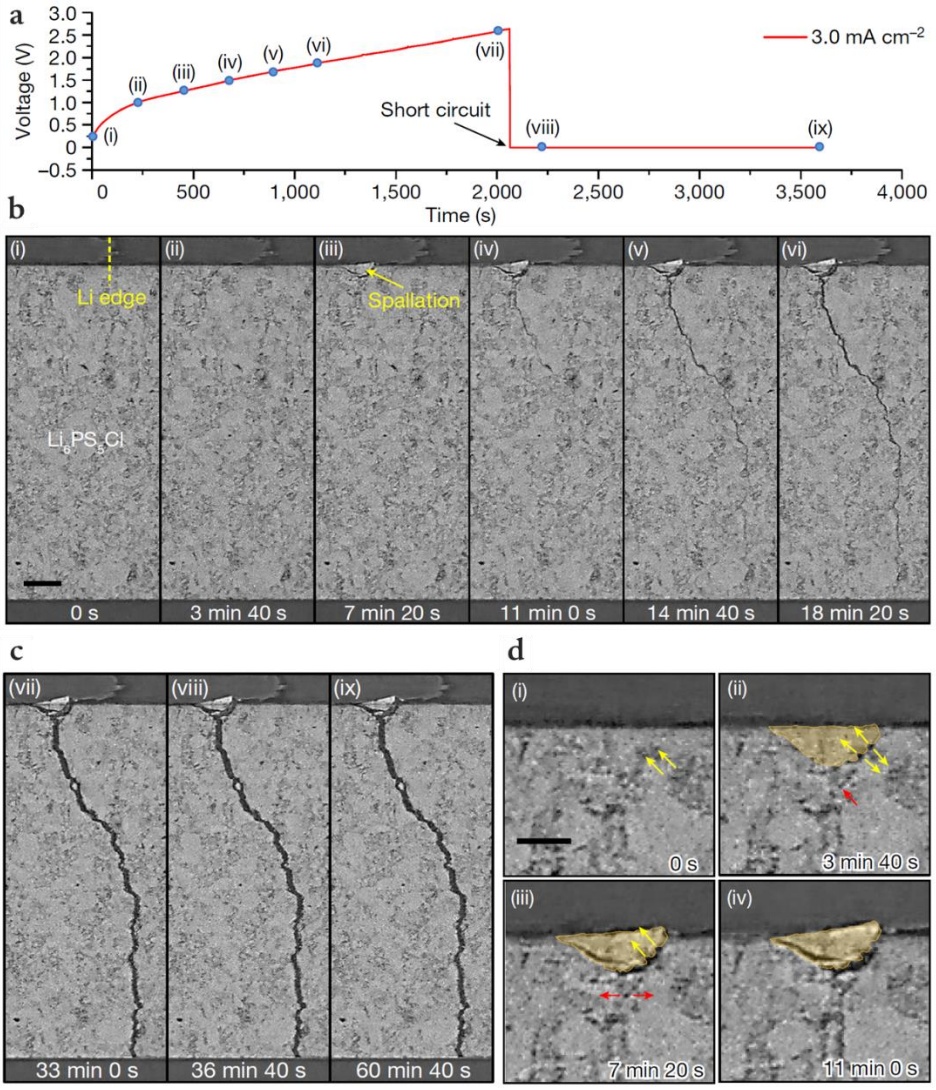

Figure 16: (b-c) *Operando* XCT virtual cross-sections during plating of a Li/Li_6PS_5Cl/ Li cell (a) showing the development of a dendrite crack from initiation through propagation to complete short circuit. d) Magnified images of the region near the plated electrode showing the formation of the spallation and transverse crack. Yellow arrows indicate pores associated with forming the spallation and red arrows indicate pores associated with propagation of the transverse crack. Adapted from Ref.[112].

In addition to directly observing a dendrite creating a short circuit through 200 μm of dense LPSCl, they proved that Li dendrite initiates from open pores filled with lithium during cell fabrication.

1.3 Conclusion

Through this state-of-the-art, we demonstrated the need to develop better batteries with higher energy density and safety. However, the transition from a conventional liquid electrolyte to a solid-state one is far from trivial as both electronic and ionic networks should be carefully maintained during cycling. It shows the importance of an in-depth characterisation of the microstructure of all battery components. Each of them and their relationship must be carefully manufactured to improve integrity. Electrolyte densification (separator) should be of central interest as this will guide fully the ionic network and avoid dendrites propagation, thus its morphology and subsequently, the associated degradation mechanisms arising from various defects must be investigated by imaging techniques to reveal its weaknesses.

Along the different chapters, the thesis will focus on the morphology of each component of a solid-state battery and their evolution during manufacturing/processing and electrochemical cycling. Electron microscopy imaging techniques, in particular SEM and FIB-SEM tomography, will be central to the multiple investigations. In the first section, the morphology of LPS, used as a separator, will be studied. LPS was selected for this study because, contrary to its sulfide counterparts, it has an amorphous structure that could i) facilitate its shaping at room temperature and ii) reduce the propagation of dendrite at grain boundaries. Beam damage and air exposure will be investigated to ensure trustworthy results as well as the calendar aging. The effect of room temperature sintering conditions such as time and pressure will be investigated to understand the impact on the morphologies and electrochemical properties.

In a second section, composite positive electrodes composed of Ni-rich NMC (NMC 622) and LPS will be investigated similarly to gather knowledge on the solid-solid interface. As both materials have disparate mechanical properties, the full densification of the composite positive electrode, exempt from defects, remains challenging to this day. Strong from the knowledge collected on the densification of LPS, improvements on the composite positive electrode will be brought by tuning the sintering conditions. Polycrystalline NMC 622 was chosen for its high specific capacity and its low volume change during lithiation, as it has already proven its capabilities in liquid electrolyte systems. A systematic approach to the description of the morphology will be applied. The description of both the ionic and the electronic networks will be done to extract meaningful morphological parameters.

In the third section, a novel microscopy technique, namely the *operando* FIB-SEM will be presented. This imaging technique was developed together with Zeiss®, from the modified manufacturing to the observation in the FIB-SEM by way of an improved transfer chamber. Several challenges will be addressed such as airtightness, electronic connection to the apparatus, adapted cell fabrication and

stack pressure. Electrochemical tests will be carried out to ensure proper cycling within the microscope chamber while keeping the beam damage as low as possible. This new approach will be applied to the same composite cathode previously characterized. Contrary to the previous *ex-situ* approach, this technique will allow the dynamic observation of the phenomenon identified in the prior section.

2

Materials, synthesis, shaping and methodologies

In this section, the materials used throughout this thesis will be presented as well as their shaping when necessary. Then, a section will be dedicated to imaging techniques applied for the different studies, both in 2D and 3D. Additionally, the numerical tools used to extract metrics and results will be presented. The sum of those tools will represent the methodology for the description of microstructures in this thesis. Hereafter, we will continue with the description of the electrochemical techniques used to assess battery performance. Lastly, the special electrochemical cell design for *operando* measurement will be presented.

2.1 Sulfide electrolytes

2.1.1 a-Li_3PS_4 or 75% Li_2S–25% P_2S_5

We focussed on one particular solid electrolyte, the amorphous Li_3PS_4. A commercial one has been bought at MSE Supplies® while an in-house solid-electrolyte was obtained through ball-milling synthesis of two solid precursors (Li_2S, Sigma-Aldrich 99.98% - P_2S_5, Sigma-Aldrich 99%). They were weighed for a 1.5 g batch and put in a ZrO_2 jar with 5 mm ZrO_2 balls. The powder mixture was milled (Fritsch, planetary mill apparatus Pulverisette 7) at 510 rpm for 360 cycles (5 min active and 15 min rest). This corresponds to a total of 30 h active ball-milling, the resting time being necessary to lower the temperature and avoid crystallization into β-Li_3PS_4[76]. A yellowish sticky powder is then obtained and stored in a glass container. The obtained powder is presented in **Figure 17**.

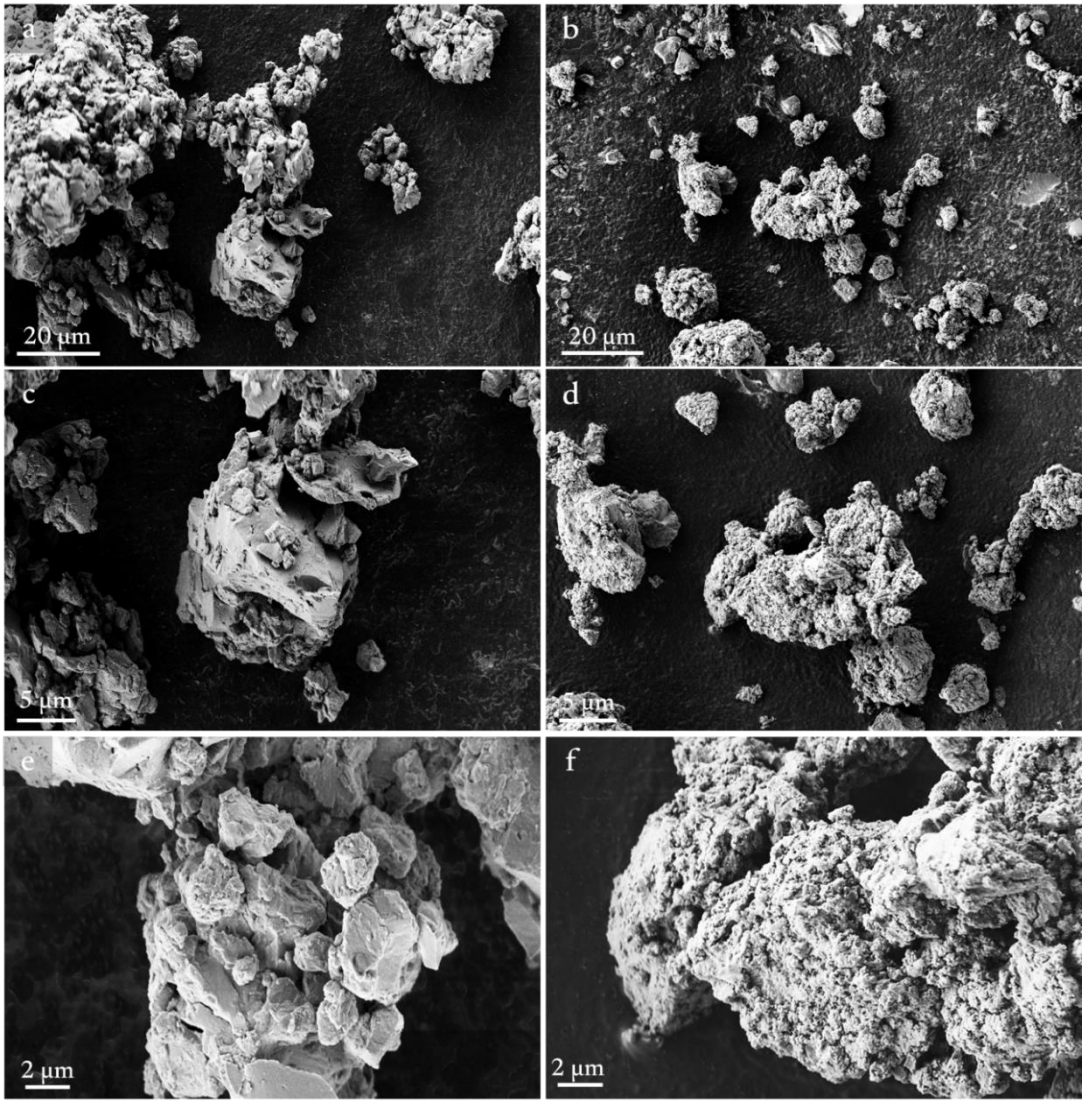

Figure 17: Secondary electron image at various magnifications of freshly synthesized LPS powder (on the left) and MSE Supplies LPS powder (on the right).

2.2 Active materials

2.2.1 NMC

NMC622 ($LiNi_{0.6}Mn_{0.2}Co_{0.2}O_2$) was purchased at MSE Supplies®. SEM images of the NMC622 are shown in **Figure 18**.

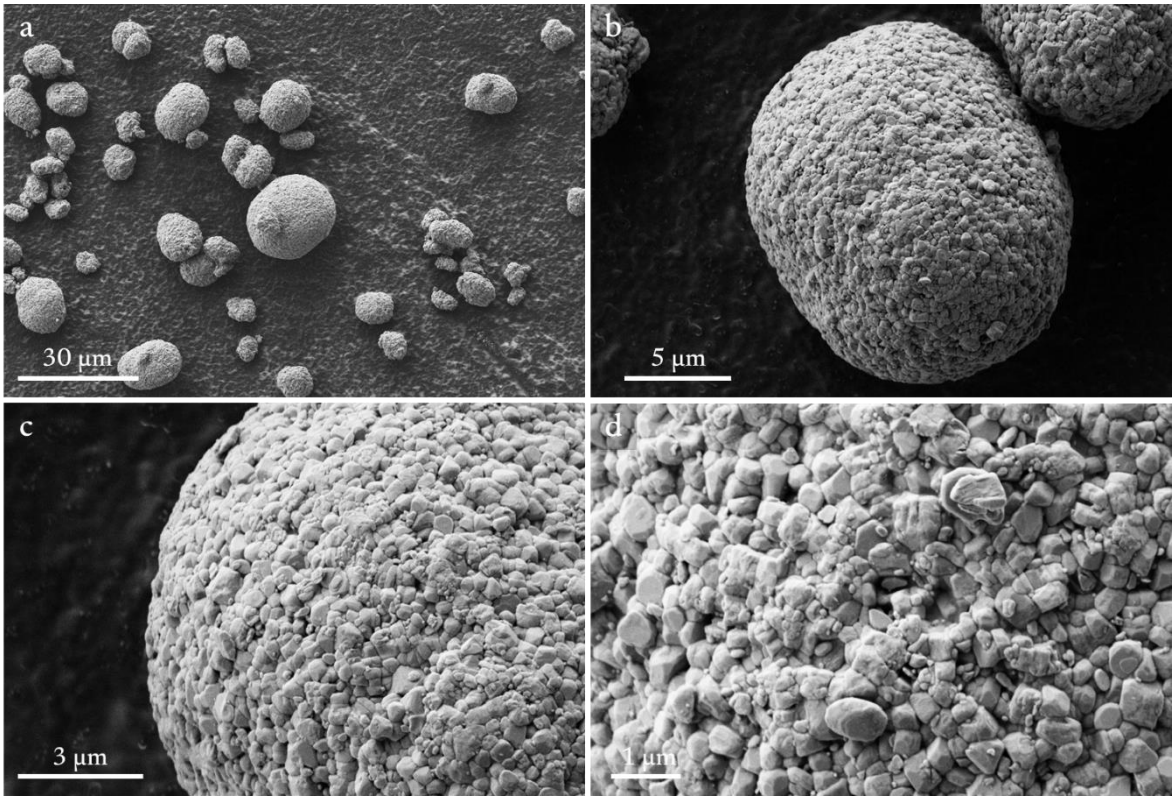

Figure 18: Secondary electron images of NMC622 particles. (a-b) single secondary particles and (c-d) a close-up of the same particle to reveal primary particles.

It consists of large spherical secondary particles composed of agglomerated nano primary spherical-like particles obtained by co-precipitation. The supplier specified a D50 included between 10 and 14 µm and delivered a first discharge capacity of more than or equal to 160 $mAh \cdot g^{-1}$ (obtained in coin cell measurement cycled at C/10 rate between 3.0 to 4.3 V vs Li^+/Li at room temperature, using Li metal as counter electrode and organic-based liquid electrolyte LP30 – 1M $LiPF_6$ in 1:1 wt:wt ethylene carbonate EC: dimethyl carbonate DMC).

2.2.2 Lithium indium.

Lithium indium reference and counter electrode are used in half-cell measurement thanks to its high stability with the solid electrolyte compared to Li metal[113]. In Li_xIn, the targeted stoichiometry was 0.3 as it offers a stable potential of 0.62 V vs Li^+/Li around this stoechiometry[114]. To do so, both

indium and lithium are weighed before making a counter electrode. Considering both film thicknesses, the counter electrode is composed of two 6 mm indium disks and one 4 mm lithium disk. The two lithium disks are placed in between the indium disk before a pressure of 127 MPa is applied for 10 min. A Li-In foil with good stoichiometry is then obtained and punched for further investigation in batteries, ensuring a large excess of available Li.

2.2.3 Lithium

Lithium metal can also be used for specific tests such as plating/stripping tests to assess the Li dendrites' propagation. Li foil is ca.50 μm and supplied by Albemarle. SEM images of Li foil are provided in **Figure 19**.

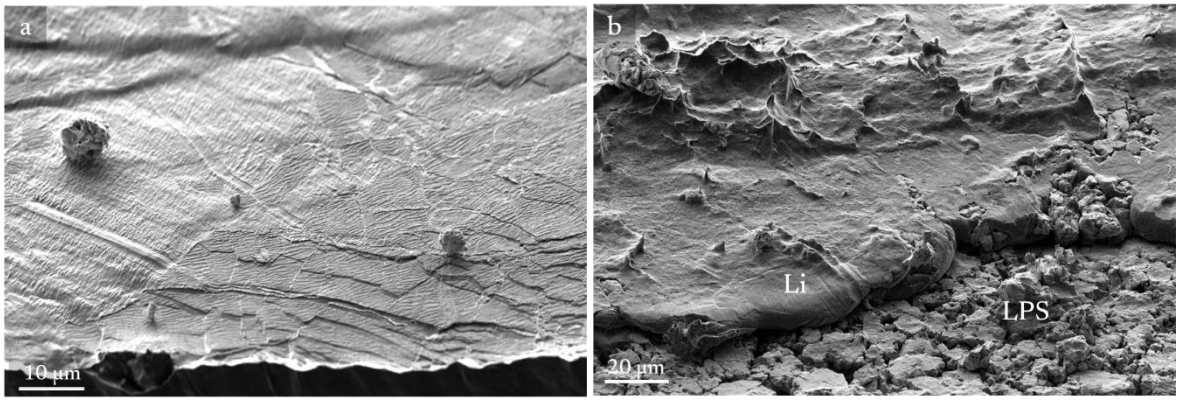

Figure 19: Lithium foil secondary electron images. a) Pristine film and b) lithium pressed on LPS at 25 MPa.

2.3 Cell design and cell fabrication

The solid-state batteries are cycled in a homemade cell already developed by LEPMI (**Figure 20**).

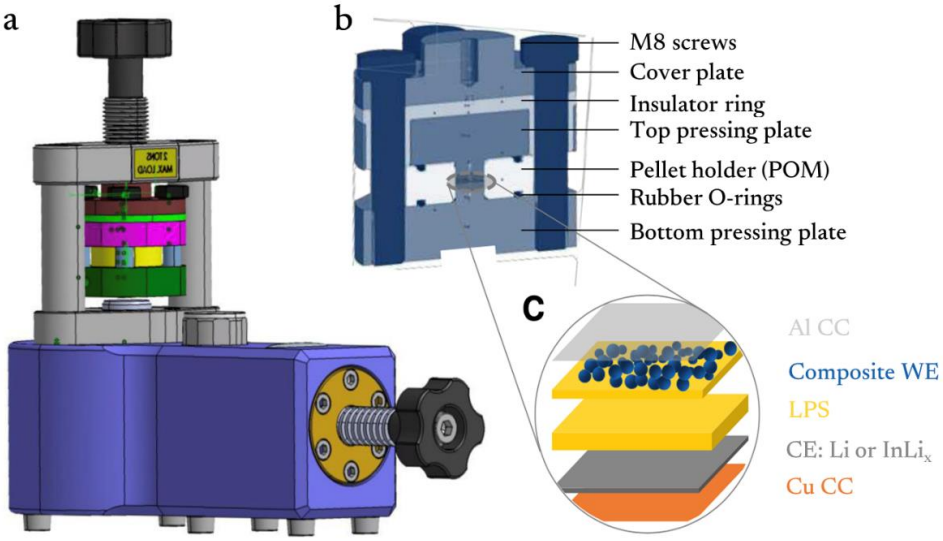

Figure 20: Illustration of high-throughput SSB platform design: a) mini-pellet press with SSB cell fitted in between the pistons, b) cross-section of the SSB cell design and c) detailed description of the SSB stack. Adapted from Ref. [115].

The cell consists of two stainless steel pressing plungers and a 7 mm POM cylinder that allows electrical insulation of the two plates. Thus, the cell serves as a pellet die for the solid electrolyte and the composite electrodes but also for electrochemical cycling. This design allows for high-throughput electrochemical characterization as both plungers can be directly connected to a potentiostat. Based on the cylinder diameter and the press capacity, the pressure can be adjusted from ca. 12.5 to 510 MPa with 12.5 MPa increments (equivalent to 0.1 to 2 tons range on the press with a 0.1 t increment).

2.3.1 Electrolyte preparation

For the separator, roughly 30 mg of LPS is added to the cell cavity (hole in the POM disk), the cell is then closed with the top plunger and the pressure is applied on the powder directly. Room temperature sintering between 255 and 510 MPa is applied to LPS powder at different times to properly investigate the impact of the sintering parameters (pressure/time) on the electrochemical performance of the solid electrolyte alone.

2.3.2 Composite electrode

For the positive electrode, composites were made with 70 w% of NMC powder (ensuring electronic network) added along with 30 w% of LPS (ensuring ionic network). This mixture is hand-mixed in a mortar for at least 10 min with a pestle. Then, once the separator is shaped, the composite mixture (ca. 5 mg) is added to the top of the separator. Once more, the composite is sintered at pressures

ranging from 127 MPa to 255 MPa for 10 min. The final thickness depends on the shaping parameter but is approximately 50 μm.

2.3.3 Platting/stripping test

For plating/stripping tests with lithium metal, the amount of powder to obtain the separator is increased from 30 mg to ca. 50 mg to avoid short-circuit. The plating/stripping conditions used are displayed in the electrochemical section.

2.3.4 Half-cell assembly

Once the composite electrode has been shaped, the bottom plunger is removed, and the counter electrode (Li or Li_xIn) is added. In half-cell, the counter electrode is pressed at 25 MPa. The pressure is applied slowly to allow the lithium to alloy with the indium, knowing that the alloy is generally obtained homogeneous in ca. 30 min. Once 25 MPa is reached, the pressure is kept for 10 min. In order to maintain the pressure in the cell, four screws are turned crosswise until the force display on the press comes back to zero. In the case of lithium used as the negative electrode, a 4 mm lithium disk is directly added to the bottom of the separator and the cell is closed. Here again, a pressure of 25 MPa for 10 min is kept before the screws are turned to maintain the pressure. The design of the cell allows for obtaining a stack pressure of a maximum ca. 127 MPa. Due to lithium adhesion to stainless steel plungers, a 7 mm Celgard® is placed between the anode and the plunger when the cell needs to be extracted and examined in the pristine state.

2.3.5 Liquid electrode preparation

Electrodes are made with a tailor-made self-standing protocol using organic solvent. NMC622 provided by Arkema was mixed directly with a conductive agent (SuperP® C65, Imerys) and PVDF-HF (Kynar Flex 2751-00, Arkema) previously solubilized at 10 % in N-methyl-2-pyrrolidone (NMP) until a formulation of 80 wt% active material and 10 wt% binder and 10 wt% and a dry extract of 30 % was reached. After 10 minutes of dispersion with an ultra turax (speed 4) and 2 h of degassing, the slurry was then coated onto an aluminium current collector (16 μm), with a doctor blade set at 250 μm. After this, the electrode is left to dry for 12 h at 70 °C. Electrodes with a diameter of 12 mm are made and dried under vacuum at 120 °C for 24 h. Typical NMC loading is around 5.0 $mg \cdot cm^{-2}$ corresponding to a theoretical surface capacity of 0.9 $mAh \cdot cm^{-2}$.

2.4 2D observations: scanning electron microscopy

2.4.1 Transfer box

Once the selected samples are extracted from the pellet holder, 2D observations using scanning electron microscopy (SEM) are precious. Two SEMs were used to do all the characterizations: for the developed surface estimation and general observations, a Zeiss Ultra 55 equipped with a Gemini® column was used. For the rest, a Zeiss Merlin equipped with a Gemini 2® column was used. As the samples are always air/moisture sensitive, a transfer box was used from the glovebox to the microscope (**Figure 21**).

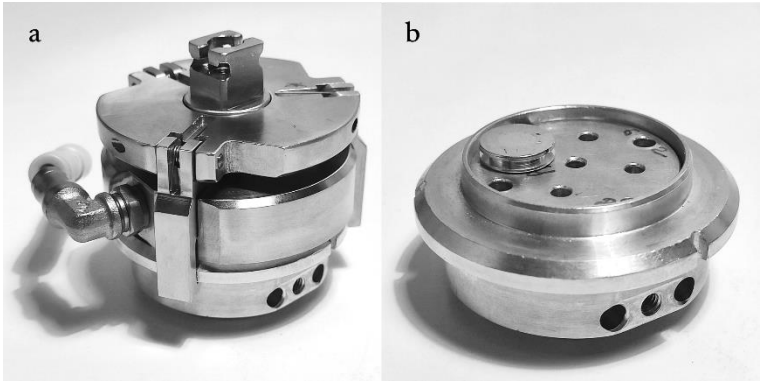

Figure 21: Pictures of Zeiss transfer box, a) closed and b) opened.

2.4.2 Surface morphology investigation

SEM is a powerful imaging technique used to observe the surface of materials at high magnification: a focus electron beam is scanned over the surface of the sample, which interacts with the materials to produce various signals. These interactions manifest with the generation of several emissions, such as backscattering, secondary electron emission, and X-ray emission, depending on the energy and angle of the incident beam. Several detectors can be used to collect the previously cited emission and highlight different areas or phases in the sample. Only the detectors used in this thesis will be presented. A scheme is presented in **Figure 22**.

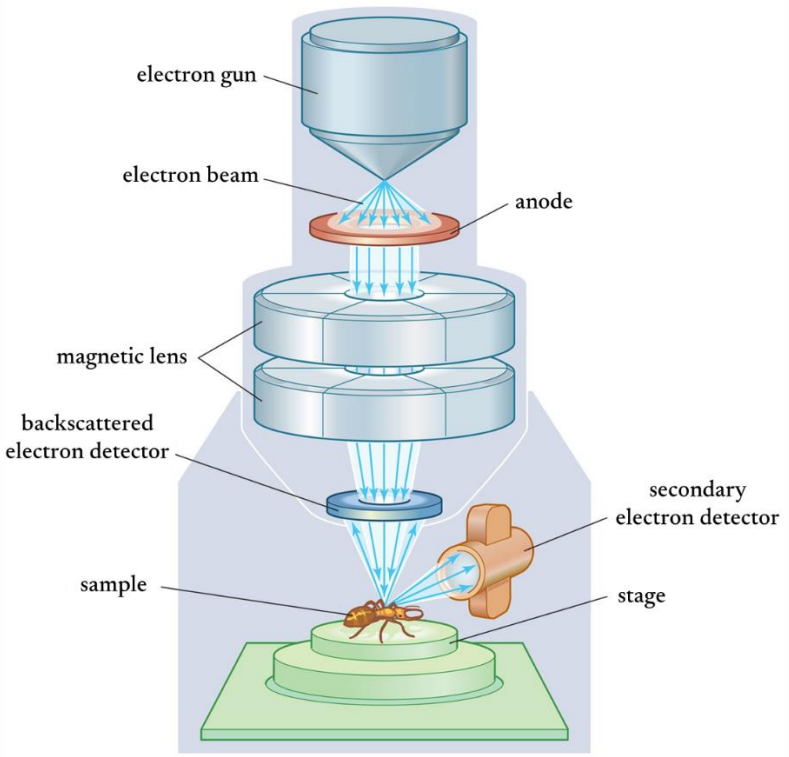

Figure 22: Scheme of scanning electron microscopy. Reprinted from Ref. [116].

When the primary electron beam strikes the sample surface, it dislodges secondary electrons from the surface. These low-energy secondary electrons, captured by a detector on the side of the chamber (named SE2 or SESI at Zeiss) provide information about the sample's topography and surface features. Another secondary electron detector is located around the primary electron beam (named In-lens at Zeiss) that will highlight the edges of the object. Simultaneously, when some of the primary electrons are scattered back out of the sample (or backscattered) due to interactions with the sample's atomic nuclei, backscattered electrons carry information about the sample's chemical composition and differentiate materials based on their mean atomic number (black pixel being low atomic number compounds and white the opposite). The backscattered electron detector is also around the primary beam and images are called ESB at Zeiss. Such images, of the same area but different contrast, can be merged into a composite image to create multi-dimensioned images. Consequently, it is easier to assign a pixel to a phase as the multiple detectors are providing complementary information of the same area.

In order to obtain spatially-resolved high-quality images, several parameters need to be carefully set. The quality of an image will directly affect the clarity, resolution and contrast of the sample's surface. First, the accelerating voltage, defining the energy of the primary electrons, will determine the penetration depth of the beam and the potential beam damage. For this reason, a lower accelerating voltage, typically in the range of 1.5 to 2 kV will be preferred as it gives better surface sensitivity. Then, the beam current refers to the number of primary electrons interacting with the sample. A

higher beam current leads to a higher signal, hence a better signal-to-noise ratio. However, excessive current can cause some beam damage on the sample as well as an increase in the beam spot size, harmful to the resolution (see **Beam damage** in **Morphologies of thiophosphates solid electrolytes**). As a result, a maximum current of 2 nA will be used for imaging. Next, the working distance (distance between the sample and the lower pole piece) will be aimed at 5 mm. This distance, fixed in a FIB-SEM by the confocal of the two beams on the sample, limits the depth of field but produces a good image resolution. Finally, other parameters such as the scan speed, the focus and the stigmatism will be set and controlled to ensure the best image quality possible.

For cross-section observation, the stage of the SEM is tilted to 54° before imaging. As the electronic beam is not normal to the plan of the cross-section face, a tilt correction of -36° is applied as well as a dynamic focus of ca. -1.5 %: this ensures obtaining a cross-section exempt of distortion with a sharp focus from top to bottom of the image.

2.5 3D observations: focus ion beam-SEM tomography

Focus ion beam-scanning electron microscopy (FIB-SEM) was used to characterize the materials' microstructures. FIB-SEM preparation and acquisition were made on a Zeiss Crossbeam 550®. A scheme of the FIB-SEM geometry is presented in **Figure 23**.

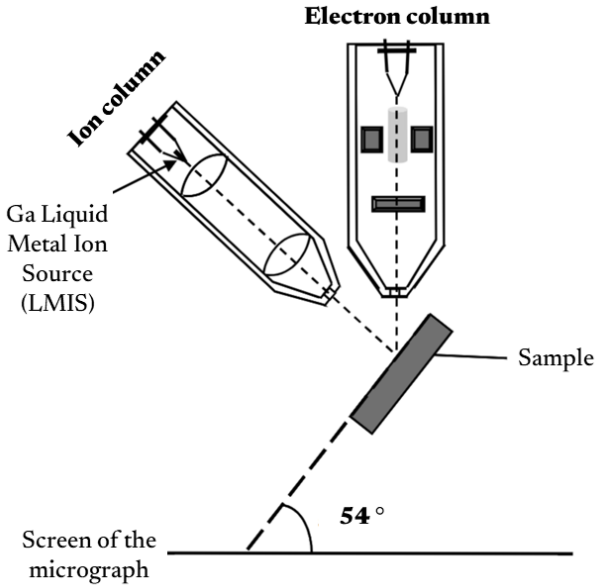

Figure 23: Schematic illustrating the geometric position of ion column, electron column and sample stage tilted to 54° at the coincidence point in the FIB-SEM chamber adapted from Ref. [117].

The FIB consists of a beam of ions, in this thesis exclusively gallium ions Ga^+, which are focused to a small spot using electromagnetic lenses. While the SEM is imaging the sample, the FIB can be used

in several manners. The first is milling: as the beam is focused, it ablates and vaporises the materials by sputtering. Gallium ions bombard the sample and knock out atoms from the surface, milling the material layer by layer. Precise trenches can be dug, and regions of interest extracted. The second is deposition: a gas precursor is injected simultaneously with the ion beam, and the gas molecules are then cracked and deposited on the surface. Protection coating can applied on the surface of the sample to reduce degradation/amorphisation due to the ion beam.

The major advantages of this technique are its excellent imaging resolution (down to a few nm up to tens of μm), its milling precision (down to a few nm) and the great contrast between the phases. In addition, as mentioned in the previous section, multiple detectors could be operating simultaneously providing even more information with a simple scan. However, this technique is destructive making the analysis of the same volume in different states impossible.

The principle of FIB-SEM tomography is based on the successive milling and imaging of a cross-section. **Figure 24** represents the workflow of a FIB-SEM tomography acquisition.

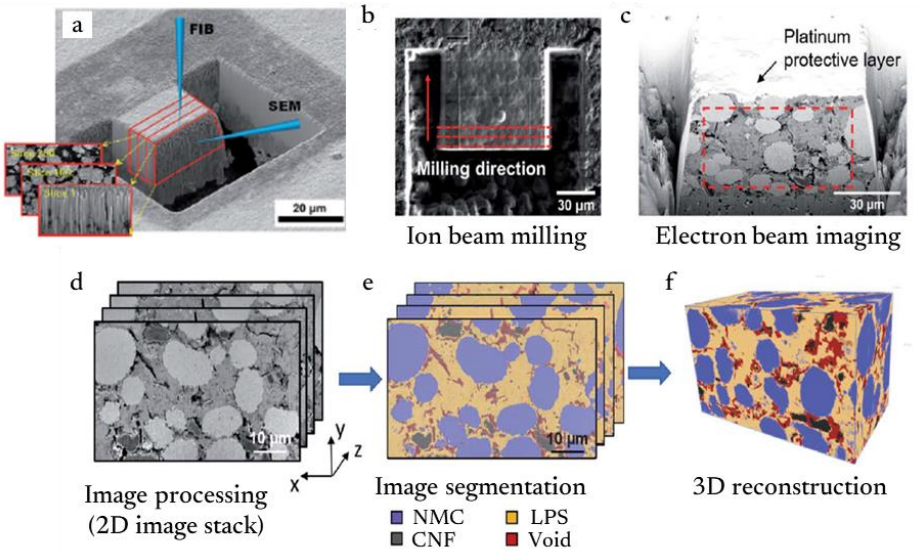

Figure 24: Workflow for FIB-SEM tomography. a) View of the region of interest with the SEM and FIB beams represented. b) Ion-beam milling and c) BSE electron beam imaging. d) 2D image stack obtained after image processing. e) The segmented data and f) its 3D reconstruction. Adapted from Ref. [64].

The sample surface is oriented at 90° relative to the ion beam. This corresponds to a tilt angle of 54° for the SEM stage (**Figure 23**). The idea is then to take an image of the cross-section of the area of interest with the electron beam (rectified by tilt correction of -36°) and then to ablate a determined thickness of material with the ions beam (**Figure 24a-b**). This process of successive imaging/milling is repeated until the area of interest has been fully imaged/milled. It ensues a pile of images along one axis, called a stack, from which volume can be reconstructed (**Figure 24d-f**). Previously to the

acquisition, a layer of carbon and/or platinum was deposited on the area of interest to prevent beam damage (**Figure 24c**).

This method is slow due to the ablation step, which is often the most time-consuming operation. On this particular microscope, SEM imaging can be performed simultaneously with ion ablation, called beam interlacing: this saves some time compared to a more "classic" process where imaging and milling are two independent processes and improve the beam stability throughout the acquisition. While the basic principle is simple, this technique requires long sample preparation and presents some challenges regarding the automation of acquisition and stability.

2.5.1 Sample preparation

A typical sample preparation for FIB-SEM tomography is described as follows: The area of interest is protected by one µm-thick layer of platinum deposited on the surface (30 kV – 3 nA). Fiducial markers are etched on the platinum and then filled with a carbon deposit (30 kV – 50 pA). Those markers both serve for the alignment correction of the successive imaging as well as the milling position. A 1 µm-thick carbon film is deposited to protect the surface of the sample (30 kV – 3 nA). Trenches around the area of interest are dug to open the cross-section of the electrolyte and reduce the shadowing effect during secondary electron imaging (30 kV – 30 nA). Those trenches' height should be one and a half times deeper than the region of interest. The cross-section is polished at the aperture used for further acquisition (30 kV – 3 nA) to obtain a flat surface. The acquisition is then started with the same settings for the cross-section polishing.

2.6 Numerical methodology for the description of morphologies

In every imaging technique, the same workflow can be found to extract numerical data from images. First, the pre-treatment of the images will aim to remove artefacts from the acquisition. Then, the images are segmented, in other words, every object pixel (or phase pixel) is assigned to a different number. Finally, algorithms can be used on segmented images to extract metrics.

2.6.1 3D FIB-SEM images pre-processing

During FIB-SEM tomography acquisition, beam instability can slightly shift the field of view. The images need then to be registered with one another. To do so, image sequences are imported and stacked, then registered using Fiji software and its plugin Multistackreg[118,119]. From the plugin, a translation registration is applied, and a transformation matrix is extracted. The shearing due to the 54° angle of the electron beam is corrected using the previously extracted transformation matrix with

an in-house Python code (available in **Appendix A: Shearing correction code**). The registered stack is then cropped to remove the blank edges.

A shadowing effect on secondary electron images can appear while advancing through the acquisition, called intensity gradient. Such gradients are removed from secondary electron images with the Xlib[120] plugin in Fiji.

When a considerable amount of curtaining is present (emerging from Ga^+ ion channelling via pores), VSNR is used[121]. Generally, three Gabor filters are used with the 2D model over two hundred iterations. All of them are set to a noise level of thirty with a $\sigma_x = 0.5$ and a zero angle. Only the σ_x is changed to twenty, thirty and fifty for the three filters.

Secondary electron and backscattered electron images are merged and exported as a .h5 file as a 4D stack. This method allows to withholding of both Z-contrast and topographic contrast in each voxel while improving the ensuing segmentation process.

2.6.2 Segmentation

The pre-treated SEM images are segmented using Ilastik software[122]. The pixel classification is trained with annotations until the output segmentation seems acceptable with minimum error in the phase identification. Practically, it consists of first making annotations every hundred images along the three axes. Once done, the segmentation results are checked in between every hundred images. If the machine learning model needs more training (considerable errors in phase identification), more annotations are done. This process is repeated until acceptable segmentation is obtained.

2.6.3 Representative elementary volume

Before any quantification is done on volumes, the representative elementary volume (REV) is calculated with an in-house Python code, inspired by Singh et al., 2020[123]. The REV corresponds to the minimum volume from which the value of interest will be constant. The deterministic REV, presented in this manuscript, is the value of interest against the studied volume. When the value of interest remains constant, the REV is reached. The code is available in **Appendix B: REV code**.

2.6.4 Quantifications

To assess the ratio of active material over the electrolyte, the volume fraction of each phase is calculated using the MorpholibJ plugin's function "Analyze Region 3D". The volume fractions are then converted to weight ratio (similar to the synthesis) using each material density.

The percolation of a phase is important for its transport properties (electronic in the case of NMC and ionic in the case of LPS). The connection among one phase is calculated by the adjacent voxel with 6 nearest neighbours (faces of the voxel), the most severe parameter to calculate connection. A percentage of connected particles can then be calculated.

Once percolation is assessed, the distances within a phase are calculated. To do so, geodesic distance maps are calculated with the MorpholibJ plugin with a marker (starting point) on the top of the volume (surface of the sample). This calculation gives the distribution of paths within a phase in a defined direction from a starting point. The geodesic map can be represented in the volume with a colour scale representing distances such as pictured in **Figure 25**.

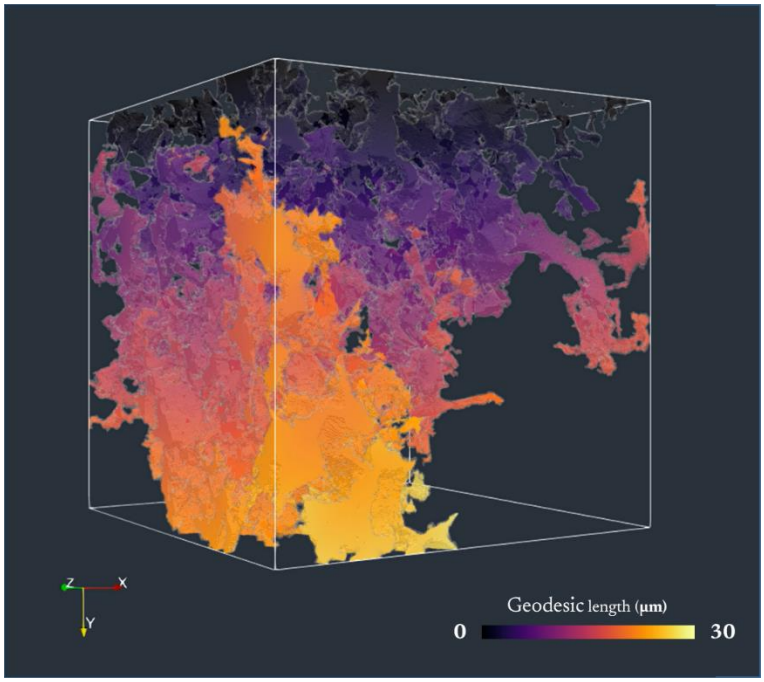

Figure 25: Geodesic distance map within the pores phase of a solid electrolyte.

Associated with the distance inside a phase, the geometric tortuosity is calculated with the ImageJ plugin made by Roque and Costa, 2020[105]: the calculations are performed in 3D while the propagation is set to the 6 near neighbours voxel. This method has the advantage of running without tremendous computational resources in a reasonable time. TauFactor has been investigated[106] and gives a similar trend as the previous plugin but it takes considerably more resources and computational time.

Now that the distances are measured, bottlenecks in the solid electrolyte could be investigated by the local thickness parameter obtained in Fiji[124]. Histograms are calculated from the 3D local thickness representation. The local thickness lookup table is adapted to the thickness maxima between all samples.

Once the conducting phases were characterized, the blocking phase, in SSB the porosity, is described. Pores size distributions are calculated using the 3D Suite[125] in Fiji. Histograms are then plotted with the Feret diameter. The cumulative histogram of the volume of pores is calculated with the associated volume of each pore over the sum of all porosity.

On the composite electrode, the inner porosity of the NMC622 is estimated by a semi-automatic process in which the inner porosity is closed by filling a few slices and the function 3D Fill Holes from 3D Suite is applied. The difference from the initial to the 3D filled holes stack is then calculated.

2.6.5 Particle size distribution estimation

Particle size distribution of the solid electrolyte is estimated by SEM as other methods such as laser diffraction analysis cannot be applied to air-sensitive samples.

A small amount of LPS powder was placed on an SEM stub before being measured at a Zeiss Ultra 55 SEM using 2 kV. Ten images were taken in random locations using a backscattered electron detector at a pixel size of 140 nm. **Figure 26** gives a representation of the estimation process.

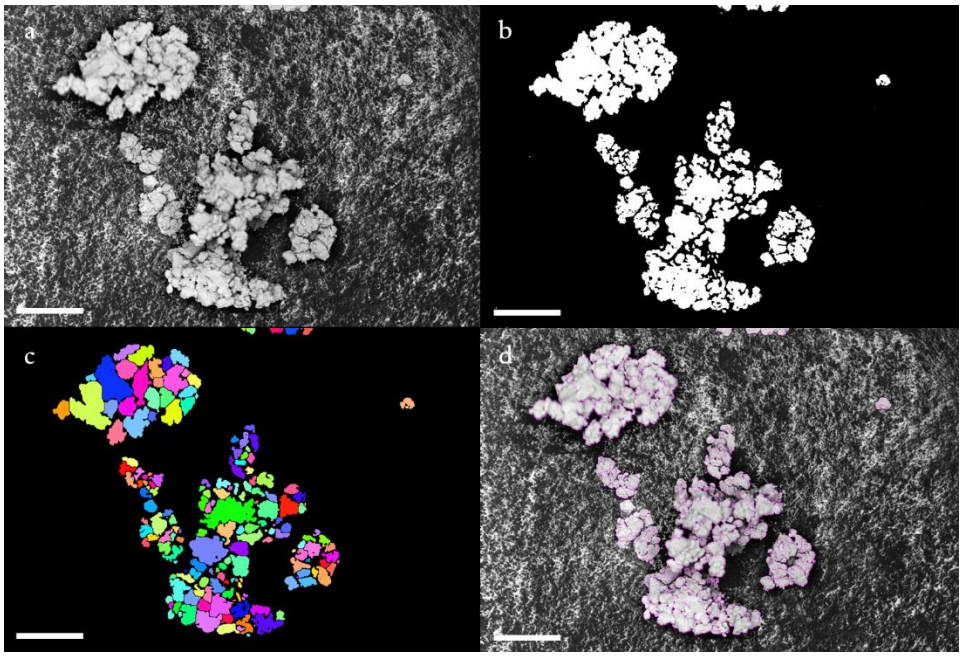

Figure 26: Overview of the size distribution estimation with a) the original BSE image, b) the segmented image, c) the watershed separation, after erosion, dilatation and labelling and d) estimation overlaid to the original image. The scale bars represent 20 µm.

The obtained SEM images are segmented using Ilastik software[122] and the segmentation images are then imported to Fiji software[118,126] (**Figure 26b**). A distance transform watershed from MorpholibJ[127] (Borgefors model) is performed to separate agglomerate particles into smaller elementary particles. Once the threshold is applied, the images are successively eroded using

morphological filters from MorpholibJ (erosion, disk kernel of radius 1) and then dilated using the built-in binary operation of Fiji (dilate, iteration 1, count 1) (**Figure 26c**). This step ensures to disconnect all the particles previously separated with the watershed operation. A histogram of the Feret diameter is calculated from the analysis of every particle using the in-built Fiji analyser.

2.6.6 Developed surface from 2D images

The developed surface of NMC is also measured by 2D images. NMC622 powder alone is pressed in the solid-state cell at different pressures and MBond resin (MBond 610 curing agent, Micro Measurements®) is then infused in the pellet. A primary vacuum is used to remove all the remaining air inside the pellet until the resin is cured (24h). The subsequent pellet is then embedded into conductive copper resin (GEPD/Cu, Escil®) at 150°C and 5 bar and then mechanically polished on a Presi® MECATEC 300 SPS. The polishing is performed until 1 µm on polishing cloths with a polycrystalline diamond suspension. A finishing step is done with crystallization-free colloidal silica (1:20 volume dilution in water) on the finishing cloth. The sample is carefully rinsed under water, dried out under pressurized air and directly brought to the Zeiss Ultra 55 SEM.

Twenty-five SEM images are acquired at a 2 kV acceleration using the backscattered electron detector at a pixel size of 28 nm. The images are then segmented in Ilastik.

The technique of mean intercept length is used to estimate the surface from 2D images which eliminate the discretisation of the surfaces by pixels. To accomplish that, four convolutions are done using directional kernels (e.g. [0 1 -1], named +X) and the number of intercepts is measured. Knowing the length between intercepts, the formula $\hat{S}_v = 4N_L$ is used where $\hat{S}_v$ is the estimated surface in μm^{-1} and N_L the number of intercepts by length unit. Measurements from the four directional kernels are averaged into the presented results.

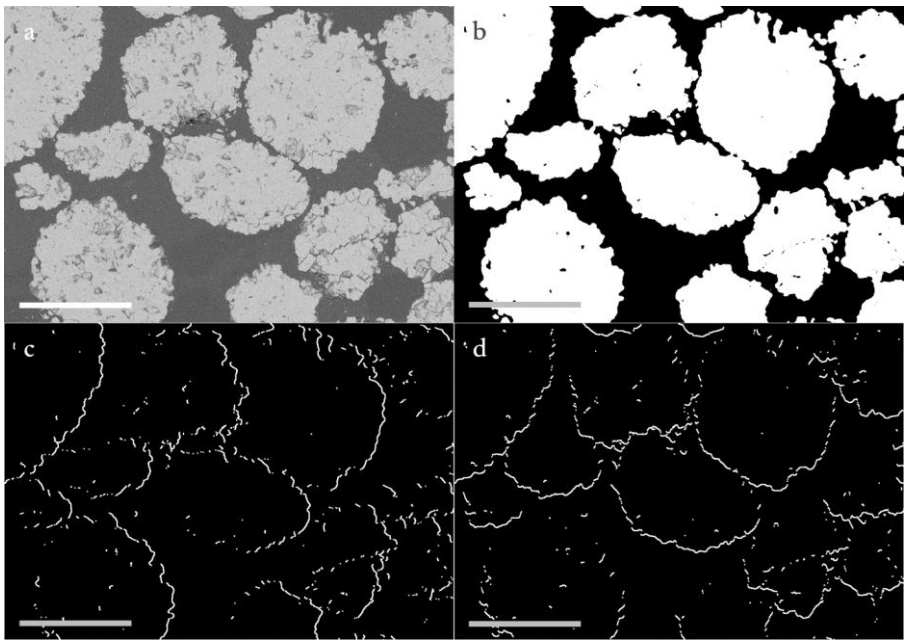

Figure 27: Developed surface estimation, a) original BSE image, b) segmented image, c-d) intercepts along +X and +Y axis respectively. Intercepts were dilated to improve the visibility of the figure. Scale bars represent 5 μm.

2.7 Electrochemical characterizations

2.7.1 Electrochemical Impedance Spectroscopy and ionic conductivity

Electrochemical impedance spectroscopy (EIS) is an effective tool used to study the electrical properties of electrochemical systems. In solid-state systems, it is the first technique used for electrochemical characterization as it monitors the ionic conductivity of the solid electrolyte, a predominant parameter in solid-state batteries. This technique involves applying a small sinusoidal potential perturbation to the system and measuring the response in terms of the resulting current (potential-EIS or PEIS). The frequency at which the perturbation signal is applied varies over a wide range, typically from a few millihertz to several megahertz, to obtain information about the system at different time scales. This allows the identification of different processes that contribute to the overall impedance of the system. One of the advantages of EIS is its ability to separate the different contributions to the system's overall impedance. To interpret the impedance spectrum, researchers often use an equivalent electrical circuit model. This model represents the various components and processes in the system as electrical elements such as resistors, capacitors, and inductors. In the context of battery materials, the equivalent circuit may include elements representing the bulk resistance (R_{bulk}) or grain boundary resistance (R_{gb}), associated with the solid electrolyte. Both resistances (R_{bulk} and R_{gb}) in equivalent circuits are represented by a resistor but the two processes have a two frequency-dependant behaviour. Higher-frequency regions of the impedance spectrum

are typically associated with bulk properties, while lower-frequency regions are more influenced by electron transport and surface properties. By monitoring the R_{gb} in LPS, EIS can confirm the amorphous nature of solid electrolytes.

EIS was used to determine the ionic conductivity of the solid-state electrolyte. A typical spectrum is presented in **Figure 28**.

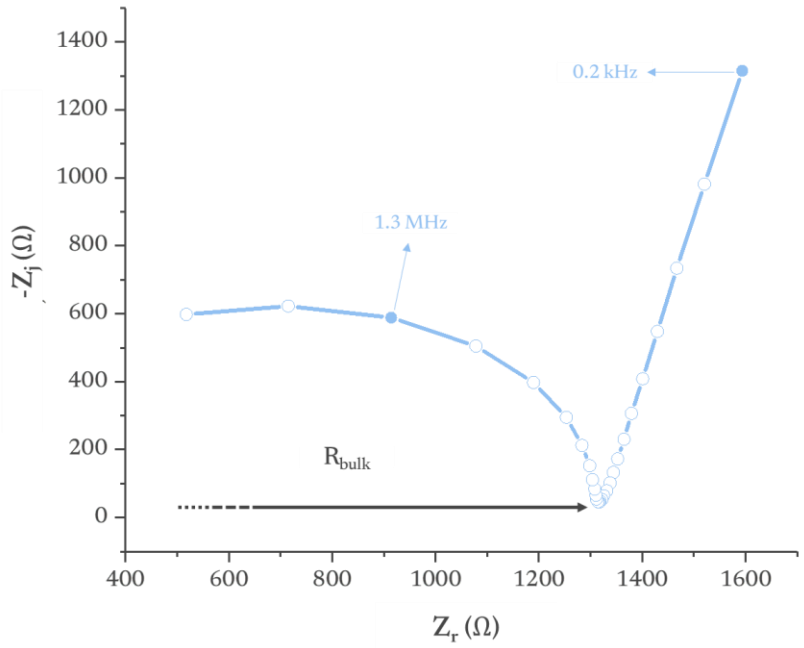

Figure 28: Typical impedance spectrum in a Nyquist plot, obtained with LPS with R_{bulk} represented.

Thanks to this Nyquist plot representation, the bulk ionic resistance can be obtained. The latter quantifies the difficulty for ions to move in the solid electrolyte, which directly affects the battery's overall electrochemical performance. On the Nyquist plot in **Figure 28** of LPS between two stainless steel plungers (ionically blocking), this corresponds to the high-frequency semi-circle: the smaller the semi-circle, the easier the ion transfer, the better the ionic conductivity of the solid electrolyte. **Equation 3** gives the relation between R_{ct} and the ionic conductivity (σ) of the material that directly emerges from the definition of resistivity:

Equation 3: Conductivity formula

$$\sigma = h / (A \times R_{ct}) \quad (3)$$

Where σ is the ionic conductivity ($mS \cdot cm^{-1}$), h is the thickness of the pellet (cm), A its area (cm^2) and R_{ct} is the charge transfer resistance ($m\Omega$).

Practically, the solid electrolyte is densified in the cell and stack pressure is kept through the screws. The impedance spectrum is then collected from 7 MHz to 100 mHz (14 measurements per frequency) with a voltage amplitude from 10 to 80 mV (adapted from the response) using a Biologic® VMP-300. At the end of the measurement, the cell is opened, and the thickness is measured using a calliper.

2.7.2 Galvanostatic cycling

Cycling is a technique to characterize the electrochemical performance and behaviour of batteries during charge and discharge. Schematic charging and capacity retention curves are presented in **Figure 29**.

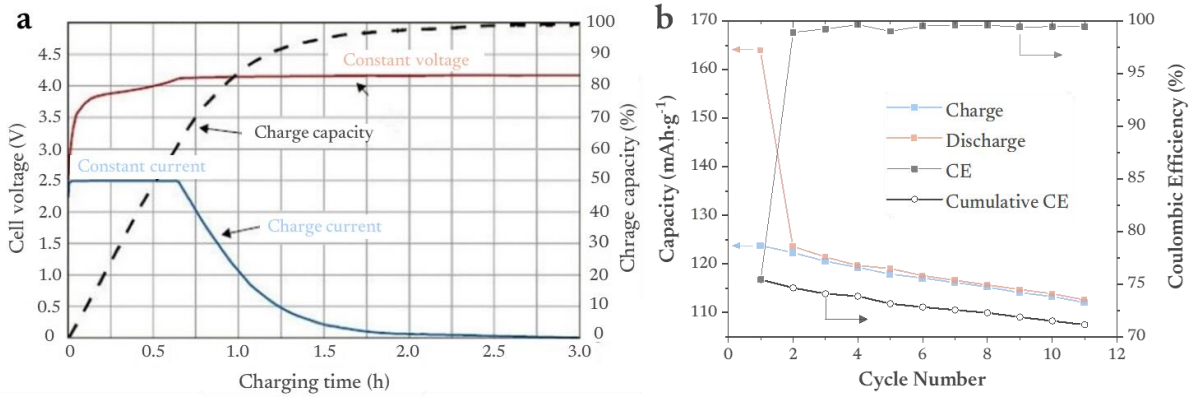

Figure 29: a) Typical charging curves. Adapted from Ref. [128] and b) the capacity retention over multiple cycles.

In galvanostatic cycling, a constant current is applied to the battery and the voltage is recorded as a function of time (red curve, from 0 to 0.75 h in **Figure 29a**). Once the voltage reaches its cut-off value (4.2 V reached at 0.75 h in **Figure 29a**), the voltage is kept constant while the current slowly decreases. This step called controlled voltage (CV), ensures that the charging process is not limited by a high polarisation of the cell. Then, this process can be repeated over multiple cycles to understand battery ageing. The current-time data corresponds to charge and discharge curves from which information could be extracted: first, the area under the blue curve (**Figure 29a**) represents the specific capacity of the battery (mAh), often normalized by the mass loading of the active material in the system (mAh·g^{-1}). Then, the coulombic efficiency (CE) could be extracted from one cycle (**Figure 29b**): it is the ratio of the discharge capacity over the charge capacity. In general, a CE of less than 100 % indicates degradations both chemical and physical in the battery. Next, the lithiation/delithiation voltage of a system can be compared to an optimised system to obtain the polarization. The latter corresponds to an increase in internal resistance.

For NMC622, the effective capacity is obtained by multiplying the theoretical capacity (276.6 $mAh \cdot g^{-1}$) with the mass of NMC in the electrode. The C-rate is chosen and the current of charge/discharge is then deducted. The C-rate, or capacity rate is the rate at which a battery is cycled relative to its maximum capacity where 1C corresponds to the full charge in 1 h and 0.2C, a full charge in 5 h. In practice, a C-rate of 0.05 (eq. to C/20) is used to cycle the SSB from 2.08 to 3.68 V vs. $InLi_{0.3}$ (equivalent to 2.7 to 4.3 V vs Li^+/Li considering $E_{InLi0.3}$ = 0.62 V vs Li^+/Li). The open circuit voltage (OCV) is measured for 30 s between each cycle.

2.7.3 Platting/stripping test

For plating/stripping of the SE, galvanostatic cycling with potential limitation (GCPL) technique is used: the current is imposed in positive mode (plate) and then reversed in negative mode (strip) and is repeated five times with 30 min OCV between each current swap. After each sequence, the current is doubled to evaluate the critical current density for the dendrite's formation. Practically, the current density was calculated at 0.05 $mA \cdot cm^{-2}$ for a current of 10 μA over a 5 mm lithium disk after 25 MPa pressing. The amount of lithium moved at the highest current of a strip has been calculated to be strictly lower than the amount of lithium available in the counter electrode.

2.7.4 Cyclic voltammetry

Cyclic voltammetry (CV) is an electrochemical technique used to investigate the electrochemical behaviour, and in particular, the electrochemical stability window of an electrolyte or a composite electrode. It provides information about the redox (reduction and oxidation) processes, and the electrochemical reversibility of a species and can give already some indications about the irreversible processes (i.e. degradation).

The voltage applied to the working electrode is cyclically varied between two upper and lower potential limits. To study the degradation in reduction, the voltage is swept between 1.4 and - 0.6 V vs Li_xIn/In while for oxidation, it is swept between 1.4 and 3.7 V vs Li_xIn/In. The cycling is performed at a specific scan rate, 100 $\mu V \cdot s^{-1}$.

2.8 Structural characterization

2.8.1 X-ray diffraction measurement at European synchrotron radiation facility (ESRF)

The high energy X-ray beam (100 keV) was used for investigating the solid electrolyte pellet (beam size ~ 5 × 20 μm^2, vertical × horizontal) as a function of depth profile at ID31. The scattered signal

was collected using a Dectris Pilatus CdTe 2M detector. The energy, detector distance and tilts were calibrated using a standard CeO_2 powder (NIST) and the 2D diffraction patterns were reduced to the presented 1D curves using the pyFAI software package [129].

2.8.2 Neutron diffraction at institute Laue Langevin (ILL)

Transparent vanadium cans of 5 mm diameter were filled with ca. 1 g of solid electrolyte, and they were sealed under an argon-filled glovebox with an indium wire. The powder neutron diffraction experiments were carried out on the D2B beamline at ILL, Grenoble, France. A wavelength of ca. 1.61Å was used.

2.9 Specific electrochemical cell for *operando* measurement

The scheme of the specific transfer box for *operando* measurement is displayed in **Figure 30**.

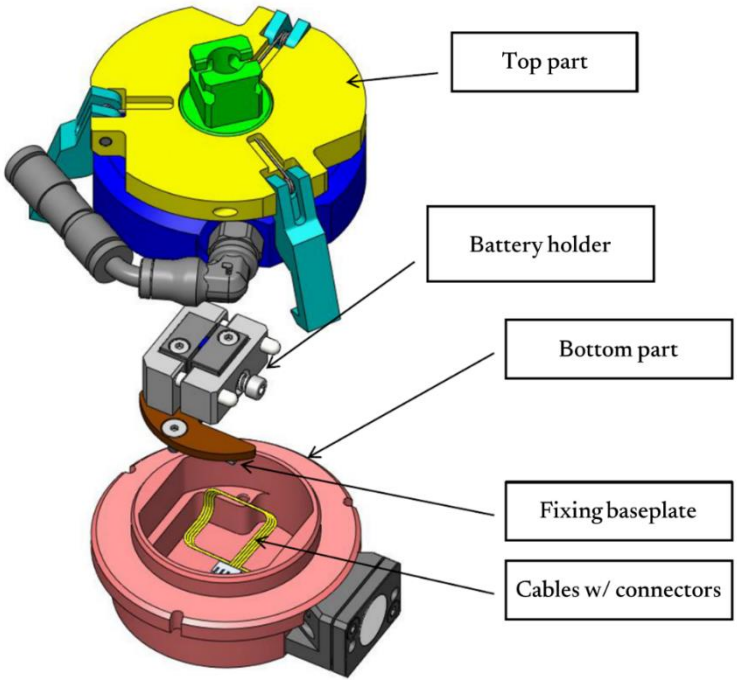

Figure 30: Scheme of the *operando* transfer box.

The bottom part ensures the connection inside the microscope and the support of the battery holder while the top part ensures the airtight transfer from the glovebox to the microscope. The battery holder consists of two plates in which the electrochemical stack (half-cell or full-cell) can be inserted. A PEEK screw maintains the stack pressure between the two plates. Due to the connection between the transfer box and the microscope, no rotation inside the SEM can be used.

The solid-state cell has been modified to obtain a half-circle cell with a directly visible flat surface. The modified cell is presented in **Figure 31**.

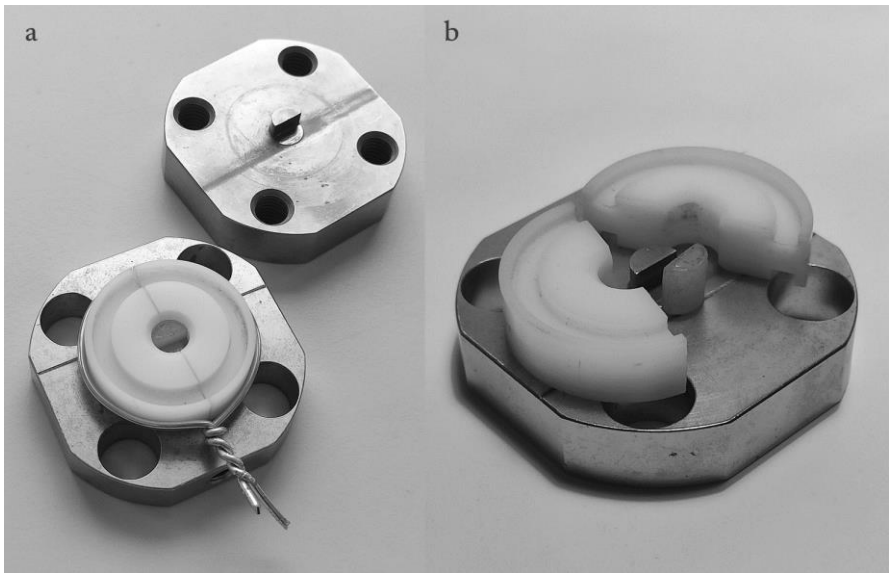

Figure 31: Modified solid-state cell to manufacture half cylindrical cell. a) Top and bottom part and b) opened bottom part.

Half of the stainless-steel pistons were milled and replaced by a Teflon® half cylinder. This ensures the electrical insulation of the battery. To avoid fracture or breakage of the pellets during extraction (or other manipulation artefacts), the POM pellet holder has been sawed in half, and held together by a steel wire when fabricating the battery.

With this *operando* cell design and the modified solid-state cell, the battery cross-section can be directly investigated. It results in the special cross-section orientation where the positive electrode is on the left of the field of view while the counter electrode is on the right.

3

Morphologies of thiophosphates solid electrolytes

In the literature, degradation processes of the solid electrolytes are related to the electrochemical activities that are supposed to cause all the chemo-mechanical processes, but it could be coming also from an early stage, the room temperature sintering of the solid electrolyte itself. As an example, it is well known that Li-ion transport is optimal in solid-state batteries if the tortuosity is reduced to unity in the 3D system. Thus, understanding the sintering from microstructures and morphologies point of view is an asset[108,130]. The study of the 3D morphology and/or microstructure of the solid electrolyte during room temperature sintering is bringing crucial information to improve their overall electrochemical performance. Before that, and foremost, as sulfide solid electrolytes are sensitive materials, the transfer solution between the glovebox and the SEM needs to be assessed as well as the effect of the electron beam on the morphology of such electrolytes.

3.1 Air exposure and beam damage

As a rule of thumb, all sulfide solid electrolytes show a high reactivity towards air and moisture, including the Li_2S-P_2S_5 family mainly Li_3PS_4 (so-called LPS). This high reactivity can lead to the decomposition of the electrolyte accompanied by outgassing of H_2S[131]. In addition to the toxicity of this gas[132], the outgassing is accompanied by irreversible changes: some studies report the chemical aspect of this decomposition[133,134] but fewer report the actual morphology evolution of RT sintered pellets. In parallel, sulfide electrolytes also suffer from electron beam damage. Indeed, LPS tends to melt and/or evaporate under prolonged high doses, a phenomenon commonly observed with transmission electron microscopy (TEM)[135]. To ensure that our methodology will not be influenced by air/moisture exposure and beam damage, we evaluated the extent of these parameters on the electrolyte morphology.

3.1.1 Air exposure

LPS was transferred from the glovebox to the SEM with a transfer chamber developed by Zeiss®. This chamber can transfer samples under argon either at atmospheric pressure or under a static vacuum. Once the first set of images was taken with the SEM under a vacuum atmosphere, the chamber was purposely open to air and moisture, kept open for 60 s and then closed again prior to a second investigation on contaminated samples. The images of pristine and air-exposed samples are presented in **Figure 32**.

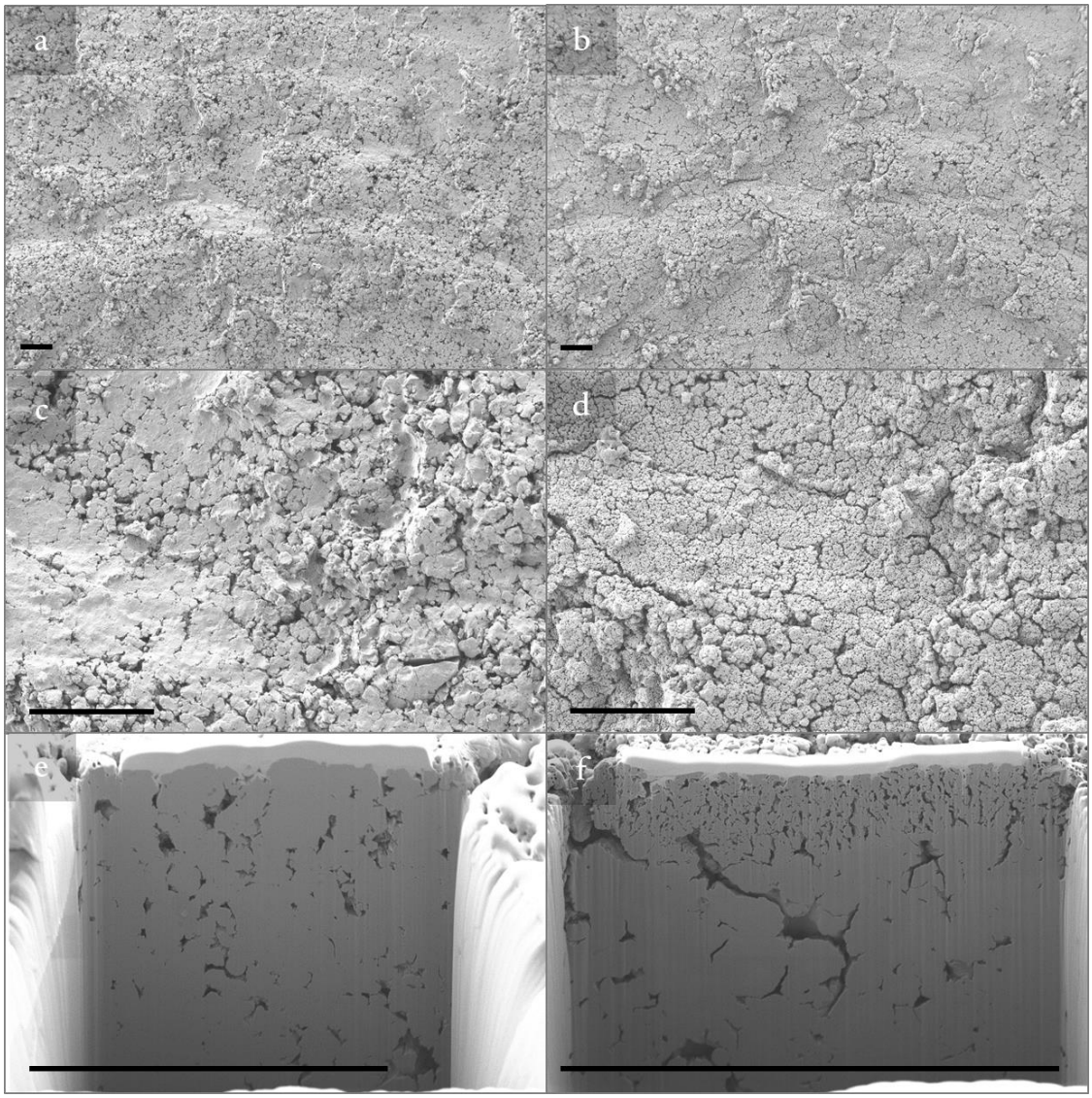

Figure 32: Secondary electrons image of pristine LPS (left) and LPS after 60 s to air exposure (right). (a) and (b) low magnification images, (c) and (d) mid-resolution images, (e) and (f) cross-section images. The scale bar represents 30 μm.

From the low magnification images, it is hard to find noticeable differences between the samples, despite some wrinkles seeming to appear at the surface of the exposed sample. At higher magnification, differences are there: the sample exposed to air/moisture seems "dry" (like the mud can look when the sun evaporates water fast), and LPS resembles a parched desert. The thickness of the dried LPS surely depends on the open porosity of the material but from the cross-section of a pellet pressed at 255 MPa for 10 min, the thickness of the dried layer is ca. 5 μm for a 60 s exposure. The reaction with air/moisture is also accompanied by the formation of crystalline phases, not present in the pristine state as shown in **Figure 33**.

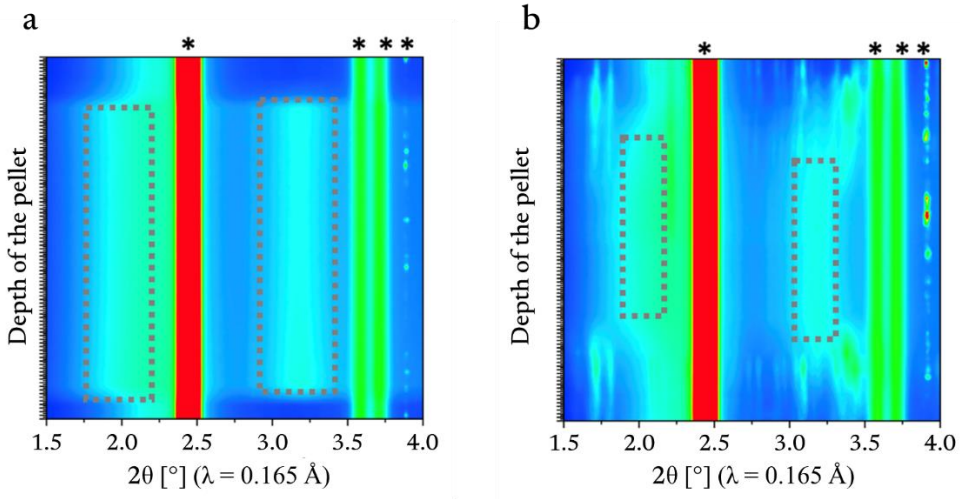

Figure 33: Wide Angle X-ray Scattering (WAXS) scans (5 µm beam size) along the depth (ca. 500 µm) of the LPS pellet from LEPMI in a) pristine and b) exposed to air. Stars indicate the diffraction of the POM pellet holder, and the dashed rectangle represents the amorphous phase.

In **Figure 33** in the pristine state, a homogenous amorphous phase can be found from the surface to the bulk. On the air-exposed sample, however, a layer of ca. 50 µm, mixing crystalline and amorphous phases is found on both exposed surfaces. Unfortunately, the formed crystalline phases could not be identified as no match has been found in the database. Nonetheless, decomposition product such as Li_2S, Li_3PO_4, S_8 and Li_3P could be expected[133,136,137]

From these results, we can see that LPS undergoes severe structural and morphological damage when being exposed to air/moisture. In addition, it is now easier to track any air/moisture exposure of the samples and to testify that the transfer chamber solution provided by Zeiss® allows air-free transfers from the glovebox to the SEM.

3.1.2 Beam damage

Another issue that can occur when working on solid electrolytes is beam damage, a well-known process happening in the electron microscopy field. To verify the effect of the beam on the LPS sample, the centre of a cross-section was continuously scanned at 2 kV – 2 nA and overall images were taken at different intervals with the same parameters. The images are presented in **Figure 34**.

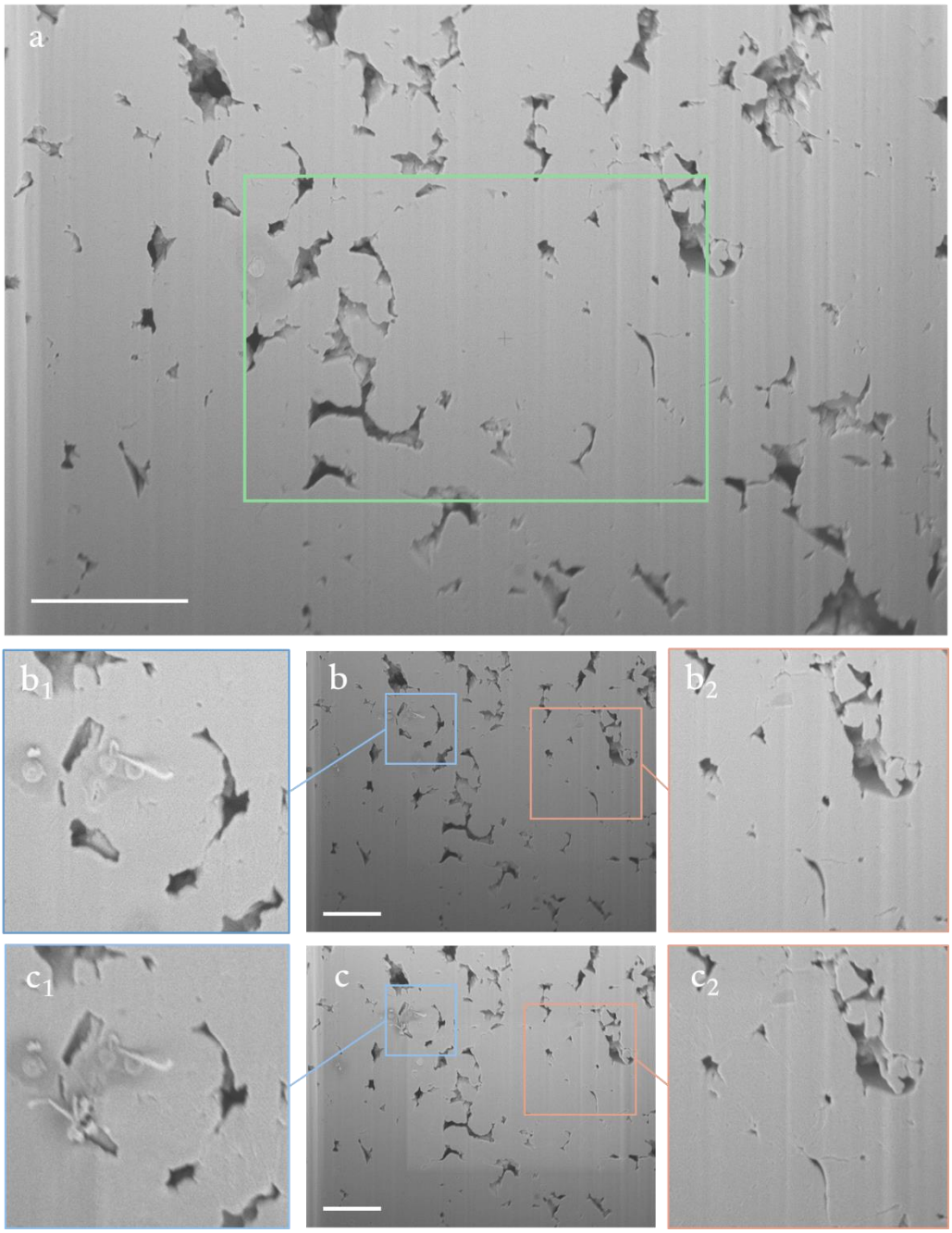

Figure 34: a) Pristine secondary electron images of a cross-section in LPS (LEPMI- 255 MPa – 10 min). The green rectangle represents the irradiation area. Secondary electron images after b) 120 s and c) after 600 s exposure. The scale bar represents 5 μm.

Two phenomena can be seen in these images: the first, highlighted by the blue squares, is the sample redeposition from which small structures grow. This process can be seen after a short exposition of 20 s and is mainly caused by the beam park position, always on the top left of the scanned region (the green rectangle in **Figure 34**). After each scan, the beam is shortly parked at this precise spot and a higher dose is taken, which in turn, "evaporates" the LPS (**Figure 34b$_1$** and **Figure 34c$_1$**). Around the beam, where the dose is less intense, the vapours can condense and redeposition occurs. The second process, highlighted by the orange squares (**Figure 34b$_2$** and **Figure 34c$_2$**), is the main type

of beam degradation observed on LPS. As the dose is better spread over the area of interest, only minor changes can be seen. It seems that the LPS is slightly melting on the surface and that edges (of porosity) are less defined. The irradiation area can be directly seen on the image after 600 s exposition as the grey value lightly rises in the centre. Nonetheless, when looking closely at the morphology of the porosity (**Figure 34b$_2$** and **Figure 34c$_2$**), hardly any differences can be pointed out, ruling out the fact that the data interpretation could be altered by beam damage radiation.

LPS is moderately damaged by the electron beam but, considering the range of doses reached with the SEM, they remain negligible for our morphological investigation. Nevertheless, the beam exposure will be reduced as much as possible during imaging and several solutions will be taken to ensure it remains negligible. First, the scanning area will be "frozen" anytime image acquiring is not necessary. In the SEM, this results in the total deflection of the beam of the sample. Second, the acceleration voltage will be kept as low as possible, e.g., in the range of 1.5 and 2 kV for imaging. Third, the beam current should be lowered as much as possible, however, this also increases the signal-to-noise ratio in the images. As seen previously, a current of 2 nA has a moderate effect on the morphologies, even after 120 s exposition, yet it gives satisfactory image quality both in secondary and backscattered electrons imaging.

3.2 Commercial or homemade electrolyte

Two options are available to obtain amorphous LPS powder, either from a supplier like MSE Supplies® or by performing the synthesis in-house. The motivation to get the powder from the provider lies in convenience as synthesis optimisation is not needed and reproducibility should be optimal. Still, a comparative study, with an in-house ball-milling synthesis, was performed with the help of the LEPMI (Laboratory of Electrochemistry and Physical chemistry of Materials and Interfaces) to assess optimal quality and select the best candidate for the rest of the thesis.

3.2.1 Comparative study of LPS quality: MSE vs LEPMI

In this section, LPS from LEPMI and MSE will be referred to as LPS_{LEPMI} and LPS_{MSE} respectively. The first point of comparison between the two materials is their structure properties. LPS_{LEPMI} has already been proven to have an amorphous structure (**Figure 33**) from which spectra have been extracted (**Figure 35**):

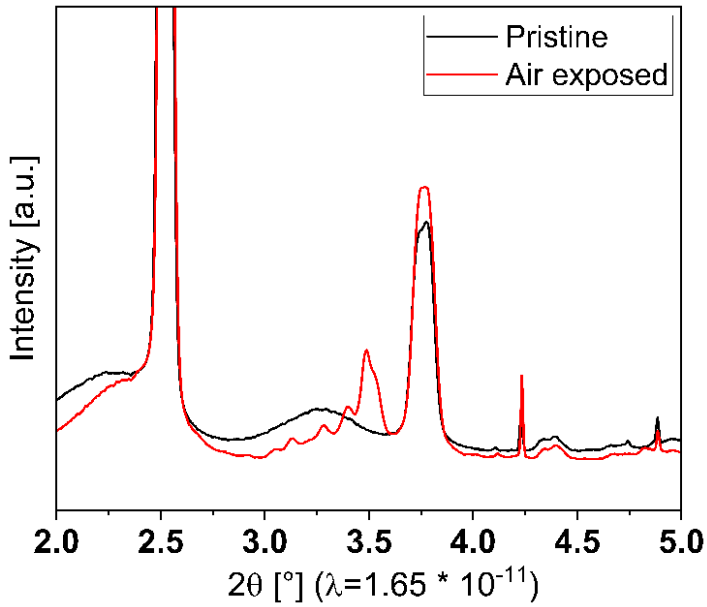

Figure 35: ESRF X-ray diffractograms of the LPS sample together with the LPS exposed to air, both measured in their POM disk and through a pouch bag.

Then LPS_{MSE} was characterized by neutron diffraction to assess its structural properties (**Figure 36**).

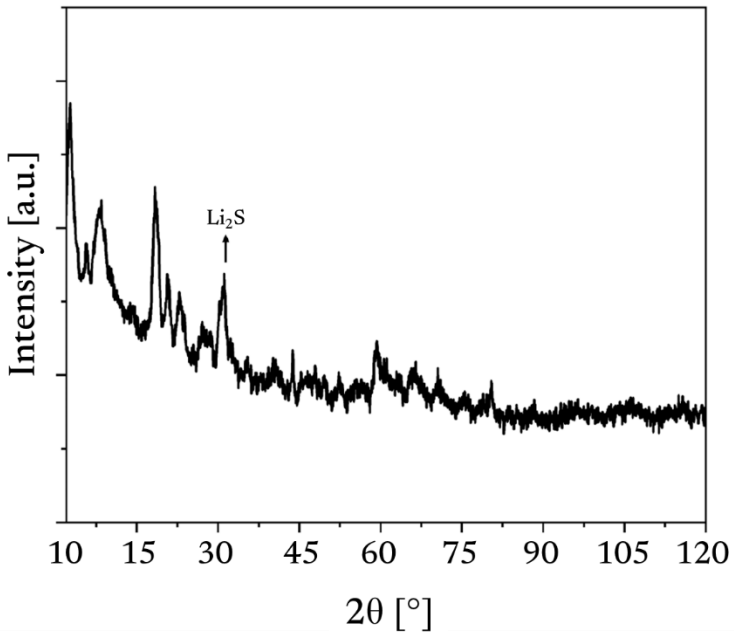

Figure 36: Neutron diffractogram of LPS_{MSE}. Sharp peaks indicate the presence of a crystalline phase. The peak corresponding to Li_2S is indicated.

From this diffraction pattern, we can see that LPS_{MSE} has a significant amount of crystalline phase (despite being commercialized under amorphous phase) and an identifiable impurity ascribed to Li_2S cubic structure. The phase identification indicates that the phase is mostly attributed to a crystalline Li_3PS_4 phase.

The two solid electrolytes, LPS type, were room temperature sintered in the same condition (382 MPa, 10 min) and FIB-SEM tomographies were acquired on the obtained pellet, presented in **Figure 37**.

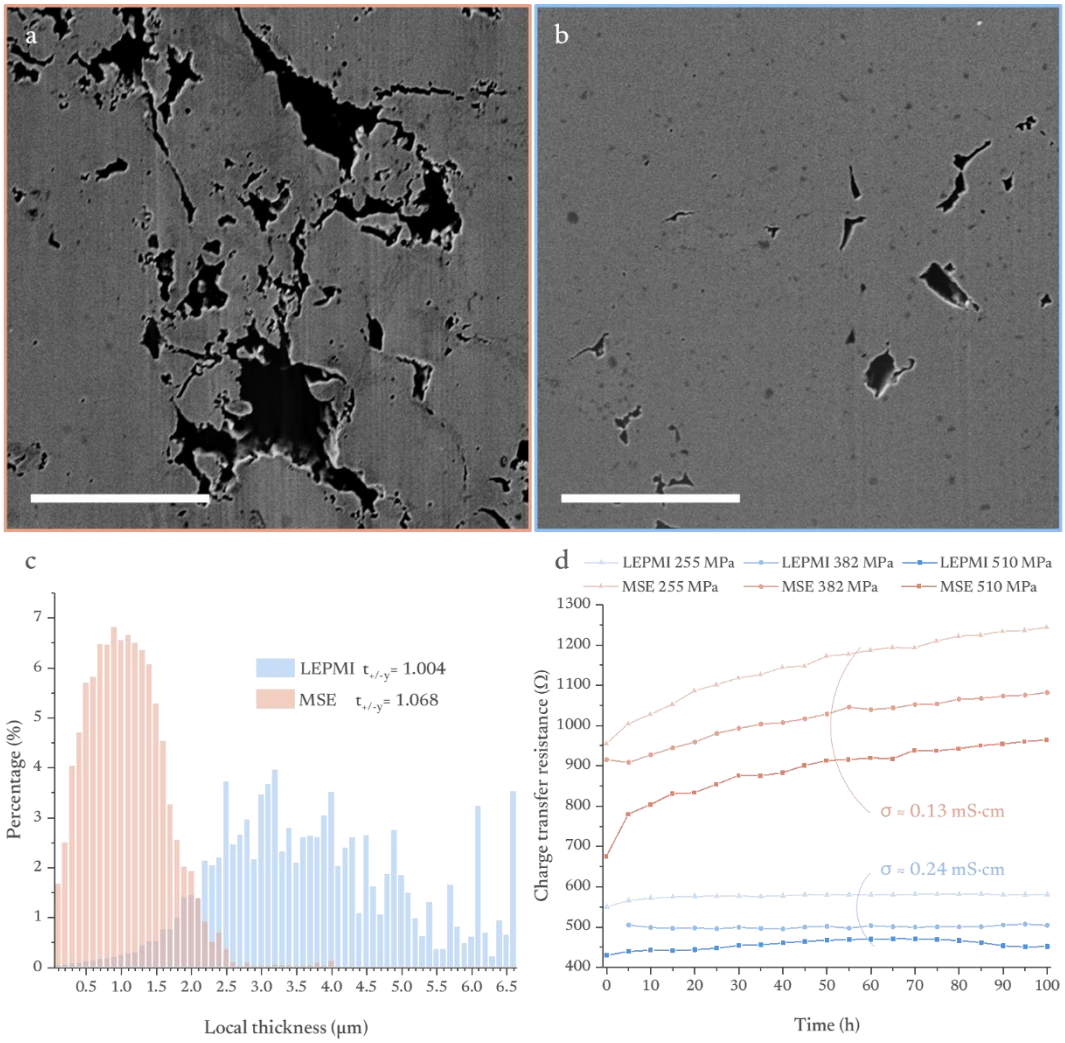

Figure 37: Results of the FIB-SEM tomographic volume on LPS_{MSE} and LPS_{LEPMI} electrolyte pressed at 382 MPa for 10 min. a) and b) secondary electron images of LPS_{MSE} and LPS_{LEPMI} electrolytes respectively. Scale bars represent 5 µm. c) the local thickness histograms and geometric tortuosity and d) the evolution of ionic resistance over time at different pressures.

After segmentation, the porosity in the LPS_{MSE} sample is measured at 17.7 vol% from which 96 % of the porosity is interconnected in the volume. On the other hand, LPS_{LEPMI} only exhibits a 1.1 %vol of porosity. In this case, the biggest interconnected porosity represents 54 % of the total porosity. Geometric tortuosity and local thickness calculations give an insight into the average length of the lithium-ion path inside the solid electrolyte and the average width of the lithium-ion channel respectively (relevant for lithium-ion transport and effective tortuosity calculation). For the former (LPS_{MSE}), this significant amount of porosity will subsequently hinder the lithium-ion path length

since the average local thickness of LPS_{MSE} is roughly 1.0 μm with a tortuosity of 1.068, whereas, for the LPS_{LEPMI}, the average local thickness is 3.7 μm with a tortuosity of 1.004.

As the porosity is known to decrease the ionic conductivity, we decided to follow the evolution of the ionic resistance (bulk resistance and grain boundaries resistance) as a function of time (**Figure 37d**) to monitor the relationship between porosity/pressure and possible relaxation of the room temperature sintering process. It can be seen that LPS_{MSE} ionic resistance greatly increases over time while LPS_{LEPMI} resistance is steadier. For the former, this could be explained by the amount of porosities remaining in LPS materials. Over time, the sample will suffer some relaxation processes leading to increase the ionic resistance, i.e., decrease the ionic conductivity. When looking at both electrolyte ionic conductivity, LPS_{LEPMI} has an average conductivity of ca. 0.24 $mS.cm^{-1}$ at 20°C close to the literature value[52] while LPS_{MSE} only has half with ca. 0.13 $mS.cm^{-1}$ at 20°C (even though supplier specification is given for ca. 1 $mS.cm^{-1}$ at room temperature). The difference between the value obtained from the room temperature sintering and the one reported by the supplier comes most probably from the temperature of the sintering. Indeed, it is well known that crystalline materials are generally sintered at high temperatures, thus at RT, there are too many porosities to provide a good Li-ion pathway.

Based on the aforementioned results, LPS_{LEPMI} electrolyte will be chosen for the rest of the studies owing to its RT sintering ability.

3.2.2 Calendar Ageing

LPS was kept in a glovebox for five months to verify its storage ability. A pellet was prepared using the same sintering condition (382 MPa – 10 min) prior to being investigated by FIB-SEM. The results are presented in **Figure 38**.

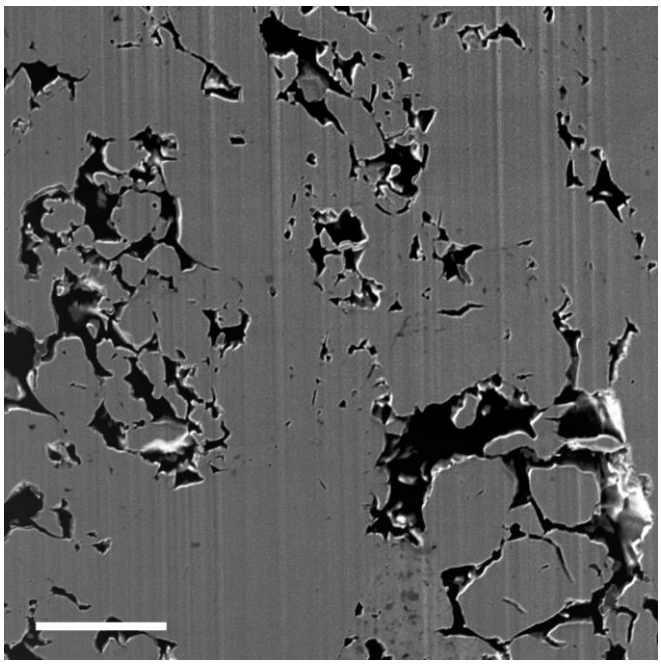

Figure 38: Secondary electron image from the FIB-SEM tomography on LPS aged 5 months in the glove box. The scale bar represents 5 μm.

From this tomography, a porosity of ca. 20 % is measured, and 98 % of the pores are interconnected. This amount of porosity results in a tortuosity of 1.060 and an average local thickness of 1.1 μm. From fresh to glovebox-stored LPS, there is a radical increase of porosity, from 1.1 to 20 % respectively. The ionic conductivity of this pellet was measured at 0.13 $mS{\cdot}cm^{-1}$, half of its initial value (**Figure 37d**). Several hypotheses can explain such behaviour, i) an exposition to air and moisture caused by a glovebox leakage in the five months and/or ii) a structural evolution of the sample during storage time, as the material is amorphous, the calendar ageing can lead to reach more stable state. Yet, it is challenging to reach a definitive conclusion on the origin of the ionic conductivity decrease since no structural investigation was conducted on this aged LPS. Nonetheless, it is safe to say that LPS undergoes calendar ageing, which will limit the sinterability of the material, leaving sizable porosity. This result is particularly important when mixing LPS with an active material. From this point, only LPS with a maximum of one month of storage will be used to ensure comparable and consistent results throughout experiments.

3.2.3 Disparity of sintering

When the pellets are sintered using the homemade circular solid-state cell, they need to be extracted from the pellet holder before observation, which almost always breaks the pellet. This breakage comes from the adhesion of the LPS to the POM pellet holder. Nonetheless, the centre of the pellet can be extracted while keeping its integrity. From the observation of the top of the pellet, a gradient of porosity can be seen on the surface of a composite electrode, presented in **Figure 39**.

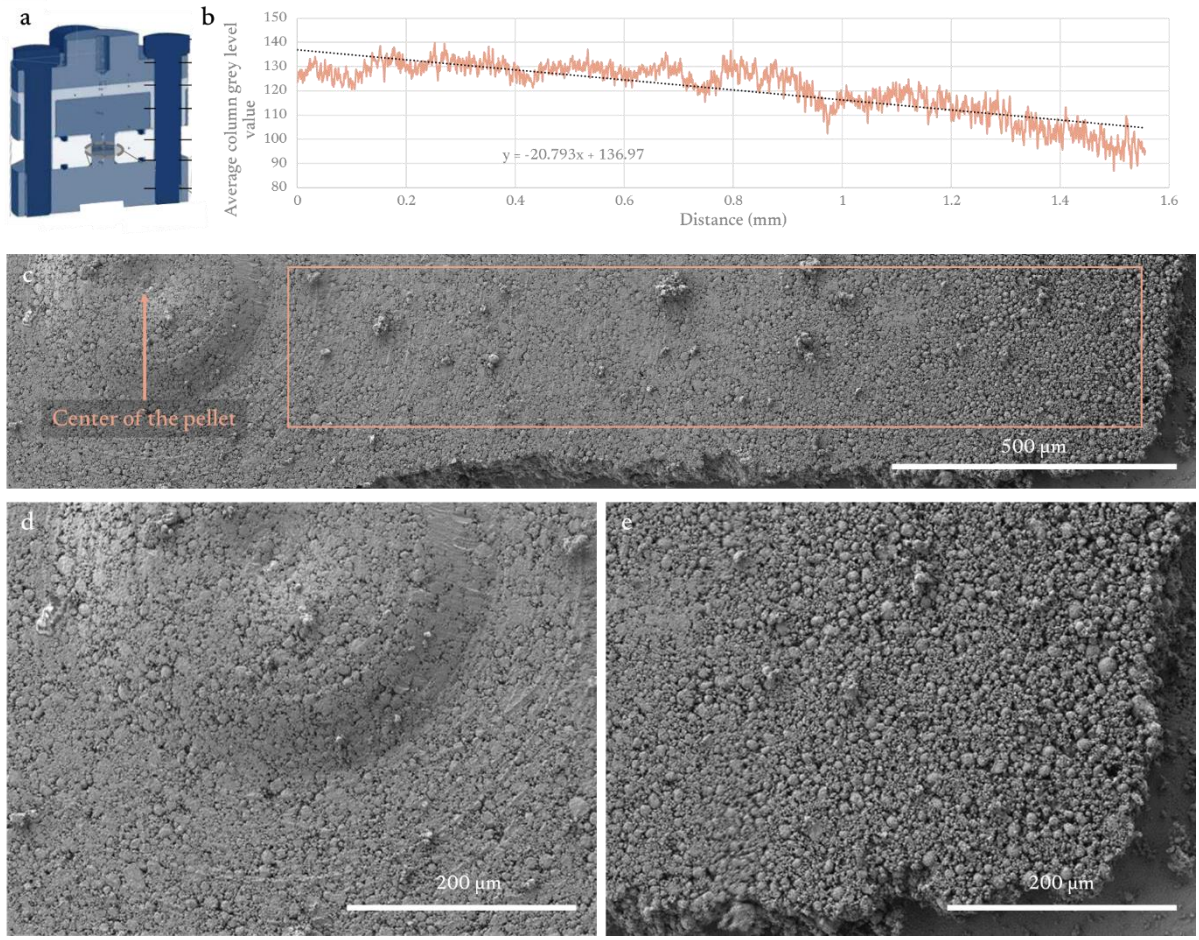

Figure 39: Disparity of sintering from centre to edge. a) The cross-section of the solid-state cell, the POM cell holder in white. b) The profile of the greyscale with LPS/NMC in grey and porosity in black from c) the stitched secondary electrons image of the top surface of a composite positive electrode. d) and e) close-up secondary electron image of the centre and the edge of the pellet respectively.

The porosity appears black on the secondary images, so when the average greyscale profile is plotted (**Figure 39b**), the porosity can be represented. Here, a distinct variation of porosity is highlighted from the centre to the edge of the sample. It is crucial to bear in mind that the solid-state cell generates a pellet with a diameter of 7 mm, and thus, only one-third of the pellet is imaged. The aforementioned results tend to indicate that the edges are less sintered than the core of the pellet. The hypotheses to explain such behaviour are i) the POM pellet holder which might be deformed by the high uniaxial pressure and/or ii) the plunger made of metal that has a small chamfer to helps their manufacturing but causes poorer pressure on the edge, and/ or iii), the dismounting of the sample consisting of extracting the pellet from the holder and putting more stress on the edge (adhesion to the POM disk) than at the centre of the pellet. By checking hypothesis ii) we can see that the chamfer is rather small (ca. 150 µm), thus it cannot be fully responsible for the "poor" edge sintering (**Figure 40**).

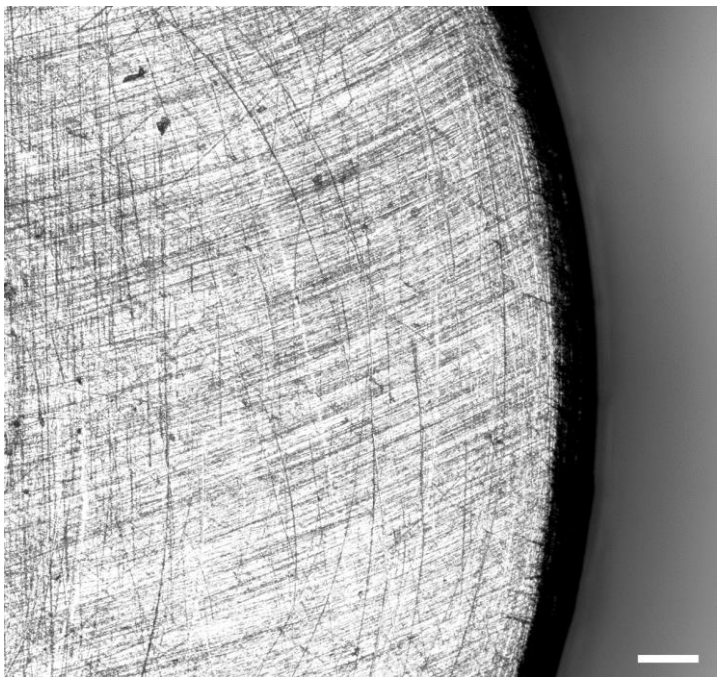

Figure 40: Optical microscopy image of the edge of the cylinder highlighting the chamfer of the solid-state cell chamfer. The scale bar represents 100 μm.

This result highlights the importance of controlling the region where the tomographic volumes are acquired to get comparable results.

3.3 Room temperature sintering of amorphous Li_3PS_4: coupling morphological evolution to electrochemical properties ‡

Presently, a comparative study will be conducted with four samples where we varied the room temperature sintering parameters (pressure and time) on amorphous LPS to monitor the morphological and electrochemical evolutions and find correlations between them. For a better comparison between the samples, all tomographs were performed in the same region of the solid electrolyte pellet (500 µm from the centre of the pellets) and in the same direction (always the same coordinate axis and the same origin) as presented in **Figure 41**.

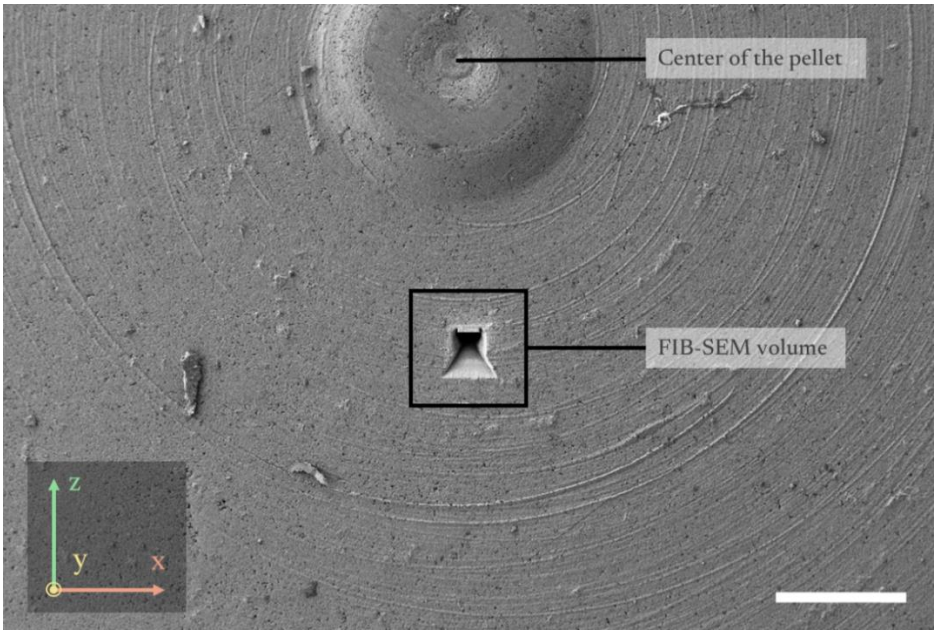

Figure 41: Top view of the pellet with the FIB-SEM tomography location, the centre of the pellet and the labelled three axes. The scale bar represents 200 µm.

All samples were made from the same batch of LPS synthesis and all the tomographies were acquired within a month, with the same volume (20 x 20 x 20 μm^3) and identical pixel size of 20 nm. No morphology of air-exposed LPS was observed for the four samples.

‡ A part of the chapter is extracted from the following article submitted to Advanced Functional Materials accepted in September 2023 "Room temperature sintering of amorphous thiophosphates solid electrolyte (Li_3PS_4): coupling morphological evolution to electrochemical properties" with the following authors Patrice Perrenot, Adrien Fauchier-Magnan, Marta Mirolo, Lauréline Lecarme, Pierre-Henri Jouneau, Adrien Boulineau, Pascale Bayle-Guillemaud, Claire Villevieille, published under CC-BY license agreement.

3.3.1 Physical and chemical characterization

As already shown in **Figure 33**, LPS is amorphous and since the material is air-sensitive and reacts with most of the solvent, it is difficult to estimate the particle size distribution of the powder by traditional methods such as laser diffraction. Thus, it was estimated using SEM images and image analysis as shown in **Figure 42**.

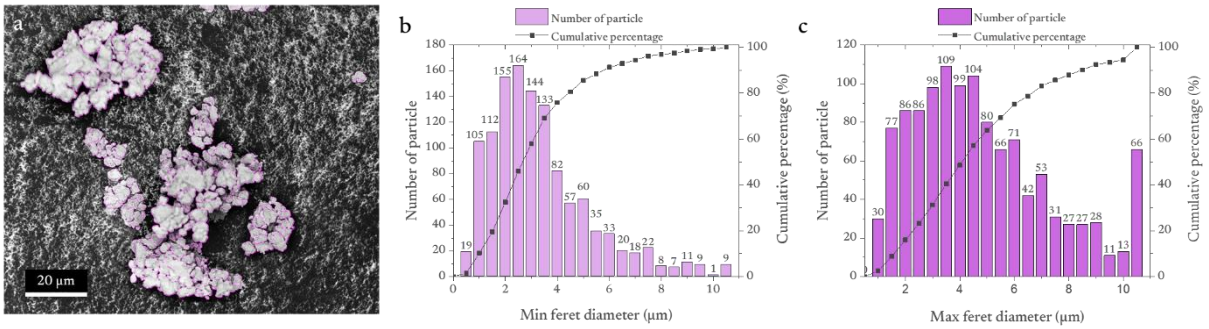

Figure 42: a) Backscattered electrons SEM images of the LPS powder with a magenta overlay showing the analysed particles. (b-c) Histograms showing the particle size distribution of LPS particles based on minimum (b) and maximum (c) Feret diameters.

From this analysis, it seems that the median diameter D50 (value of particle diameter at 50 % in the cumulative distribution) of the powder is between 2.5 and 4 µm from the minimum and maximum Feret diameter histogram respectively. This result might be slightly overestimated for two reasons: i) the LPS particles tend to agglomerate to form clusters that are hardly separable and ii) the image analysis procedures do not separate all the particles as seen on the backscattered electron image with the magenta overlay. Nonetheless, this method gives a satisfactory estimation of the size of the particles before the sintering process.

3.3.2 Shaping/room temperature sintering

3.3.2.1 Densification

As can be seen in **Figure 43**, the most important parameter to control is the pressure as, at higher pressure (510 MPa), the solid electrolyte is way denser than the one at 255 MPa. As such, it looks like pressing for a longer time is only reducing marginally the amount of porosity. Unfortunately, the images here are only 2D and cannot reflect the behaviour of the solid electrolyte in 3D, thus image reconstructions in 3D using algorithms are crucial to point out differences.

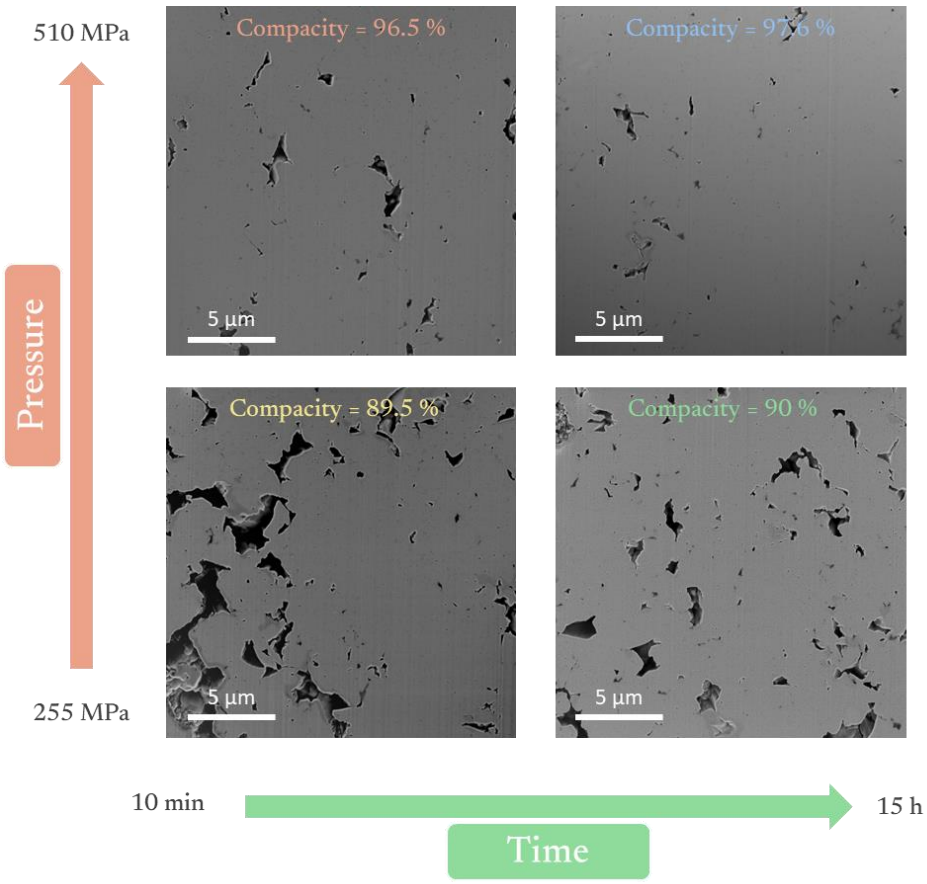

Figure 43: Secondary electron image extracted from the FIB-SEM stacks for the four different samples as a function of applied time/pressure.

Several parameters can be extracted from the image analysis (**Table 3**), the first one being the densification of the solid electrolyte. Here, we dissociate the contribution from Li_3PS_4 solid electrolyte from the one of Li_2S, considered as an impurity. When sintered at 255 MPa for a short time (10 min), an average densification of ca. 89.3% is obtained, while when sintered at 510 MPa, an average densification of ca. 96.4% is obtained, showing that the pressure has a beneficial impact in reducing the porosity of the solid electrolyte. Pressing for a longer time (15 h instead of 10 min) at the same pressure does not change the overall porosity of the solid electrolyte since the densification reached ca. 89.9% and 97.3% for the sample pressed at 255 MPa and the one pressed at 510 MPa, respectively. As such, the key parameter for proper densification and reducing the overall porosity remains the pressure.

Table 3: Summary of the results obtained from the investigations led on the FIB-SEM 3D reconstruction.

Samples	255 MPa 10 min	255 MPa 15 h	510 MPa 10 min	510 MPa 15 h
LPS vol. fraction (%)	89.3	89.9	96.4	97.3
Li_2S vol. fraction (%)	0.2	0.1	0.1	0.3
Porosity vol. fraction (%)	10.5	10.0	3.5	2.4
$\tau_{+/-y}$ tortuosity in LPS + Li_2S	1.032	1.030	1.009	1.007
Average local thickness in LPS + Li_2S (µm)	0.96	0.99	1.28	1.21
Std. dev. local thickness in LPS + Li_2S (µm)	0.39	0.40	0.50	0.42
Min length to connect top and bottom through porosities (µm)	22.06	22.60	25.48	X
Min-max tortuosity to connect through porosities	1.103 - 1.475	1.130 - 1.454	1.274 -1 .537	X

3.3.2.2 Local thicknesses & geometric tortuosity

Unfortunately, the solid electrolytes are not 100% dense which implies that the remaining porosity will cause a higher tortuosity impacting the Li-ion transport and can be the nucleation point to fracture propagation and dendrites penetration.

For the sample pressed for 10 min at 255 MPa (**Table 3**), the densification of 89.3% results in a slightly high average tortuosity of around 1.030 (compared to the ideal 100% compacity leading to

tortuosity of 1) in the sintering direction. The tortuosity here seems low considering the amount of porosity visible in the 3D images, but this calculation is an average of every possible path connecting the top to the bottom of the investigated volume (ideal Euclidian/straight path of 20 μm and real mean pathway found to be 20.6 μm). When higher pressure is applied (**Table 3**), the tortuosity drastically decreases to 1.009 (theoretical path of 20 μm, and real mean pathway found to be 20.18 μm). In both cases, the geometric tortuosity parameter seems almost negligible as compared to the ideal tortuosity of 1. Applying the pressure for a longer time does not change the average tortuosity, meaning again that a key parameter for sintering is the pressure more than the time applied.

As such, the geometric tortuosity alone might not be the most adapted metric to assess the Li-ion transport properties[4], especially since a small pore will be negligible for the Li-ion pathways, whereas a large pore interconnected through the full volume might drastically influence the Li-ion transport. Indeed, the geometrical tortuosity only describes the length of the lithium through the volume as it calculates all the possible paths and averages their distances, thus only partially describing Li-ion transport. It is known that physical bottlenecks could hinder the flux of ions and therefore the distribution of these diameters is important. The local thickness measurements can address the description of the bottlenecks by giving the distribution of the diameter of the Li-ion channels. Local thickness measurement can then address better the Li-ion transport hindrance within the solid electrolyte as depicted in **Figure 44**.

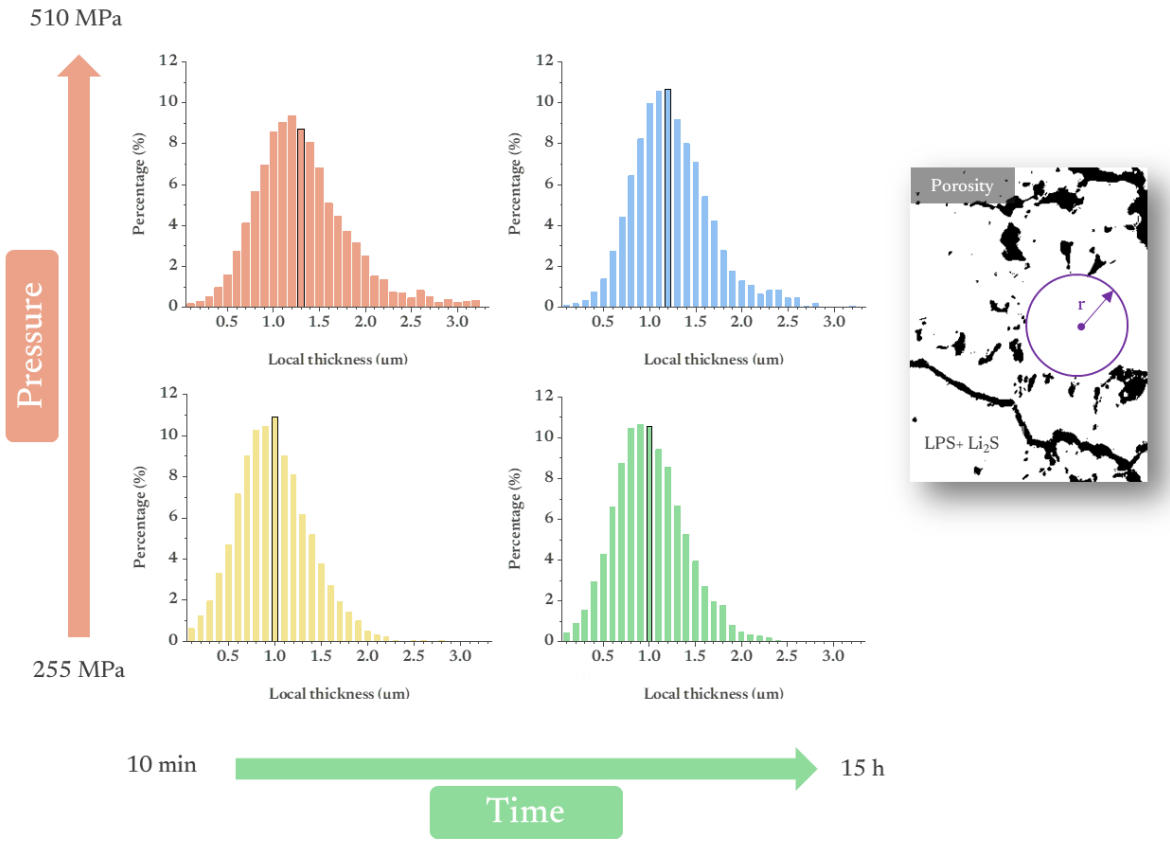

Figure 44: Local thickness histograms and the 2D representation of local thickness measurements. On the histograms, the black outlined bar represents the mean diameter. On the 2D representation, LPS and Li_2S are represented in white and the porosity in black.

For the samples pressed for 10 min at 255 MPa, the average local thickness (or the average distance between pores) is slightly lower than 1 µm whereas increasing the pressure to 510 MPa leads to an average of 1.28 µm in diameter, thus improving the transport by ca. 30 %. The same trend can be observed between the samples pressed for 15 h with a 20% increase from 255 MPa to 510 MPa (local thickness increasing from 0.99 µm to 1.2 µm). Moreover, the distribution of the diameter of the samples sintered at 510 MPa is more spread out toward wider diameter: there is a decrease of small diameters while an increase of the maximum diameters leading us to conclude that the Li-ion transport is better in more sintered sample (higher pressure). However, the effect of a longer sintering time seems to have only limited consequences on the distribution of local thicknesses.

Still based on those analyses, it seems that time does not influence the sintering properties of the solid electrolyte, which is surprising at first glance, as merging solid/solid interface requires energy, thus time should be a crucial parameter as well. Additional parameters are extracted from the 3D investigation to shed light on the role of time on the pressure that should be applied.

3.3.2.3 Pores size distribution and geodesic distance map through the pores

In the previous section, a focus has been aimed at describing the overall sintering parameters on the solid electrolyte, now the second target is the description of the pores. One can represent the porosity on each slice along the three axis X, Y and Z as shown in **Figure 45**. This representation allows i) to check the homogeneity of pores in the volume, and ii) to understand if the uniaxial pressure is leading to anisotropic distribution of the pores on the electrolyte volume.

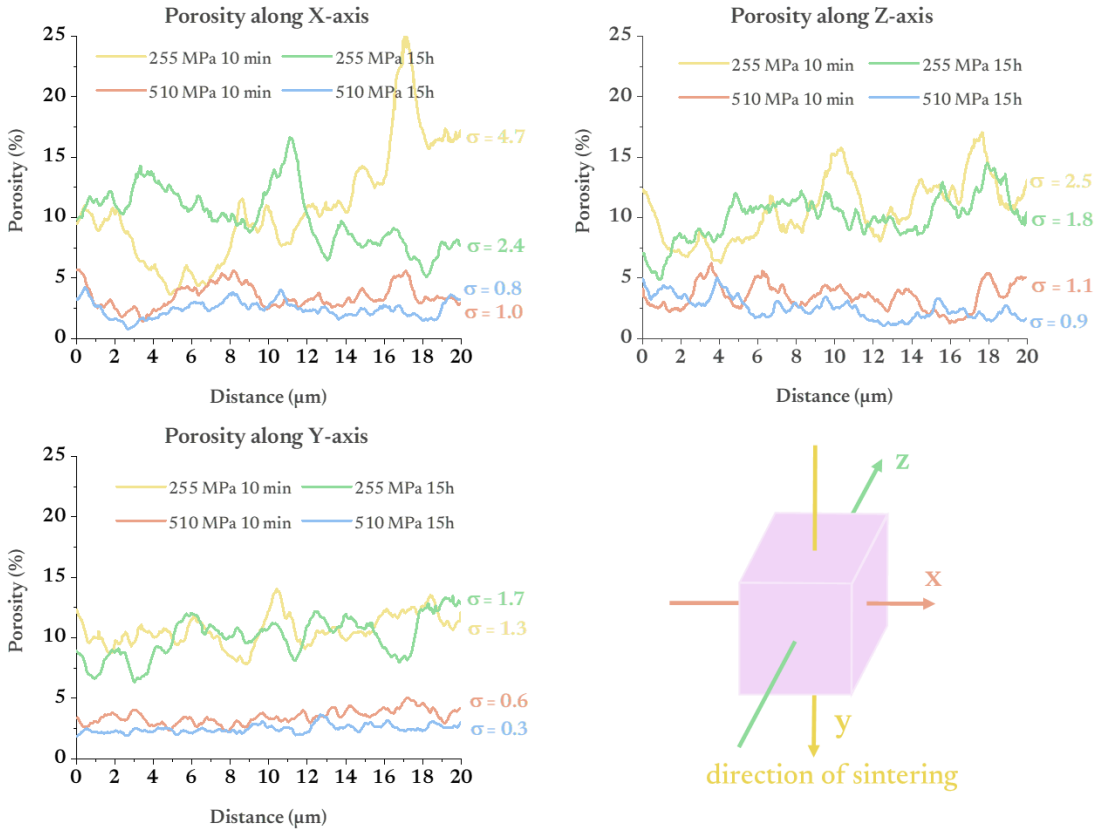

Figure 45: Porosity per slice along the three axes with the standard deviation of porosity, Y axis toward the centre (same axis as the applied pressure), X and Z axes toward the edge of the pellet.

As discussed previously, the samples sintered at 255 MPa show higher porosity on each slice compared to the samples sintered at 510 MPa (the overall porosity being the average of the porosity of every slice). On the samples pressed at 255 MPa, the variation of porosity between the slices is considerable compared to the samples pressed at 510 MPa suggesting that the pores at 255 MPa are substantially larger and not homogeneously distributed on the overall volume. The same result could be extracted from the representative elementary volume (REV) plots in **Figure 46** where a smaller representative elementary volume is found with a +/- 5% confidence interval for the 10 min pressed samples at 510 MPa compared to the one at 255 MPa:

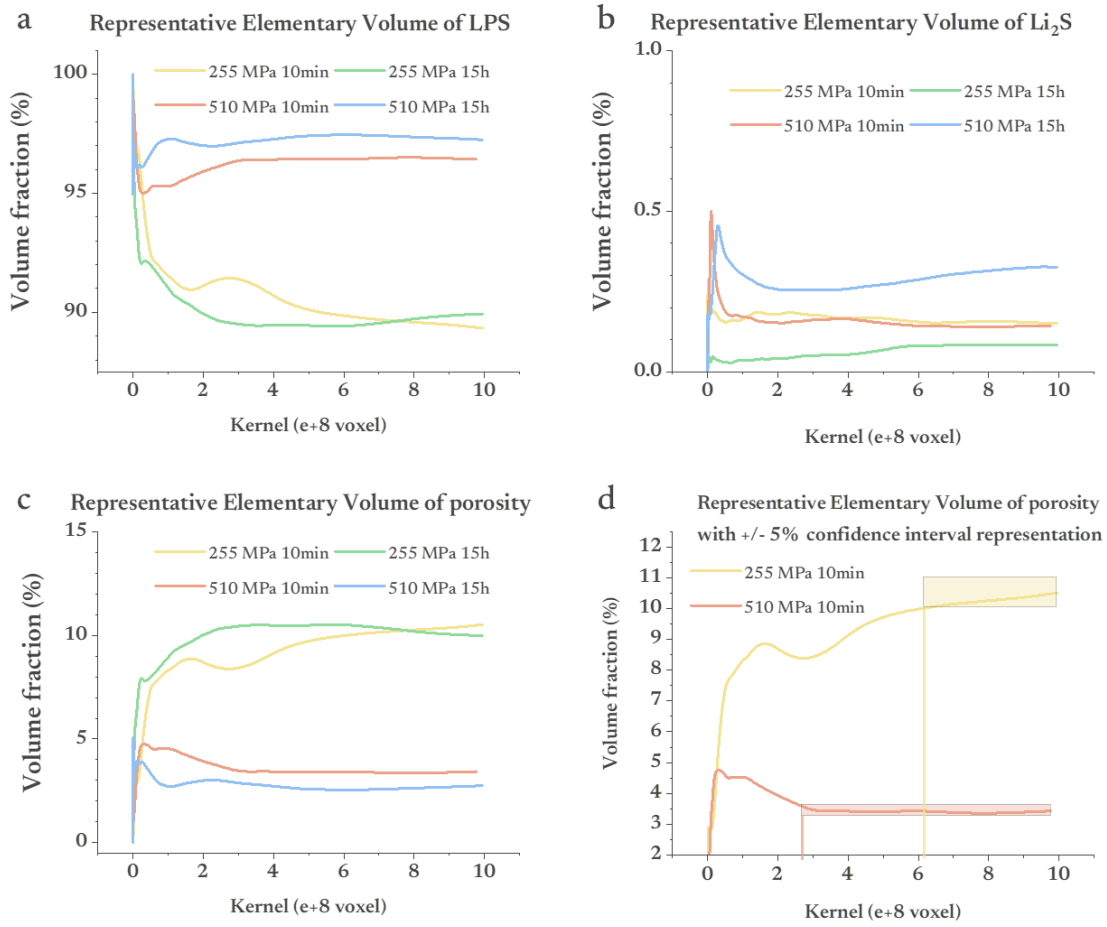

Figure 46: Representative Elementary Volume (REV) plots for a) LPS, b) Li_2S, c) porosity and d) close-up on porosity for samples sintered for 10 min with a +/- 5% confidence interval representation.

Once again, this indicates a greater pores homogeneity, in size and distribution throughout the volume in the samples sintered at 510 MPa, even with a short pressure time.

When looking closer at the fluctuations of porosity (**Figure 45**) along the three axes or, in other terms, the standard deviation along each axis, a trend can be seen: on every sample, the lowest fluctuation in porosity is always seen on the Y-axis. This result suggests that there is a greater uniformity along the direction of uniaxial pressure than in the plan of the pellet. This behaviour observed is clear once correlated to the cell design. The pressure is applied along the Y-axis, as represented in **Figure 41,** with two stainless steel plates, maintained on the cell by screws. On the X and Z-axis, the cell could slightly distort as a POM disk is used to ensure the electrical isolation of the pellet (previously exposed in **Figure 39**). Despite the wall thickness of 1 cm and its stiff design, it is possible that the POM disk could be more "ductile" than the stainless-steel plates, leading to a "pressure relaxation" of the SE in the plane of the pellet. At this stage, the difference between the X and Z-axis is difficult to explain since the sample is a cylinder and no difference is expected between the X and Z-axis.

So far, we demonstrated that the pressure is a key parameter to control for improving the room temperature sintering and that the time seems to have yet a negligible impact. However, looking carefully at the porosity within the volume, we can see some evolution that might have a time dependency. For all samples, two different populations of pores can be detected: the first consists of large pores, superior to tens of μm, not homogeneously distributed in the volume, that are mainly interconnected and most probably responsible for Li-ion transport hindrance. The second population consists of small unconnected pores (below 1 μm in diameter) spread out through the volume, most probably caused by the large particle size distribution of the solid electrolyte powder. Both populations can be seen on every sample (**Figure 47**) even though the proportion of large pores is considerably smaller in the samples pressed at 510 MPa.

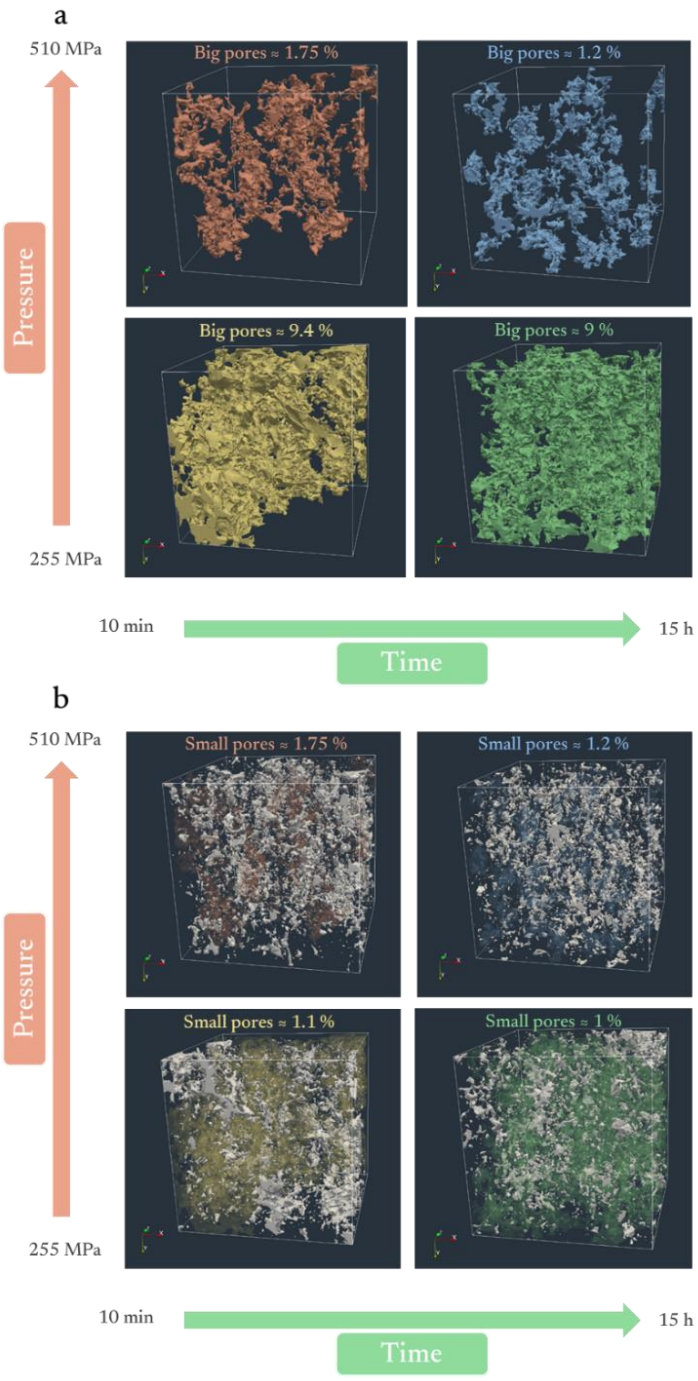

Figure 47: a) large pores and b) small pores visualisations within the volume of the four samples and their corresponding porosity.

The main differences here lie in the interconnection of the porosities. The geodesic distance map through the pores is a representation that can help address the dendrites' propagation and the path Li metal can take to travel in the pores during cell assembly. It shows the direct path that lithium metal could effortlessly take, either during the building of the cell or during the electrochemical activities. These geodesic distances are represented in **Figure 48**.

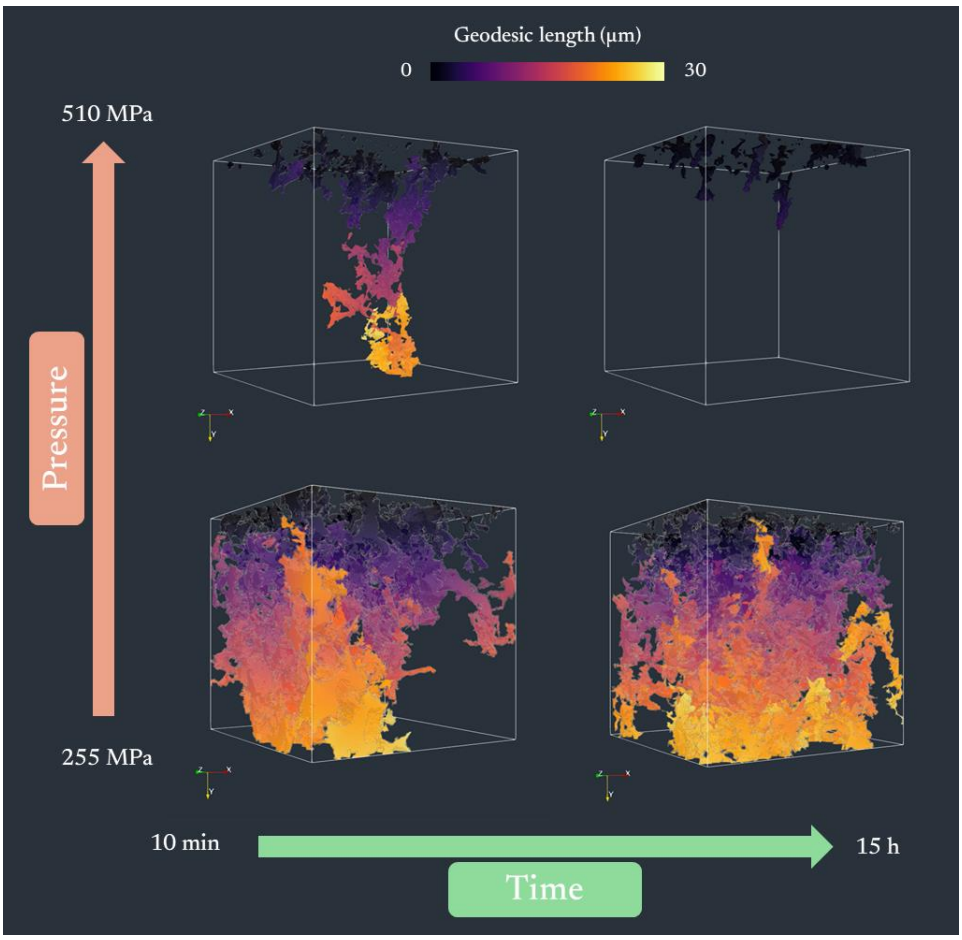

Figure 48: 3D geodesic distance map through the pores for the four samples, calculated from the top, and propagated to the bottom.

The distance calculation starts from the top plane of the volume and propagates through the pores along the Y-axis (simulating the lithium metal deformation during cell fabrication with lithium metal on the starting top plane). For samples sintered at 255 MPa and the sample sintered at 510 MPa for 10 min, there is a percolation of porosities along the Y-axis that could promote dendrite growth as there is a direct path through pores from the top to the bottom of the separator. Even though the height of the studied volume here is roughly 25 times lower than the separator used in this setup (ca. 500 µm), there would probably be a direct path for lithium to propagate through the porosities network and create short-circuit. Or at least, if a path of more than 20 µm exists at the surface of the separator, it would help to propagate faster the dendrites through the whole volume. However, on the sample sintered at 510 MPa for 15 h, the percolation of pores is lost, and the path of possible Li-metal propagation is drastically restricted. As unbelievable as it can be, this result suggests that sintered solid electrolytes, with porosity as low as 3.5 vol.% (or 97.5 % compacity, sample at 510 MPa, 10 min), could have a direct path for lithium metal propagation. Indeed, solid electrolytes serve as a separator in solid-state batteries and an electrode will be shaped directly in contact with its surface. Lithium metal negative electrode will be pressed directly onto the separator and taking into consideration the low young modulus of Li metal and its yield strength[138], the lithium might fill the

open pores from the surface to the core. Due to the challenges associated with milling and imaging metal lithium alongside LPS, conventional FIB-SEM tomography could not be performed at the interface Li-M | LPS. Consecutively, only fractographies were observed, purely providing qualitative data, of the Li penetration profile. Li metal (50 μm foil) was pressed on the surface of LPS at 25 MPa. Fractography observations made on the samples at 255 MPa 10 min and 510 MPa 15 h are presented in **Figure 49**.

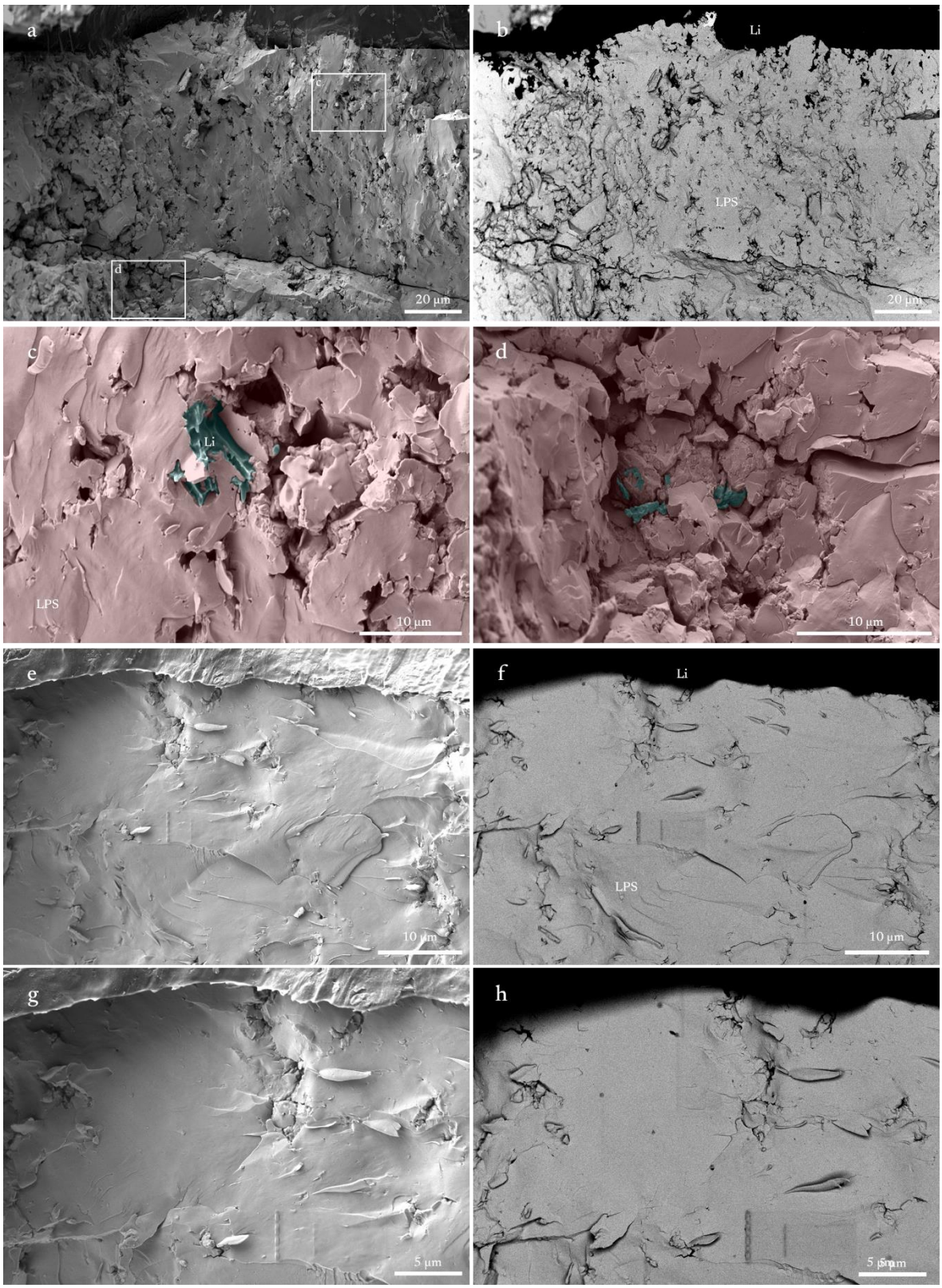

Figure 49: Fractography of Li | LPS interface of (a-d) for 255 MPa, 10 min and (e-h) for 510 MPa, 15 h. a) Global secondary electron image and b) the corresponding backscattered image. On a), squares represent the close-up images c) and d) where lithium penetration has been identified. e) Global secondary electron image and f) the corresponding backscattered image. g-h) Close-up secondary and backscattered images respectively from e and f).

For the sample sintered at 255 MPa for 10 min, the penetration of lithium has been observed as deep as 82 µm from the Li | LPS interface (**Figure 49d**) while no penetration has been observed on the sample 510 MPa, 15 h. The result of the latter sample, however, needs to be mitigated since an air-exposed morphology has been identified at the surface of the LPS pellet (**Figure 49g-h**).

Figure 50 gives the pore size distribution for each sample, the cumulative number of pores and the cumulative volume fraction each class represents.

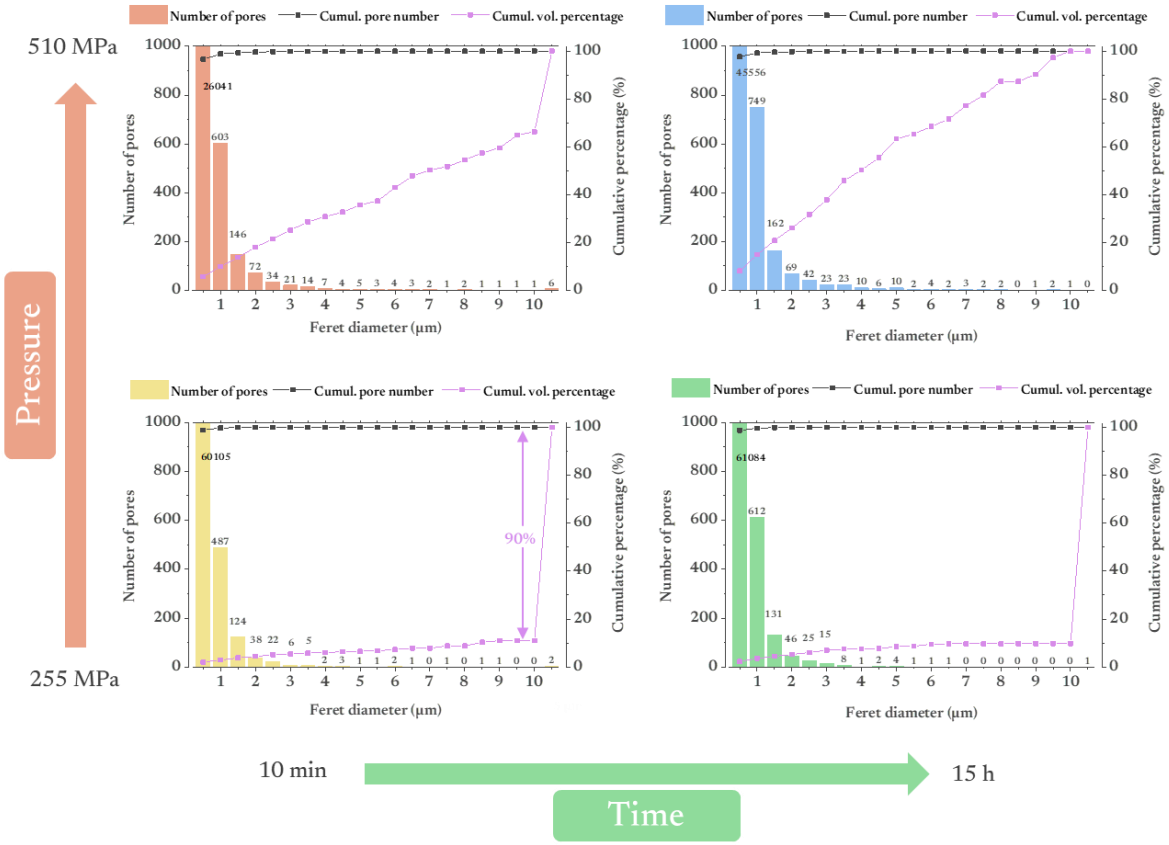

Figure 50: Pore size distribution and cumulative volume fraction for each sample.

It can be seen that a large number of small pores (lowest Feret diameters) are present in every sample, but their corresponding volume fraction is negligible in the case of low pressure and close to 20 % for pores of ca. 1 µm at 510 MPa and 15 h. This is quite promising as small porosities should not impact the Li-ion transport within the solid electrolyte, however, they can contribute to propagating i) the dendrites if they start to be formed, and ii) the cracks if stress/strain occurs in this area. At 255 MPa, ca. 90 % of the overall porosity is contained in two distinct pore sizes (higher than 10 µm) when sintered for 10 min and only one pore for the sample sintered for 15 h. Both extremely large porosities are most probably responsible for cell failure (dendrites propagation along the full stack volume) and major Li-ion transport hindrances. When looking at the pellets sintered at 510 MPa for 15 h, a clear microstructural change can be seen with a drastic reduction of big pores. The slope of the cumulative

volume fraction of porosity is free from drastic increases. This result implies that the sintering is a slow governed process. To reduce and "close" the big porosity, only time seems to play a role so far, reducing the probability of generating Li dendrites paths.

So far, we demonstrated the impact of pressure and the time this pressure is applied to the solid electrolyte microstructure. However, additional properties are needed to properly determine the parameters improving the electrochemical performance of the solid electrolyte. The following part is dedicated to assessing the impact of the room temperature sintering parameters on the electrochemical properties of the solid electrolyte as well as looking at the structural properties in the depth of the solid electrolyte during and after sintering.

As demonstrated in **Figure 33**, LPS (powder) is amorphous with a small amount of Li_2S considered as an impurity. We wanted to know if the sintering parameters (pressure and time) could influence the structural properties of the solid electrolyte, especially in the depth of the solid electrolyte pellet. Thanks to the synchrotron source we can track the vertical Y profile of our four samples by Wide Angle X-ray Scattering (WAXS) technique, using a beam size of 5 μm in the vertical direction. It means that for each sample we collected ca. 100 diffractograms in the pellet volume, helping to chase local structural changes. Based on our *ex-situ* investigation and whatever the room temperature sintering condition used (time and/or pressure) to densify the LPS solid electrolyte, the samples remain all amorphous in the Z position similarly to the LPS powder. As the structure of the *ex-situ* samples could have evolved with time (relaxation as an example), we performed an *in-situ* experiment by incrementally increasing the applied pressure (from 25 MPa up to 255 MPa) on the sample while following the structural stability. Similarly, when the sample reached 255 MPa, we still collected the sample as a function of time to mimic the results from long-term sintering. As can be observed in **Figure 51a-b**, no modification can be seen on the contour plot representation, nor the waterfall one showing that the amorphous nature of the solid electrolyte is kept whatever the time/pressure applied.

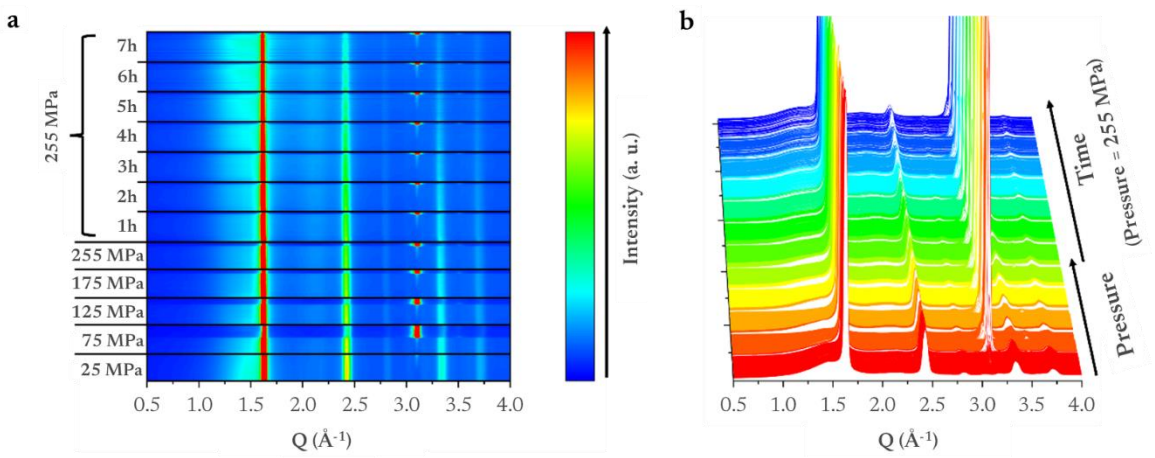

Figure 51: a) Contour plot representation of the X-ray diffractograms collected at the synchrotron source (ID31 - ESRF) during an *in-situ* room temperature sintering test, the colour indicates a change in the intensity of the diffractogram; b) the waterfall representation of the same experiment, each colour indicated a change in the pressure and/or time. All the peaks seen in the diffractograms are related to the sample holder.

Based on our data analysis relying on morphological and structural investigation, the best sample is the one having the least remaining porosity and from which there is no connection between the porosity thus, the sample sintered at 510 MPa for 15 h. Now, we performed additional electrochemical tests, mostly the platting/stripping test, and cyclic voltammetry measurements to determine the most important parameters on top of the ionic conductivity.

3.3.3 Electrochemical characterization

3.3.3.1 Ionic transport

In solid electrolytes, the Li-ion transport is ensured by the bulk ionic conductivity and the presence of grain boundaries. Based on the FIB-SEM investigation and solid electrolyte nature (amorphous), we logically did not identify any grain boundaries. The ionic conductivity of LPS was measured by EIS measurement at different temperatures (**Figure 52a-b**). The high-frequency processes corresponding to ionic transport were fitted using the equivalent circuit presented in **Figure 52c-d**. The activation energies were extracted from the temperature-dependent Arrhenius plot as shown in **Figure 52e**.

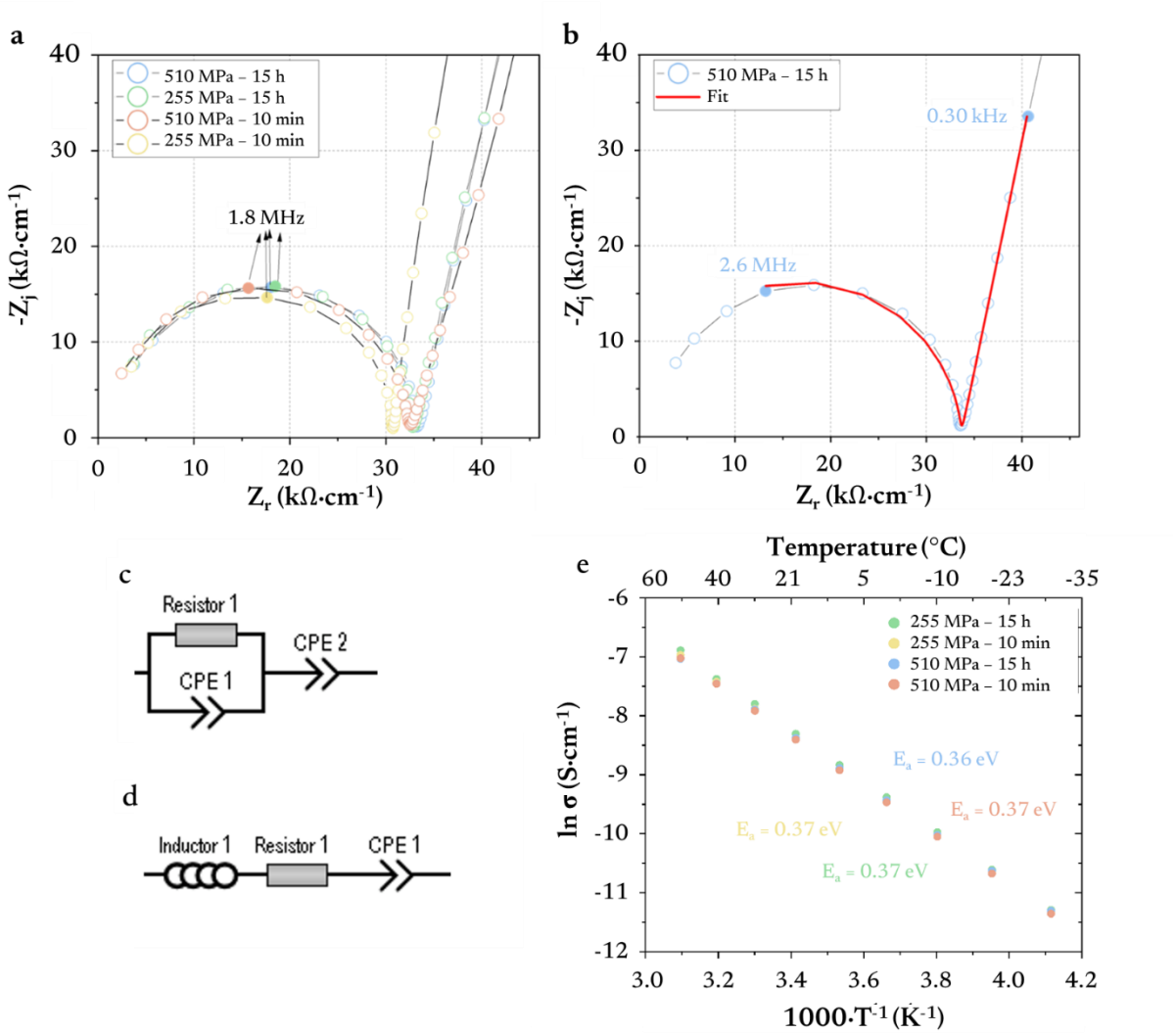

Figure 52: a) Impedance spectra obtained at 0 °C for the four samples. b) Example of the impedance fit obtained using the RelaxIS software. c) Equivalent circuit used for determining the ionic resistance (R1) and the associated capacitance or Constant Phase Element (CPE1). CPE2 represents the blocking behaviour of the stainless-steel electrodes. d) Equivalent circuit employed when the HF semi-circle is not well defined. e) Temperature dependence of the ionic conductivity of LPS as a function of the shaping parameter (time and pressure). The normalisation is made with the thickness of the pellets after the measurement. The activation energy was obtained from the linear regression fit of the Arrhenius plot.

The activation energies are similar for all the samples ca 0.37 ± 0.01 eV and in good agreement with the literature[139,140]. This result is somehow logical as it is not expected that the pressure/time could have an impact on the transport phenomenon occurring in the electrolyte. The calculated capacitance of the high frequency (C_{HF}) phenomenon is determined according to **Equation 4**[141].

Equation 4: Calculation of high-frequency capacitance.

$$C_{HF}=\left(Q_{HF}\right)^{\frac{1}{\alpha}} \times \left(R_{HF}\right)^{\frac{1-\alpha}{\alpha}} \quad (4)$$

Where Q_{HF} represents the constant phase element parameter (CPE) in $Fs^{(\alpha-1)}$.

Above 30 °C, the semi-circle at HF is not properly defined making it difficult to accurately estimate the value of the capacitance due to the large error bar (**Figure 52c-d** is the equivalent circuit when the semi-circle is not visible). In the temperature range [30 °C, -30 °C], C_{HF} for all the samples is constant (ca. $5.4 \pm 0.6 \times 10^{-11}$ F). This value corresponds to the bulk transport in the solid electrolyte as already reported in the literature[142]. Even at low temperatures, the contribution of the grain boundaries is not visible (confirmed by FIB-SEM) in agreement with the amorphous character of the solid electrolyte as seen by *in-situ* XRD.

As mentioned, the ionic conductivity is quite often linked to the compacity of the solid electrolyte. Indeed, a highly porous material will present a poor ionic conductivity that will increase if the material is properly densified. However, a threshold exists, where at some point and despite the presence of some porosity, the ionic conductivity will be roughly the same[143]. As can be seen in **Figure 52e**, pressure and time applied on LPS powder seem to have a little influence on the obtained ionic conductivity showing that, already after 10 min and 255 MPa, we reach the threshold of good conductivities with remaining porosity. However, with lower pressure and (thus higher porosity content), we can see that the ionic conductivity dropped (**Figure 53**). Based on this result, it means that the ionic conductivity remains the same once we reach the threshold (here around 200 MPa) and so whatever the remaining porosity content in the sample.

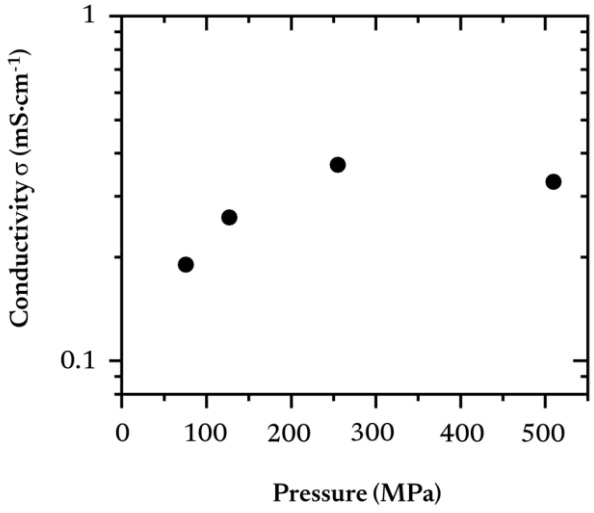

Figure 53: Ionic conductivities recorded as a function of the pressure applied, for a sample pressed during 10 min.

Once the threshold is reached, the ionic conductivities are roughly the same, the difference might be coming from i) the estimation of the thickness of the pellet causing a non-negligible error bar on the measurement and/or ii) the relaxation of the sample during the measurement causing artefact on the thickness. For the latter, the thickness measurement can be performed before the experience, or after the measurement. To identify if this parameter influences the overall ionic conductivity, we measured the sample before (before the measurement, respectively after 10 min or 15 h applied pressure) and after ionic conductivity measurement (where the cells are closed with the fabrication pressure and are opened after 15 days). The results are presented in **Figure 54.**

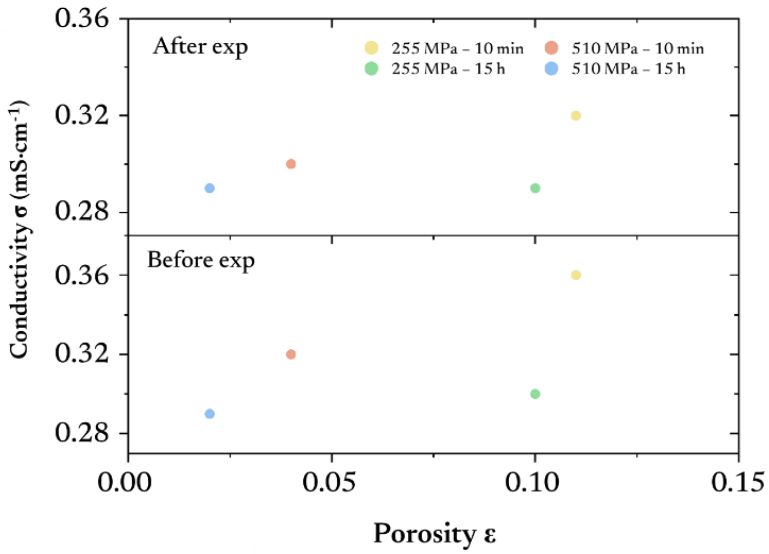

Figure 54: Ionic conductivities measured at 25 °C as a function of the porosity (estimated by FIB-SEM). (top) With the thickness measured just after the conductivity measurement and (bottom) with the one measured before the EIS measurement, i.e., after cell assembly.

If one compares the ionic conductivity as a function of when the thickness is measured (before or after the EIS measurement), we can see that after the EIS measurement, the difference between all the samples is drastically reduced compared to the thickness measurement performed before the measurement. We notice that for the samples pressed at 510 MPa, the thickness measured before and after the EIS experiment does not change, independently of the time at which the pressure was applied. On the other hand, at 255 MPa, the thickness changes significantly. This behaviour, which we ascribed to a relaxation process, can be linked to the low Young's modulus of the LPS solid electrolyte (15-25 GPa[46,143]) indicating that if a cell is closed under pressure, the sintering process might still continue. Sakuda *et al.*[143] note that the ionic conductivities do not increase after a certain fabrication pressure while the porosity seems to decrease, indicating that the pressure applied by the cell can still affect the morphology of the solid electrolyte. Furthermore, it has been observed for the amorphous electrolyte that, if sufficient fabrication pressure is applied, a small stacking pressure (> 50 MPa) is sufficient to obtain a stable ionic conductivity value[53]. Therefore, it is important to measure the thickness before and after the experiment, especially when the applied stacking pressure

is high. The results of the ionic conductivity as well as the morphology of the samples are all summarized in **Table 4**.

Table 4: Summary of the ionic conductivities and the relation to the porosity for the four samples. TA stands for conductivity measured with the thickness taken before measurement, whereas TB stands for the thickness measured after the EIS measurement. Calculation of the theoretical volume (using mass and density) compared to the experimental one obtained with the thickness of the pellet measured before measurement. The pore volumes are estimated by V_{exp}-V_{theo}. The final error is calculated by propagated error laws for macroscopic porosity.

	255 MPa 10 min	**255 MPa 15 h**	**510 MPa 10 min**	**510 MPa 15 h**
Theoretical volume (mm^3)	16.0 ± 0.1	16.0 ± 0.1	16.0 ± 0.1	16.0 ± 0.1
Experimental volume (mm^3)	18.8 ± 0.1	18.0 ± 0.1	16.1 ± 0.1	16.1 ± 0.1
Pore volume (mm^3)	2.9 ± 0.2	2.1 ± 0.2	0.2 ± 0.2	0.2 ± 0.2
Porosity estimated with the thickness (%)	15.2 ± 1.2	11.6 ± 1.2	1.1 ± 1.4	1.1 ± 1.4
Porosity estimated by FIB-SEM (%)	10.5	10.0	3.5	2.4
Ionic conductivity TB ($mS.cm^{-1}$)	0.36	0.32	0.30	0.29
Ionic conductivity TA ($mS.cm^{-1}$)	0.32	0.29	0.30	0.29

3.3.3.2 Resistance evolution

As already discussed, the room temperature sintering can "continue" once the cell is closed at a dedicated pressure, as we demonstrated with the evolution of the thickness of the pellet. Thus, we followed the evolution of the ionic resistance as a function of time for the four samples during 180 h, performing an EIS measurement every 10 min (**Figure 55**).

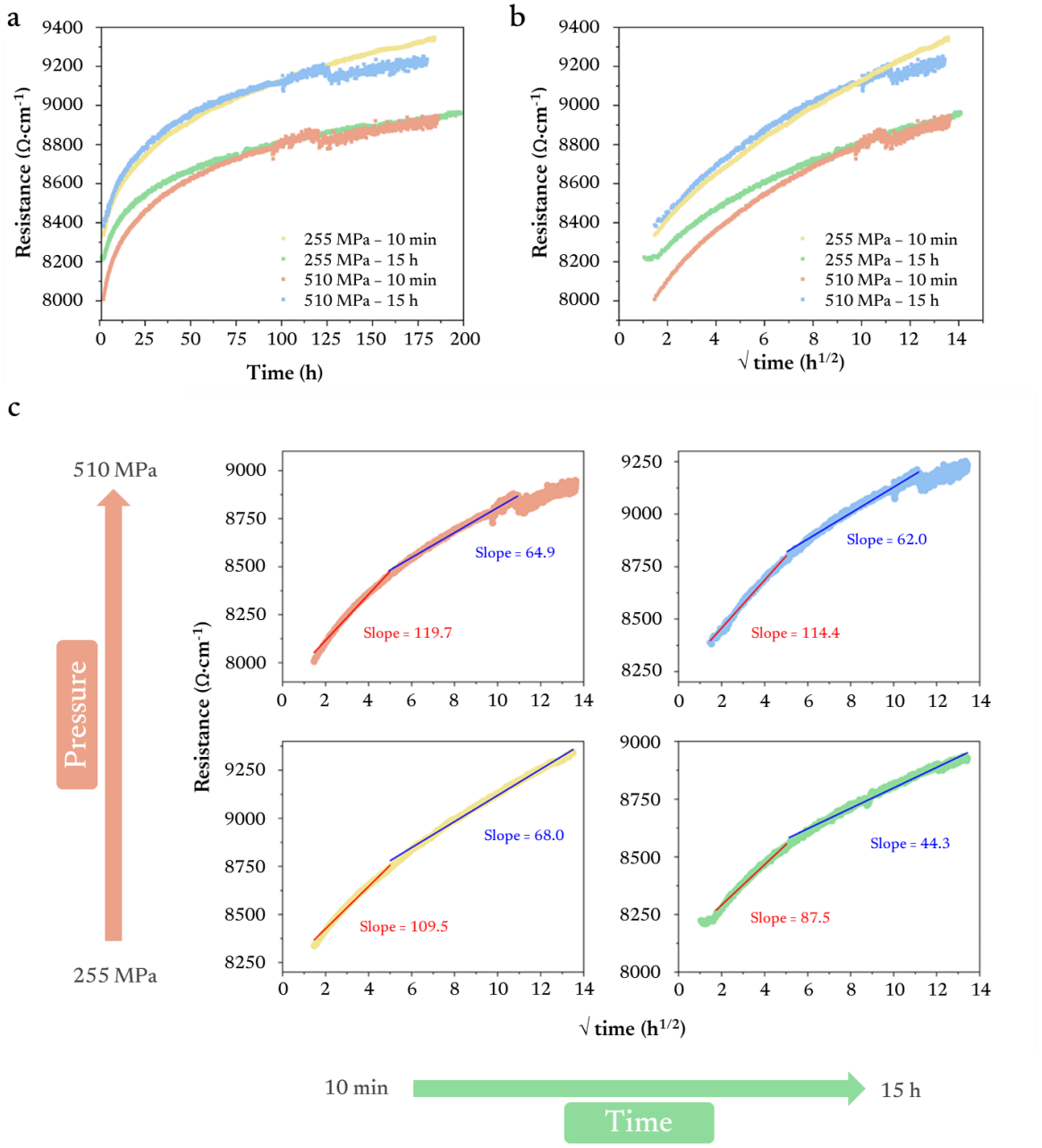

Figure 55: Evolution of the ionic resistance as a) a function of time; b) a function of the square root of time for all four samples and c) their linear regression used to fit the curve.

As shown in **Figure 55**, we can see for all samples that the ionic resistance is increasing as a function of time in a nonlinear manner (following more a logarithm profile, **Figure 55a**). First, there is a sharp increase of the resistance during the first 25 h, followed by a "stabilisation".

Several reasons can explain this phenomenon: i) the evolution of the porosity inside the sample since the cell is closed at a certain pressure, as we demonstrated that the thickness evolves with time, ii) a "distortion" of the pellet due to the design of the cell (POM disk), and/or iii) a surface reaction of the solid electrolyte in contact with stainless-steel. As seen, hypotheses (i) and (ii) are both linked to the porosity evolution whereas hypothesis (iii) is linked to surface reaction. Generally, when a surface

reaction is occurring in the cell, the resistance follows a linear trend versus the square root of time. This representation is used to describe diffusion-controlled solid-state reactions, especially the evolution of the solid electrolyte interphase (SEI)[144,145]. In the present case (**Figure 55b**), we can see that the evolution of the resistance as a function of the square root of time is not fully linear showing that surface reaction cannot solely explain the evolution of the resistance. Thus, the two pre-cited hypotheses are most probably valid.

We attempted a linear regression on the curves extracted from **Figure 55b**. As can be seen in **Figure 55c**, two linear regressions are needed to fit the curve signifying that two different processes are happening. We believe that the first one, having a sharper slope, is linked to the relaxation of the porosity that occurs relatively fast when the cell is closed, whereas the second one is seen as the surface reaction with the stainless steel. In any case, the change of ionic conductivities is ca. 10 % at the end of the measurement for all samples, exhibiting the same trend.

3.3.3.3 Electrochemical stability window

In order to assess the LPS electrochemical stability window, we performed some cyclic voltammetry (CV) measurements as a function of the sintering condition.

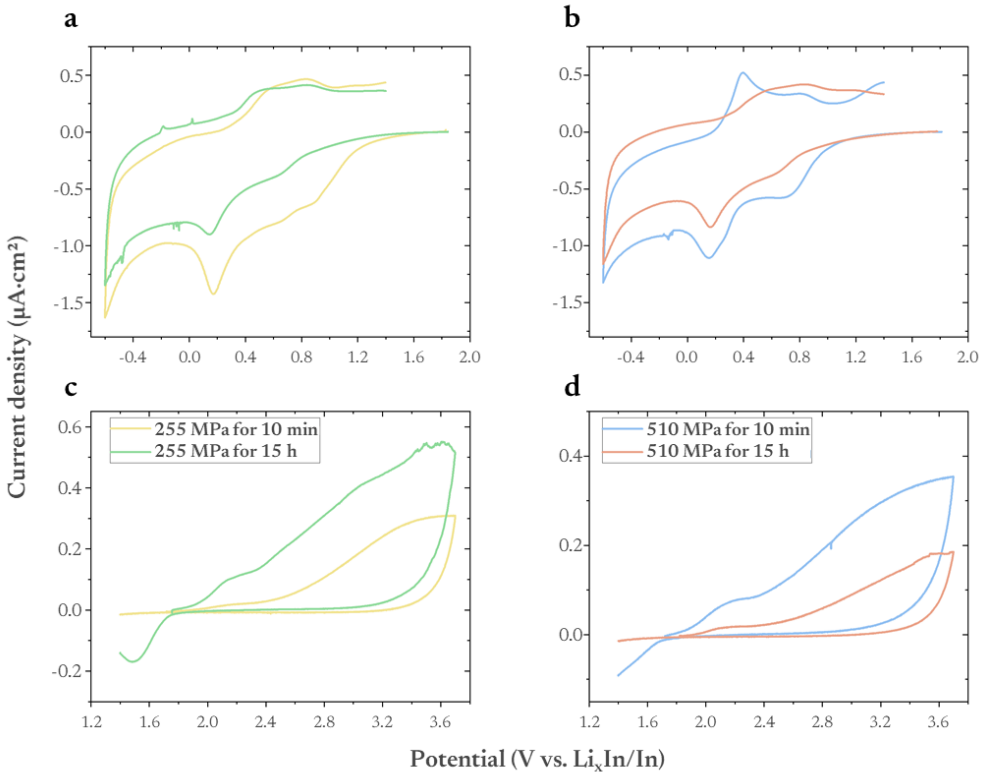

Figure 56: Cyclic voltammetry at 100 µV/s in reduction for (A) 255 MPa and (B) 510 MPa. Oxidation mode at (C) 255 MPa and (D) 510 MPa. The green line corresponds to 255 MPa 15h, yellow to 255 MPa 10 min, blue to 510 MPa 15h and red to 510 MPa 10 min.

For the cells cycled in reduction, we can notice two main peaks, one between 0.6-0.8 V and the other around 0.1-0.2 V vs Li_xIn/In. The charges involved in the process are roughly the same regardless of the time and the pressure applied. According to the literature, these reactions could be linked to the reduction of phosphorus species and Li_2S. For the former, several compounds with different oxidation states Li_3P, LiP, Li_3P_7 and LiP_7 might be formed caused by the reduction of P^{5+} to P^0, the second peak might be then the further reduction of P^0 into P^3([146]). However, there is no clear trend between degradation and pressure or time for the reduction scan, only the sample the most dense (510MPa and 15h pressure applied) seems to have way more defined peaks in reduction, which might be coming to the surface roughness of the sample, meaning that the counter electrode is properly attached to the stack, improving the current distribution during cycling[147].

During oxidation processes, we can see that the samples pressed for 15 hours (for both pressures) display a higher anodic current. The first peak around 2.2 V appears much more clearly for the 15 h samples and according to the literature, this peak is attributed to the oxidation of the sulfur anions from Li_2S[147–149].

Based on these results, we can see that the electrochemical properties of all samples are similar whatever the pressure/time applied on the solid electrolyte pellet. For the samples the most densified (510 MPa and 15 h), the processes are better defined which is most probably linked to a better current distribution. Indeed, the sample has less porosity and less surface rugosity, improving the current distribution within the cell.

3.3.3.4 Li plating/stripping

A last parameter that we assessed while investigating the room temperature sintering of the solid electrolyte is the ability to plate/strip Li using different currents (**Figure 57**). It consists of applying a constant current during 5 cycles and progressively increasing this current for the next five cycles. Once the five currents are measured, the cell is back to the first current. Depending on the porosity of the solid electrolyte, the Li plating/stripping test can also help determine the critical current at which the dendrites are formed and propagated.

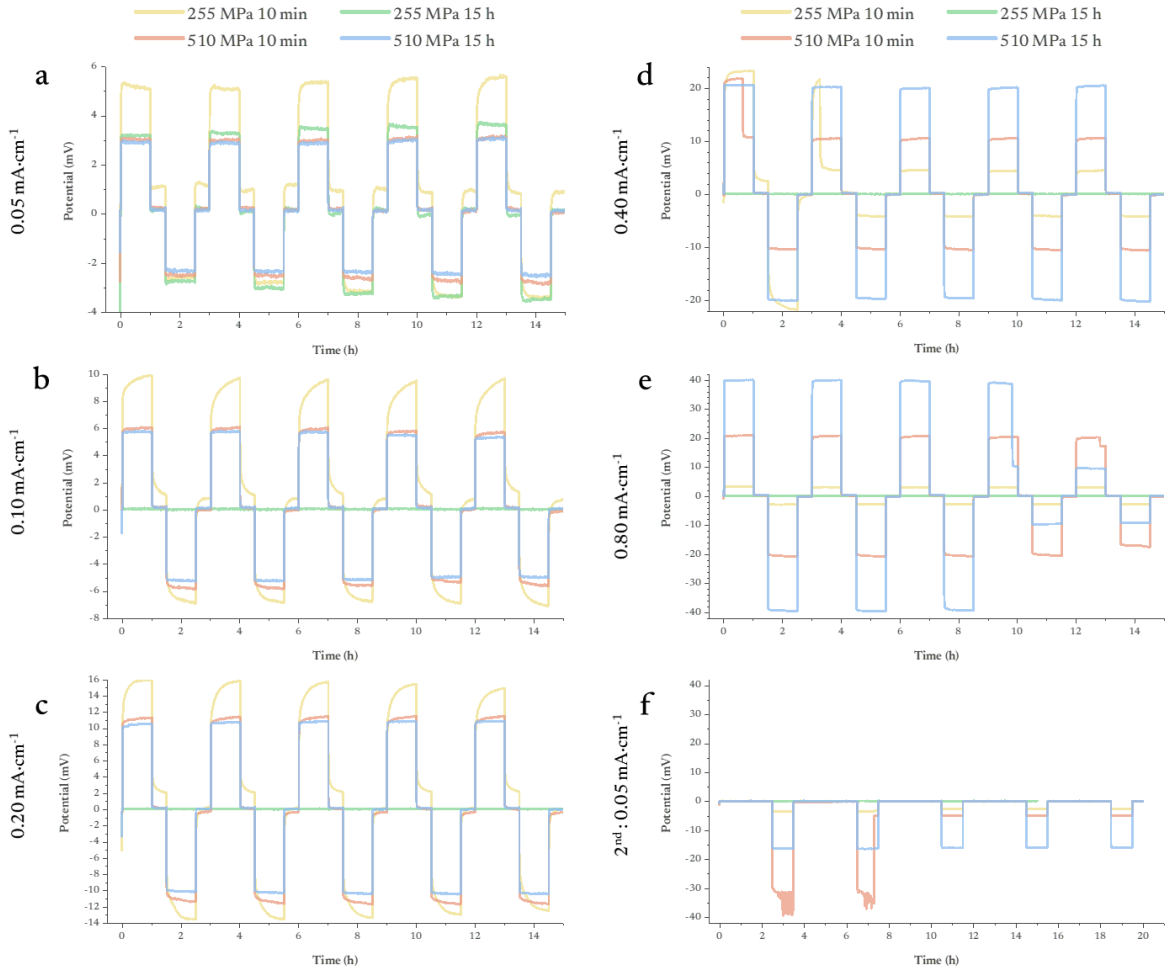

Figure 57: Lithium plating/stripping experiment applied on the four sintered solid electrolytes for 10 min and 15 h. The current density corresponds to a) 0.05 mA·cm^{-2} b) 0.10 mA·cm^{-2} c) 0.2 mA·cm^{-2} d) 0.4 mA·cm^{-2} and e) 0.8 mA·cm^{-2}and back to f) 0.05 mA·cm^{-2}.

At the lowest current density (0.05 mA·cm^{-2}), we observe the typical behaviour of Li plating/stripping, with positive and negative polarisation (less than 5 mV). The polarization follows the porosity of the samples, it is less important for the densest materials (15 h at 510 MPa) and higher for the most porous ones (255 MPa and 10 min). When applying a higher current (0.1 mA·cm^{-2}), the polarisation splitting between the less dense and denser materials intensifies, leading to higher polarisation for the 255 MPa and 10 min sample and surprisingly the sample sintered at 255 MPa for 15 h short-circuited. One reason for the short-circuited behaviour could be the dendrites, being easier to propagate in the less dense samples, as seen by the geodesic maps **(Figure 48)**. The overpotential continues to increase for the sample 255 MPa – 10 min and a noticeable change can be seen in the shape of the polarisation curves. Indeed, we can see a tail at the end of the potentiostatic plateau when the current is increasing, characteristic of contact loss[43,44]. At the lowest applied current, the plating/stripping test follows an Ohmic behaviour, but when the current is increased, the Ohmic behaviour is lost. This phenomenon is more pronounced for the samples sintered at lower pressure. Several reasons can explain this behaviour: i) the surface contact between the Li counter electrode

and the solid electrode pellet, as the surface rugosity plays a role (**Figure 58**); ii) the degradation products generated at the interface once the Li is in contact with the solid electrolyte pellet; iii) once the Li is plated or stripped, mossy Li is deposited at the surface and compete with fresh Li; fresh Li does not suffer any polarization and the mossy one is covered most probably with insulating surface decomposition products (Li_2S, Li_3P, etc.), and, iv) the possible cracks/pores that can develop between the Li metal layer and the solid electrolyte caused by the inhomogeneous Li plating/stripping. We already discussed the first two points and demonstrated that they play a key role in the noticed polarisation. For points (iii) and (iv), both can indeed play a role since the contact at the interface is always a weak point in solid-state batteries; there is no doubt that Li plating/stripping would not be homogeneous, and that mossy/fresh Li will compete. Therefore, voids will be created at the interface between the solid electrolyte and the Li metal counter electrode.

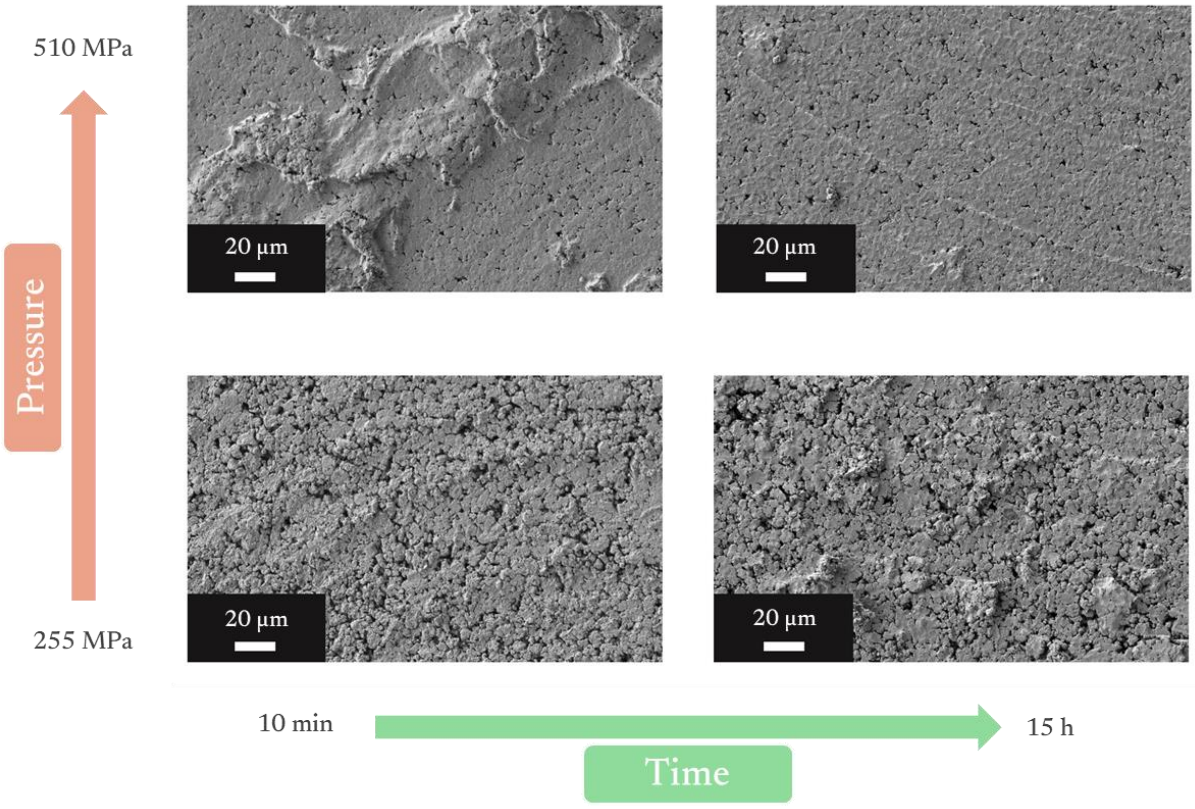

Figure 58: Secondary electron SEM images showing the surface rugosity of the pellet after the sintering process applied.

Continuing increasing the current (0.2 $mA \cdot cm^{-2}$), the trend is the same for the three remaining samples, expected that the polarisation will continue to increase. At a current of 0.4 $mA \cdot cm^{-2}$, the sample sintered at 255 MPa and 10 min has a high polarisation before breaking down, showing a dendrite formation. The same observation is done on the sample sintered at 510 MPa, 10 min: the drop from 22 to 10 mV corresponds to the formation of a dendrite.

Increasing the current to 0.8 mA·cm^{-2}, the denser sample (510 MPa for 15 h) is the only one to withhold such current but sees its polarisation suddenly decreasing after the fourth cycle, showing a dendrite formation. At this point, except for the sample sintered at 255 MPa for 15 h that prematurely short-circuited at 0.1 mA·cm^{-2}, the three remaining samples continue to plate/strip to higher current, but signs of failure start to appear in the form of a drop in the polarisation curves at different current depending on their sintering parameters. Once back to the starting current, all samples either short-circuited or are not anymore plating/stripping reversibly, a sign of soft shorts[150].

The understanding of plating/striping behaviour is far from trivial, but some tendencies can be discussed. The denser samples, sintered at 510 MPa are less prone to dendrites at a low current density than their counterpart sintered at 255 MPa, which agrees with the geodesic map showing that the porosities are connected through the full volume of the solid electrolyte guiding the dendrites. Unsurprisingly, the samples sintered for a longer time (15 h instead of 10 min) leads to later dendrite formation, which is in coherence with the previous fractography observation. The open porosity has a direct impact on the critical current density a cell can reach against lithium metal. A stack pressure of 25 MPa is sufficient to creep lithium inside the pores and subsequently increase the active surface between LPS and lithium metal, proportionally to open porosity.

3.4 Conclusions

In this chapter, we investigated the room temperature sintering of an amorphous solid electrolyte LPS type.

First, we exposed our methodology and set-up ensuring the reliability of our results by minimizing beam time exposure and air/moisture exposure.

Then, a comparison between commercial and homemade LPS electrolytes was made. Due to poor ionic conductivity and a mediocre RT sintering ability, the commercial LPS was discarded. These poor properties might come from the crystalline phase inside the commercial electrolyte. Nonetheless, we showed that homemade LPS still undergo degradation even when stored in a moisture-free environment. Therefore, LPS is a time-sensitive electrolyte and a fresh batch should be employed to guarantee reliable observations.

We first demonstrated that pressure is a key parameter to reduce the overall porosity whereas the time this pressure is applied has an impact on the overall porosity (their dimension) and the pore's connection. Whatever the samples and the sintering parameters used, they all possess the same ionic conductivity meaning that already with ca. 10% of remaining porosity, we reach a threshold. Thus, one cannot only rely on ionic conductivity for selecting the best solid electrolyte. Indeed, the distribution of the porosity within the sample seems to be the most crucial parameter since it can

guide the dendrites formation and is responsible for mechanical fracture. The best sintering condition is thus a high pressure applied (in the present case 510 MPa) to reduce the amount of porosity, but also a longer sintering time to avoid connection of the porosity through the full solid electrolyte volume leading to fewer fractures as caused by a lot of interconnected porosities.

Finally, LPS is a soft material, easy to sinter at room temperature, exempt from grain boundaries and its amorphous nature is preserved even after shaping. Despite an ionic conductivity tenfold lower than its crystalline counterpart Li_6PS_5Cl, LPS still shows an easy processability owing to its favourable Young's modulus.

4

Composite positive electrode in solid-state batteries

The mass production of solid-state batteries will only be possible if one can control several interfaces, especially those of the composite positive electrode between the solid electrolyte and the electroactive materials[59,151]. To achieve this, a fine understanding of both the chemistry and the morphology is required to minimize the chemo-mechanical degradation, important parameters to control[57,152,153] since they lower the electrochemical performance and increase the overall cell resistance during cycling. However, chemical degradation is a well-known process already reported in conventional Li-ion batteries and thus knowledge acquired on coating and protective layers can directly be applied to solid-state batteries[154–161]. The mechanical degradations are more difficult to tackle since these issues do not exist in conventional Li-ion batteries due to the wetting properties of the liquid electrolyte and the porous nature of the composite electrode compared to the solid-state one. Thus, the electroactive materials breathing[60,67,68] occurring during cycling might lead to additional irreversible degradation[61–65] that could be buffered depending on the Young modulus of the solid electrolyte and depending on the embedded properties of the electroactive material within the solid electrolyte matrix[66]. The main morphological consequence is the cracking of polycrystalline NMC along the grain boundaries during cycling[68–71]. In this chapter, we investigate using FIB-SEM and electrochemical methods, the composite positive electrode morphology, uniting the formerly characterized LPS with the polycrystalline NMC622. The morphology of polycrystalline NMC used in solid-state will first be detailed, and then several parameters controlling the shaping of the composite electrode will be investigated before showing the electrochemical signature of the composite.

4.1 Description of NMC622 morphology

Polycrystalline NMC622 consists of numerous small crystals called primary particles, which are co-precipitated to form an agglomerate, later called secondary particles. Typical images of polycrystalline NMC622 are presented in **Figure 59**.

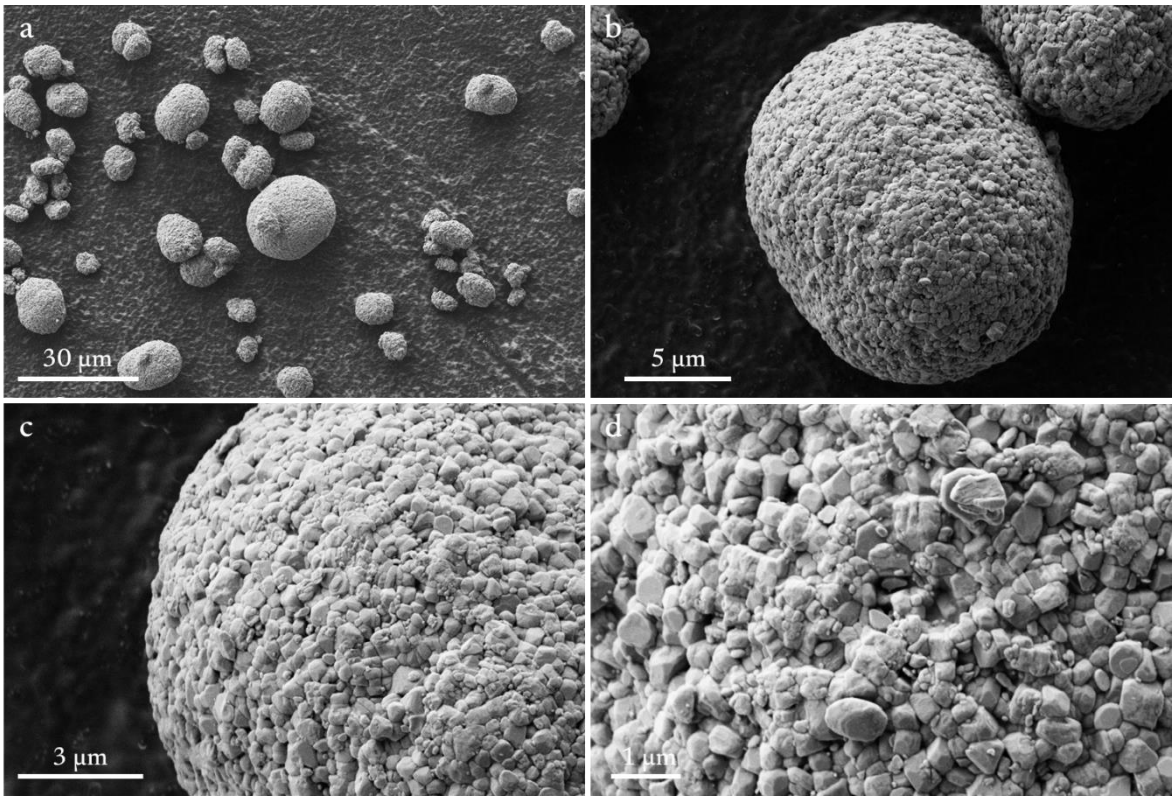

Figure 59: Secondary electron images of NMC 622 at different magnifications a) and b) showing secondary particles and c) and d) showing primary particles.

The primary particles are single crystals ranging in size from several tens to a few hundred nanometers (**Figure 59d**). The size and shape of the agglomerates they form are tailored by the co-precipitation parameters. Secondary particles have a size ranging from one to a few tens of micrometres. The supplier of the powder specifies a D50 between 9 and 14 µm in agreement with the SEM observations.

As composite electrodes are obtained by RT sintering mixing NMC622 and LPS, the behaviour of NMC under pressure seems interesting to investigate first. To ensure proper cycling, three main parameters should be considered, electronic transport, ionic transport, and solid-state diffusion within the particles. The composite electrode must then be optimized to fulfil the first two main criteria since the last one is linked to the properties of the active materials. To ensure good electronic and ionic percolation, a solid-state composite electrode must be sintered to avoid any porosity as well as the elements should be homogeneously mixed to ensure proper 3D electronic/ionic pathways. The

electronic network is fully ensured by NMC particles (as no conductive carbon is introduced), and the ionic network solely relies on LPS. For NMC622, the effective electronic conductivity was reported to be ca. 5.9 mS·cm^{-1} at 28 °C and this conductivity increases with the Ni content in the structure[162]. The ionic conductivity of NMC is at least 100 times smaller than the one of LPS (ca. 8.7 x10^{-6} mS·cm^{-1} for NMC532[163] versus ca. 0.4 mS·cm^{-1}), meaning that we can someone follow the electronic/ionic network by following NMC and LPS respectively[164]. As the LPS is significantly softer than NMC (ca. 20 GPa for LPS[52] and ca. 199 GPa for NMC 111[165]), the contact between LPS and NMC should be optimal, since LPS could be deformed to follow NMC secondary particle morphology. However, with the ratio used to maximize the energy density and to ensure good electronic percolation, NMC particles will be in contact with NMC particles, and it is believed that the NMC secondary particles could fracture along the grain boundaries of the primary particles under pressure by contact point between them. To assess this fracturing, we performed a preliminary investigation, where only NMC particles were uniaxially pressed and infused with fluid resin. As can be seen, NMC622 is fracturing along grain boundaries depending on the pressure applied and the estimated developed surface area is presented in **Figure 60**.

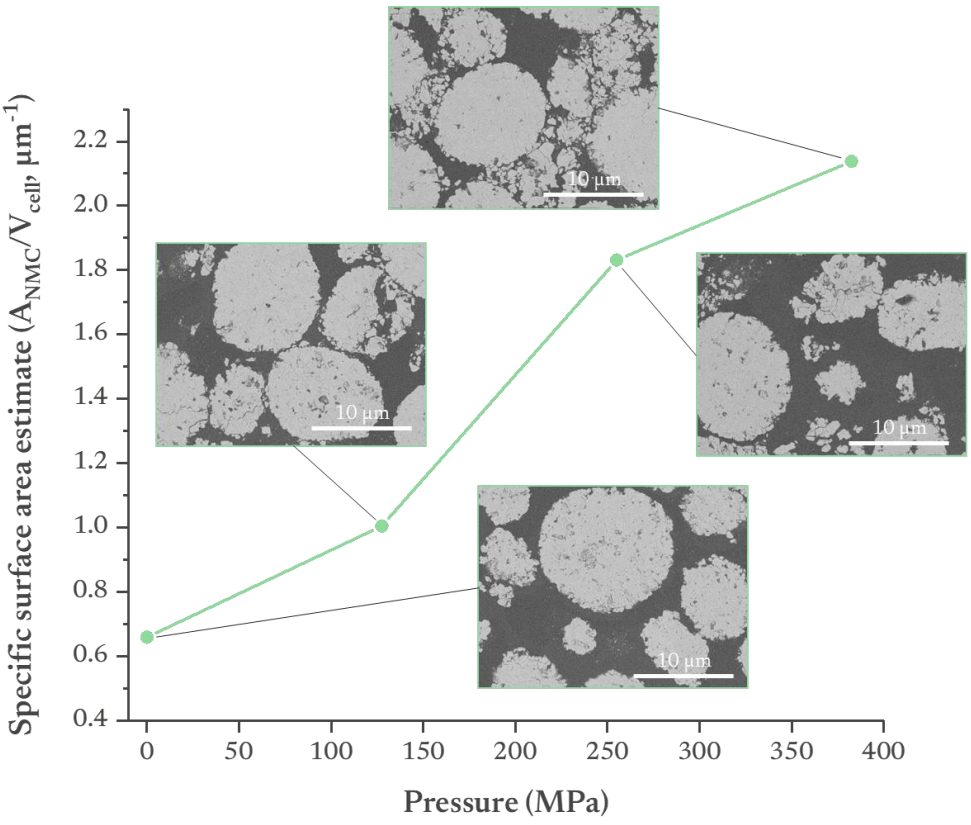

Figure 60: Estimation from 2D images of the developed specific surface area of NMC622 as a function of the applied pressure.

The developed surface area estimated is equivalent to the NMC surface area over its volume (A_{NMC}/V_{cell}), later presented for tomographic volumes. The initial developed surface area is ca.

0.66 μm^{-1} and increases with the applied pressure as expected by the secondary particle fracturing along the grain boundaries (**Figure 59**). As mentioned previously, NMC622 secondary particles are synthesized by the co-precipitation method to obtain a spherical shape consisting of the agglomeration of primary nanoparticles. At only 127 MPa, the developed surface area almost doubled from its initial state and at 255 MPa, it had almost tripled from 0.66 to 1.83 μm^{-1}. As such, the development of a large surface area is not particularly detrimental to the electrochemical performance only if the broken pieces remain electronically and ionically connected and if a passivation layer is not developing as a function of the surface area causing battery fading. However, this should not be the case in solid-state systems since the fracturing generally happens at the surface of the particle and propagates to the core. At the surface, the contact between NMC and LPS is still good but the solid electrolyte will not fill the gap meaning that the path of Li-ion through the NMC layers structure will be lengthen. These fractures will thus decrease the rate at which the battery could be cycled and additionally disconnect the inner part of the particle, leading to dead volume/weight.

4.2 NMC in composite electrode

Based on these results, we consider two different times for the shaping of the composite electrode at 255 MPa for 10 min and 15 h to optimize the sintering of LPS without damaging the NMC particles too much. In addition, based on a previous study on the LPS morphology[164], we expect a longer sintering to slightly reduce the porosity as well as improve the contact between NMC and LPS. For the sake of clarity, we will refer to the two samples as 255-10m and 255-15h respectively.

4.2.1 Electrochemical characterizations

Before any investigation related to the microstructure of the composite electrode, we first perform some electrochemical tests to see the impact of the sintering properties on the composite electrode. The two composite electrodes were tested in half-cell (vs. InLi metal). By carefully investigating the electrochemical data, we can already hint at the chemical and mechanical degradation occurring inside the electrochemical cell that we tried to summarize in **Figure 61**.

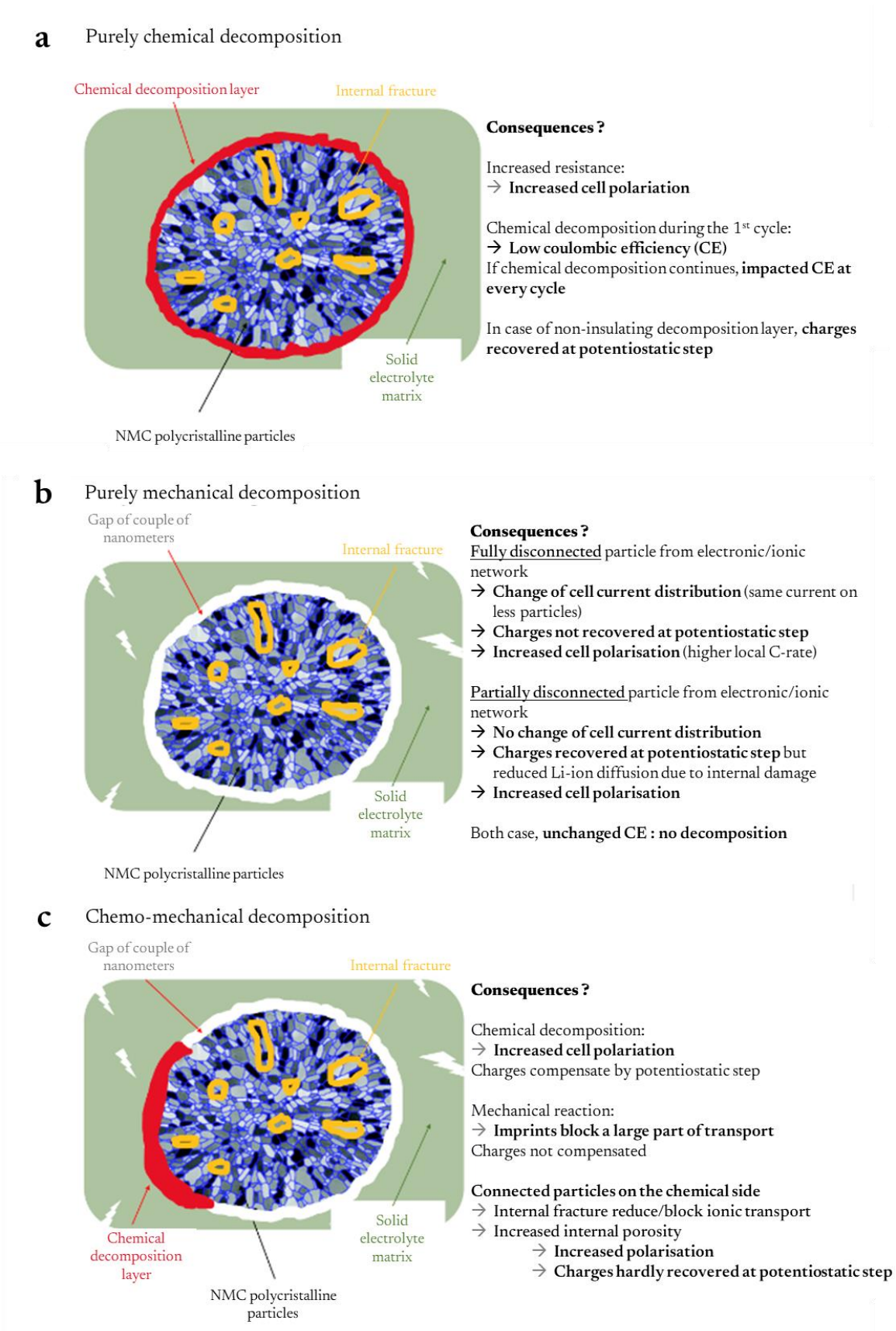

Figure 61: Scheme representing the degradation that might occurred in the solid-state batteries with the consequences on the electrochemical data.

When comparing cycling data, the specific capacity retention is not the same for both composite electrodes, and the sole difference between them is the way they were processed (**Figure 62**), showing that the time the pressure is applied plays a role in electrochemical cycling.

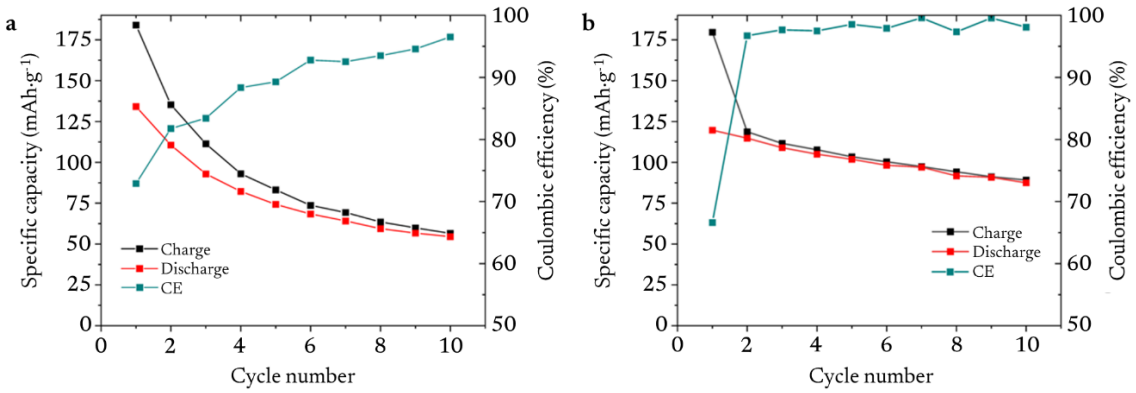

Figure 62: Specific capacity retention for the cell NMC622 vs. Li_xIn cycled at C/20 rate at RT, a) composite compressed at 255 MPa for 10 min, b) composite compressed at 255 MPa for 15 h.

The composite electrode compressed for a longer time outperforms the cell compressed for only a short time. After 10 cycles, the composite 255-15h still delivers more than 100 mAh/g, whereas the 255-10m delivers less than 50 mAh/g. In both cases, we can note a poor Coulombic efficiency (CE) during the first cycle being lower than 85 % and 70 % for 255-10m and 255-15h respectively. The difference between them is supposed to mostly come from the intimate contact between the electroactive material and the solid electrolyte. Indeed, with a more compressed electrode, it is assumed to get more contact between the particles, and thus a greater chemical decomposition. Here, we believe that the decompositions observed during the first cycle are mostly dominated by chemical degradation, as witnessed by the poor electrochemical stability windows of LPS solid electrolyte, described in the chapter **Morphologies of thiophosphates solid electrolytes** (**Electrochemical stability window**, **Figure 56**, **p. 90**). Looking now at the other cycles, the tendency for the Columbic efficiency is drastically different for the two samples, i) for the 255-10m, the CE remains low for several cycles, indicating additional chemical decomposition within the cell whereas ii) for the 255-15h, the CE increases directly to reach 97-98% for the next 10 cycles, indicating that the decomposition processes are significantly reduced. This behaviour is counterintuitive and cannot be solely explained by chemical degradation. If the chemical degradation was the main cause of fading, the cell with supposedly better contact would have the worst electrochemical signature which is not the case. This indicates that mechanical stability is also playing a key role in improving the overall electrochemical performance. Indeed, once the chemical decomposition occurs in the cell, it leads to a polarization building up and increases the contribution of charge gathered through the potentiostatic step; however, if the decomposition is caused by mechanical fractures or by particles being disconnected from the electronic/ionic network, then the potentiostatic step would not lead

to gather additional charges. Following this discussion, we looked at the evolution of the polarization curves during cycling for both samples (**Figure 63**) to estimate the resistance building up within the cell.

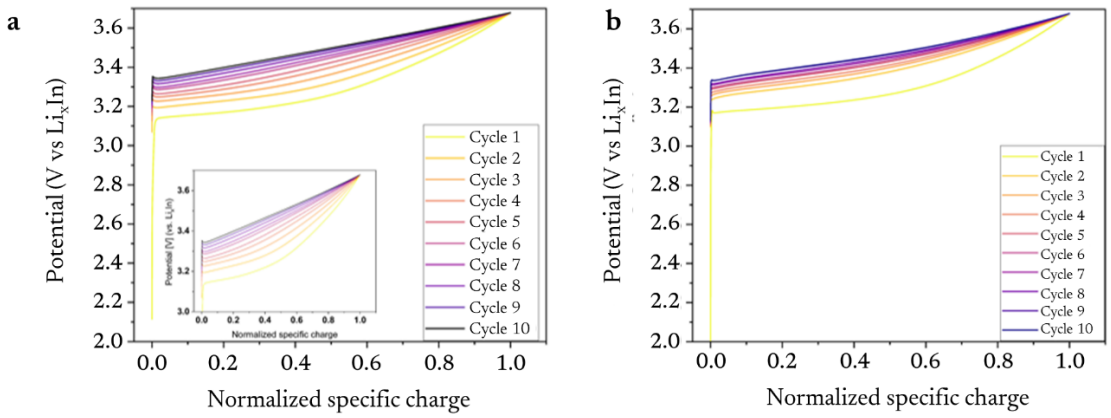

Figure 63: Normalized galvanostatic curves during charging highlighting the evolution of the polarisation along cycling of a) delithiation of the composite electrode compressed at 255 MPa for 10 min, b) delithiation of the composite electrode compressed at 255 MPa for 15.

Upon delithiation of NMC particles (**Figure 63a**), the polarization is building up in both compressed electrodes, slightly more for the 255-10m than for the 255-15h. For the latter, we can see a strong evolution between the first and the second cycle then a kind of small polarization after each cycle, whereas for the 255-10m, the evolution between the first and second cycle is less sharp, but the evolution between each cycle is more important. It shows that the chemical degradations occur cycle after cycle, but they are more marked for the least compressed electrode, as already proven by the CE. Again, this result is counterintuitive since in theory, the better the contact between the materials, the greater the chemical degradation, showing again that processes other than chemical ones are playing a role. Looking now at the evolution of current during the potentiostatic step (**Figure 64**), the behaviour is different between the two composite electrodes.

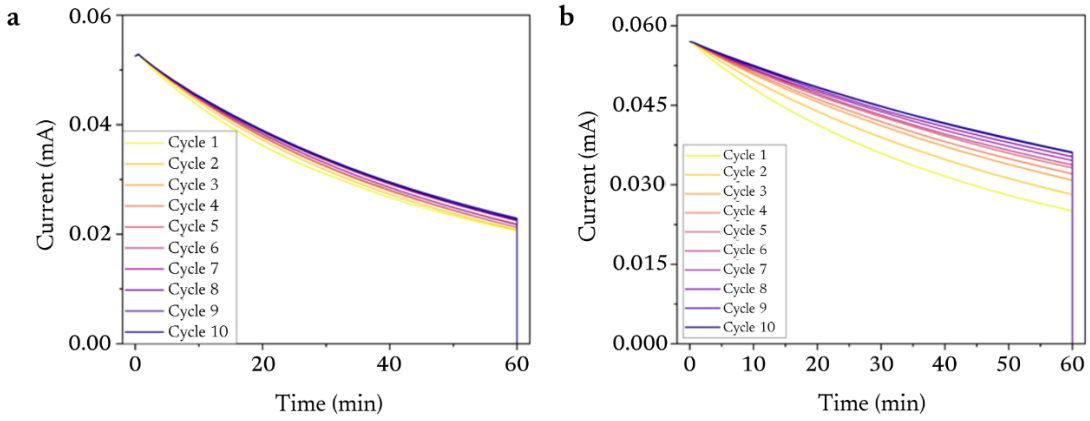

Figure 64: Evolution of the current response during the one-hour potentiostatic step, a) composite compressed at 255 MPa for 10 min, b) composite compressed at 255 MPa for 15 h.

As shown for the 255-10m (**Figure 64a**), we notice that the current during the potentiostatic step is always the same, with no evolution between each cycle. This is rather surprising since the specific charge decreases during cycling and the polarization increases, in theory, the potentiostatic step should deliver more charges to compensate for the ohmic drop seen in the galvanostatic cycles. Nonetheless, this may not be the case if these charges are inaccessible due to mechanical fractures and reduced contact between the electroactive material and the solid electrolyte. For the 255-15h (**Figure 64b**), we see that the current is less and less important cycle after cycle, which indicates that the cell also suffers some mechanical and chemical issues.

Based on the previous analyses of the electrochemical data, we believe that both chemical and mechanical issues play a role with the chemical one being the most important during the first cycle, whereas the mechanical one appears to be important for the other cycles. Once the mechanical ones play a role, the charges are no longer accessible because they are no longer connected to the electronic/ionic network. We thus conducted a full investigation relying on FIB-SEM tomography to understand the role of the microstructure in the composite electrodes as a function of the RT sintering parameters.

4.2.2 Morphological characterizations

Tomographic volumes were acquired by FIB-SEM for the two pristine composite electrodes. Their following 3D reconstructions are displayed in **Figure 65**.

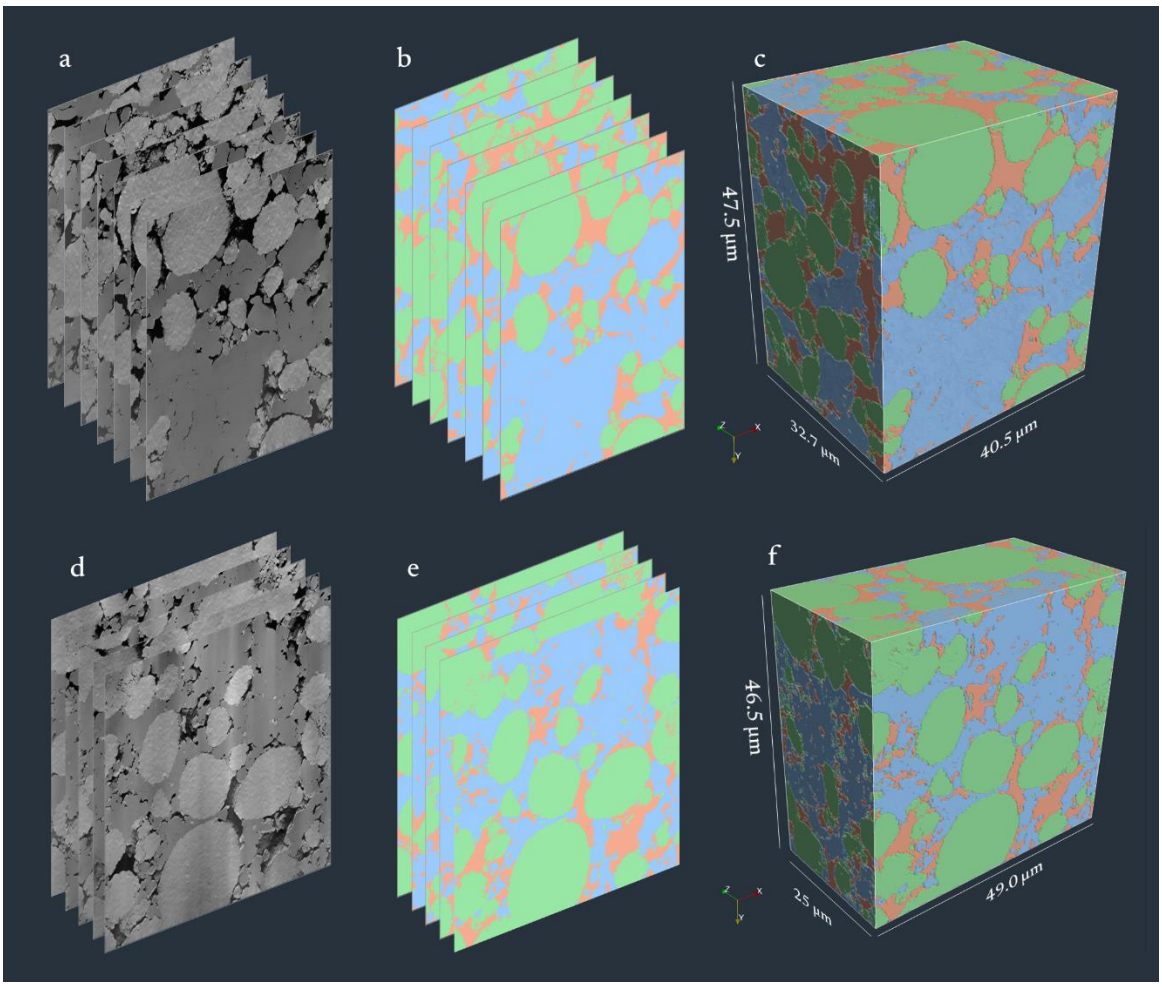

Figure 65: Composite electrode pressed at 255 MPa for a) – c) 10 min and d) – f) 15 h. a), d) Secondary electron images, b), e) segmented images and c), f) 3D reconstruction with NMC 622 in green, LPS in blue and porosity in orange.

The representative elementary volumes (REV) are obtained on each phase for both tomographic volumes and plots are presented in **Figure 66**.

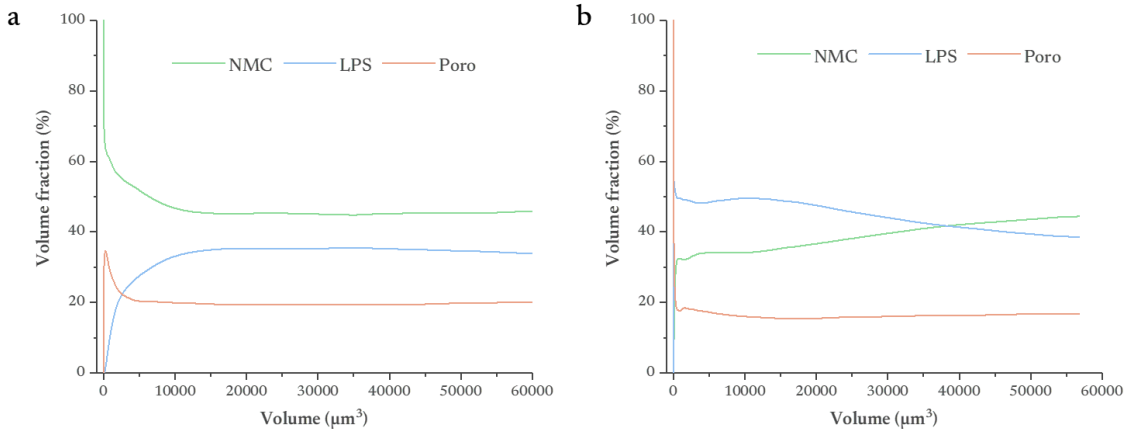

Figure 66: Representative elementary volumes (REV) of the three segmented phases, NMC622, LPS and porosity of the sample sintered at a) 255 MPa for 10 min and b) 255 MPa for 15 h.

Based on the data processing, we can extract several parameters divided into three categories: the first category will report general quantification of the volume fraction; the second will report the description of the ionic network, i.e. the LPS only; the third category will report the electronic network, i.e. the NMC. All these parameters are summarized in **Table 5**.

Table 5: Summary of all the results extracted from tomographic volumes. Composite electrode made with 70:30 wt.% NMC622:LPS ratio. Conversion to weight percentage to volume fraction is made using the density ρ_{LPS} = 1.88 g·cm^{-3} and ρ_{NMC} = 4.6 g·cm^{-3}.

	Metrics	Targeted	255 MPa		
			10 min	15 h	15 h 1st charge
Volume fraction (%)	**NMC**	51	45.9	44.4	51.9
	LPS	49	33.7	38.6	29.8
	Porosity	/	20.2	16.7	18.1
	Unmarked	/	0.2	0.3	0.2
	NMC:LPS ratio	51:49	58:42	53:47	64:36
Ionic network	**$\tau_{+/-y}$ tortuosity LPS**	/	1.52	1.29	1.31
	Average local thickness (μm)	/	1.76	1.40	1.37
	Std. dev. local thickness (μm)	/	0.88	0.72	0.80
Electronic network	**%connected$_{NMC}$**	/	98.1	97.3	98.3
	A_{CAM}/V_{cell} (μm^{-1})	/	0.79	0.80	1.05
	%coverage$_{NMC}$	/	25%	76%	42%
	$\tau_{+/-y}$ tortuosity NMC	/	1.37	1.57	1.41

As expected, the densification is always critical, and porosity must be reduced to a minimum to avoid electronic/ionic transport hindrance. In both composites, we found significant porosity, 20.2 vol.% for the 255-10m and 16.7 vol.% for the 255-15h, as shown in **Figure 67** and despite these high values, the cells can cycle.

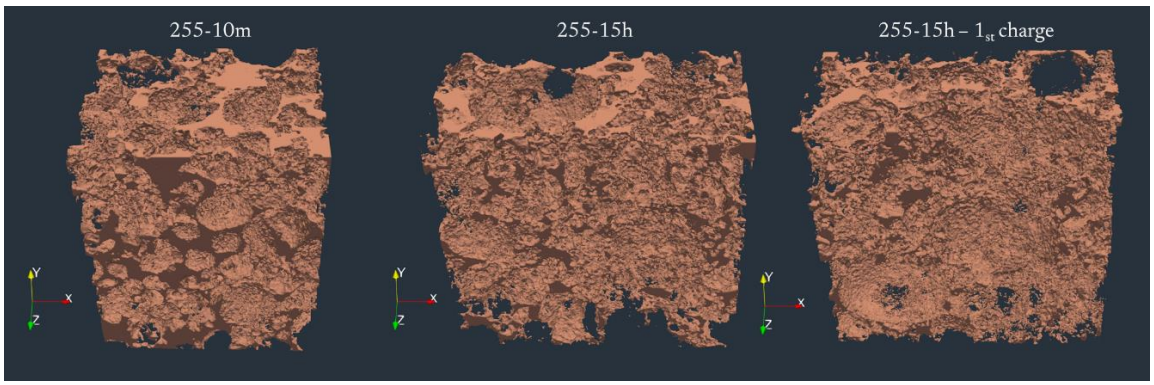

Figure 67: 3D reconstruction of the FIB-SEM tomographic volumes of the composite electrode sintered a) 255 MPa and 10 min; b) 255 MPa and 15 h, and c) 255 MPa and 15 h after the first charge.

An additional issue with porosity is their location within the sample and the connection between them. Located partially at the surface of the active materials would mean, at best, a drastic hindrance of the transport and a high polarization (poor interfacial contact), at worst, a full disconnection of the particle. Connected porosity within the sample could lead to a fragile mechanical ability (possible fracture along the pellet). Here, porosity in the two samples is mainly interconnected (98.1% and 97.3% for the 255-10m and the 255-15h respectively), thus impacting the electrochemical response of the samples.

Two additional metrics can be used to characterize the ionic network: i) geometric tortuosity that describes the mean length of every possible path in the composite electrode from the current collector toward the separator, and ii) local thickness that describes the diameter of these paths. The local thickness distribution and geometric tortuosity are shown in **Figure 68** for both samples.

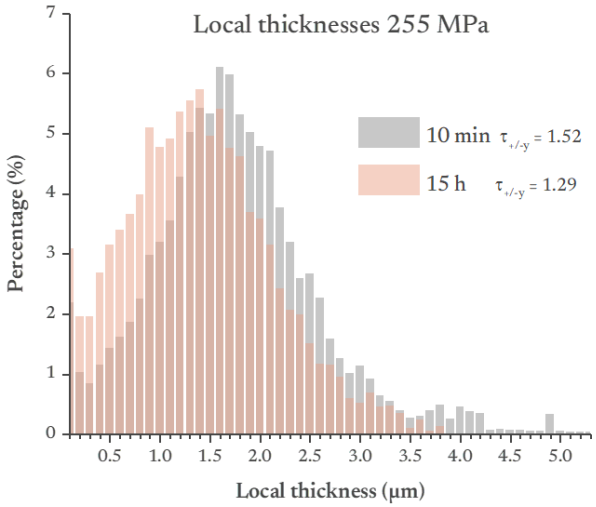

Figure 68: Local thickness distribution of the electrolyte in the composite positive electrode for the 10 min sample in grey and the 15 h sample in orange.

It can be seen that the average local thickness is slightly greater for the 255-10m than for the 255-15h with 1.76 μm and 1.40 μm respectively, meaning that the sample pressed for a longer time has more randomly distributed pores, which decreases the local thickness. Despite the lower local thickness, the tortuosity along the sintering axis (and lithium-ion transport paths) is smaller for the 255-15h than for the 255-10m with 1.29 and 1.52 respectively. This means that the transport is less hindered in the 255-15h despite the smaller Li-ion channel observed by local thickness measurement.

To gather additional information about the ionic and electronic pathways within the composite electrode, we performed some DC polarization measurements. The goal is to use a blocking system either for ions (using stainless steel / composite electrode / stainless steel configuration) or for electrons (using stainless steel/ Li-In/ SE/ composite/ SE/ Li-In/ stainless steel configuration) as shown in **Figure 69** (for the electronic conductivity), **Figure 70** (for the ionic conductivity).

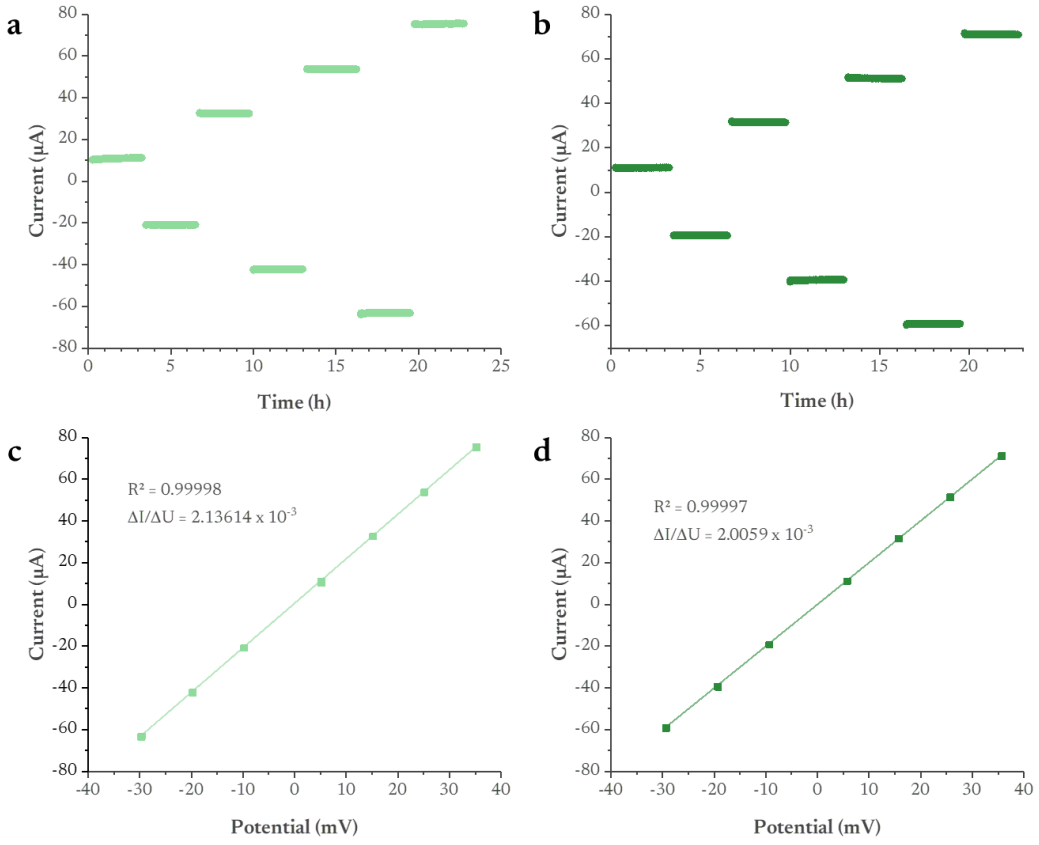

Figure 69: Results of electronic DC polarization measurements using an ion-blocking symmetric configuration (stainless steel / composite electrode / stainless steel). (a-b) Current response versus time for the 10 min and 15 h compressed electrode, respectively, and (c-d) corresponding linear Ohmic behaviour of the composite electrode.

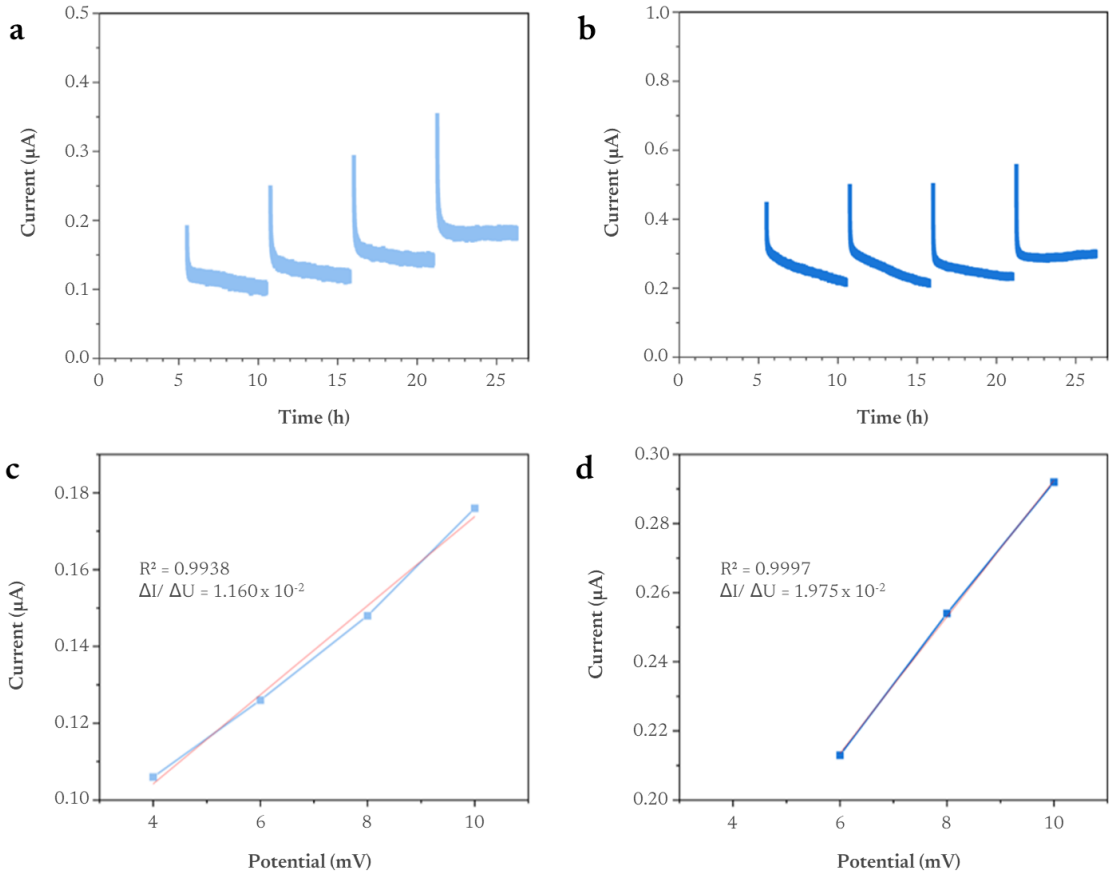

Figure 70: Results of ionic DC polarization measurements using an electron-blocking symmetric configuration (stainless steel/ Li-In/ SE/ composite/ SE/ Li-In/ stainless steel). (a-b) Current response against time for the 10 min and 15 h compressed electrode, respectively, and (c-d) corresponding linear ohmic behaviour of the composite electrode.

From the previous graphs, the effective electronic and ionic conductivities of the composites can be extracted (**Figure 69** and **Figure 70** respectively). Knowing the electronic conductivity of NMC alone[162] and the ionic conductivity of LPS[164], the effective tortuosity can be calculated with **Equation 5**[166].

Equation 5: Calculation of tortuosity factor

$$\tau_i = \frac{\varphi_i \times \sigma_{0,i}}{\sigma_{eff,\ i}} \qquad (5)$$

With τ_i the tortuosity factor, φ_i is the volume percentage of the conducting phase, $\sigma_{0,i}$ is the conductivity of the pure conducting phase, $\sigma_{eff,i}$ is the effective conductivity of the composite electrode. The index $i \in$ {el, ion} refers to the electronic or ionic phase.

The obtained results are summarized in **Table 6**.

Table 6: Summary of the ionic/electronic tortuosity extracted from the DC polarisation test.

Composite electrode	Effective electronic conductivity ($mS \cdot cm^{-1}$)	Electronic tortuosity factor	Effective ionic conductivity ($mS \cdot cm^{-1}$)	Ionic tortuosity factor
255-10m	1.04	11.0	0.010	19.3
255-15h	1.10	11.4	0.017	13.9

As shown, the two composite electrodes have roughly the same electronic conductivity, thus the same tortuosity factors which is logical since in both cases we have the same ratio of NMC particles, and they seem to be connected similarly as demonstrated in **Table 6** and that no conductive agent was added. For the ionic pathway, we can see a difference with less tortuosity and better effective ionic conductivity, as expected by the ionic network characterized previously (**Table 6**). Those results show that our methodology based on microstructural investigation can be used to complement electrochemical performance to assess the electronic/ionic pathway. Based on these results, the electrochemical performance should be better for the sample with the lowest tortuosity.

Another parameter that needs to be considered is the electronic network within the composite electrode which seems to be similar in both composite electrodes based on the DC polarization test. In general, conductive agents are used to improve the electronic percolation in the composite electrode. However, in the present case of the fundamental understanding of the microstructure within the composite electrode and as long-term cycling nor fast charging is the scope of the thesis, we decided to only assess the electronic transport of the NMC particles. Moreover, as the carbon additives promote interfacial reactions and enhance the electrolyte decomposition[58,167,168], we decided to make our composite electrode free of carbon. Thus, the electronic connection is only ensured by the contact between NMC particles in 3D. In both samples, most of the NMC particles are connected (98.1 % and 97.3 % for the 255-10m and the 255-15h respectively). The remaining small fraction of unconnected NMC is generally linked to primary particles that fractured during the electrode preparation as they are entirely covered by LPS.

Both ionic and electronic networks rely on the homogeneous coverage of NMC by LPS (to ensure ionic connection) and NMC by NMC to ensure 3D electronic percolation. Thus, the surface coverage of the NMC (surface of the NMC, A_{NMC}) particles is of high importance. We believe that the NMC particles do not serve for ionic pathway, since the LPS ionic conductivity is higher than the one of the NMC particles. Each particle of NMC is either exposed to LPS ($A_{NMC\ active}$) or the porosity ($A_{NMC\ inactive}$). Thus, the coverage of NMC could be deduced from **Equation 6**.

Equation 6: Calculation for the percentage of coverage of NMC particles.

$$\%\text{coverage}_{NMC} = \frac{A_{NMC\ active}}{A_{NMC}} \times 100 \qquad (6)$$

One can see a drastic change at the interface between the NMC and the SE (**Table 5**) only 25 % of the surface of the NMC is in contact with the LPS in the 255-10m sample, showing that an ionic limitation is excepted here leading to poor electrochemical performance while it increases to 76 % for the 255-15h, expected to have better ionic transport, thus better electrochemical performance. Based on this result, we can better understand the electrochemical performance of both composite electrodes as seen in **Figure 62**, where the 255-15h sample outperforms the 255-10m sample, highlighting the importance of LPS/NMC connection.

4.2.3 Electrochemical properties & microstructural evolution during cycling

As shown, we fully characterized the composite electrode as a pristine material. However, during cycling, NMC622 is experiencing some volume changes due to the lithiation/delithiation process that can lead to microstructural evolution. First, we report in **Figure 71**, the respective electrochemical response of the composite electrodes and compare it to the cycling of NMC622 electrode materials in classical organic electrolytes.

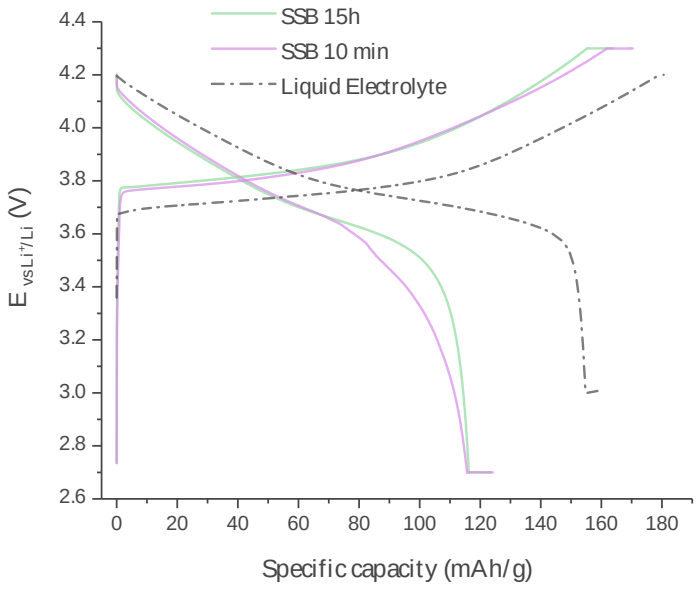

Figure 71: First galvanostatic cycling of 255-10m (purple) and 255-15h (green) at C/20 rate between 2.7 and 4.2 V vs. Li+/Li with a potential hold of 1 h. The liquid electrolyte cell was cycled at a C/10 rate between 3.0 and 4.3 V vs. Li^+/Li.

Compared to an optimized liquid-based cell, the solid-state cells are more polarized (ca. 0.1 V) indicating a higher resistance, as expected since i) no conductive agent was added to the composite electrode and ii) the probable chemical decomposition is more detrimental in solid-state batteries than in a liquid-based cell. Nevertheless, and since we are using a very slow rate, both solid-state batteries show acceptable electrochemical performance as can be seen in **Figure 62**.

To understand the role of the microstructure during cycling, the sample 255-15h was investigated after the 1st charge (3D analysis), the 1st discharge and after 11 cycles (2D analyses). For the end of the first charge of 255-15h, the REV plot shown in **Figure 72d** confirms the representativeness of the three phases. The reconstruction is shown in **Figure 72a-c** and additional images comparing the pristine sample and end-of-charge sample can be found in **Figure 73**.

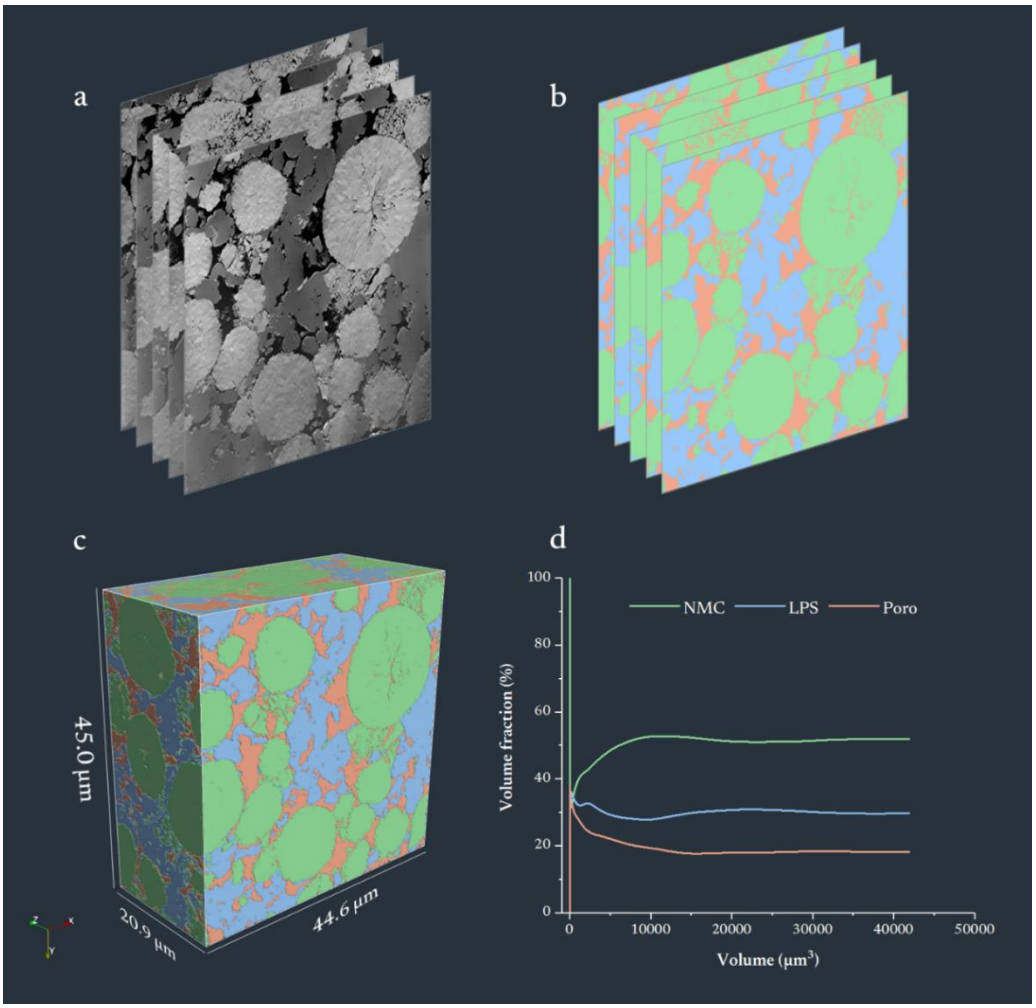

Figure 72: Composite electrode pressed at 255 MPa for 15 h after the first charge. a) Secondary electron images, b) segmented images and c) 3D reconstruction with NMC622 in green, LPS in blue and porosity in orange. d) Representative elementary volume of the three segmented phases, NMC, LPS and porosity.

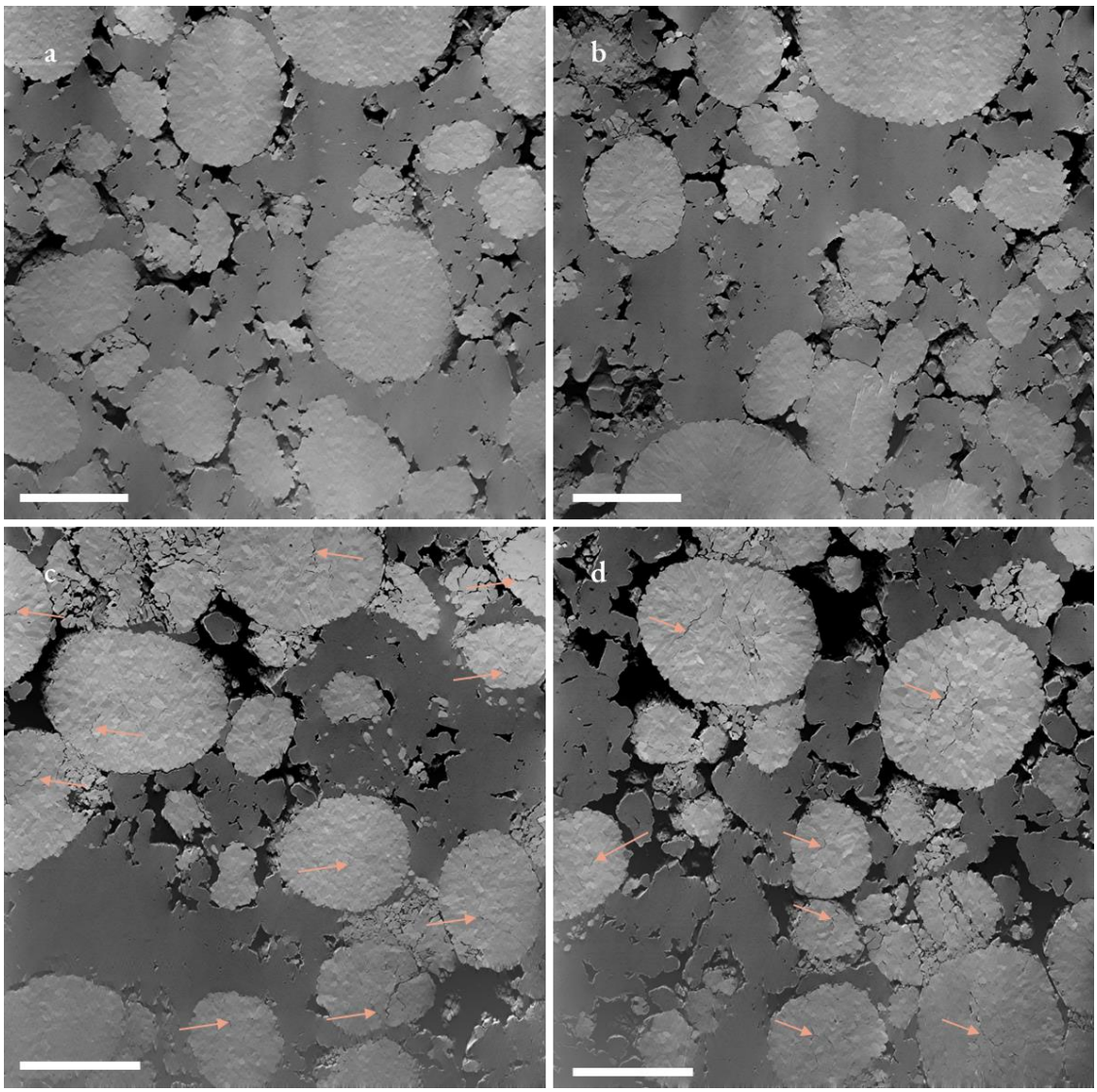

Figure 73: Secondary electron image extracted from the composite electrode (255 MPa and 15 h) stack of a, b) pristine state; c, d) at the end of the first charge; the orange arrows highlight the internal fracture of the NMC622 particles. Scale bars represent 10 μm.

During delithiation, NMC622 undergoes some structural changes, especially an overall volume shrinkage with a large c lattice increase generating distortion of the crystal structure[67,68]. This leads to the inner fracturing of NMC secondary particles (**Figure 73c-d**) as is discussed further in this section. The shrinkage of NMC volume (ca. 4 %[66]) leads to an increase of 1.4 % in porosity at the end of charge which is more or less logical given the volume fraction of NMC used in the composite electrode (**Table 5**). The small difference between the theoretical volume change and the observed volume change could be explained by i) the local elasticity of LPS (Young's modulus), and/or ii) the thick LPS separator (ca. 500 μm) acting as a spring elastically absorbing the deformation and/or iii) the InLi counter electrode expansion[169]. However, it is hard to discriminate one from the others as FIB-SEM tomographic volume has a narrow field of view compared to X-ray computed tomography.

Nevertheless, we demonstrated something similar with the Sn negative electrode cycled with LPS. We believe that working hypotheses i) and ii) are playing a key role here[98].

Looking at the ionic network (**Figure 74**), the local thickness shows the same trends as the pristine sample but slightly more spread to smaller and larger thicknesses.

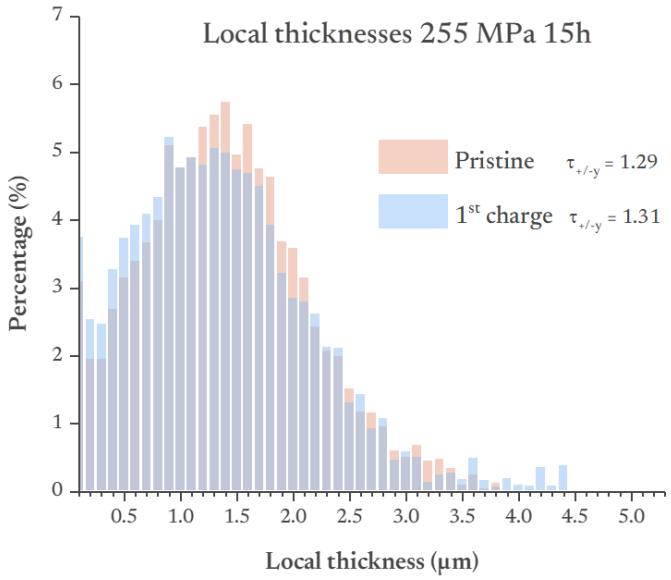

Figure 74: Local thickness distribution of the electrolyte in the composite positive electrode pressed for 15 h for the pristine sample in orange, and after the first sample charge in blue.

The tortuosity remains equivalent to the pristine state showing that the electrochemical activity of the NMC is not detrimental to the composite electrode integrity during the first charge (with 4 % expansion). It is well described that the volume expansion increases with the Ni content inside the NMC[13,68]. It is expected from Conforto *et al.* that polycrystalline NMC fractures (in this case NMC811) will increase the tortuosity by a factor of 2 after 40 cycles due to an increase in the length of the pathway for lithium diffusion [170]. Even if NMC622 suffers less from a volume expansion than NMC811 (4 % vs. 5.5 %[61] respectively), the length of the pathway for lithium diffusion will eventually increase with NMC622 as both NMC have the same degradation mechanism from fracturing.

Concerning the electronic network, the NMC connection is similar before and after cycling. However, a higher surface area of NMC (A_{NMC}/V_{cell}) is found on the sample after the first charge going from 0.80 to 1.05 μm^{-1}. Even if the volume fraction of NMC is different between the two tomographies (44.4 vol% to 51.9 vol% respectively before and after the charge), the difference remains significant. Indeed, even when the surface area of NMC is normalized to its volume fraction (A_{NMC}/V_{NMC}), the ratio still rises from 1.80 to 2.03 μm^{-1} before and after the first charge respectively.

This observation could be explained by the fracturing of the NMC during cycling[69,73]. Indeed, charged NMC particles show cracks within the secondary particle (**Figure 75**) coming from the change in the lattice parameters caused by the delithiation, which is later counted as a more developed surface area A_{NMC}.

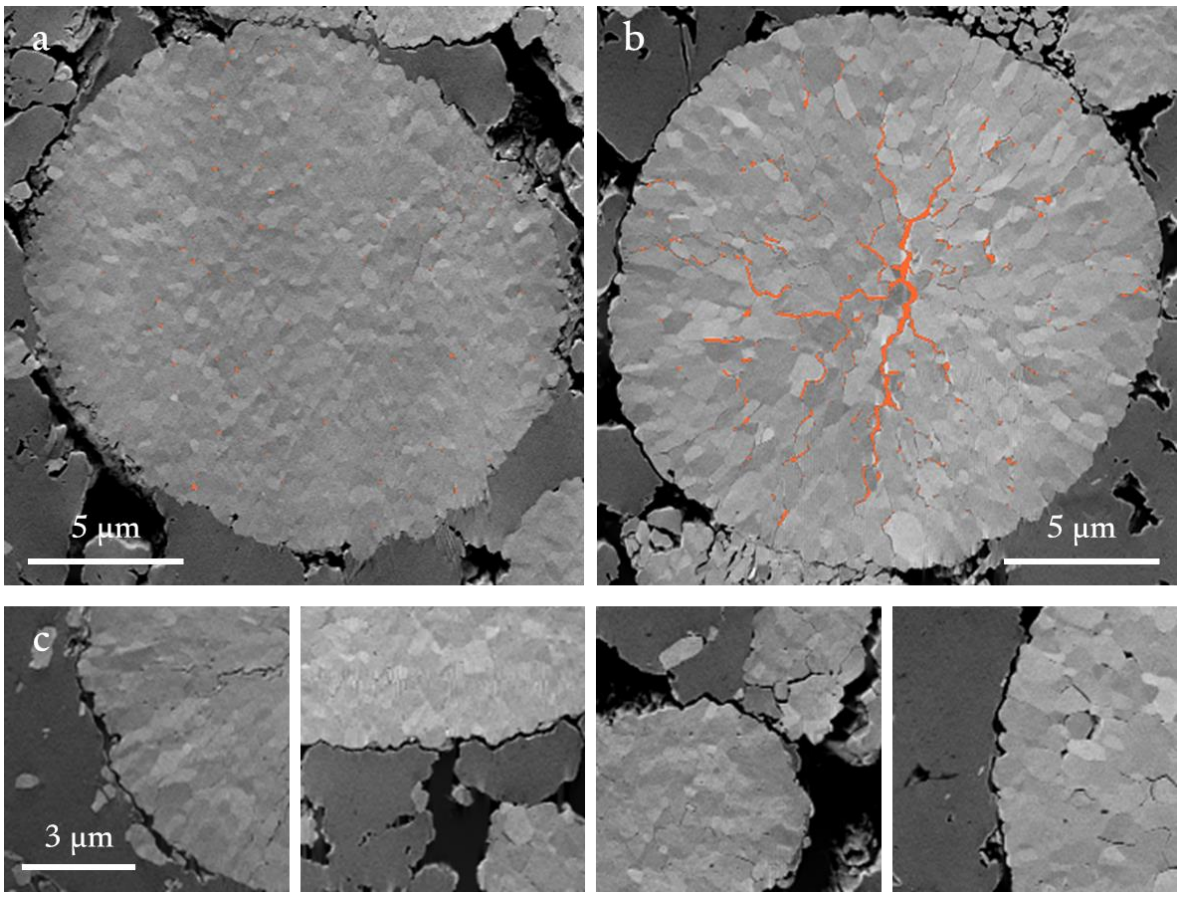

Figure 75: NMC in the composite positive electrode (secondary electron image) sintered for 15 h at 255 MPa in a) pristine state and b) after the 1st charge extracted from the FIB-SEM stacks with the NMC in light grey, the LPS in dark grey and the porosity in black. The inner porosity is highlighted in orange. c) Imprint of the NMC on the LPS underlying the NMC volume change, secondary electron images extracted from the FIB-SEM stack at the charge state.

Tsai *et al.* study on Li-rich NMC showed that the fractures of NMC initiate at the core of the particle to later propagate to the surface[73]. The same phenomenon has been seen by Cadiou *et al.* where NMC811 internal porosity increases with cycling before opening the secondary particle[69]. The same observation could be seen here on NMC622 (**Figure 75b**). Nonetheless, contrary to Cadiou's study with liquid electrolytes, fractures here are a cause of lithium path lengthening and particle disconnection. The NMC inner porosity in its pristine state is estimated to be ca. 1.3 % of the overall porosity while it increases to ca. 2.5 % in the charge state, a value that doubles in only one charge. However, since we have demonstrated that the composite electrode is somehow breathing during charging and since the electrolyte has a certain Young modulus, we also investigate the composite electrode after one full cycle, i.e. at the end of the lithiation of NMC particles. When comparing the

sample at the end of the charge (**Figure 75** and **Figure 73c-d**) to the one collected at the end of the discharge (**Figure 76**), we see that a fraction of the inner NMC porosity is partially recovered as some fracture seems to "closed up" (to a certain extent) and some remaining, hindering the diffusion of Li-ion within the particles. Additionally, it can be seen in **Figure 76** that at the interface between LPS and NMC622, the NMC622 particles left an imprint on the LPS matrix, very similar to the one reported in **Figure 75c**. This means a gap is generated at the interface between NMC and LPS that will block the electronic/ionic transport, hence, impacting the electrochemical performance (as already stated above). This result shows that the mechanical processes play a key role in reducing the electrochemical performance of the cell (as discussed already at the beginning of this chapter).

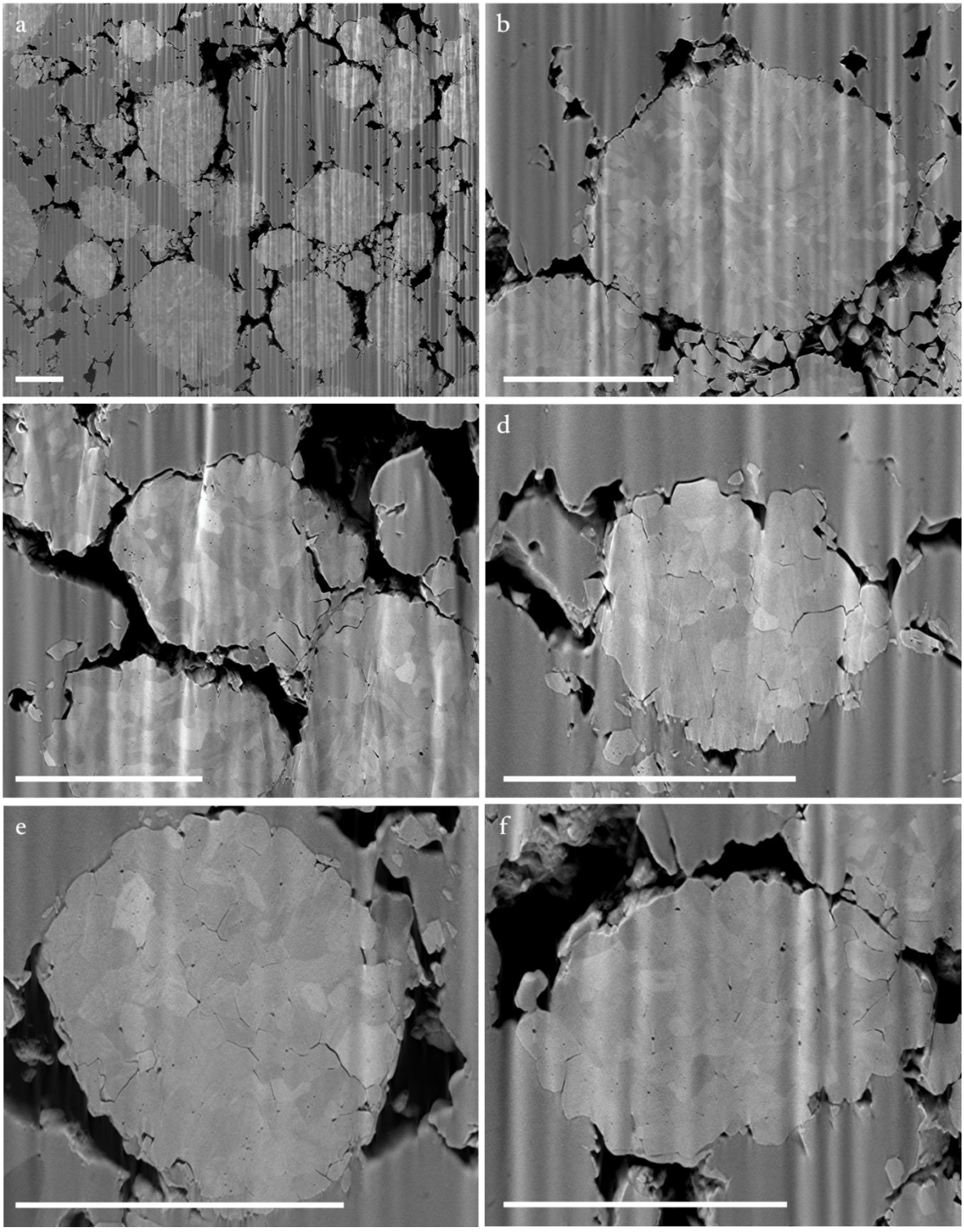

Figure 76: a) Secondary electron image of the overall cross-section of the composite electrode (255 - 15h) after 1 cycle (discharge) and b), to f) close-ups. Scale bars represent 10 μm.

Carrying on our investigations, we checked the evolution of the microstructure of the composite electrode after 11 cycles, when more than 30 % of the specific capacity was lost. As shown in **Figure 77**, fractures inside the NMC particles are no longer closing up after the successive charge/discharge processes. This indicates that after a certain number of cycles, the mechanical fractures will lead to a decrease in the electrochemical performance (as seen, especially for the poorly sintered composite

electrode 255-10m) due to the Li-ion transport hindrance within the particles but also due to the gap of a few nm (NMC imprint) let inside the LPS matrix, hindering the electronic and ionic transport.

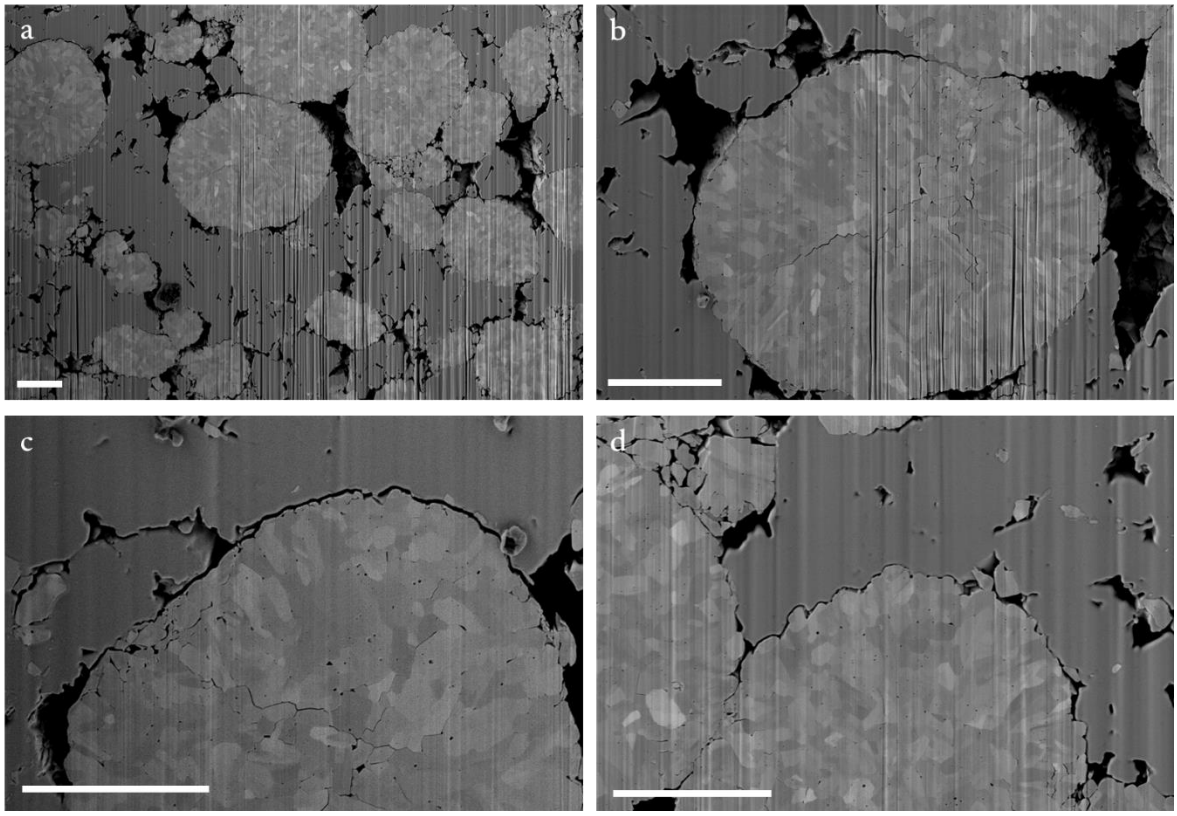

Figure 77: a) Secondary electron image of the overall cross-section of the 255 MPa-15 h composite electrode after 11 cycles and b), c), d) close-ups. Scale bars represent 4 μm.

This evolution could be even more detrimental if considering that hundreds of charges will be performed in commercial systems, leading to more fractures created. Additionally, if the cracking happens near the surface of the NMC particle, it could generate additional dead particles that will either be disconnected from the electronic/ionic network or both. This cracking induced by shrinkage opens up NMC surfaces to the porosity yielding to a decrease in the coverage by LPS. This phenomenon is clearly visible on NMC particles which have kept their integrity (**Figure 75a-b** and **Figure 77**), but it could happen to any particle that participates in the electrochemical processes. As the solid electrolyte would not be able to accommodate the internal NMC fracturing imposed by the electrochemical activities, this would be detrimental to the specific capacity of the cell. In addition, when comparing the developed surface area of NMC obtained in the first estimate (c.a. 1.8 μm^{-1} at 255 MPa) to the surfaces obtained from the tomographic volume in the pristine state (c.a. 0.8 μm^{-1} at 255 MPa), it can be seen that LPS act as a buffer that mitigates the NMC fractures.

Finally, the percentage of coverage of the NMC by LPS decreases significantly after a single charge down to 42 % as expected from NMC particle shrinkage. This change in volume leaves a visible imprint of the NMC on the LPS and creates a gap of a few hundred nm between the active material

and the electrolyte (**Figure 75c**) showing again the difficulty of controlling properly the solid/solid interface, despite favourable Young's modulus from LPS.

4.3 Conclusion

In this section, the evolution of the morphology of the composite positive electrode made with solid electrolyte LPS and NMC622 was conducted. We first demonstrated that the morphology of the polycrystalline NMC particles is not properly adapted for composite electrodes for solid-state batteries, as the particles, designed for good wetting in the liquid electrolyte, start to fracture under pressure. Nonetheless, it has been shown that the NMC fracturing induced by pressure is mitigated by the addition of soft material like LPS. The latter acts as a buffer between the secondary NMC particle by avoiding direct contact points and part of the pressure is redistributed to sinter the SE. Ionic and electronic conductive networks within the composite were calculated by microstructural investigation and electrochemical techniques both showing the same trend. Both are impacted by the overall large porosity remaining in the composite electrode. Then, it was found that most of the NMC are electronically connected to the current collector at 255 MPa (98.1 %, 97.3 % and 98.3 for the 10 min, 15 h pristine and 15 h after the first charge respectively). It means that, in this cycling condition, the addition of conductive carbons is not necessary as it would consequently degrade LPS and it would be difficult to differentiate between a porosity and a conductive agent in our microstructural investigation. Moreover, it was established that a longer sintering time slightly decreases porosity and subsequently decreases geometric tortuosity, improving ionic transport. In addition, longer sintering time promotes an optimized contact between LPS and NMC without increasing the sintering pressure which ultimately would degrade even more NMC's morphology. We identify that the better cycling of the sample sintered 15 h originates from the more intimate connection between NMC and LPS despite showing first an enhanced chemical decomposition. Unfortunately, after the first charge, NMC shrinkage leads to the decohesion of the active material and the solid electrolyte, leading to low cycling ability for further cycles.

It has become evident that polycrystalline NMC was first and foremost developed and engineered for liquid electrolytes. Indeed, NMC fracturing, induced either by cycling or pressure (calendering) was balanced by the constant wetting by the liquid electrolyte and electronic connection by the conductive agent. However, solid-solid interfaces induce new dynamics between materials and formerly engineered materials will perhaps not find their application in future solid-state systems, or not as they presently are.

Generally, when it comes to microstructural investigation carried out by FIB-SEM, all morphological investigations are performed *ex-situ* which can bias the conclusion because of the number of samples to be investigated, the possible air/moisture exposure and the possible beam damage. Additionally,

in the case of battery, it is extremely challenging to monitor the dynamics of cycling since it would require too many samples and still, relaxation processes could occur between the end of the cycling, the cell disabling and the investigation. For those reasons, we decided to pursue our effort to give a proper understanding of the microstructural evolution of the composite electrode during cycling by specifically developing an electrochemical cell allowing an *operando* by FIB-SEM.

5

Operando FIB-SEM revealing the dynamics of morphological changes

As shown in the previous chapter, *ex-situ* investigations provide some valuable results in understanding morphological evolution but still present some drawbacks. First, the time to investigate one phenomenon is tremendous: multiple samples need to be independently fabricated and cycled. Then, each samples need to be extracted, prepared, transferred, imaged, treated and analysed. A major problem arising from these successive steps is the possibility of altering the sample. The cell previously under pressure may undergo relaxation and, more particularly, the extraction of the battery from the POM pellet holder causes the integrity of the battery to fall apart. The pellet shatters in multiple pieces and further analyses of the entire cell is seldom succeeded. This shattering is even more pronounced when the SE is nearly fully sintered (510 MPa). Still, the rough extraction might create other artefacts such as cracks, not present in the sample before extraction. For these reasons, the need for *operando* techniques with adapted sample preparation becomes more apparent. Recently, *in-situ* SEM has been performed to study interfaces between metal lithium and sulfide electrolytes leading to precious observation [110]. Nonetheless, the incapacity to reveal buried interfaces in SEM reduces the reach of the investigation. Only surfaces could be observed and interfaces where the electrochemical reactions are taking place remain buried. In that direction, a novel *in-situ* technique, namely *operando* FIB-SEM, which compromises most of the precited drawbacks has been developed. Indeed, this technique allows high-resolution dynamic morphology analysis of bulk materials as an SEM is used. In addition, this technique is laboratory-based and does not require access to large-scale facilities such as Synchrotron radiation.

5.1 Challenges

Developing and validating a novel *operando* technique is not as trivial as it seems, and major challenges must be addressed. First and foremost is the air-tightness of the transfer box, which is a primary concern when observing moisture-sensitive materials; the second is the adaptation of the connection from the cell to the potentiostat ensuring the correct current delivery while under high vacuum; the third is the preservation of the stack pressure on the cell; and forth, but not least, is the control of the pellet shape according to FIB-SEM observation limitations.

To overcome these challenges, a co-development has been carried out with the help of Smail Chalal, R&D engineer at Zeiss and Eric Salamand, mechanical design engineer at Défi Systèmes.

5.1.1 Preserving air-tightness

The most important challenge is ensuring a transfer from the glovebox to the microscope without moisture degradation. Indeed, only a couple of examples can be found in the literature since only solid-state batteries can be investigated under high vacuum since liquid electrolytes would evaporate. In the *in-situ* study of Yadav *et al.*, the major drawback was the pristine morphology of the β-LPS which appeared to correspond to moisture exposed sample, as seen in the first result chapter of this thesis (**Air exposure**, **p. 58**)[110,171]. To control properly the transfer from the laboratory to the FIB-SEM, the choice was made to modify the transfer box from Zeiss, which had already proven its efficiency and sturdiness for moisture-sensitive samples, and to develop inside the electrochemical part needed for *operando* cycling. The outer parts of the transfer box ensure airtight transfers while the inside has been redesigned.

5.1.2 Electrical connections

Multiple challenges lie in the electrical connection, especially the continuity of the connection from the cell to the potentiostat through all the apparatus gates. Lemo® connectors were selected to connect the transfer box to the stage of the microscope, and the stage to the door of the microscope, as they can withstand high vacuum with their robust and high-quality design and are easily installed/removed (push/pull connectors). Next, in this present study, only two cables were used for galvanostatic cycling, but the presence of five cables makes this design versatile for future improvements (temperature sensor or reference electrode). Then, the quality of the connection needs to be excellent, as poor shielding and leakage current can bring artefacts in the electrochemical answer. Finally, it was chosen to insulate the *operando* battery holder from the microscope stage as some current might be injected through the stage touch alarm which could generate additional artefacts on the electrochemical measurement.

5.1.3 Stack pressure

Stack pressure is essential when it comes to cycling on Li-ion batteries that they are employing liquid or solid electrolytes. In the case of SSB, the applied pressure maintains the intimate contact between the different components ensuring good electrochemical cycling. Unfortunately, the transfer box design is already crammed, and no motor could have been included to monitor and stabilize the stack pressure. Alternatively, a single PEEK screw, mounted on a spring, is maintaining the pressure while being guided by two PEEK pins: this solution presents the advantage to be easily manipulated in the glovebox (**Figure 78**) in addition to being insulating. Additionally, as mentioned in the previous chapter, the stack pressure does not need to be extremely high, if the sintering of the solid electrolyte and the composite electrode is well mastered before electrochemical cycling.

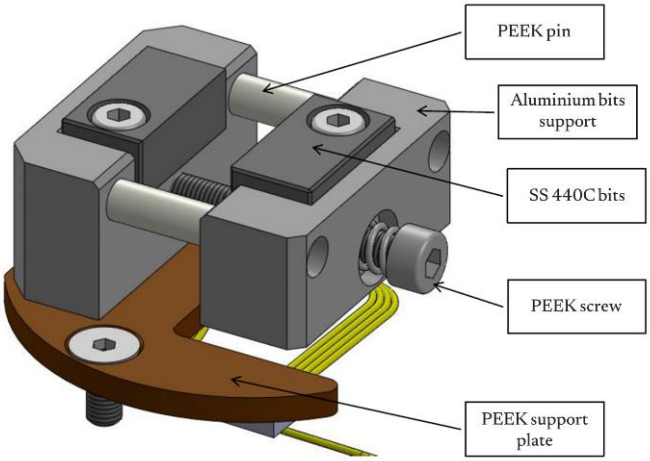

Figure 78: *Operando* cell design.

Nonetheless, the pressure cannot be controlled precisely. With the use of a torque wrench, the maximum pressure obtainable with the PEEK screw is estimated at ca. 15 kPa which is significantly lower than the typical stack pressure found in solid-state cells (ca. 50 MPa). Such a low pressure might affect the electrochemical response of the cell by giving high resistance, leading us to potentially change the upper and lower cut-off potential of the composite electrode and/or to use an extremely small current. The following results gathered in this chapter have been performed at this lower pressure, but the design of the *operando* cell can be further improved by replacing the PEEK guide with insulated stainless-steel screws which can withhold higher pressure (estimated pressure in the MPa range).

5.1.4 Cell shape on 2D observations

Due to the FIB-SEM observation restrictions such as the working distance at the coincidence position between the FIB and the SEM, the sample must be at a certain height in the transfer box. Moreover, a flat surface is necessary to have a wider area of observation and reduce shadowing effects.

In the literature[110], a large cell was prepared (ca. 10 mm) and then mechanically broken into three equal pieces in a die pelletizer shown in **Figure 79b**.

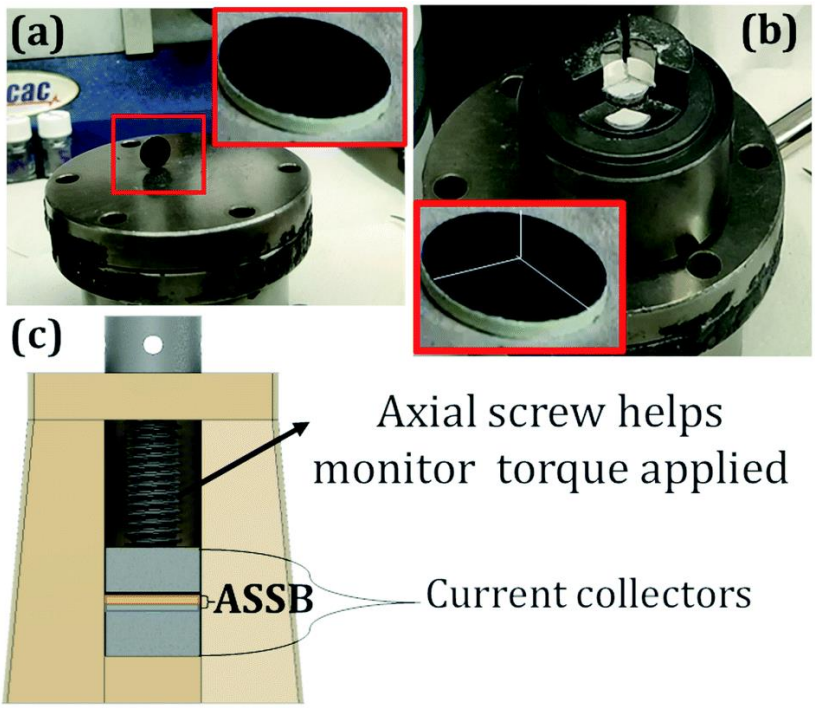

Figure 79: Battery assembly steps (a) self-standing pellet with SE and a cathode composite. (b) Mechanical breaking of the pellet inside a die pelletizer to obtain three pieces of battery. (c) The mounted battery in a homemade *in-situ* cell (IS_cell). Reprinted from Ref. [110].

One piece was mounted on the edge of the *in-situ* cell before being observed. This method of mechanical breakage of the pellet is criticized as it could induce some delamination between the electrodes and the separator, or it could initiate cracks inside the pellet that could be misattributed to fracture happening during cycling. Moreover, as the *operando* cell cannot rotate inside the FIB-SEM chamber due to the cabling, the sample must be prepared to ensure the direct investigation of the cross-section. To solve both aforementioned obstacles, the conventional solid-state cell used for cycling and room temperature sintering has been modified to provide a half-cylindrical cell without any breakage. The modified solid-state cell is presented in **Figure 80**. This methodology has the advantage of sintering the materials in a similar way that the one presented in the previous chapter, thus it allows a fair comparison between the *operando* cell results to the one collected by the *ex-situ* method.

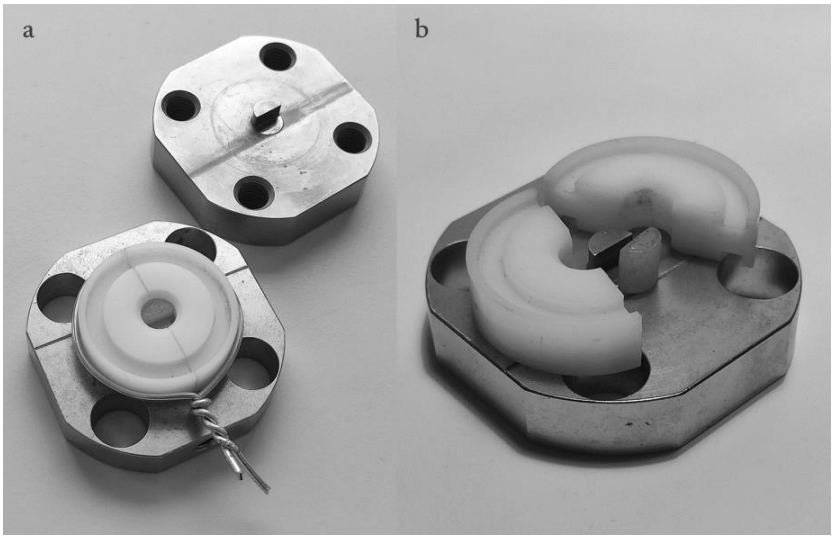

Figure 80: Modified solid-state cell to make a half-cylindrical pellet. a) Top and bottom part and b) opened bottom part.

After room temperature sintering, the electrochemical stack presents a flat surface suitable for cross-sectional investigation. Furthermore, the flat surface reduces the shadowing effect and eases further digging by the FIB. Once the battery is assembled, it can be transferred to the battery holder within the *operando* transfer box (**Figure 81**).

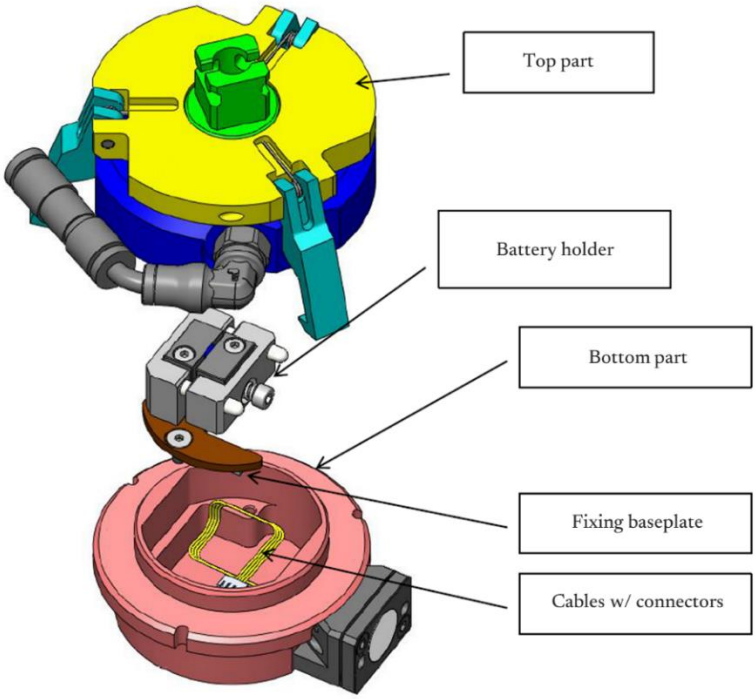

Figure 81: Scheme representing the transfer box that can be adapted to the FIB-SEM chamber along with the special electrochemical cell adapted to the transfer box.

5.2 Influence of the beam on the battery and its electrochemistry

Once the cell is plugged inside the FIB-SEM chamber analysis, the cell shows an open circuit voltage (OCV) of 1.9 V vs. Li^+/Li which is rather low for an NMC622 vs. Li cell, since ca. 2.1 V vs Li^+/Li was obtained in conventional solid-state cell (**Figure 82a**). Additionally, the impedance spectrum was collected and as expected for the poor pressure applied, the resistance is rather high and an inductance loop is visible and most probably coming from the cable passing through the SEM apparatus. (**Figure 82b**). Nevertheless, as explained, by cycling at a very low current and/or by changing the upper/lower cut-off to compensate for the ohmic drop, we should still be able to cycle properly our *operando* cell within the FIB-SEM chamber.

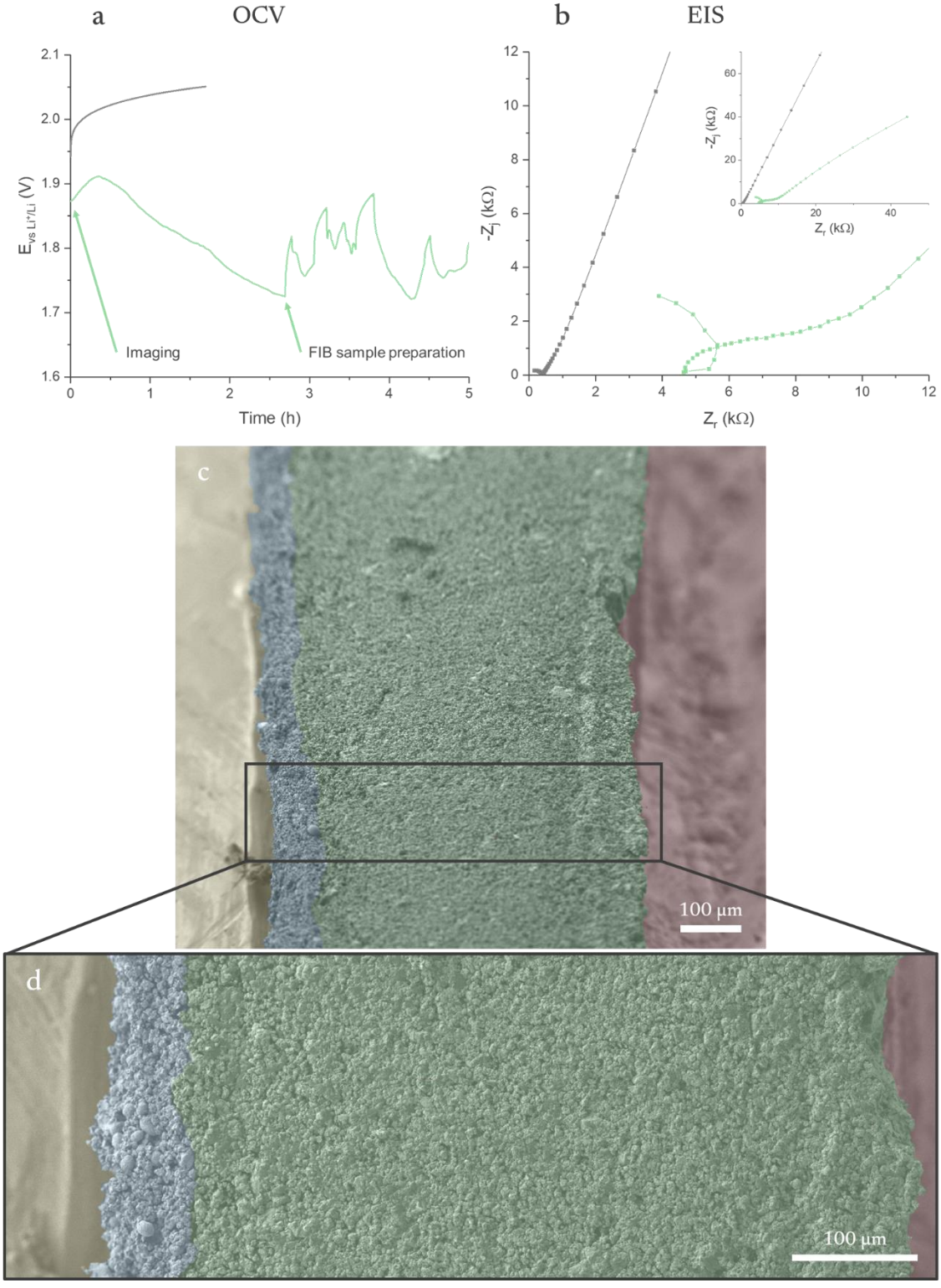

Figure 82: Comparison of SSB cell (grey lines) with *operando* cell (green lines) of a) open circuit voltage and b) Nyquist plot showing the electrochemical impedance signature of the *operando* cell. c, d) Secondary electron images of the surface of the pristine *operando* sample c) with a 54° tilt angle and d) with a 0° tilt angle. The current collector is highlighted in yellow, the composite electrode in blue (indicative), the separator in green and the negative electrode in red.

While digging the trench on the battery stack under the SEM to reveal an optimal cross-section to be further investigated during cycling, we noticed a variation of OCV of ca. 0.2 V, most probably coming from the ion beam and referring to the beam damage process. The pristine surface is presented in **Figure 82c**. From the primary observation, the interface between the solid electrolyte and the composite electrode is hardly visible, indicating optimal contact during shaping. Furthermore, the densification of the solid electrolyte (separator) and the composite electrode corresponds to what is generally obtained in our conventional cell[164,172]. Image analyses obtained from the cross-section reveal surface fractions of 39.6 % for NMC, 38.6 % for LPS and 21.8 % for porosity which is in agreement with our previous investigation of the composite electrode presented in the chapter **Composite positive electrode in solid-state batteries** (**Table 5**, **p. 106**). The general cross-section is presented in **Figure 83**.

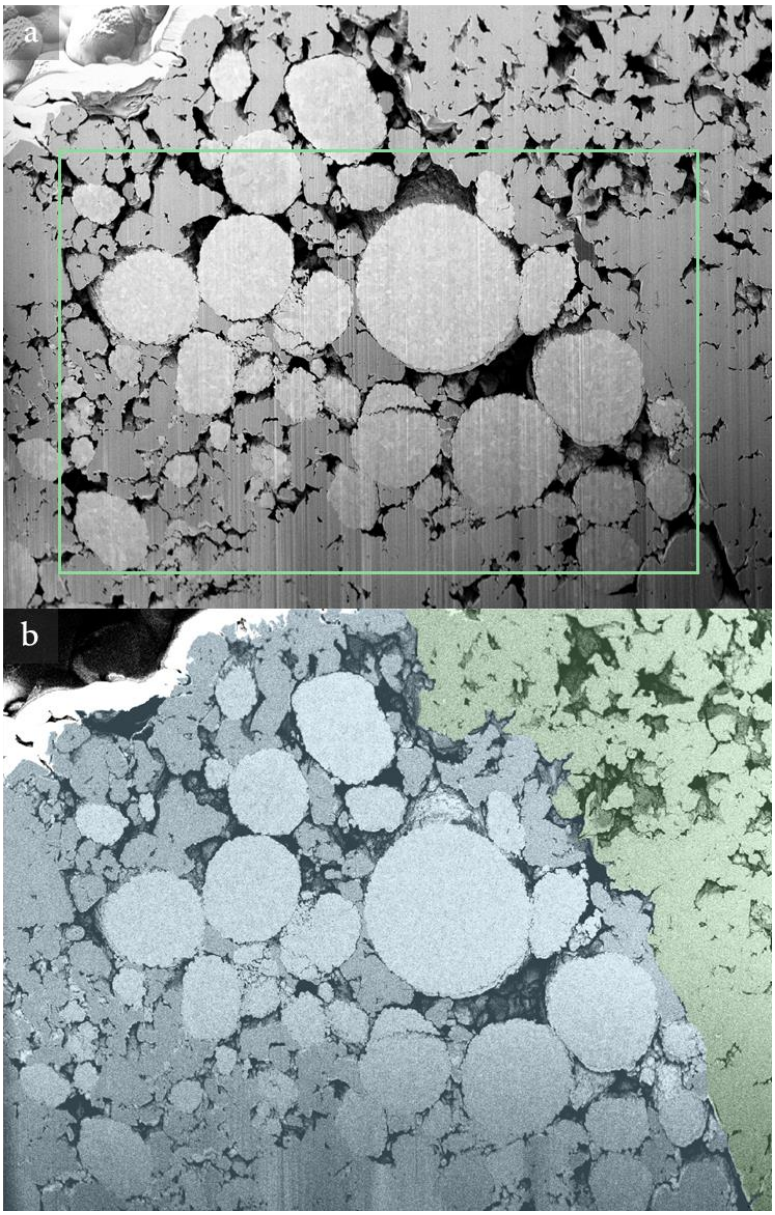

Figure 83: Cross-section at the pristine state from a) secondary electron and b) backscattered electron signal. On a) the green rectangle indicates the location where the volume fraction has been measured. On b), the blue overlay represents the composite positive electrode and the green overlay represents the separator.

5.3 Beam damage during cycling

As shown in **Figure 82a**, the ion beam is generating an overpotential of 200 mV on the electrochemical curve, leading us to take into account potential beam damage. So before starting the electrochemical investigation of the NMC composite under the beam, we first monitor the beam damage on the LPS. As a reminder, no morphological changes were observed at a pixel size of 15 nm after 10 min exposition at 2 nA in the *ex-situ* sample (see chapter **Morphologies of thiophosphates solid electrolytes**, **Beam damage**, **p. 60**). However, while cycling, with a higher pixel size (ca.

42.5 nm) and the same current applied on SEM, the cross-section surface is sensitive to the beam as the contrast between LPS and NMC fades slowly as shown in **Figure 84**.

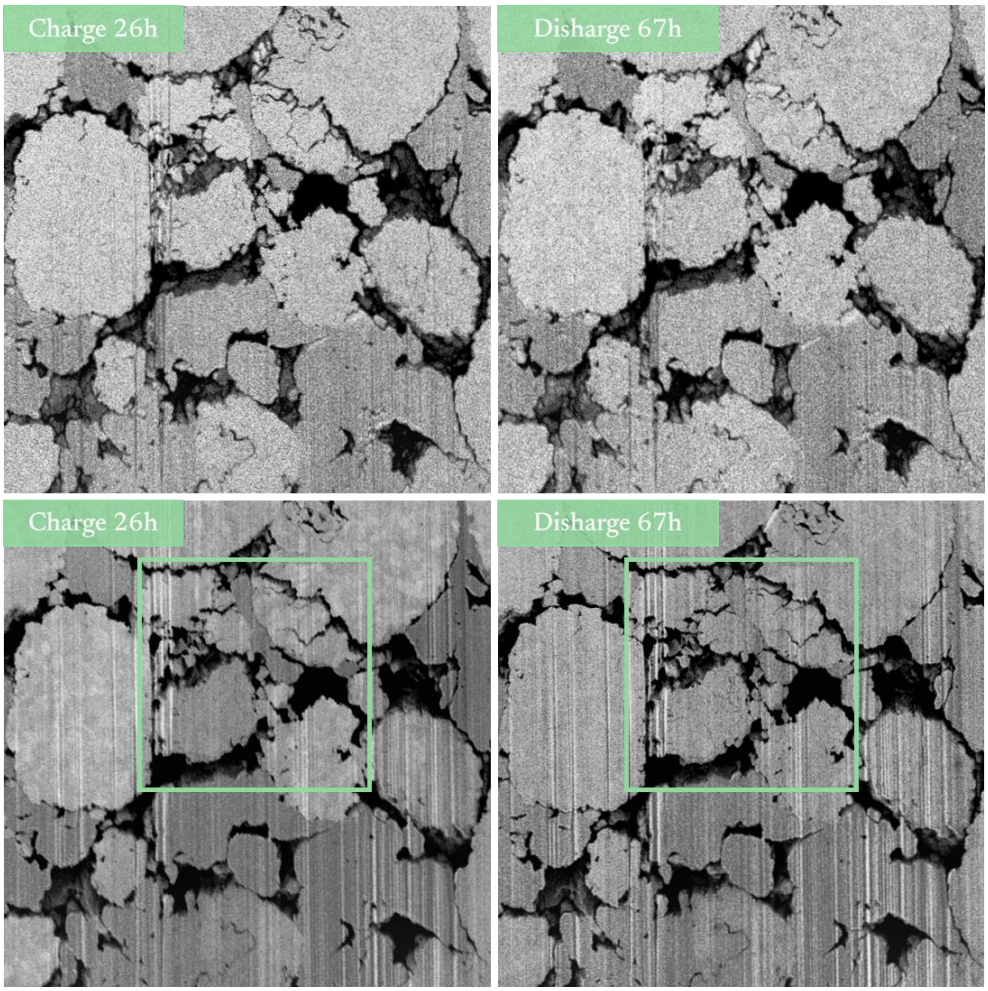

Figure 84: Images highlighting beam damage at the mid-charge (26h) and the end of the discharge (67h) on (top) backscattered electron image and (bottom) secondary electron images.

It can be seen on the secondary electron (SE) images (**Figure 84**, bottom) that the contrast between LPS and NMC is slowly lost compared to backscattered electron (BSE) images (**Figure 84**, top). Moreover, on SE images, the multiple primary grains within the NMCs can be distinguished at 26 h of charge while they disappear at 67 h of the discharge. From these observations and the different depths of electron generation (BSE are produced deeper in the primary excitation volume than SE), we can assume that the cross-section is slowly being coated by a layer in the nm range, leading to a loss of contrast in the SE images. This layer could be a hydrocarbon contamination emerging from i) the pumping system, ii) the degassing from other internal SEM components part (e.g. *operando* stage) and iii) the sample (including the handling and preparation)[173,174]. Hypotheses i) and ii) are implausible as the system vacuum was held for six hours at below 10^{-6} mbar before imaging and the parts going inside the chamber are always handled with gloves. The contamination must then come from the handling and the preparation of the sample in the glovebox.

This contamination could be avoided by i) carefully preparing the sample in a hydrocarbon-free environment and ii) reducing the dose exposed to the sample[175] (by reducing either the exposure time or the beam current). Option i) requires a glovebox exempt of volatile organic compounds, which is often impossible when liquid electrolytes are manipulated. Option ii) is the most costly in terms of image quality as a low exposition time and low beam current will increase the noise in the images. Nonetheless, this contamination resulting in a loss of contrast between phases does not affect the microstructure nor the morphology of the composite cathode and further observations will not be affected by the beam.

5.4 *Operando* observations

Due to the relatively low stack pressure applied to the battery, the internal impedance of the battery is notably higher when compared to a cell in a standard configuration (as shown in **Figure 82b**). This high internal resistance leads us to adjust the current of the cycling rate to minimize polarization during the cycling process. The current was progressively increased (**Figure 85**) from 2 μA to 20 μA. At the sight of the high polarization at 20 μA, the current was chosen at 15 μA. Equivalent to the active material inside the cell, this would correspond to a theoretical rate of ca. C/60. Nevertheless, due to the low stack pressure and the *operando* cell configuration (where the cell is slightly above the current collector shown in **Figure 82b, c** to minimize shadowing effects), some NMC particles could be isolated, without contributing to the actual capacity. In this direction, the actual rate experienced by NMC particles could be higher than C/60. The rate presented here is hence only an estimation and should be considered with caution. The galvanostatic cycling is presented in **Figure 85**.

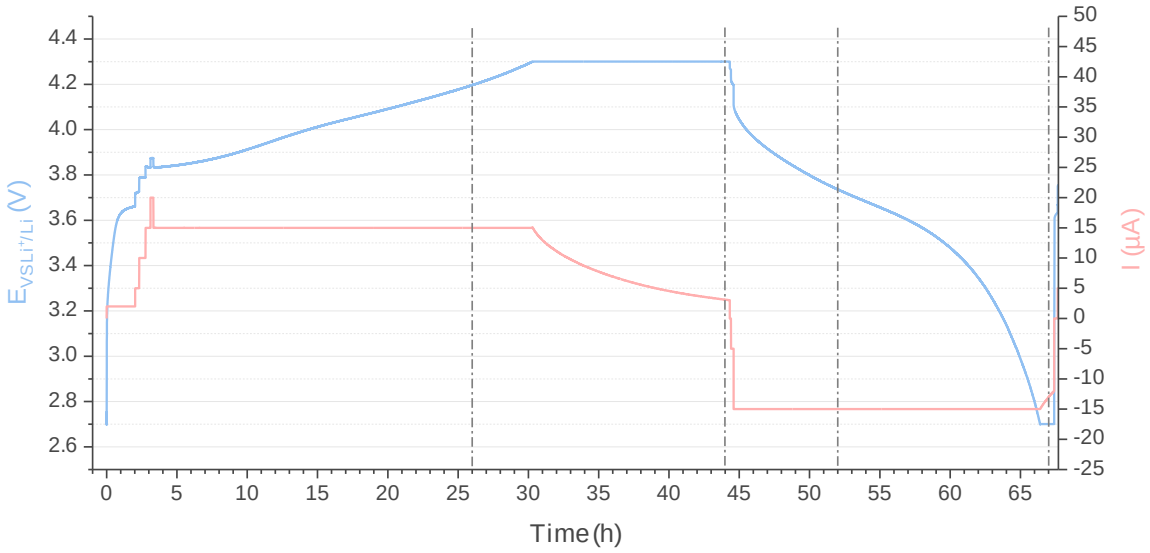

Figure 85: Galvanostatic cycling at ca. C/60 rate between 2.7 and 4.3 V vs. Li^+/Li with a potential hold until one-fifth of the initial current (15 µA) is reached. The dashed grey lines indicate the time the images were acquired.

As multiple information can be extracted from this *operando* measurement cell, we will first focus on the electroactive materials side (NMC particle fracturing), and then we will be looking at the interfacial contact between the NMC particle and LPS.

5.4.1 NMC particle investigation

As expected from the literature and as already reported by our group[172], the polycrystalline particles of NMC622 fracture during the sintering process of the composite electrode fabrication. Then, during the first charge (i.e. delithiation), particles that were intact before starting cycling begin to fracture along the multiple grain boundaries inside of the polycrystalline material. These fractures are both caused by the sintering, increasing surface area before cycling and by the overall volume shrinkage of the NMC622 during cycling[5,68,69,74]. With an elongation of the c-axis during the early cycling stage before a drastic reduction in the second half of the charge (leading to a c-parameter shorter than the one of the pristine material[67,176]), this causes a drastic distortion and internal fractures along the grain boundaries[66,177] as shown in **Figure 86b, c**. This type of fracture has already been observed in Li-rich NMC positive electrode materials by X-ray ptychography technique, and their extent was found in relation to the size of the particles[73]. Nonetheless, using NMC primary particles (known as single crystal) could halt inter-granular fractures and alleviate mechanical performance loss[61,178,179].

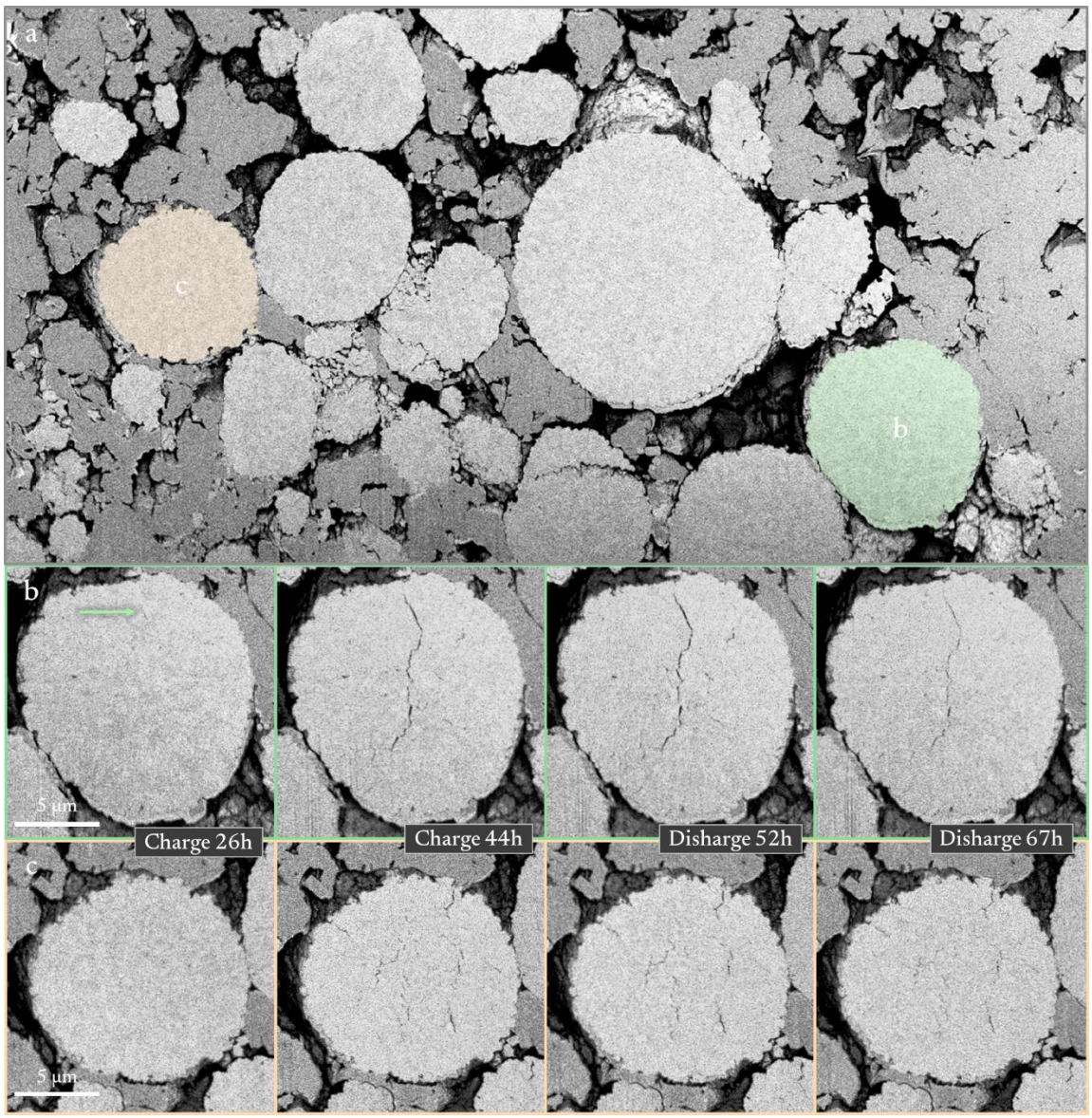

Figure 86: a) Backscattered image of the wide field cross-section view with followed NMCs highlighted at the pristine state. b-c) Backscattered images of two NMC622 particles at various time stamps highlighting the fractures during cycling, b) NMC located at the separator and c) NMC located at ca. 50 µm from the separator. The green arrow indicates the initiation of the fracture.

The first observation shows that a delithiation front across the positive electrode can be seen in **Figure 86**, arising from a poor ionic percolation (see chapter **Composite positive electrode in solid-state batteries**, **Table 6**, **p. 110**). Indeed, the NMC particles close to the separator (**Figure 86b**) show an initiation of fracture at the 26th hour (eq. to ca. 76 % of SOC) while on the NMC particles far from the separator (**Figure 86c**), the fractures only appear visible at the end of the potentiostatic plateau (44 h, eq. to ca. 99 % of SOC). The former indicates that the ionic pathway is short since, close to the separator (source of Li), the NMC is first delithiated, whereas, close to the current collector, the delithiation did not even start. At this stage, it indicates that, due to porosity, the ionic pathways are not optimal in the composite electrode leading to a lithiation gradient within the composite electrode. The gradient is caused by the low ionic conductivity of the composite

(linked to the poor sintering of the composite electrode and the volume fraction of the ion-insulating phase, i.e. NMC and porosity) coupled to the poor pressure applied for the *operando* measurement[59]. We can also note that some particles are not suffering any fracture during cycling which can be explained by i) the particles being disconnected from the electronic and ionic network, and/or ii) tougher grain boundaries between primary particles in the NMC, and/or iii) different lithium stoichiometry within the NMC particles. It appears that hypothesis i) is the most likely considering the amount of porosity in the positive electrode, the limited LPS-NMC connection and the low stack pressure.

During the lithiation of the NMC (e.g. discharge), the volume of the particle increases again, leading to a peculiar behaviour as the internal fractures partially recover. This behaviour is, at first, counterintuitive since the particles are again undergoing anisotropic volume changes. The fractures could have expanded but it appears that the fractures are partially recovered, and no new fractures appear. From the comparison of those two NMCs at different locations in the positive electrode, it appears that the fracturing is more drastic in particles close to the separator, indicating a deeper delithiation. In **Figure 86b** (NMC located at the separator), a fracture as wide as ca. 120 nm is formed during the charge. This fracture has a length of roughly 9 μm, crossing two-thirds of the particle and is being partially recovered at the end of the discharge (still visible with a pixel size of 42.5 nm). In **Figure 86c** (NMC located at ca. 50 μm from the separator), few fractures almost disappear (fracture widths become smaller than the pixel size of 42.5 nm) but the majority remain as shown on the close-up image with a smaller pixel size at the end of the discharge (**Figure 87**). Here again, it appears that the NMC particles close to the separator recover fractures better than the NMC particles far from the separator. The latter are the first particles to lithiate, the first ones to undergo volume changes and better recover from internal fractures.

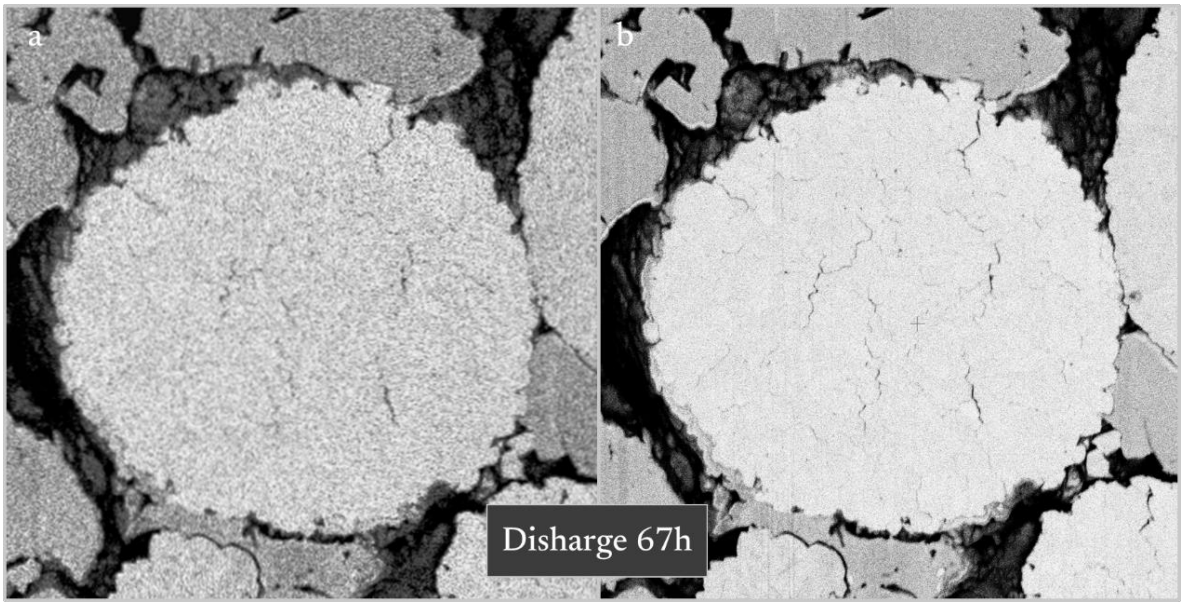

Figure 87: Identical NMC backscattered electron imaged with a) a pixel size of 42.5 nm and b) a pixel size of 13 nm.

These results show two main processes, the first one is that the lithiation/delithiation is easier close to the separator, i.e. where there is more Li available and ii) the mechanical dynamics are not the same close to the separator and close to the current collector.

However, as shown in **Figure 87b** with a higher resolution, the fractures that "partially recovered" are still present. The dynamics of the NMC fractures could be coming from i) the volume change of NMC primary particles, ii) the Young's modulus of the solid electrolyte which acts like a spring as demonstrated with the Sn composite electrode and amorphous LPS[98] and/or iii) the casing of the cell acting like a spring. For the latter, the pressure is maintained by a Teflon screw which seems rather weak to compensate for the swelling of the stack. Hypothesis ii) is obvious when high volume change active material like Sn are used. But here, on NMC intergranular fractures, the effect seems rather modest. Therefore, NMC volume change during lithiation will mainly reduce the gap of the created fractures during delithiation but never go back to its pristine state. It is hard to determine the width of the gap at which the lithium-ion will no longer diffuse between the two primary grains separated by the fracture but a few nm could be enough to shut the diffusion down. One fracture will not necessarily isolate the primary particle as multiple pathways still exist in the secondary particle of NMC.

During the first charge, we saw that the NMC particles are fracturing internally, which can lead to a poor solid-state diffusion inside the NMC particles hindering the rate capability of the cell. It is expected that after a couple of cycles, a full disconnecting from the electronic and ionic network could occur as demonstrated in our previous study[172]. Indeed, as LPS does not cover fully the NMC particles, the path length of lithium inside the NMC will be drastically lengthened if not ruptured.

When this happens not only locally but everywhere in the composite electrode, the polarization of the cell will increase as well as the electrochemical performance will decrease.

In addition to volume expansion/shrinkage causing fracturing in the polycrystalline active material, the battery stacks must manage such volume evolution to preserve intimate contact between the LPS matrix and the NMC particles by counteractions. LPS has favourable mechanical properties and could locally adapt to volume changes[48]. In addition, the presence of porosity could lower the effective Young's modulus of the separator or positive electrode, better adapting to the morphological changes[180]. It was proven that a thick LPS separator could act as a spring with metallic tin, a high volume changes active material[98]. Moreover, at the macroscopic scale, the In-Li counter electrode expands during lithiation as the positive electrode delithiated which could also preserve contact[113].

5.4.2 Interfacial contact

We previously showed that NMC is undergoing volume changes due to lithiation/delithiation. To maintain the battery performance, the LPS matrix surrounding the NMC particles must then locally adapt to these changes. Unfortunately, along the first charge, we can notice the decohesion of LPS particles from the NMC at the interfacial contact, as shown in **Figure 88c, d**.

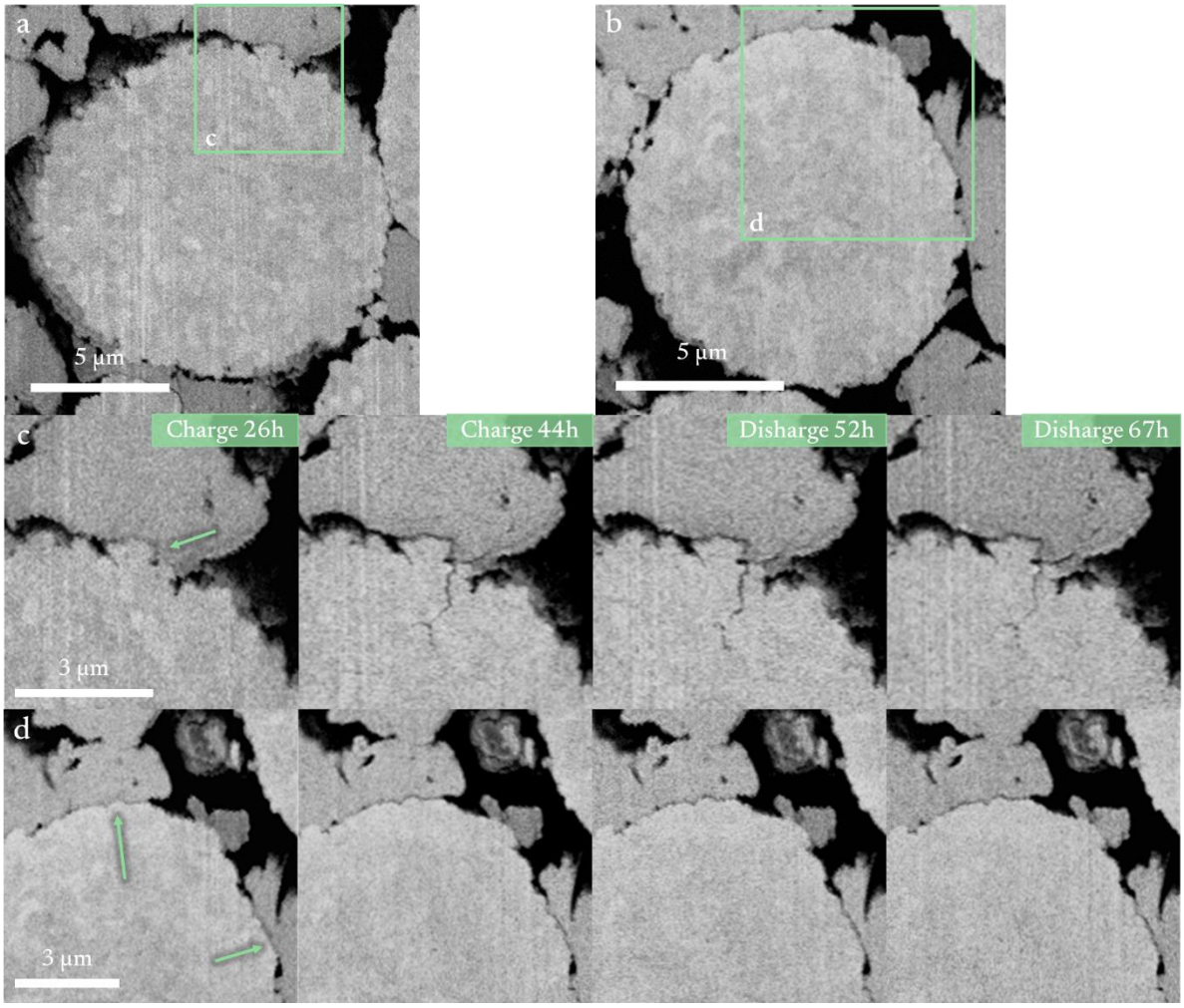

Figure 88: a and b) Secondary electron images of entire NMC particle and c and d) close-ups of NMC/LPS interfaces at various time stamps highlighting the decohesion between NMC and LPS. The green arrows indicate the interface where evolution is observed.

This decohesion process is less obvious to monitor due to its nanometric dimension but appears at the end of the charge and is still present at the end of the discharge despite the lithiation of the NMC. During the delithiation, the volume shrinkage of NMC leaves an imprint on the LPS matrix, the gap between the NMC particles and the LPS matrix is ca. 40 nm, sufficient to hinder the ionic/electronic transport properties at the interface. However, at this stage, the images are just displaying a 2D vision, and a part of the particles might be still connected but not in the field of view. On the other side during lithiation, the contact appears to be lost permanently as a gap is still visible at the end of the discharge.

A higher-resolution image of this decohesion process is shown in **Figure 89**.

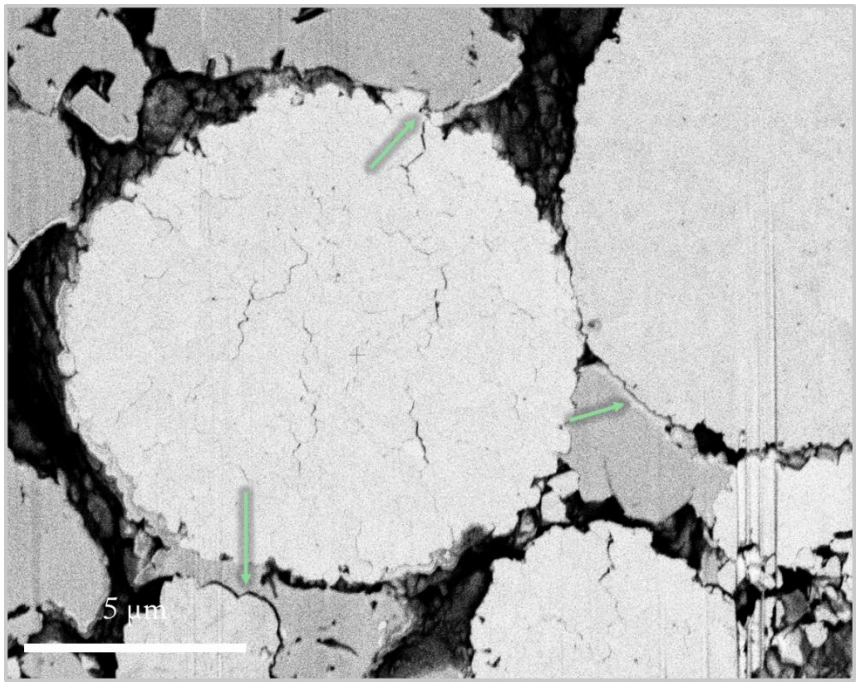

Figure 89: Close-up backscattered image of the fractured NMC and NMC/LPS interface decohesion at the end of the discharge after 67h with a pixel size of ca. 13.3 nm. The green arrows indicate the interface where decohesions happen.

As the decohesion processes are observed in 2D, this does not mean that this decohesion is always homogeneous around the particles. Some LPS-NMC connections remain within the composite, confirmed by the electrochemical cycling of the cell. Nevertheless, considering the limited contact of NMC with the LPS shown in **Figure 88a, b** (%coverage$_{NMC}$ calculated at 75 % and 25 % at the pristine and charged state, in the chapter **Composite positive electrode in solid-state batteries**, **Table 5**, **p. 106**), the path of lithium inside the particles will be impacted. If considering the plan of the cross-section of NMC as the path of lithium-ion diffusion inside the particle from the LPS matrix, a geodesic distance map can show the change of pathways with a perfect case (no fractures, no decohesion, **Figure 90a**) to a more realistic case (fractures and decohesion, **Figure 90b-c**).

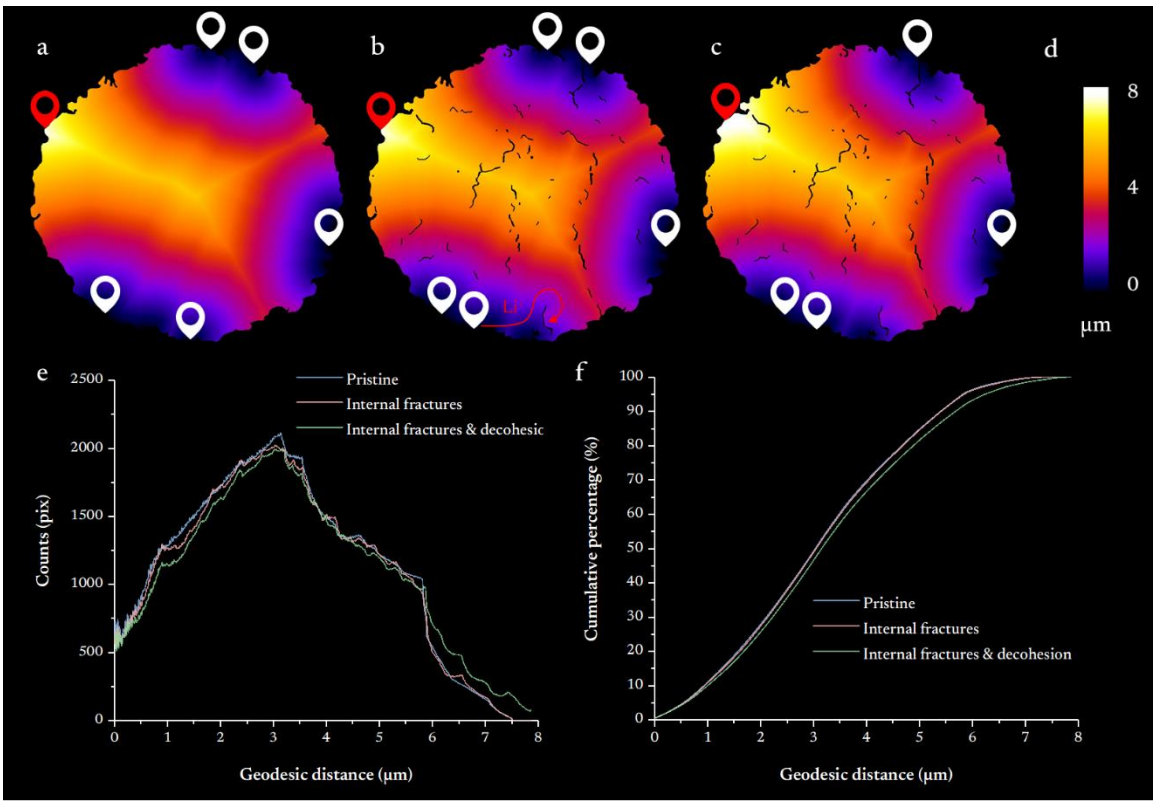

Figure 90: a, b, c) Geodesic distance maps of the lithium-ion paths inside NMC622 particles from the NMC-LPS interface (where lithium-ion will insert/dislodge NMC structure, represented by a white marker) toward the inside of the secondary NMC particle (furthest distance represented by a red marker) from **Figure 89**. Calculations were made a) without internal fracture and LPS connection (pristine), b) with internal fractures and LPS connection and c) with internal fracture and degraded LPS connection (decohesion). d) The colour scale bar of the geodesic distance maps, e) the distribution of the distances and f) the cumulative percentage of the distances.

Although this representation is only at the 2D level, ignoring the crystallographic orientation of each grain (thus the real lithium-ion pathway normal the c-plan), we can see that the path of lithium is elongated (**Figure 90a-c**). Fractures inside NMC will lengthen the path of lithium-ion to diffuse throughout the NMC secondary particle. As the geodesic distance map colour observation is not obvious, a distribution of the distances inside the particle as well as its cumulative percentage are presented in **Figure 90e** and **Figure 90f** respectively: the internal fracture will increase the lithium path inside the NMC particles as the lithium-ion will have to diffuse around them but the increased length is moderate. The decohesion, on the other hand, will increase both the path length (because some connections in the LPS matrix were lost). They also increase the bottlenecks at the interface NMC/LPS as less area connects the two, considering the same amount of lithium-ion exchanged (upper part of the NMC undergoing decohesion as shown in **Figure 90c**). At 50 % of the cumulative percentage, the average distance difference is 0.125 µm between the pristine state and the fractured and decohesioned state. The lengthening of the path appears moderate but i) it only represents the first charge of the system, so this phenomenon will continue to increase and ii) it does not consider the diffusion of lithium strictly perpendicular to the c-axis crystal orientation. As batteries are

targeted to undergo thousands of cycles, fractures and interfacial decohesion will be even more pronounced, thus the lengthening lithium path and/or completely isolating NMC grains enhancing the ageing and worsening the electrochemical performance. If we simulate now a secondary particle after hundreds of cycles (where fractures are propagating everywhere and tend to block the diffusion), the lithium-ion path lengthening becomes obvious (**Figure 91**).

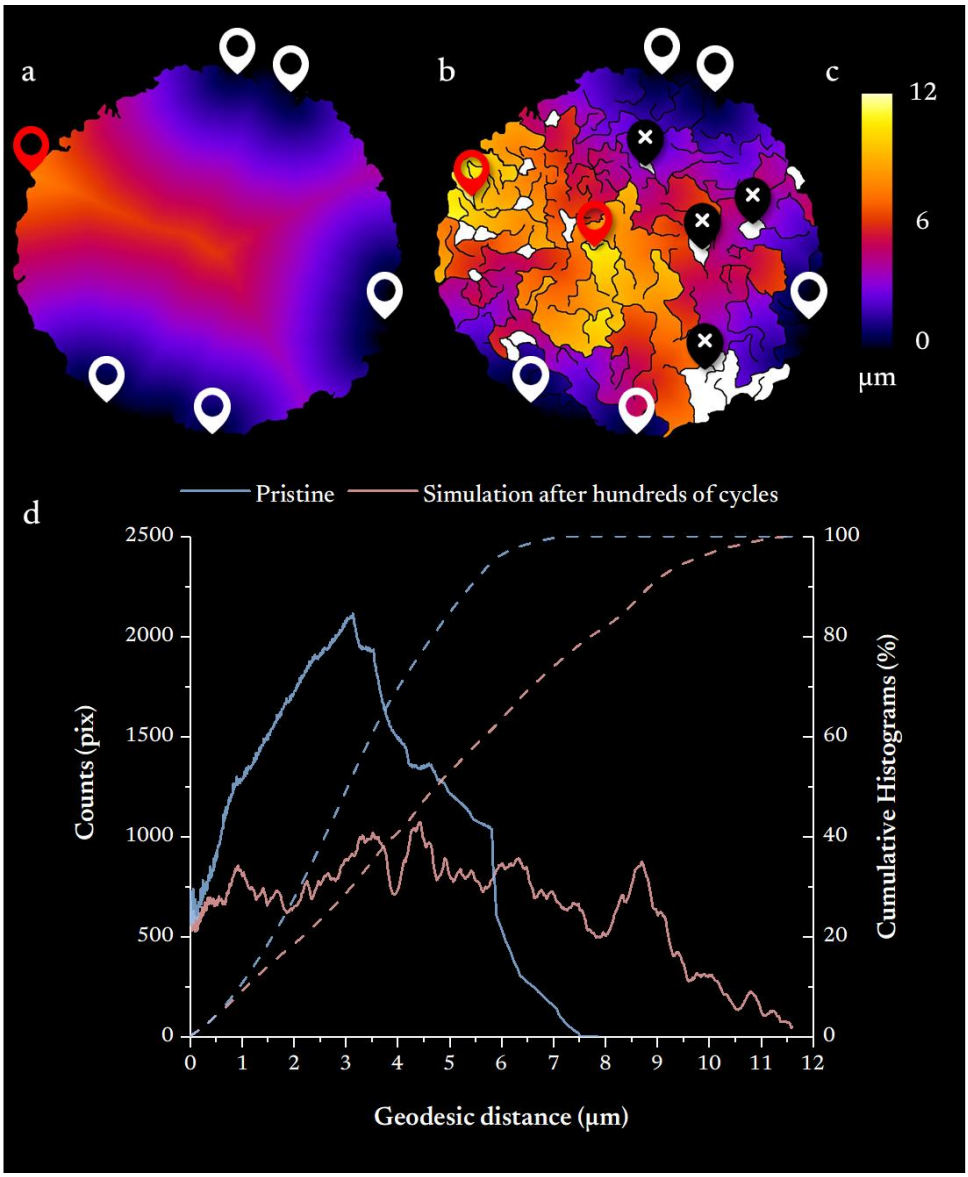

Figure 91: a, b) Geodesic distance maps of the lithium-ion paths inside NMC622 particles from the LPS-NMC interface (white marker) toward the inside of NMC particles (furthest distance represented by a red marker). Black markers represent completely disconnected primary particles. Calculations were made on a) pristine state, on b) on 100 cycle simulation where NMC secondary particle kept fracturing. c) The colour scale bar of the geodesic distance maps and d) the distribution of the distances and the cumulative percentage of the distances.

In **Figure 91b**, the fractures drastically increase the geodesic distances within the particle. In addition, fractures also fully disconnect primary particles (white area) which lithium-ion will no

longer be able to access. The average distance rises from 3.1 to 4.9 µm from the pristine to the simulated fractures while the maximum length increases from 7.5 to 11.6 µm. Once again, these geodesic distance maps only consider the pathway of lithium-ion in the plan of cross-section, but such observation could be extrapolated to 3D microstructures of secondary NMC particles.

5.4.3 Dynamics of the composite electrode

Another interesting observation is the heterogeneous displacements of various regions as shown in **Figure 92** and **Figure 93**. Indeed, the composite electrode in solid-state batteries relies on a very complex organization and suffers drastic chemo-mechanical degradation. As shown in **Figure 92** and **Figure 93**, we can somehow follow the mechanism behind the lithiation and delithiation and a so-called "re-organization" of the composite electrode.

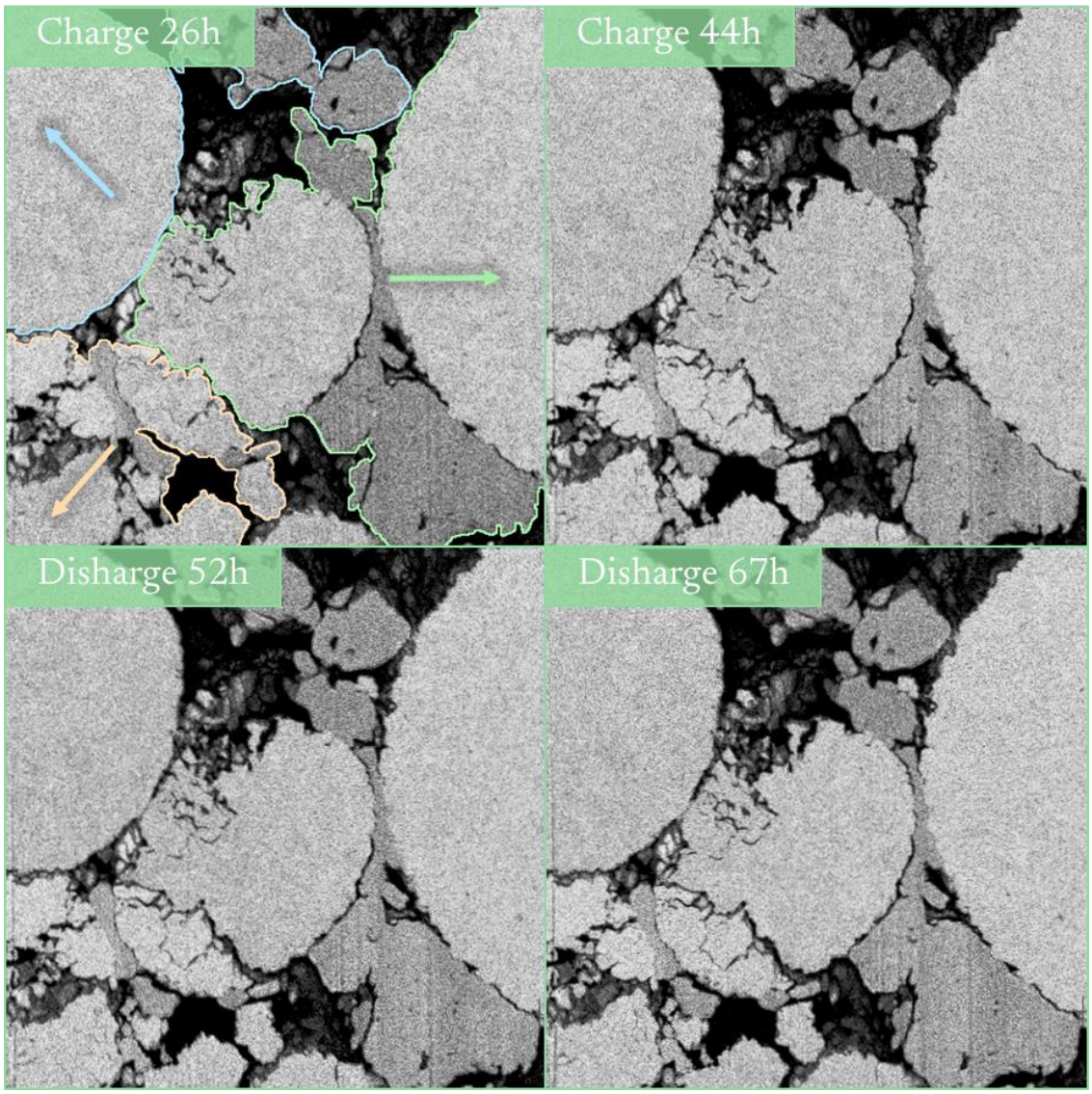

Figure 92: Heterogeneous displacements of various regions on backscattered electron images. Each separate region is highlighted by the distinct colour edges and their direction of displacements by the arrows.

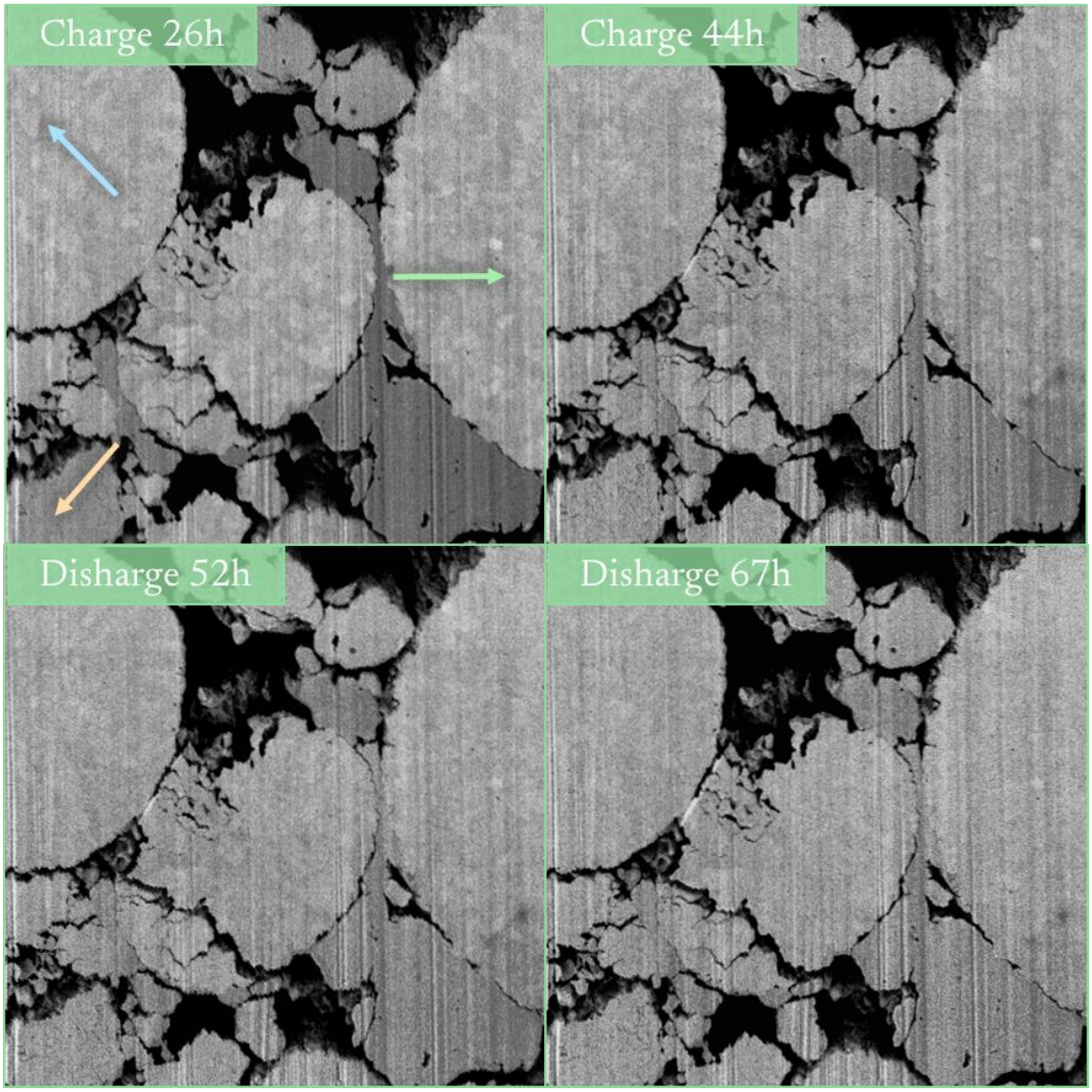

Figure 93: Heterogeneous displacements of various regions on secondary electron images. Each separate region's displacements are highlighted by arrows.

In this figure, three regions composed of NMC particles and LPS can be distinguished by their displacements. A gap appears to grow between two NMCs (the blue and green region, more visible on secondary images in **Figure 93**) while the NMC fractured from the shaping appears to split. This observation highlights that not only the active material is changing in a fixed environment through cycling, but agglomerates of active material and electrolyte move together. It is hard to attribute the displacement and their direction from a cross-section, but it is safe to say that the displacement of meaningful regions in the battery is caused by the volume changes of the NMC. It appears that some LPS-NMC contact is still and that the entire block moves with the lithiation and delithiation processes.

5.5 Conclusion

In this chapter, a novel *operando* technique using a FIB-SEM has been presented. Few improvements could be made to the setup to tackle the existing issues. First, as mentioned earlier, the stack pressure needs to be controlled and adjusted to mimic the functioning of real SSBs. To do so, the PEEK guide will be replaced by stainless steel screws that could withhold pressure in the MPa range. Then, the electrical connections must be insulated from parasitic currents to obtain additional information about the impedance spectrum. Next, to avoid contamination and later contrast loss in SE images, the entire box should be cleaned and handled in a glovebox exempt from organic compounds.

Furthermore, although this technique only allows the study of cross-sections, morphological changes were observed during cycling. Due to the swelling of the active material during lithiation/delithiation, three regions composed of NMC and LPS were distinguished due to opposite displacements creating gaps in the cell. In addition, the study of the solid-state composite positive electrode with NMC622 and LPS showed different observations most likely to have a detrimental effect on the battery performance. Indeed, the fracturing of polycrystalline NMC has been observed at the grain boundaries as well as the decohesion of the NMC and LPS. Such morphological changes will increase the path of lithium-ion within the NMC as fracture will oppose the diffusion. Moreover, the decohesion creates a bottleneck for the lithium-ion extraction of the NMC as they become less and less numerous through cycling.

General conclusion

This PhD thesis was carried out in the context of the existing limitations of current lithium-ion batteries, now ubiquitous in our daily lives. There is a growing need for safer and more energy-dense solutions as batteries are poised to play a pivotal role in decarbonizing energy sources, crucial to address environmental concerns related to climate change. Over the past three decades, lithium-ion batteries have been extensively optimized, making their widespread adoption inevitable. Nonetheless, they have now reached a "glass ceiling" in terms of energy density. This threshold is directly tied to the materials and electrolytes used in these systems, each with its limitations.

To break this ceiling, a new generation of lithium-ion batteries must be found to answer the ever-growing energy and safety demands. The objective of this thesis is to study the microstructure evolution of separator and composite electrodes in solid-state systems, in order to, one day, surpass the conventional lithium-ion battery. Among the plethora of solid-state systems available, we selected amorphous Li_3PS_4 (LPS) for its good ionic conductivity as well as favourable mechanical properties combined with the active material $LiNi_{0.6}Mn_{0.2}Co_{0.2}O_2$ (NMC622) used as the positive electrode. The transition from a liquid to a solid electrolyte drastically changes the interactions and dynamics between materials inside the battery, requiring a full investigation of their shaping and their microstructure evolution along cycling.

Can we trust the morphological observation made in this thesis?

While LPS is a promising SSE candidate, it presents several challenges, including its sensitivity to beam damage, reactivity to air and moisture, and ageing issues. We conducted experiments to verify that the morphology of the LPS remains unaffected by the SEM beam, thus validating our observations. While air and moisture reactivity are hardly avoidable by nature, the transfer box solution from the glovebox to the microscopes preserves the LPS from any degradation. In addition,

we found that calendar ageing has a detrimental effect on the densification of LPS, emphasizing the importance of using fresh LPS for consistent observation.

What is the importance of sintering parameters on the morphology of the electrolyte and its subsequent electrochemical properties?

In the first chapter, we focused exclusively on exploring LPS, especially the parameters controlling its room temperature sintering, to establish a link between electrochemical performance and its microstructure. Pressure primarily affects the overall level of porosity, whereas sintering time affects the morphology and connection of the remaining pores, highlighting that room-temperature sintering is a slow process. The ionic conductivity was not found to be a relevant parameter here, since even with low pressure and a high amount of porosity (more than 10%) similar values were reached (ca. 0.3mS/cm). More relevant parameters such as the geodesic map from the lithium metal anode side and local thicknesses reveal that the morphology of these pores plays a crucial role in how metal lithium penetrates the SSE as a function of the stack pressure in solid-state systems. More open pores facilitate lithium penetration and increase the risk of degradation due to increased interfaces, ultimately leading to premature failure. Optimizing pressure and sintering time therefore becomes essential and is seldom recognized. The choice of SSE cannot solely rely on ionic conductivity. Morphological analysis is equally critical as it directly impacts lithium metal usage[164].

Could the electroactive materials developed for liquid electrolytes be directly applied in solid-state systems?

The primary target of solid-state battery investigation consists of testing materials acquired through the know-how developed for liquid-based electrolytes. Thus, we investigated the morphology of the active material NMC, a polycrystalline material optimised for good wetting with a liquid electrolyte, with the LPS formerly studied. Such composite positive electrode combines a crystalline, hard and fragile active material, NMC, with an amorphous, soft and compliant electrolyte, LPS. Polycrystalline NMC faces challenges related to fractures under pressure along grain boundaries, which LPS can only partially accommodate as the pressure is used to sinter LPS powder into a densified ionic network. Because of polycrystalline NMC fragility, composite positive electrodes cannot be densified with excessive pressure, as previously identified as optimal for LPS alone. Longer sintering times can i) improve the densification of the composite positive electrode, ii) optimise the contact between the solid electrolyte and the electroactive material (better ionic pathway) while iii) better preserving the polycrystalline NMC microstructure; ultimately fewer fractures improve the electronic transport. However, longer sintering times have an impact on the electrochemical performance which leads first to a lower initial coulombic efficiency (CE) due to chemical degradation of LPS emerging from the increased LPS-NMC surface area. Nonetheless, it was proven

to be beneficial in the subsequent cycles, keeping a proper ionic/electronic pathway within the composite electrode. In addition to fractures due to the room-temperature sintering process, polycrystalline NMC undergoes modest expansion and shrinkage (ca. 4%) during cycling, resulting in significant internal fractures along grain boundaries and changes in porosity. These evolutions impact the contact between NMC and LPS causing poorer electronic/ionic pathways. Despite LPS being an amorphous material with a favourable mechanical property such as a high elastic modulus, decohesion between NMC and LPS is happening through cycling. Even though partial contact is regained during the lithiation of NMC, some decohesions are permanent[172]. In light of these findings, it is clear that the electroactive materials developed for liquid electrolyte systems may not be directly applicable to solid-state systems. Their morphology evolutions (fractures, volume changes) could only be accommodated by the liquid nature of the electrolyte, ensuring the full wetting of the particles and calling for better materials that could hold pressure better.

How can we push the limit of laboratory imaging techniques with high resolution?

Based on our investigation showing the importance of the microstructure evolution of materials inside solid-state battery systems, we developed a novel setup for the *operando* FIB-SEM observation of solid-state batteries. The application of *operando* techniques has provided invaluable insights into the dynamic evolution of battery morphologies. However, it is important to acknowledge the challenges that must be overcome to fully exploit the potential of *operando* studies. These challenges include preserving airtightness for sample transfer, establishing reliable connections from the cell to the potentiostat, maintaining adequate stack pressure during the investigation, and shaping samples based on 2D observations. While these challenges have yet to be completely addressed, significant progress has been made in observing the morphological changes in NMC-LPS composite positive electrodes. These observations have confirmed the formerly identified morphological evolutions in the previous chapter such as fracturing of NMC and decohesion within the positive electrode material. Furthermore, novel morphological evolutions, characterized by heterogeneous displacements possibly arising from varying sticking properties and the NMC-LPS contact, have been identified. In addition, to visualize these morphological changes, this *operando* technique has also provided dynamic insights into the delithiation process and the propagation of the lithium front across the positive electrode. However, there is still room for improvement, particularly in achieving higher stack pressures to reduce the internal resistance of the cell, thereby enhancing the cycling rate, closer to real battery operation. This flaw has already been addressed by switching PEEK guides into sturdy stainless steel screws but, unfortunately, could not be tested.

The thesis objectives and the gathered results can now be summarized in **Figure 94** showing a schematic of the challenges in solid-state systems with metal lithium, LPS separator and NMC/LPS positive electrode composite.

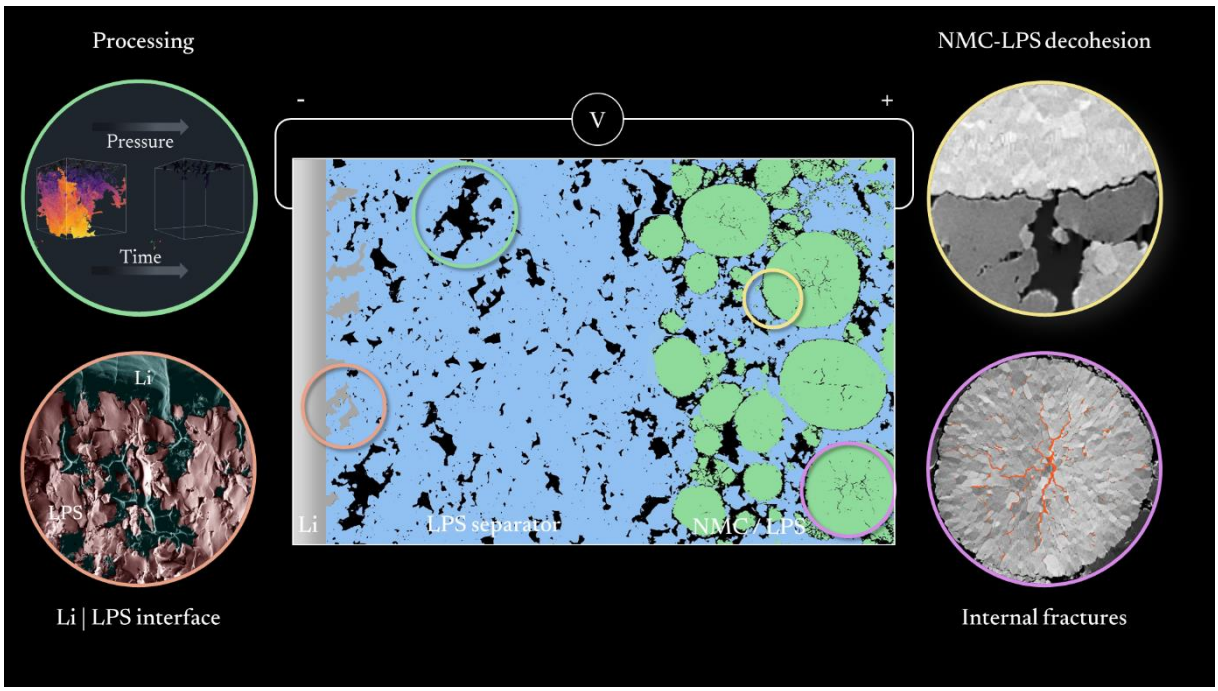

Figure 94: Schematic of the scientific challenges hindering the system Li-M | LPS | poly-NMC / LPS.

In the future research perspectives, several promising directions emerge for advancing solid-state battery technology. First of all, the volumes acquired during this thesis, on the solid electrolyte and the composite positive electrode, will serve as the basis for simulation. Indeed, more and more multiphysic simulations need experimental microstructures and morphologies to better understand charge/discharge mechanism regarding the morphology and foresee solid-state battery performance, especially at high C-rate[181,182].

Within the choice of solid electrolytes, delving into the crystalline counterpart, Li_6PS_5Cl presents an interesting path. Although LPSCl shows better ionic conductivity, it still suffers limited densification (roughly 12 % at 380 MPa in **Figure 95**), prompting a need for innovative approaches to overcome this challenge and showing that temperature can also be a parameter to test for achieving better sintering. Similarly, alternative processes, mostly used in the metallurgy field, such as Hot Isostatic Pressing (HIP), could be investigated to boost densification in solid-state systems while keeping components integrity[183,184].

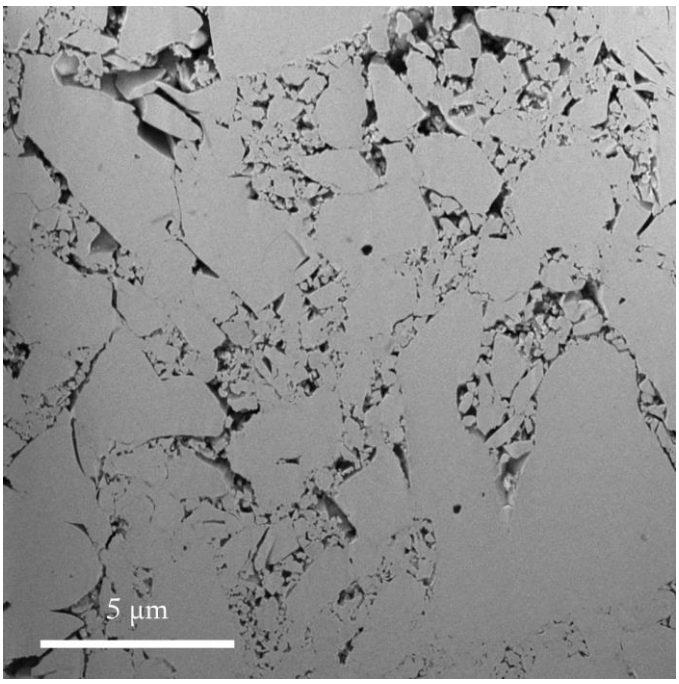

Figure 95: Cross-section of LPSCl pressed at 380 MPa supplied by NEI.

Shifting the focus to the positive electrode component, investigating the crystal orientation of polycrystalline NMC offers a unique opportunity to anticipate and avoid weak grain boundaries, through advanced synthesis, ultimately contributing to the longevity and efficiency of solid-state batteries. Electron backscattered scattering diffraction (EBSD) could bring answers to preferential orientations in polycrystalline NMC[79] (**Figure 96**). However, some improvements still must be made to alleviate shifts during acquisition and to enhance surface diffraction with better sample preparation (**Figure 96b-c**).

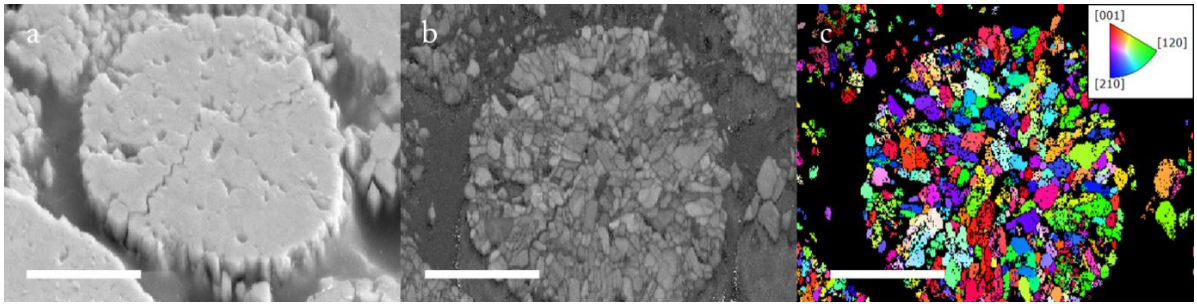

Figure 96: EBSD map of NMC 622 pressed at 255 MPa. a) Secondary electron image, b) index quality IQ map and c) IPFX orientation map. Scale bars represent 5 µm.

More realistically and according to the literature, exploring single crystal active materials devoid of carbon additives opens up intriguing possibilities. This aims to enhance the structural integrity of the positive electrode while preserving or boosting the electrochemical performance[6,61,62,179].

On the instrumental front, further development of instrumentation in collaboration with Zeiss holds potential. This entails refining the design of *operando* setups, with a particular emphasis on

stack pressure control and electrical contacts. The addition of two stainless screws has been recently done ensuring higher stack pressure for cycling but could not unfortunately be tested (**Figure 97**). These enhancements will provide a more comprehensive understanding of the dynamic morphological changes occurring within solid-state batteries during operation as the positive electrode side but also digging into Li metal dendrites propagation.

Figure 97: Improved *operando* cell with two stainless steel screws to achieve higher stack pressure.

Lastly, a clear and accessible methodology to extensively characterize morphologies and microstructure applied to lithium-ion batteries becomes essential. This methodology, used as a systematic approach will enable researchers to extract critical metrics for battery performance more effectively, fostering a deeper comprehension of solid-state systems. These perspectives collectively contribute to the ongoing evolution and optimization of solid-state battery technology, addressing key challenges and paving the way for safer, more efficient, and high-performance energy storage solutions.

Résumé en français

Introduction

La nécessité mondiale de lutter contre le changement climatique et de promouvoir les énergies durables a stimulé la recherche multidisciplinaire. Les batteries au lithium-ion, malgré leurs limites en matière de sécurité et de charge rapide, sont devenues des candidates prometteuses pour soutenir les énergies renouvelables, la mobilité électrique et la stabilité du réseau électrique. Cependant, les limites technologiques de batterie Li-ion conventionnelles deviennent de plus en plus apparentes. L'utilisation du lithium métal, l'électrode la plus énergétique, ne peut pas être appliquée à un électrolyte liquide car elle crée des dendrites entre les électrodes et provoque par la suite un court-circuit, souvent associé à un emballement thermique. Ce processus, couplé aux préoccupations en matière de sécurité liées à l'utilisation d'électrolytes liquides organiques provoquant des événements de défaillance thermique, a incité à s'orienter vers des solutions plus innovantes et durables.

Fondées sur les principes de sécurité renforcée, de densités énergétiques plus élevées et de plages de température de fonctionnement plus étendues, les batteries tout solides, dans lesquelles un électrolyte solide remplace un électrolyte liquide, ont émergé au premier plan en tant que moteurs d'un avenir à faible émission de carbone. Le passage de l'électrolyte liquide à l'électrolyte solide est illustré dans la **Figure 98**.

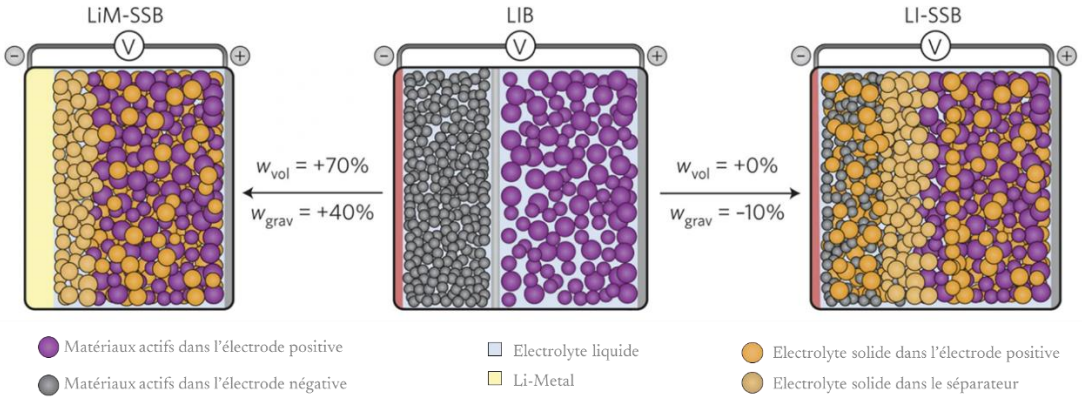

Figure 98: Batteries lithium-ion conventionnelles (au milieu, LIB) contiennent une électrode négative et positive poreuse. Dans une batterie tout solide au lithium-ion avec une anode classique (à droite, LI-SSB), l'électrolyte liquide dans les électrodes est complètement remplacé par un électrolyte solide. Les changements de densité énergétique sont estimés en fonction de l'augmentation de la densité entre le liquide et le solide, en tenant compte de la grande capacité spécifique du lithium métal (à gauche, LiM-SSB) et du remplacement complet du graphite et de l'électrolyte de l'anode. Adapté de la référence [4].

Cependant, remplacer un électrolyte liquide par un électrolyte solide est loin d'être trivial, et le principe de base de l'assemblage des cellules et de l'ingénierie doit être soigneusement étudié, car le savoir-faire acquis dans les batteries Li-ion conventionnelles ne peut pas être appliqué directement aux batteries tout solide. Parmi les électrolytes solides existants, les électrolytes solides à base de soufre

(ou électrolyte soufrés) sont des candidats prometteurs car ils offrent des avantages tels que i) une sécurité accrue en raison de leur caractère non inflammable, ii) contrairement à leurs homologues aux électrolytes solides, une excellente conductivité ionique à température ambiante, iii) un coût réduit par rapport au sel de lithium coûteux, et iv) une fabrication et une synthèse faciles. Cependant, malgré ces avantages, des défis persistent, en particulier en raison des interfaces solide/solide très difficiles à contrôler. Ce choix de passer de l'électrolyte liquide organique modifie fondamentalement la dynamique de la batterie, en particulier dans la microstructure et les morphologies des composants à la fois à l'échelle macroscopique et à l'échelle microscopique.

Les électrolytes soufrés présentent l'avantage de pouvoir être densifiés à température ambiante en n'appliquant que de la pression (appelée frittage à température ambiante) mais leur densification complète est rarement obtenue, ce qui pourrait avoir un impact sur leurs propriétés électrochimiques. Les défis deviennent encore plus complexes lorsque l'électrolyte soufrés ductile est densifié aux côtés de matériau actif dur, comme dans une électrode composite, compte tenu de leurs propriétés mécaniques disparates.

La complexité inhérente des matériaux, de leurs interfaces et les processus dynamiques au sein de ces batteries a incité l'intégration de techniques de caractérisation avancées et en particulier de techniques d'imagerie. Dans cette perspective, le FIF-MEB (faisceau d’ion focalisé couplé à un microscope électronique à balayage) présente une résolution notablement élevée par le MEB, révélant les interfaces enfouies grâce au FIF et ainsi, offrant des analyse volumétrique, cruciale pour la détermination des paramètres de morphologie tels que la tortuosité ou la percolation. Par ailleurs, la forte plage de résolution est adaptée à l'investigation des microstructures et des morphologies des matériaux utilisés dans les batteries.

Cette thèse est structurée autour de quatre chapitres. Le premier chapitre introduit le contexte en présentant le principe de fonctionnement de la batterie au lithium-ion, englobant ses caractéristiques diverses, puis en se penchant sur les défis du développement des batteries tout solide. Une attention particulière sera portée aux électrolytes solides soufrés, en différenciant les électrolytes amorphes des électrolytes cristallins. Du fait de la nature fixe des batteries tout solide, le chapitre mettra en évidence le rôle essentiel des morphologies dans les différents composants de la batterie. De plus, le chapitre introduira les techniques d'imagerie utilisées pour scruter ces morphologies, en explicitant les informations pouvant être tirées de telles analyses. L'accent de cet état de l'art réside dans la compréhension profonde de l'importance des microstructures dans chaque composant des batteries tout solide, présentant des matériaux en évolution dans un système fixe.

À travers cet état de l'art, trois questions demeurent en suspens :

1. Quel est l'impact de la morphologie de l'électrolyte sur ses propriétés électrochimiques ultérieures ?

2. Les matériaux développés pour les électrolytes liquides peuvent-ils être directement appliqués aux systèmes tout solide ?

3. Comment repousser les limites des techniques d'imagerie à haute résolution en laboratoire ?

Nous tenterons dans les trois chapitres suivants de répondre à ces questions et d'explorer le lien entre paramètres de mise en forme, morphologies et propriétés électrochimiques. Le deuxième chapitre se concentre sur l'investigation du séparateur dans une batterie tout solide, en utilisant exclusivement l'électrolyte solide soufré LPS amorphe. Une étude approfondie sur le LPS sera présentée, élucidant l'interaction complexe entre la mise en forme, la morphologie et les performances électrochimiques par rapport au lithium métal.

Dans le troisième chapitre, le LPS précédemment étudié sera mélangé avec le NMC622 pour créer des composites d'électrode positive. Ces électrodes positives composites seront caractérisées sur le plan électrochimique tandis que leurs morphologies seront évaluées. L'évolution de la morphologie, dépendante à la fois des paramètres de mise en forme et du cyclage sera présentée, mettant en lumière l'obstacle morphologique principal à surmonter dans les batteries tout solide.

Le quatrième chapitre se concentrera sur le développement d'une nouvelle technique *operando* au sein d'un FIF-MEB. Après avoir présenté en détail la configuration ainsi que les défis à relever, l'évolution des morphologies à l'intérieur d'une électrode positive composite, précédemment identifiée dans le chapitre trois, sera de nouveau étudiée, mais avec la technique *operando*.

Morphologies des électrolytes solides soufrés

Dans ce chapitre, nous avons étudié le frittage à température ambiante d'un électrolyte solide soufrés amorphe de type LPS. Tout d'abord, nous avons exposé notre méthodologie et notre configuration expérimentale, garantissant la fiabilité de nos résultats et observations en minimisant l'exposition au faisceau et à l'air/l'humidité. Ensuite, une comparaison entre l'électrolyte LPS commercial et fait maison a été réalisée. En raison d'une faible conductivité ionique et d'une capacité médiocre de frittage à température ambiante, l'électrolyte LPS commercial a été écarté. Ces propriétés médiocres pourraient être dues à la phase cristalline présente dans l'électrolyte commercial. Néanmoins, nous avons montré que l'électrolyte LPS fait maison subit toujours une dégradation même lorsqu'il est stocké dans un environnement exempt d'humidité. Par conséquent, l'électrolyte LPS est sensible au temps et un lot frais doit être utilisé pour garantir des observations fiables.

Nous avons ensuite mené une étude sur les propriétés électrochimiques de LPS mise en fore à deux pressions (255 MPa et 510 MPa) et deux temps différents (10 min et 15 h). Nous avons tout d'abord démontré que la pression est un paramètre clé pour réduire la porosité globale tandis que le temps où cette pression est appliquée a un impact sur la connexion des pores (**Figure 99**).

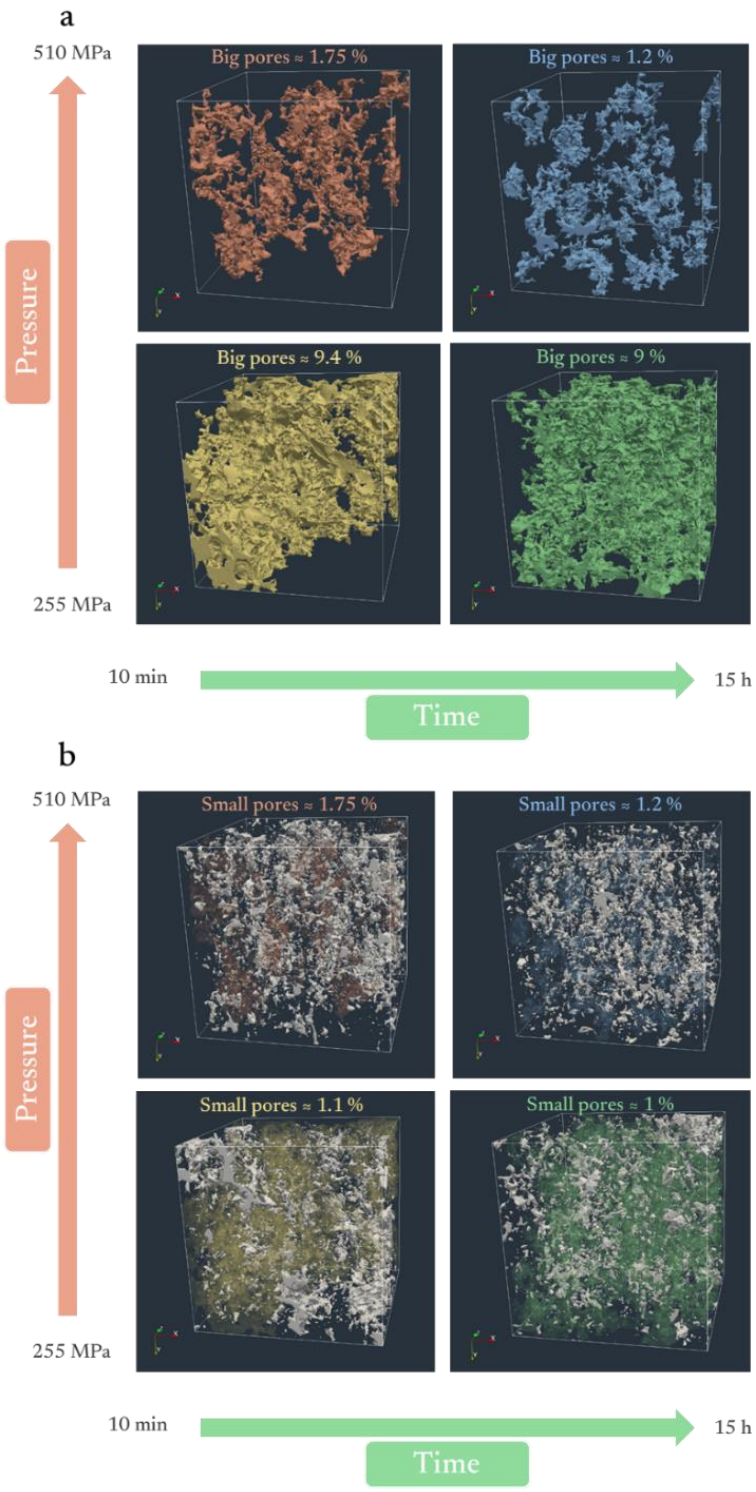

Figure 99: a) Visualisations des pores larges et b) des pores petits à l'intérieur du volume des quatre échantillons et leur porosité correspondante.

Quels que soient les échantillons et les paramètres de frittage utilisés, ils possèdent tous la même conductivité ionique, ce qui signifie qu'avec environ 10 % de porosité résiduelle, nous atteignons un seuil. Ainsi, on ne peut pas seulement se fier à la conductivité ionique pour sélectionner le meilleur électrolyte solide. En effet, la distribution de la porosité à l'intérieur de l'échantillon semble être le

paramètre le plus crucial, car elle peut guider le fluage du lithium lors de l'assemblage de la cellule ainsi que la formation des dendrites de lithium, responsable de la rupture mécanique, lors de la déposition/extraction du lithium comme le montre la **Figure 100**.

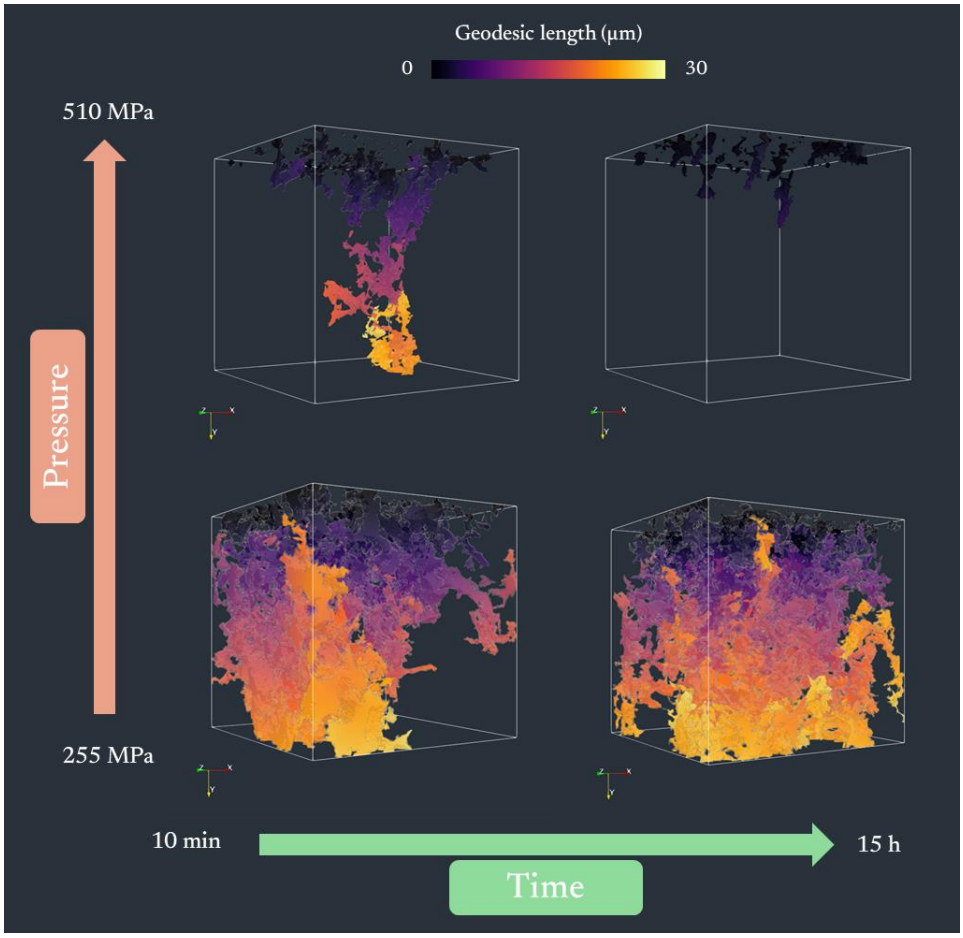

Figure 100: Distance géodésique 3D à travers les pores pour les quatre échantillons, calculée depuis le sommet et propagée vers le bas.

Les meilleures conditions de frittage consistent donc en l'application d'une pression élevée (dans le cas présent, 510 MPa) pour réduire la quantité de porosité, mais aussi en un temps de frittage plus long pour éviter la connexion de la porosité à travers l'ensemble du volume de l'électrolyte solide, ce qui entraîne moins de fractures dues à de nombreuses porosités interconnectés comme le montre la **Figure 100**.

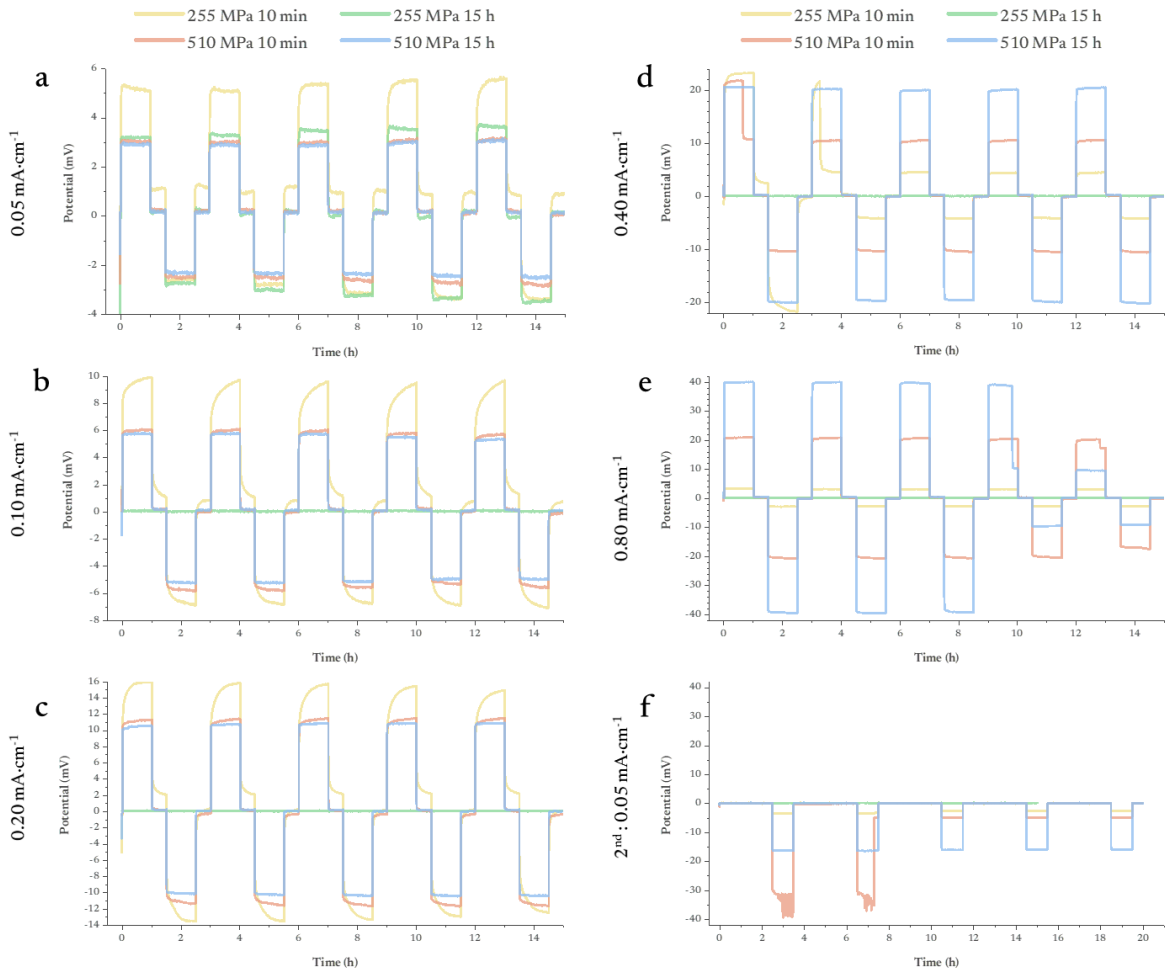

Figure 101: Expérience de déposition/extraction de lithium appliquée aux quatre électrolytes solides frittés pendant 10 minutes et 15 heures. La densité de courant correspond à a) 0,05 mA·cm^{-2}, b) 0,10 mA·cm^{-2}, c) 0,2 mA·cm^{-2} d) 0,4 mA·cm^{-2} et e) 0,8 mA·cm^{-2} et retour à f) 0,05 mA·cm^{-2}.

En conclusion, l'électrolyte LPS est un matériau souple, facile à fritter à température ambiante, exempt de joints de grains, et sa nature amorphe est préservée même après la mise en forme. Malgré une conductivité ionique dix fois plus faible que son homologue cristallin Li_6PS_5Cl, le LPS montre toujours une facilité de transformation en raison de son module d'Young favorable.

Electrode positive composite dans les batteries tout-solide

Dans ce chapitre, nous avons étudié l'évolution de la morphologie de l'électrode positive composite fabriquée avec l'électrolyte solide LPS et le NMC622. Nous avons tout d'abord démontré que la morphologie des particules de NMC polycristallin n'est pas adaptée pour une électrode composite destinée aux batteries tout-solide. En effet, les particules, conçues pour une bonne mouillabilité dans l'électrolyte liquide, commencent à se fissurer sous pression. (**Figure 102**).

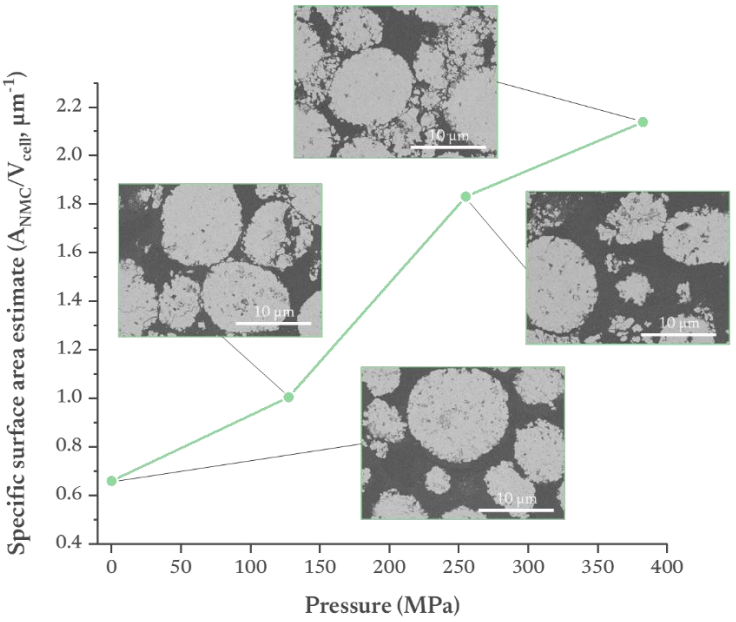

Figure 102: Estimation d'image 2D de la surface developpée des NMC622 en fonction de la pression appliquée.

Cependant, il a été démontré que la fissuration du NMC induite par la pression est atténuée par l'ajout d'un matériau souple comme le LPS. Ce dernier agit comme un tampon entre les particules secondaires de NMC en évitant les points de contact directs, et une partie de la pression est redistribuée pour fritter le SE. Les réseaux conducteurs ioniques et électroniques à l'intérieur du composite ont été calculés par une enquête microstructurale et des techniques électrochimiques, montrant toutes deux la même tendance. Les deux sont affectés par la grande porosité globale subsistante dans l'électrode composite. Ensuite, il a été constaté que la plupart des particules de NMC sont électroniquement connectées au collecteur de courant à 255 MPa. Cela signifie que, dans ces conditions de cyclage, l'ajout de carbones conducteurs n'est pas nécessaire, car cela dégraderait par conséquent le LPS et il serait difficile de différencier entre une porosité et un agent conducteur dans notre enquête microstructurale. De plus, il a été établi qu'un temps de frittage plus long réduit légèrement la porosité et, par conséquent, diminue la tortuosité géométrique, améliorant ainsi le transport ionique. De plus, un temps de frittage plus long favorise un contact optimisé entre le LPS et le NMC sans augmenter la pression de frittage, ce qui finirait par dégrader encore davantage la

morphologie du NMC. Nous identifions que le meilleur cyclage de l'échantillon fritté pendant 15 heures provient de la connexion plus intime entre le NMC et le LPS, malgré une première décomposition chimique améliorée. Malheureusement, après la première charge, le retrait du NMC entraîne la décohésion du matériau actif et de l'électrolyte solide, ce qui limite la capacité de cyclage pour les cycles ultérieurs (**Figure 103**).

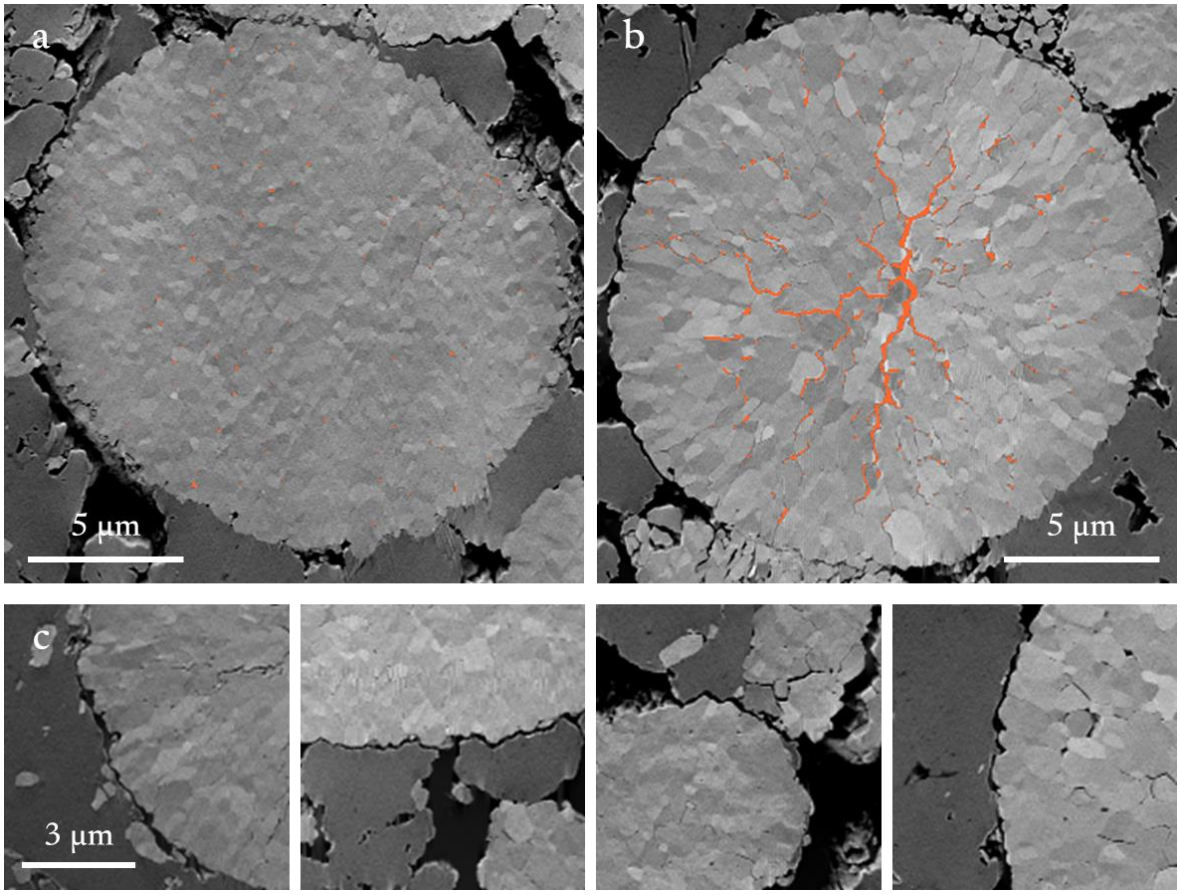

Figure 103: NMC dans l'électrode positive composite (image aux électrons secondaires) fritté pendant 15 heures à 255 MPa en a) état initial et b) après la première charge, extraites des piles FIF-MEB avec le NMC en gris clair, le LPS en gris foncé et la porosité en noir. La porosité interne est mise en évidence en orange. c) Empreinte du NMC sur le LPS mettant en évidence le changement de volume du NMC, images d'électrons secondaires extraites de la pile FIB-SEM à l'état de charge.

Il est devenu évident que le NMC polycristallin a été développé et conçu en premier lieu pour les électrolytes liquides. En effet, la fissuration du NMC, qu'elle soit induite par le cyclage ou par la pression (calandrage), était équilibrée par la mouillabilité constante de l'électrolyte liquide et la connexion électronique par l'agent conducteur. Cependant, les interfaces solide-solide induisent de nouvelles dynamiques entre les matériaux, et les matériaux précédemment conçus ne trouveront peut-être pas leur application dans les futurs systèmes à l'état solide, du moins pas tels qu'ils sont actuellement.

Operando FIF-MEB révélant les dynamiques des changements morphologiques dans les composites d'électrode positive

Dans ce chapitre, une nouvelle technique *operando* utilisant un FIF-MEB a été présentée. Bien que cette technique permette uniquement l'étude de coupes transversales, des changements morphologiques ont été observés pendant le cyclage. L'étude de l'électrode positive composite avec NMC622 et LPS a montré différentes observations susceptibles d'avoir un effet néfaste sur les performances de la batterie. En effet, en raison du gonflement du matériau actif lors de la lithiation/délithiation, la fracturation du NMC polycristallin a été observée au niveau des joints de grains ainsi que la décohésion du NMC et du LPS (**Figure 104**).

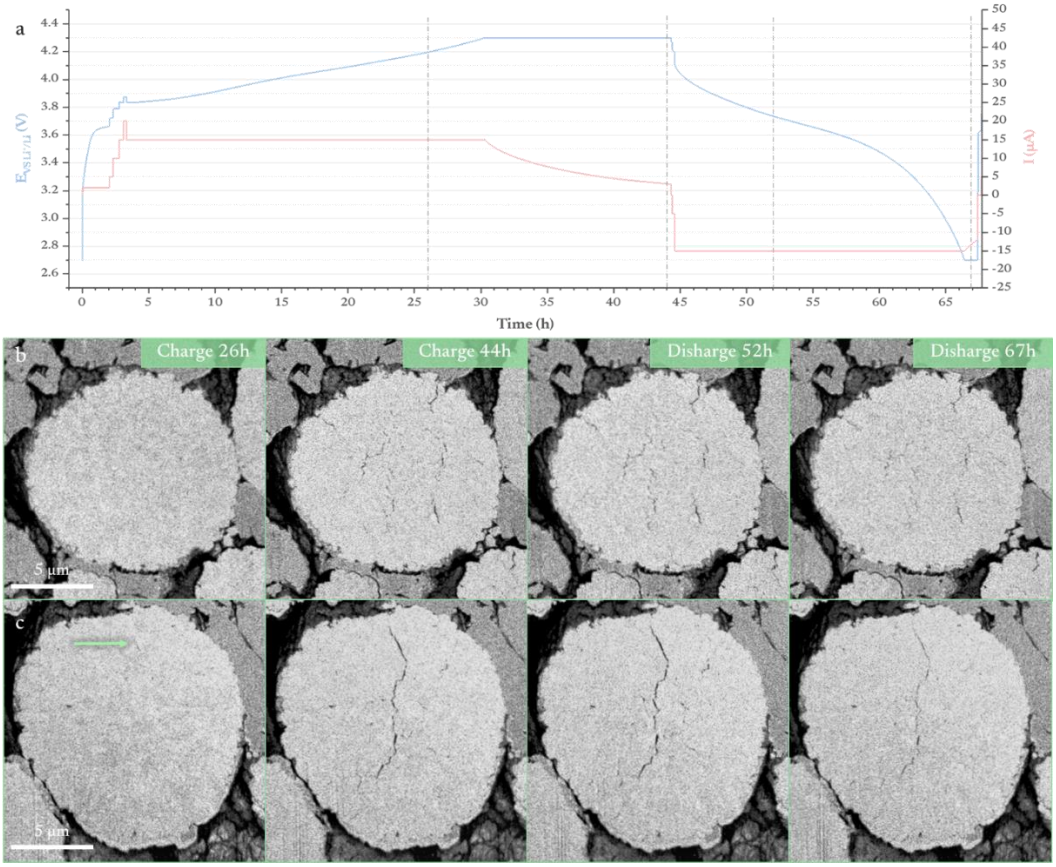

Figure 104: a) Cyclage galvanostatique à un régime de charge d'environ C/60 entre 2,7 et 4,3 V par rapport à Li^+/Li avec un maintien en potentiel jusqu'à ce qu'un cinquième du courant initial (15 µA) soit atteint. Les lignes grises en pointillés indiquent le moment où les images ont été acquises.

b) et c) Images en électrons rétrodiffusés de deux particules de NMC622 à différents moments, mettant en évidence la fracturation pendant le cyclage, b) NMC situé à environ 50 µm du séparateur, c) NMC situé au niveau du séparateur. La flèche verte indique le début de la fracture.

Plus intéressant encore, trois régions composées de NMC et de LPS ont été distinguées en raison de déplacements opposés créant des espaces vides dans la cellule (**Figure 105**).

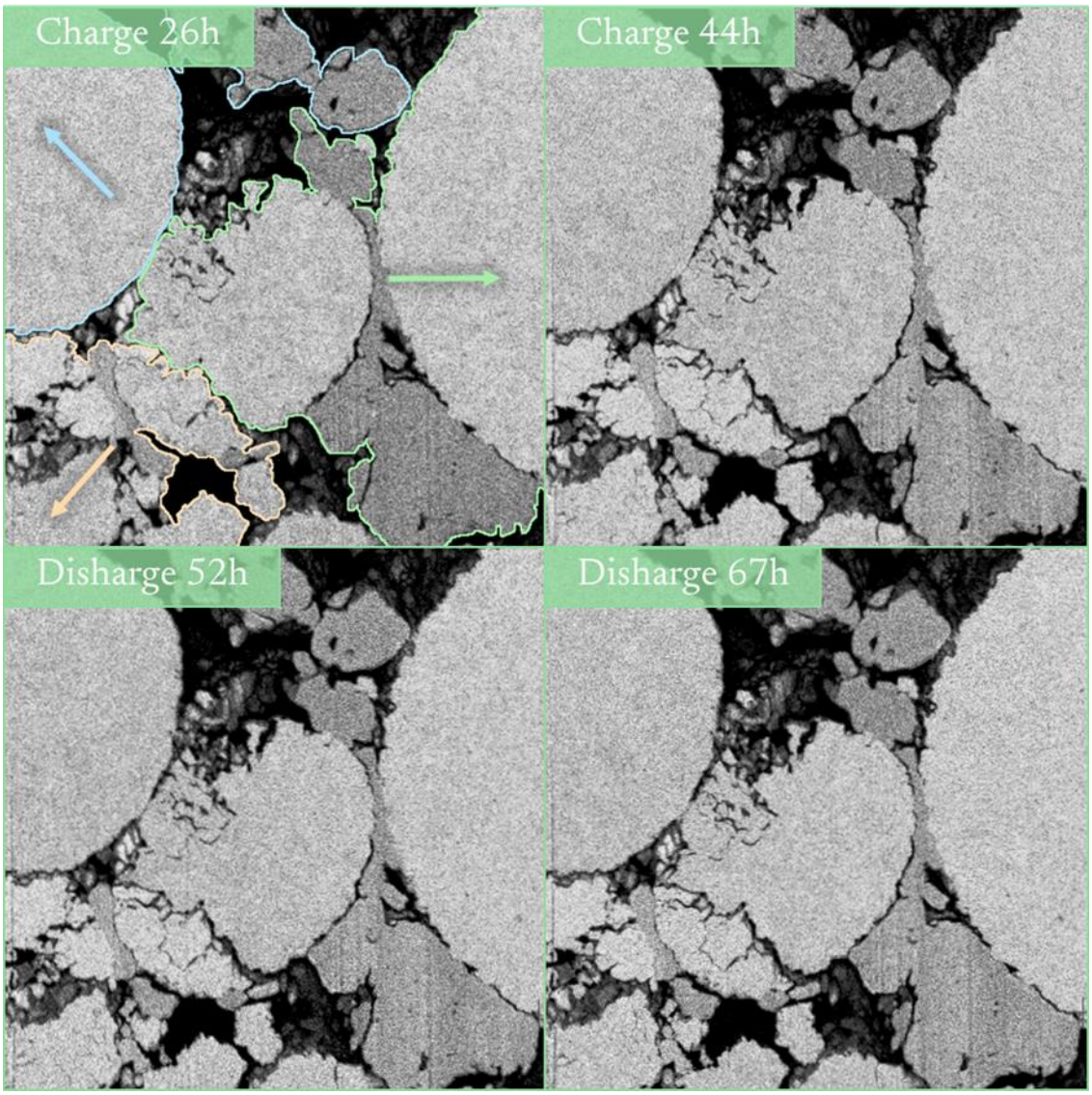

Figure 105: Déplacements hétérogènes de différentes régions. Chaque région distincte est mise en évidence par les contours de couleur distincte et leur direction de déplacement par les flèches.

Ces mouvements peuvent être la traduction d'adhérence différentes entre particules et électrolyte solide au sein de l'électrode positive composite.

En plus de ces observations, quelques améliorations pourraient être apportées à la configuration pour résoudre les problèmes existants. Tout d'abord, comme mentionné précédemment, il est nécessaire de contrôler et d'ajuster la pression de la pile pour reproduire le fonctionnement des véritables batteries à état solide. Pour ce faire, le guide en PEEK sera remplacé par des vis en acier inoxydable capables de supporter des pressions dans la plage des MPa. Ensuite, les connexions électriques doivent être isolées des courants parasites afin d'obtenir des spectres d'impédance plus représentatifs. Enfin, pour éviter la contamination et la perte de contraste ultérieure dans les images SE, l'ensemble de la boîte doit être nettoyé et manipulé dans une boîte à gants exempte de composés organiques.

Conclusion

Cette thèse a été menée dans le contexte des limites existantes des batteries lithium-ion actuelles, désormais omniprésentes dans notre vie quotidienne. Il existe un besoin croissant de solutions plus sûres et à plus haute densité énergétique, car les batteries sont appelées à jouer un rôle essentiel dans la décarbonation des sources d'énergie, ce qui est crucial pour répondre aux préoccupations environnementales liées au changement climatique. Au cours des trois dernières décennies, les batteries lithium-ion ont été largement optimisées, rendant leur adoption généralisée inévitable. Néanmoins, elles ont désormais atteint un "plafond de verre" en termes de capacité de stockage d'énergie. Ce seuil est directement lié à l'architecture et aux matériaux utilisés dans ces systèmes, chacun ayant ses propres limitations. L'utilisation du lithium métallique offre la possibilité d'une augmentation significative de la densité énergétique dans les systèmes à l'état solide, jusqu'à présent impossible à utiliser dans les batteries Li-ion liquides organiques traditionnelles en raison de problèmes de sécurité.

Pour briser ce plafond, une nouvelle génération de batteries lithium-ion doit être trouvée pour répondre aux demandes croissantes en matière d'énergie et de sécurité. L'objectif de cette thèse est d'étudier un nouveau système Li-ion, c'est-à-dire les systèmes à l'état solide, afin de surpasser un jour la batterie lithium-ion conventionnelle telle que nous la connaissons aujourd'hui. Parmi la pléthore de systèmes à l'état solide disponibles, nous avons étudié et observé le système à l'état solide associant le Li_3PS_4 amorphe (LPS) au matériau actif $LiNi_{0.6}Mn_{0.2}Co_{0.2}O_2$ (NMC622) à l'électrode positive et le lithium métal ou le lithium indium à l'électrode négative. Le passage d'un électrolyte liquide à un électrolyte solide change radicalement les interactions et la dynamique entre les matériaux à l'intérieur de la batterie, nécessitant une réévaluation de nos méthodes et approches de traitement.

Quel est l'impact de la morphologie de l'électrolyte sur ses propriétés électrochimiques ? Dans le premier chapitre, nous nous sommes exclusivement concentrés sur l'exploration du LPS, sa morphologie sous différents paramètres de traitement et son comportement électrochimique ultérieur. Bien que le LPS soit un candidat prometteur en tant qu'Électrolyte à l'état solide, il présente plusieurs défis, notamment sa sensibilité aux dommages causés par le faisceau SEM, sa réactivité à l'air et à l'humidité, ainsi que des problèmes de vieillissement. Nous avons mené des expériences pour vérifier que la morphologie du LPS reste inchangée par le faisceau SEM, validant nos observations pour le reste du projet. Bien que la réactivité à l'air et à l'humidité soit difficile à éviter, nous avons constaté que le vieillissement par calendrier avait un effet néfaste sur la densification du LPS, soulignant l'importance d'utiliser du LPS frais pour des observations cohérentes. Sur ce dernier point, la densification est presque complète à 510 MPa, la pression et le temps ayant des effets variables sur la formation des pores et la structure du réseau. La pression affecte principalement le

niveau général de porosité, tandis que le temps de frittage affecte la morphologie et la connexion des pores restants, mettant en évidence que le frittage à température ambiante est un processus lent. Malgré ces défis, le plateau de conductivité ionique est atteint de manière constante, et la morphologie de ces pores joue un rôle crucial dans la pénétration du lithium métallique dans l'Électrolyte à l'état solide en raison de la pression exercée dans les systèmes à l'état solide. Les pores plus ouverts facilitent la pénétration du lithium et augmentent le risque de dégradation due à une augmentation des interfaces, ce qui conduit finalement à une défaillance prématurée. Par conséquent, l'optimisation de la pression et du temps de frittage devient essentielle et est rarement reconnue. Le choix de l'Électrolyte à l'état solide ne peut pas uniquement reposer sur la conductivité ionique. L'analyse de la morphologie est tout aussi critique car elle a un impact direct sur l'utilisation du lithium métallique. Les défis liés à la réactivité du LPS et du NMC avec le lithium métallique, à l'obtention d'une densification complète tout en maintenant la conductivité ionique, doivent être abordés, potentiellement en utilisant des revêtements ou une chimie humide (uniquement si la conductivité ionique n'est pas gravement entravée par ce processus comme c'est le cas aujourd'hui).

Les matériaux développés pour les électrolytes liquides peuvent-ils être directement appliqués dans les systèmes à l'état solide ? Dans le deuxième chapitre, nous avons approfondi la morphologie du matériau actif NMC, optimisé pour l'électrolyte liquide, avec le LPS précédemment étudié sur les propriétés électrochimiques. Le NMC polycristallin est confronté à des défis liés aux fractures sous pression, que le LPS ne peut que partiellement accommoder. Des temps de frittage plus longs peuvent améliorer la densification de l'électrode positive composite tout en préservant la microstructure du NMC polycristallin. Il est également important de noter que des temps de frittage plus longs peuvent entraîner une efficacité coulombienne initiale plus faible en raison de la dégradation chimique du LPS résultant de la surface accrue de contact entre le LPS et le NMC. Néanmoins, les cycles ultérieurs bénéficient de ce meilleur contact, améliorant finalement l'efficacité coulombienne. Au cours du cyclage, le NMC polycristallin subit une expansion et une contraction modérées (environ 4 %), ce qui entraîne d'importantes fractures internes le long des joints de grains et des changements de porosité. Ces évolutions affectent le contact entre le NMC et le LPS, largement perdu lors de la délithiation et partiellement récupéré lors de la lithiation. De plus, les fractures internes affecteront le trajet des ions lithium au sein de l'électrode positive composite, soit en l'allongeant, soit en déconnectant complètement le matériau actif. À la lumière de ces constatations, il est clair que les matériaux développés pour les systèmes d'électrolytes liquides ne sont peut-être pas directement applicables aux systèmes à l'état solide. Leurs évolutions morphologiques (fractures, variations de volume) ne peuvent être accommodées que par la nature liquide de l'électrolyte, garantissant le mouillage complet des particules. L'électrolyte solide ne peut pas s'ajuster et résister à de telles évolutions. Les défis liés à la réactivité du LPS et du NMC pour le premier cycle, à la nécessité d'une densification complète et à la résolution des problèmes de décohésion sont des

obstacles importants. Les solutions potentielles incluent l'exploration de revêtements pour réduire la décomposition et le développement de monocristaux pour réduire les variations de volume.

Comment repousser les limites des techniques d'imagerie en laboratoire à haute résolution ? Dans ce troisième et dernier chapitre, nous avons développé une nouvelle configuration pour l'observation *operando* par FIB-SEM des batteries à l'état solide. L'application de techniques *operando* a fourni des informations inestimables sur l'évolution dynamique des morphologies des batteries. Cependant, il est important de reconnaître les défis qui doivent être surmontés pour exploiter pleinement le potentiel des études *operando*. Ces défis comprennent la préservation de l'étanchéité à l'air lors du transfert des échantillons, l'établissement de connexions fiables de la cellule au potentiostat, le maintien d'une pression d'empilement adéquate et la mise en forme des échantillons sur la base d'observations en 2D. Bien que ces défis n'aient pas encore été complètement résolus, des progrès significatifs ont été réalisés dans l'observation des évolutions morphologiques dans les électrodes positives composites NMC-LPS. Ces observations ont confirmé les évolutions morphologiques précédemment identifiées dans le chapitre précédent, telles que la fracturation du NMC et la décohésion au sein du matériau de l'électrode positive. De plus, de nouvelles évolutions morphologiques, caractérisées par des déplacements hétérogènes résultant probablement de propriétés de collage variables et du contact NMC-LPS, ont été identifiées. En plus de visualiser ces changements morphologiques, cette technique *operando* a également fourni des informations dynamiques sur le processus de délithiation et la propagation du front de lithium à travers l'électrode positive. Cependant, il y a encore des possibilités d'amélioration, notamment en atteignant des pressions d'empilement plus élevées pour réduire la résistance interne de la cellule, améliorant ainsi la vitesse de cyclage, plus proche du fonctionnement réel des batteries. Cette lacune a déjà été abordée en remplaçant les guides en PEEK par des vis en acier inoxydable robustes, mais malheureusement, elle n'a pas pu être testée.

Dans les perspectives de recherche future, plusieurs directions prometteuses émergent pour faire progresser la technologie des batteries à l'état solide. Dans le choix des électrolytes solides, l'étude de l'homologue cristallin, le LPSCl, présente un chemin intéressant. Bien que le LPSCl montre une meilleure conductivité ionique, il souffre encore d'une densification limitée, ce qui nécessite des approches innovantes pour surmonter ce défi. Des procédés alternatifs, principalement utilisés dans le domaine de la métallurgie, tels que le frittage isostatique à chaud (HIP), pourraient être étudiés pour augmenter la densification dans les systèmes à l'état solide. L'exploration de revêtements sur les surfaces de lithium-métal offre la possibilité de réduire les réactions de surface entre les électrolytes solides sulfures, tels que le LPS ou le LPSCl, et le lithium, améliorant la stabilité et les performances des batteries à l'état solide.

En se concentrant sur le composant cathodique, l'étude de l'orientation cristalline du NMC polycristallin offre une opportunité unique d'anticiper et d'éviter les joints de grains faibles, grâce à une synthèse avancée, contribuant finalement à la longévité et à l'efficacité des batteries à l'état solide. De manière plus réaliste et conformément à la littérature, l'exploration de matériaux actifs monocristallins dépourvus d'additifs de carbone ouvre des perspectives intéressantes. Cela vise à améliorer l'intégrité structurelle de l'électrode positive tout en préservant ou en renforçant les performances électrochimiques.

Sur le plan instrumental, le développement continu de l'instrumentation en collaboration avec Zeiss présente un potentiel. Cela implique d'affiner la conception des configurations *operando*, en mettant particulièrement l'accent sur le contrôle de la pression d'empilement et les contacts électriques. Ces améliorations permettront de mieux comprendre les évolutions morphologiques dynamiques qui se produisent au sein des batteries à l'état solide pendant leur fonctionnement.

Enfin, une méthodologie claire et accessible pour caractériser de manière approfondie les morphologies et la microstructure appliquée aux batteries lithium-ion devient essentielle. Cette méthodologie, utilisée comme approche systématique, permettra aux chercheurs d'extraire de manière plus efficace des métriques critiques pour les performances des batteries, favorisant une compréhension plus profonde des systèmes à l'état solide. Ensemble, ces perspectives contribuent à l'évolution continue et à l'optimisation de la technologie des batteries à l'état solide, en abordant les principaux défis et en ouvrant la voie à des solutions de stockage d'énergie plus sûres, plus efficaces et à haute performance.

Bibliography

1. In focus: Batteries – a key enabler of a low-carbon economy. https://commission.europa.eu/news/focus-batteries-key-enabler-low-carbon-economy-2021-03-15_en.
2. Rojas, O. E. & Khan, M. A. A review on electrical and mechanical performance parameters in lithium-ion battery packs. *J. Clean. Prod.* **378**, 134381 (2022).
3. Le Cras, F. & Bloch, D. De Volta aux accumulateurs Li-ion - Développement des batteries au lithium. *Ressour. Énergétiques Stock.* (2016) doi:10.51257/a-v1-be8620.
4. Janek, J. & Zeier, W. G. A solid future for battery development. *Nat. Energy* **1**, 1–4 (2016).
5. Li, P., Zhao, Y., Shen, Y. & Bo, S.-H. Fracture behavior in battery materials. *J. Phys. Energy* **2**, 022002 (2020).
6. Nam, J. S. *et al.* Densification and charge transport characterization of composite cathodes with single-crystalline $LiNi_{0.8}Co_{0.15}Al_{0.05}O_2$ for solid-state batteries. *Energy Storage Mater.* **46**, 155–164 (2022).
7. Liu, D. *et al.* Review of Recent Development of *In Situ*/*Operando* Characterization Techniques for Lithium Battery Research. *Adv. Mater.* **31**, 1806620 (2019).
8. López, I., Morey, J., Ledeuil, J.-B., Madec, L. & Martinez, H. A critical discussion on the analysis of buried interfaces in Li solid-state batteries. *Ex situ* and *in situ* / *operando* studies. *J. Mater. Chem. A* **9**, 25341–25368 (2021).
9. Schultz, C. Anti-aging for batteries? – secrets of science. https://www.shimadzu-webapp.eu/magazine/issue-2016-2_en/anti-aging-for-batteries/ (2015).
10. Liu, W. *et al.* Nickel-Rich Layered Lithium Transition-Metal Oxide for High-Energy Lithium-Ion Batteries. *Angew. Chem. Int. Ed.* **54**, 4440–4457 (2015).
11. Tarascon, J.-M. & Armand, M. Issues and challenges facing rechargeable lithium batteries. *Nature* **414**, 359–367 (2001).
12. Lee, S. & Manthiram, A. Can Cobalt Be Eliminated from Lithium-Ion Batteries? *ACS Energy Lett.* **7**, 3058–3063 (2022).
13. Noh, H.-J., Youn, S., Yoon, C. S. & Sun, Y.-K. Comparison of the structural and electrochemical properties of layered $Li[Ni_xCo_yMn_z]O_2$ (x = 1/3, 0.5, 0.6, 0.7, 0.8 and 0.85) cathode material for lithium-ion batteries. *J. Power Sources* **233**, 121–130 (2013).

14. Shellikeri, A. *et al.* Investigation of Pre-lithiation in Graphite and Hard-Carbon Anodes Using Different Lithium Source Structures. *J. Electrochem. Soc.* **164**, A3914 (2017).
15. Nzereogu, P. U., Omah, A. D., Ezema, F. I., Iwuoha, E. I. & Nwanya, A. C. Anode materials for lithium-ion batteries: A review. *Appl. Surf. Sci. Adv.* **9**, 100233 (2022).
16. Etiemble, A. *et al.* Evolution of the 3D Microstructure of a Si-Based Electrode for Li-Ion Batteries Investigated by FIB/SEM Tomography. *J. Electrochem. Soc.* **163**, A1550–A1559 (2016).
17. Keller, C. *et al.* Low-Cost Tin Compounds as Seeds for the Growth of Silicon Nanowire–Graphite Composites Used in High-Performance Lithium-Ion Battery Anodes. *ACS Appl. Energy Mater.* **6**, 5249–5258 (2023).
18. Grandjean, M., Meyer, T., Haon, C. & Chenevier, P. Selection and Optimisation of Silicon Anodes for All-Solid-State Batteries. *ECS Meet. Abstr.* **MA2022-01**, 408 (2022).
19. Sila. *Sila* https://www.silanano.com/about-us.
20. Wang, R., Cui, W., Chu, F. & Wu, F. Lithium metal anodes: Present and future. *J. Energy Chem.* **48**, 145–159 (2020).
21. Steiger, J., Kramer, D. & Mönig, R. Microscopic observations of the formation, growth and shrinkage of lithium moss during electrodeposition and dissolution. *Electrochimica Acta* **136**, 529–536 (2014).
22. Song, B. *et al.* Dynamic Lithium Distribution upon Dendrite Growth and Shorting Revealed by *Operando* Neutron Imaging. *ACS Energy Lett.* **4**, 2402–2408 (2019).
23. Han, S. Structure and dynamics in the lithium solvation shell of nonaqueous electrolytes. *Sci. Rep.* **9**, 5555 (2019).
24. Dahbi, M., Ghamouss, F., Tran-Van, F., Lemordant, D. & Anouti, M. Comparative study of EC/DMC LiTFSI and $LiPF_6$ electrolytes for electrochemical storage. *J. Power Sources* **196**, 9743–9750 (2011).
25. Garcia, B. & Armand, M. Aluminium corrosion in room temperature molten salt. *J. Power Sources* **132**, 206–208 (2004).
26. Khomenko, V., Raymundo-Piñero, E. & Béguin, F. High-energy density graphite/AC capacitor in organic electrolyte. *J. Power Sources* **177**, 643–651 (2008).
27. Arbizzani, C., Gabrielli, G. & Mastragostino, M. Thermal stability and flammability of electrolytes for lithium-ion batteries. *J. Power Sources* **196**, 4801–4805 (2011).
28. Golubkov, A. W. *et al.* Thermal runaway of large automotive Li-ion batteries. *RSC Adv.* **8**, 40172–40186 (2018).
29. Guo, Y. *et al.* Solid-state lithium batteries: Safety and prospects. *eScience* **2**, 138–163 (2022).
30. Janek, J. & Zeier, W. G. Challenges in speeding up solid-state battery development. *Nat. Energy* **8**, 230–240 (2023).
31. Oh, J. *et al.* Elastic Binder for High-Performance Sulfide-Based All-Solid-State Batteries. *ACS Energy Lett.* **7**, 1374–1382 (2022).
32. Liu, Z. *et al.* Strategies to improve electrochemical performances of pristine metal-organic frameworks-based electrodes for lithium/sodium-ion batteries. *SmartMat* **2**, 488–518 (2021).
33. Li, C. *et al.* An advance review of solid-state battery: Challenges, progress and prospects. *Sustain. Mater. Technol.* **29**, e00297 (2021).

34. Li, Z. *et al.* Ionic Conduction in Polymer-Based Solid Electrolytes. *Adv. Sci.* **10**, 2201718 (2023).
35. Murugan, R., Thangadurai, V. & Weppner, W. Fast Lithium Ion Conduction in Garnet-Type $Li_7La_3Zr_2O_{12}$. *Angew. Chem. Int. Ed.* **46**, 7778–7781 (2007).
36. Kodama, M., Ohashi, A. & Hirai, S. *In situ* X-ray computational tomography measurement of single particle behavior of sulfide solid electrolyte under high-pressure compression. *J. Power Sources Adv.* **4**, 100019 (2020).
37. Tsukasaki, H., Mori, S., Shiotani, S. & Yamamura, H. Ionic conductivity and crystallization process in the Li_2S–P_2S_5 glass electrolyte. *Solid State Ion.* **317**, 122–126 (2018).
38. Boulineau, S., Courty, M., Tarascon, J.-M. & Viallet, V. Mechanochemical synthesis of Li-argyrodite Li_6PS_5X (X=Cl, Br, I) as sulfur-based solid electrolytes for all solid state batteries application. *Solid State Ion.* **221**, 1–5 (2012).
39. Wang, S. *et al.* High-Conductivity Argyrodite Li_6PS_5Cl Solid Electrolytes Prepared via Optimized Sintering Processes for All-Solid-State Lithium–Sulfur Batteries. *ACS Appl. Mater. Interfaces* **10**, 42279–42285 (2018).
40. Schwietert, T. K., Vasileiadis, A. & Wagemaker, M. First-Principles Prediction of the Electrochemical Stability and Reaction Mechanisms of Solid-State Electrolytes. *JACS Au* **1**, 1488–1496 (2021).
41. Kudu, Ö. U. *et al.* A review of structural properties and synthesis methods of solid electrolyte materials in the Li_2S – P_2S_5 binary system. *J. Power Sources* **407**, 31–43 (2018).
42. Doux, J.-M. *et al.* Pressure effects on sulfide electrolytes for all solid-state batteries. *J. Mater. Chem. A* **8**, 5049–5055 (2020).
43. Singh, D. K. *et al.* Li_6PS_5Cl microstructure and influence on dendrite growth in solid-state batteries with lithium metal anode. *Cell Rep. Phys. Sci.* **3**, 101043 (2022).
44. Kasemchainan, J. *et al.* Critical stripping current leads to dendrite formation on plating in lithium anode solid electrolyte cells. *Nat. Mater.* **18**, 1105–1111 (2019).
45. Cao, D. *et al.* Nondestructively Visualizing and Understanding the Mechano-Electrochemical Origins of "Soft Short" and "Creeping" in All-Solid-State Batteries. *Adv. Funct. Mater.* **n/a**, 2307998 (2023).
46. Hikima, K., Totani, M., Obokata, S., Muto, H. & Matsuda, A. Mechanical Properties of Sulfide-Type Solid Electrolytes Analyzed by Indentation Methods. *ACS Appl. Energy Mater.* **5**, 2349–2355 (2022).
47. Farzanian, S. *et al.* Mechanical Investigation of Composite Cathode Degradation in All-Solid-State-Batteries. (2023).
48. Athanasiou, C. E. *et al.* Rate-dependent deformation of amorphous sulfide glass electrolytes for solid-state batteries. *Cell Rep. Phys. Sci.* **3**, 100845 (2022).
49. Masias, A., Felten, N., Garcia-Mendez, R., Wolfenstine, J. & Sakamoto, J. Elastic, plastic, and creep mechanical properties of lithium metal. *J. Mater. Sci.* **54**, 2585–2600 (2019).
50. Sakuda, A., Hayashi, A., Takigawa, Y., Higashi, K. & Tatsumisago, M. Evaluation of elastic modulus of Li_2S–P_2S_5 glassy solid electrolyte by ultrasonic sound velocity measurement and compression test. *J. Ceram. Soc. Jpn.* 4 (2013).
51. Sastre, J. *et al.* Blocking lithium dendrite growth in solid-state batteries with an ultrathin amorphous Li-La-Zr-O solid electrolyte. *Commun. Mater.* **2**, 1–10 (2021).

52. Sakuda, A., Hayashi, A. & Tatsumisago, M. Sulfide Solid Electrolyte with Favorable Mechanical Property for All-Solid-State Lithium Battery. *Sci. Rep.* **3**, 2261 (2013).
53. Cronau, M., Szabo, M., König, C., Wassermann, T. B. & Roling, B. How to Measure a Reliable Ionic Conductivity? The Stack Pressure Dilemma of Microcrystalline Sulfide-Based Solid Electrolytes. *ACS Energy Lett.* **6**, 3072–3077 (2021).
54. McGrogan, F. P. *et al.* Compliant Yet Brittle Mechanical Behavior of Li_2S–P_2S_5 Lithium-Ion-Conducting Solid Electrolyte. *Adv. Energy Mater.* **7**, 1602011 (2017).
55. Ates, T. *et al.* Elucidating the Role of Microstructure in Thiophosphate Electrolytes – a Combined Experimental and Theoretical Study of β-Li_3PS_4. *Adv. Sci.* **9**, 2105234 (2022).
56. Garcia-Mendez, R., Mizuno, F., Zhang, R., Arthur, T. S. & Sakamoto, J. Effect of Processing Conditions of $75Li_2S$-$25P_2S_5$ Solid Electrolyte on its DC Electrochemical Behavior. *Electrochimica Acta* **237**, 144–151 (2017).
57. Tsukasaki, H. *et al.* Analysis of structural and thermal stability in the positive electrode for sulfide-based all-solid-state lithium batteries. *J. Power Sources* **367**, 42–48 (2017).
58. Walther, F. *et al.* Influence of Carbon Additives on the Decomposition Pathways in Cathodes of Lithium Thiophosphate-Based All-Solid-State Batteries. *Chem. Mater.* **32**, 6123–6136 (2020).
59. Neumann, A. *et al.* Analysis of Interfacial Effects in All-Solid-State Batteries with Thiophosphate Solid Electrolytes. *ACS Appl. Mater. Interfaces* **12**, 9277–9291 (2020).
60. Aiken, C. P. *et al.* A Survey of *In Situ* Gas Evolution during High Voltage Formation in Li-Ion Pouch Cells. *J. Electrochem. Soc.* **162**, A760 (2015).
61. Doerrer, C. *et al.* High Energy Density Single-Crystal NMC/Li_6PS_5Cl Cathodes for All-Solid-State Lithium-Metal Batteries. *ACS Appl. Mater. Interfaces* **13**, 37809–37815 (2021).
62. Kim, S. Y., Cha, H., Kostecki, R. & Chen, G. Composite Cathode Design for High-Energy All-Solid-State Lithium Batteries with Long Cycle Life. *ACS Energy Lett.* **8**, 521–528 (2023).
63. Strauss, F. *et al.* Impact of Cathode Material Particle Size on the Capacity of Bulk-Type All-Solid-State Batteries. *ACS Energy Lett.* **3**, 992–996 (2018).
64. Shi, T. *et al.* Characterization of mechanical degradation in an all-solid-state battery cathode. *J. Mater. Chem. A* **8**, 17399–17404 (2020).
65. Kroll, M. *et al.* Sheet-type all-solid-state batteries with sulfidic electrolytes: Analysis of kinetic limitations based on a cathode morphology study. *J. Power Sources* **505**, 230064 (2021).
66. Liu, Y., Hamam, I. & Dahn, J. R. A Study of Vinylene Carbonate and Prop-1-ene-1,3 Sultone Electrolyte Additives Using Polycrystalline $Li[Ni_{0.6}Mn_{0.2}Co_{0.2}]O_2$ in Positive/Positive Symmetric Cells. *J. Electrochem. Soc.* **167**, 110527 (2020).
67. Märker, K., Reeves, P. J., Xu, C., Griffith, K. J. & Grey, C. P. Evolution of Structure and Lithium Dynamics in $LiNi_{0.8}Mn_{0.1}Co_{0.1}O_2$ (NMC811) Cathodes during Electrochemical Cycling. *Chem. Mater.* **31**, 2545–2554 (2019).
68. Ryu, H.-H., Park, K.-J., Yoon, C. S. & Sun, Y.-K. Capacity Fading of Ni-Rich $Li[Ni_xCo_yMn_{1-x-y}]O_2$ ($0.6 \leq x \leq 0.95$) Cathodes for High-Energy-Density Lithium-Ion Batteries: Bulk or Surface Degradation? *Chem. Mater.* **30**, 1155–1163 (2018).
69. Cadiou, F. *et al.* Morphological Evolution of NMC Secondary Particles Through *in situ* electrochemical FIB/SEM experiment. 16 (2022).
70. Song, B. *et al.* Nano-structural changes in Li-ion battery cathodes during cycling revealed by FIB-SEM serial sectioning tomography. *J. Mater. Chem. A* **3**, 18171–18179 (2015).

71. Ruess, R. *et al.* Influence of NCM Particle Cracking on Kinetics of Lithium-Ion Batteries with Liquid or Solid Electrolyte. *J. Electrochem. Soc.* **167**, 100532 (2020).
72. Koerver, R. *et al.* Capacity Fade in Solid-State Batteries: Interphase Formation and Chemomechanical Processes in Nickel-Rich Layered Oxide Cathodes and Lithium Thiophosphate Solid Electrolytes. *Chem. Mater.* **29**, 5574–5582 (2017).
73. Tsai, E. H. R. *et al.* Correlated X-Ray 3D Ptychography and Diffraction Microscopy Visualize Links between Morphology and Crystal Structure of Lithium-Rich Cathode Materials. *iScience* **11**, 356–365 (2019).
74. Yari, S., D'Haen, J., Van Bael, M. K., Hardy, A. & Safari, M. Fracture-induced aging anomalies in $LiNi_{0.6}Mn_{0.2}Co_{0.2}O_2$ electrodes. *Electrochem. Commun.* **132**, 107134 (2021).
75. Ke, X., Wang, Y., Ren, G. & Yuan, C. Towards rational mechanical design of inorganic solid electrolytes for all-solid-state lithium ion batteries. *Energy Storage Mater.* **26**, 313–324 (2020).
76. Kudu, Ö. U. *et al.* Structural details in Li_3PS_4: Variety in thiophosphate building blocks and correlation to ion transport. *Energy Storage Mater.* **44**, 168–179 (2022).
77. Wang, Z. *et al. In Situ* STEM-EELS Observation of Nanoscale Interfacial Phenomena in All-Solid-State Batteries. *Nano Lett.* **16**, 3760–3767 (2016).
78. Otoyama, M., Kowada, H., Sakuda, A., Tatsumisago, M. & Hayashi, A. *Operando* Confocal Microscopy for Dynamic Changes of Li^+ Ion Conduction Path in Graphite Electrode Layers of All-Solid-State Batteries. *J. Phys. Chem. Lett.* **11**, 900–904 (2020).
79. Quinn, A. *et al.* Electron Backscatter Diffraction for Investigating Lithium-Ion Electrode Particle Architectures. *Cell Rep. Phys. Sci.* **1**, 100137 (2020).
80. Chen, B., Zhang, H., Xuan, J., Offer, G. J. & Wang, H. Seeing is Believing: *In Situ/Operando* Optical Microscopy for Probing Electrochemical Energy Systems. *Adv. Mater. Technol.* **5**, 2000555 (2020).
81. Liu, Z. *et al.* Three-dimensional morphological measurements of $LiCoO_2$ and $LiCoO_2/Li(Ni_{1/3}Mn_{1/3}Co_{1/3})O_2$ lithium-ion battery cathodes. *J. Power Sources* **227**, 267–274 (2013).
82. Vanpeene, V. *et al.* Dynamics of the Morphological Degradation of Si-Based Anodes for Li-Ion Batteries Characterized by *In Situ* Synchrotron X-Ray Tomography. *Adv. Energy Mater.* **9**, 1803947 (2019).
83. Pandya, R., Mathieson, A., Boruah, B. D., de Aguiar, H. B. & de Volder, M. Interrogating the Light-Induced Charging Mechanism in Li-Ion Batteries Using *Operando* Optical Microscopy. *Nano Lett.* **23**, 7288–7296 (2023).
84. Merryweather, A. J., Schnedermann, C., Jacquet, Q., Grey, C. P. & Rao, A. *Operando* optical tracking of single-particle ion dynamics in batteries. *Nature* **594**, 522–528 (2021).
85. Patel, A. N., Maddar, F. M. & Loveridge, M. J. Real-Time *Operando* SEM Investigation into Lithium Ion Battery Degradation. *ECS Meet. Abstr.* **MA2019-01**, 561 (2019).
86. Chen, C.-Y. *et al.* In situ Scanning Electron Microscopy of Silicon Anode Reactions in Lithium-Ion Batteries during Charge/Discharge Processes. *Sci. Rep.* **6**, 36153 (2016).
87. Yamamoto, Y., Iriyama, Y. & Muto, S. Analysis of Void Volume in Composite Electrode of All-solid-state Lithium-ion Battery Employing FIB-SEM and Union Operation Image Processing. *Microsc. Microanal.* **23**, 314–315 (2017).

88. Almar, L., Joos, J., Weber, A. & Ivers-Tiffée, E. Microstructural feature analysis of commercial Li-ion battery cathodes by focused ion beam tomography. *J. Power Sources* **427**, 1–14 (2019).
89. Liu, H. *et al.* Three-dimensional investigation of cycling-induced microstructural changes in lithium-ion battery cathodes using focused ion beam/scanning electron microscopy. *J. Power Sources* **306**, 300–308 (2016).
90. Zhou, X., Zhu, L. & Liu, Y. *Operando* Investigation of Energy Storage Material by FIB-SEM System. *Microsc. Microanal.* **27**, 440–442 (2021).
91. Dayani, S., Markötter, H., Schmidt, A., Widjaja, M. P. & Bruno, G. Multi-level X-ray computed tomography (XCT) investigations of commercial lithium-ion batteries from cell to particle level. *J. Energy Storage* **66**, 107453 (2023).
92. Bond, T., Gauthier, R., Gasilov, S. & Dahn, J. R. In-Situ Computed Tomography of Particle Microcracking and Electrode Damage in Cycled NMC622/Graphite Pouch Cell Batteries. *J. Electrochem. Soc.* **169**, 080531 (2022).
93. Di Lecce, D. *et al.* X-ray Nano-computed Tomography of Electrochemical Conversion in Lithium-ion Battery. *ChemSusChem* **12**, 3550–3561 (2019).
94. Hogrefe, C. *et al.* Cross-Sectional In Situ Optical Microscopy with Simultaneous Electrochemical Measurements for Lithium-Ion Full Cells. *J. Electrochem. Soc.* **169**, 050519 (2022).
95. Cadiou, F. Étude de l'impact de la microstructure sur les propriétés effectives électriques des batteries lithium-ion. 199 (2020).
96. Xu, C. *et al.* Operando visualization of kinetically induced lithium heterogeneities in single-particle layered Ni-rich cathodes. *Joule* **6**, 2535–2546 (2022).
97. Chen-Wiegart, Y. K., Liu, Z., Faber, K. T., Barnett, S. A. & Wang, J. 3D analysis of a $LiCoO_2$–$Li(Ni_{1/3}Mn_{1/3}Co_{1/3})O_2$ Li-ion battery positive electrode using x-ray nano-tomography. *Electrochem. Commun.* **28**, 127–130 (2013).
98. Wu, X. *et al. Operando* Visualization of Morphological Dynamics in All-Solid-State Batteries. *Adv. Energy Mater.* **9**, 1901547 (2019).
99. Jousseaume, T., Colin, J.-F., Chandesris, M., Lyonnard, S. & Tardif, S. *How Beam Damage Can Skew Synchrotron Operando Studies of Batteries*. https://chemrxiv.org/engage/chemrxiv/article-details/63ca64de3e8656699689de43 (2023) doi:10.26434/chemrxiv-2023-rfp8j.
100. Jiang, N. Electron beam damage in oxides: a review. *Rep. Prog. Phys.* **79**, 016501 (2015).
101. Egerton, R. F., Li, P. & Malac, M. Radiation damage in the TEM and SEM. *Micron Oxf. Engl. 1993* **35**, 399–409 (2004).
102. Abrams, H. Grain size measurement by the intercept method. *Metallography* **4**, 59–78 (1971).
103. Taillon, J. A., Pellegrinelli, C., Huang, Y.-L., Wachsman, E. D. & Salamanca-Riba, L. G. Improving microstructural quantification in FIB/SEM nanotomography. *Ultramicroscopy* **184**, 24–38 (2018).
104. Ebner, M., Chung, D.-W., García, R. E. & Wood, V. Tortuosity Anisotropy in Lithium-Ion Battery Electrodes. *Adv. Energy Mater.* **4**, 1301278 (2014).
105. Roque, W. L. & Costa, R. R. A. A plugin for computing the pore/grain network tortuosity of a porous medium from 2D/3D MicroCT image. *Appl. Comput. Geosci.* **5**, 100019 (2020).

106. Cooper, S. J., Bertei, A., Shearing, P. R., Kilner, J. A. & Brandon, N. P. TauFactor: An open-source application for calculating tortuosity factors from tomographic data. *SoftwareX* **5**, 203–210 (2016).
107. Chung, D.-W., Ebner, M., Ely, D. R., Wood, V. & García, R. E. Validity of the Bruggeman relation for porous electrodes. *Model. Simul. Mater. Sci. Eng.* **21**, 074009 (2013).
108. Lu, X. *et al.* 3D microstructure design of lithium-ion battery electrodes assisted by X-ray nano-computed tomography and modelling. *Nat. Commun.* **11**, 2079 (2020).
109. Conder, J., Marino, C., Novák, P. & Villevieille, C. Do imaging techniques add real value to the development of better post-Li-ion batteries? *J. Mater. Chem. A* **6**, 3304–3327 (2018).
110. Yadav, N. G. *et al.* Study of failure modes in two sulphide-based solid electrolyte all-solid-state batteries via *in situ* SEM. *J. Mater. Chem. A* **10**, 17142–17155 (2022).
111. Zhou, X. *et al. In Situ* Focused Ion Beam-Scanning Electron Microscope Study of Crack and Nanopore Formation in Germanium Particle During (De)lithiation. *ACS Appl. Energy Mater.* **2**, 2441–2446 (2019).
112. Ning, Z. *et al.* Dendrite initiation and propagation in lithium metal solid-state batteries. *Nature* **618**, 287–293 (2023).
113. Santhosha, A. L., Medenbach, L., Buchheim, J. R. & Adelhelm, P. The Indium–Lithium Electrode in Solid-State Lithium-Ion Batteries: Phase Formation, Redox Potentials, and Interface Stability. *Batter. Supercaps* **2**, 524–529 (2019).
114. Webb, S. A., Baggetto, L., Bridges, C. A. & Veith, G. M. The electrochemical reactions of pure indium with Li and Na: Anomalous electrolyte decomposition, benefits of FEC additive, phase transitions and electrode performance. *J. Power Sources* **248**, 1105–1117 (2014).
115. Wu, X., El Kazzi, M. & Villevieille, C. Surface and morphological investigation of the electrode/electrolyte properties in an all-solid-state battery using a Li_2S-P_2S_5 solid electrolyte. *J. Electroceramics* **38**, 207–214 (2017).
116. Scanning electron microscope (SEM) | Definition, Images, Uses, Advantages, & Facts | Britannica. https://www.britannica.com/technology/scanning-electron-microscope (2023).
117. Schlesinger, M., Paunovic, M. & Meng-Burany, X. *Modern Electroplating*. (John Wiley & Sons, Ltd, 2010). doi:10.1002/9780470602638.
118. Schindelin, J. *et al.* Fiji: an open-source platform for biological-image analysis. *Nat. Methods* **9**, 676–682 (2012).
119. Thévenaz, P. EPFL | Biomedical Imaging Group | TurboReg History. http://bigwww.epfl.ch/publications/thevenaz1201.html (2012).
120. Xlib. *ImageJ Wiki* https://imagej.github.io/plugins/xlib/index.
121. Fehrenbach, J., Weiss, P. & Lorenzo, C. Variational Algorithms to Remove Stationary Noise: Applications to Microscopy Imaging. *IEEE Trans. Image Process.* **21**, 4420–4430 (2012).
122. Berg, S. *et al.* ilastik: interactive machine learning for (bio)image analysis. *Nat. Methods* **16**, 1226–1232 (2019).
123. Singh, A. *et al.* On Representative Elementary Volumes of Grayscale Micro-CT Images of Porous Media. *Geophys. Res. Lett.* **47**, e2020GL088594 (2020).
124. Dougherty, R. & Kunzelmann, K.-H. Computing Local Thickness of 3D Structures with ImageJ. *Microsc. Microanal.* **13**, (2007).

125. Ollion, J., Cochennec, J., Loll, F., Escudé, C. & Boudier, T. TANGO: a generic tool for high-throughput 3D image analysis for studying nuclear organization. *Bioinformatics* **29**, 1840–1841 (2013).
126. Schneider, C. A., Rasband, W. S. & Eliceiri, K. W. NIH Image to ImageJ: 25 years of image analysis. *Nat. Methods* **9**, 671–675 (2012).
127. Legland, D., Arganda-Carreras, I. & Andrey, P. MorphoLibJ: integrated library and plugins for mathematical morphology with ImageJ. *Bioinformatics* **32**, 3532–3534 (2016).
128. Charge-Discharge Curves: How to get the most out of your Li-Ion Cells. *Imperial Society of Innovative Engineers* https://imperialsociety.in/charge-discharge-curves-how-to-get-the-most-out-of-your-li-ion-cells/ (2022).
129. Ashiotis, G. *et al.* The fast azimuthal integration Python library: PyFAI. *J. Appl. Crystallogr.* **48**, 510–519 (2015).
130. Habte, B. T. & Jiang, F. Effect of microstructure morphology on Li-ion battery graphite anode performance: Electrochemical impedance spectroscopy modeling and analysis. *Solid State Ion.* **314**, 81–91 (2018).
131. Muramatsu, H., Hayashi, A., Ohtomo, T., Hama, S. & Tatsumisago, M. Structural change of Li_2S–P_2S_5 sulfide solid electrolytes in the atmosphere. *Solid State Ion.* **182**, 116–119 (2011).
132. Sawaya, A. & Menezes, R. G. Hydrogen Sulfide Toxicity. in *StatPearls* (StatPearls Publishing, Treasure Island (FL), 2023).
133. Mi, C. & Hall, S. R. Preparation and degradation of high air stability sulfide solid electrolyte $75Li_2S{\cdot}25P_2S_5$ glass-ceramic. *Solid State Ion.* **389**, 116106 (2023).
134. Yersak, T. A., Zhang, Y., Hao, F. & Cai, M. Moisture Stability of Sulfide Solid-State Electrolytes. *Front. Energy Res.* **10**, (2022).
135. Nomura, Y. & Yamamoto, K. Advanced Characterization Techniques for Sulfide-Based Solid-State Lithium Batteries. *Adv. Energy Mater.* **13**, 2203883 (2023).
136. Chen, Y.-T. *et al.* Investigating dry room compatibility of sulfide solid-state electrolytes for scalable manufacturing. *J. Mater. Chem. A* **10**, 7155–7164 (2022).
137. Yang, S. *et al.* Studies on the inhibition of lithium dendrite formation in sulfide solid electrolytes doped with LiX (X = Br, I). *Solid State Ion.* **377**, 115869 (2022).
138. Xu, C., Ahmad, Z., Aryanfar, A., Viswanathan, V. & Greer, J. R. Enhanced strength and temperature dependence of mechanical properties of Li at small scales and its implications for Li metal anodes. *Proc. Natl. Acad. Sci.* **114**, 57–61 (2017).
139. Wu, X., El Kazzi, M. & Villevieille, C. Surface and morphological investigation of the electrode/electrolyte properties in an all-solid-state battery using a Li_2S-P_2S_5 solid electrolyte. *J. Electroceramics* **38**, 207–214 (2017).
140. Hayashi, A., Hama, S., Morimoto, H., Tatsumisago, M. & Minami, T. Preparation of Li_2S–P_2S_5 Amorphous Solid Electrolytes by Mechanical Milling. *J. Am. Ceram. Soc.* **84**, 477–79 (2001).
141. Hsu, C. H. & Mansfeld, F. Technical Note: Concerning the Conversion of the Constant Phase Element Parameter Y_0 into a Capacitance. *Corrosion* **57**, (2001).
142. Irvine, J. T. S., Sinclair, D. C. & West, A. R. Electroceramics: Characterization by Impedance Spectroscopy. *Adv. Mater.* **2**, 132–138 (1990).
143. Sakuda, A., Hayashi, A. & Tatsumisago, M. Sulfide Solid Electrolyte with Favorable Mechanical Property for All-Solid-State Lithium Battery. *Sci. Rep.* **3**, 2261 (2013).

144. Wenzel, S., Leichtweiss, T., Krüger, D., Sann, J. & Janek, J. Interphase formation on lithium solid electrolytes—An *in situ* approach to study interfacial reactions by photoelectron spectroscopy. *Solid State Ion.* **278**, 98–105 (2015).
145. Wenzel, S., Sedlmaier, S. J., Dietrich, C., Zeier, W. G. & Janek, J. Interfacial reactivity and interphase growth of argyrodite solid electrolytes at lithium metal electrodes. *Solid State Ion.* **318**, 102–112 (2018).
146. Zhu, Y., He, X. & Mo, Y. Origin of Outstanding Stability in the Lithium Solid Electrolyte Materials: Insights from Thermodynamic Analyses Based on First-Principles Calculations. *ACS Appl. Mater. Interfaces* **7**, 23685–23693 (2015).
147. Tan, D. H. S. *et al.* Elucidating Reversible Electrochemical Redox of Li_6PS_5Cl Solid Electrolyte. *ACS Energy Lett.* **4**, 2418–2427 (2019).
148. Dewald, G. F. *et al.* Experimental Assessment of the Practical Oxidative Stability of Lithium Thiophosphate Solid Electrolytes. *Chem. Mater.* **31**, 8328–8337 (2019).
149. Ohno, S., Rosenbach, C., Dewald, G. F., Janek, J. & Zeier, W. G. Linking Solid Electrolyte Degradation to Charge Carrier Transport in the Thiophosphate-Based Composite Cathode toward Solid-State Lithium-Sulfur Batteries. *Adv. Funct. Mater.* **31**, 2010620 (2021).
150. Menkin, S. *et al.* Insights into Soft Short Circuit-based Degradation of Lithium Metal Batteries. *Faraday Discuss.* 10.1039.D3FD00101F (2023) doi:10.1039/D3FD00101F.
151. Al-Salih, H., Houache, M. S. E., Baranova, E. A. & Abu-Lebdeh, Y. Composite Cathodes for Solid-State Lithium Batteries: "Catholytes" the Underrated Giants. *Adv. Energy Sustain. Res.* **3**, 2200032 (2022).
152. Oh, Y. S., Kim, M., Kang, S., Park, J.-Y. & Lim, H.-T. Redox activity of Li_2S–P_2S_5 electrolyte inducing chemo-mechanical failure in all-solid-state batteries comprising sulfur composite cathode and Li–Si alloy anode. *Chem. Eng. J.* **442**, 136229 (2022).
153. Strauss, F. *et al.* Influence of electronically conductive additives on the cycling performance of argyrodite-based all-solid-state batteries. *RSC Adv.* **10**, 1114–1119 (2020).
154. Kim, A.-Y. *et al.* Stabilizing Effect of a Hybrid Surface Coating on a Ni-Rich NCM Cathode Material in All-Solid-State Batteries. *Chem. Mater.* **31**, 9664–9672 (2019).
155. Liang, J. *et al. In Situ* Li_3PS_4 Solid-State Electrolyte Protection Layers for Superior Long-Life and High-Rate Lithium-Metal Anodes. *Adv. Mater.* **30**, 1804684 (2018).
156. Walther, F. *et al.* The Working Principle of a Li_2CO_3/$LiNbO_3$ Coating on NCM for Thiophosphate-Based All-Solid-State Batteries. *Chem. Mater.* **33**, 2110–2125 (2021).
157. Payandeh, S., Strauss, F., Mazilkin, A., Kondrakov, A. & Brezesinski, T. Tailoring the $LiNbO_3$ coating of Ni-rich cathode materials for stable and high-performance all-solid-state batteries. *Nano Res. Energy* **1**, e9120016 (2022).
158. Liang, J. *et al.* A gradient oxy-thiophosphate-coated Ni-rich layered oxide cathode for stable all-solid-state Li-ion batteries. *Nat. Commun.* **14**, 146 (2023).
159. Jiang, H. *et al.* Insights into interfacial chemistry of Ni-rich cathodes and sulphide-based electrolytes in all-solid-state lithium batteries. *Chem. Commun.* **58**, 5924–5947 (2022).
160. Xin, F. *et al.* Electrochemical Characterization and Microstructure Evolution of Ni-Rich Layered Cathode Materials by Niobium Coating/Substitution. *Chem. Mater.* **34**, 7858–7866 (2022).

161. Xin, F. *et al.* Li–Nb–O Coating/Substitution Enhances the Electrochemical Performance of the $LiNi_{0.8}Mn_{0.1}Co_{0.1}O_2$ (NMC 811) Cathode. *ACS Appl. Mater. Interfaces* **11**, 34889–34894 (2019).
162. Wang, S., Yan, M., Li, Y., Vinado, C. & Yang, J. Separating electronic and ionic conductivity in mix-conducting layered lithium transition-metal oxides. *J. Power Sources* **393**, 75–82 (2018).
163. Amin, R. & Chiang, Y.-M. Characterization of Electronic and Ionic Transport in $Li_{1-x}Ni_{0.33}Mn_{0.33}Co_{0.33}O_2$ (NMC333) and $Li_{1-x}Ni_{0.50}Mn_{0.20}Co_{0.30}O_2$ (NMC523) as a Function of Li Content. *J. Electrochem. Soc.* **163**, A1512 (2016).
164. Perrenot, P. *et al.* Room temperature sintering of amorphous thiophosphates solid electrolyte (Li_3PS_4): coupling morphological evolution to electrochemical properties. *Wiley Advanced Functional Materials - Accepted* (2023).
165. Cheng, E. J. *et al.* Mechanical and physical properties of $LiNi_{0.33}Mn_{0.33}Co_{0.33}O_2$ (NMC). *J. Eur. Ceram. Soc.* **37**, 3213–3217 (2017).
166. Rana, M. *et al.* Toward Achieving High Areal Capacity in Silicon-Based Solid-State Battery Anodes: What Influences the Rate-Performance? *ACS Energy Lett.* **8**, 3196–3203 (2023).
167. Yoon, K., Kim, J.-J., Seong, W. M., Lee, M. H. & Kang, K. Investigation on the interface between $Li_{10}GeP_2S_{12}$ electrolyte and carbon conductive agents in all-solid-state lithium battery. *Sci. Rep.* **8**, 8066 (2018).
168. Zhang, W. *et al.* The Detrimental Effects of Carbon Additives in $Li_{10}GeP_2S_{12}$-Based Solid-State Batteries. *ACS Appl. Mater. Interfaces* **9**, 35888–35896 (2017).
169. Wu, X. *Operando* characterization of degradation phenomena in all-solid-state batteries with a sulfide-based solid electrolyte. (ETH Zurich, 2019). doi:10.3929/ethz-b-000352747.
170. Conforto, G. *et al.* Editors' Choice—Quantification of the Impact of Chemo-Mechanical Degradation on the Performance and Cycling Stability of NCM-Based Cathodes in Solid-State Li-Ion Batteries - IOPscience. https://iopscience.iop.org/article/10.1149/1945-7111/ac13d2 (2021).
171. Yadav, N. *et al.* Understanding the Battery Degradation Mechanism in All-solid-state Batteries via *In-situ* SEM. *Microsc. Microanal.* **27**, 105–106 (2021).
172. Perrenot, P., Bayle-Guillemaud, P. & Villevieille, C. Composite electrode ($LiNi_{0.6}Mn_{0.2}Co_{0.2}O_2$) engineering for thiophosphate solid-state batteries: morphological evolution and electrochemical properties. *ACS Energy Letters - Submitted*.
173. Postek, Michael. T. An approach to the reduction of hydrocarbon contamination in the scanning electron microscope. *Scanning* **18**, 269–274 (1996).
174. Egerton, R. F., Li, P. & Malac, M. Radiation damage in the TEM and SEM. *Micron* **35**, 399–409 (2004).
175. Hugenschmidt, M., Adrion, K., Marx, A., Müller, E. & Gerthsen, D. Electron-Beam-Induced Carbon Contamination in STEM-in-SEM: Quantification and Mitigation. *Microsc. Microanal.* **29**, 219–234 (2023).
176. Quilty, C. D. *et al.* Probing Sources of Capacity Fade in $LiNi_{0.6}Mn_{0.2}Co_{0.2}O_2$ (NMC622): An *Operando* XRD Study of Li/NMC622 Batteries during Extended Cycling. *J. Phys. Chem. C* **124**, 8119–8128 (2020).

177. Quilty, C. D. *et al.* Impact of Charge Voltage on Factors Influencing Capacity Fade in Layered NMC622: Multimodal X-ray and Electrochemical Characterization. *ACS Appl. Mater. Interfaces* **13**, 50920–50935 (2021).
178. Qian, G. *et al.* Single-crystal nickel-rich layered-oxide battery cathode materials: synthesis, electrochemistry, and intra-granular fracture. *Energy Storage Mater.* **27**, 140–149 (2020).
179. Moiseev, I. A. *et al.* Single crystal Ni-rich NMC cathode materials for lithium-ion batteries with ultra-high volumetric energy density. *Energy Adv.* **1**, 677–681 (2022).
180. Lemaitre, J. A Continuous Damage Mechanics Model for Ductile Fracture. *J. Eng. Mater. Technol.* **107**, 83–89 (1985).
181. Kim, S., Wee, J., Peters, K. & Huang, H.-Y. S. Multiphysics Coupling in Lithium-Ion Batteries with Reconstructed Porous Microstructures. *J. Phys. Chem. C* **122**, 5280–5290 (2018).
182. Knorr, T. *et al.* Simulation-Based and Data-Driven Techniques for Quantifying the Influence of the Carbon Binder Domain on Electrochemical Properties of Li-Ion Batteries. *Energies* **15**, 7821 (2022).
183. Duva, J. M. & Crow, P. D. The densification of powders by power-law creep during hot isostatic pressing. *Acta Metall. Mater.* **40**, 31–35 (1992).
184. Bocanegra-Bernal, M. H. Hot Isostatic Pressing (HIP) technology and its applications to metals and ceramics. *J. Mater. Sci.* **39**, 6399–6420 (2004).

Table of figures

Table of equations

List of tables

Appendices

Appendix A: Shearing correction code

```
import matplotlib.pyplot as plt
import re

input_file  = "Z:\\3D FIB\\ELECTROLYTE\Article\\2t 12h\\Pre-Treatment\\TM.txt"
output_file = "Z:\\3D FIB\\ELECTROLYTE\Article\\2t 12h\\Pre-
Treatment\\TM2.txt"

correct_x = True
correct_y = True

with open(input_file) as f:
        content = list(f)
        content_len = len(content)

nb_images = int((content_len-3)/10)
pattern = "(\d+\.\d+)(\s+)(\d+\.\d+)"
xy_ini = re.search(pattern, content[9])
x_ini = float(xy_ini.group(1))
y_ini = float(xy_ini.group(3))

dx, dy, integrate_dx, integrate_dy = [], [], [], []
indx, indy  = 0, 0

for i in range(nb_images):
    aa = re.search(pattern, content[10*i+5])
    ndx = float(aa.group(1))-x_ini
    indx = indx + ndx
    dx.append(ndx)
    integrate_dx.append(indx)
    ndy = float(aa.group(3))-y_ini
    indy = indy + ndy
    dy.append(ndy)
    integrate_dy.append(indy)

# ---------------------------------------------------------------------

i_cor = [0, nb_images-1]
x_cor = [0, 0]
y_cor = [0, 0]

ddx, ddy = [x_cor[0]], [y_cor[0]]
for cor in range(len(i_cor)-1):
    delta_x = -((integrate_dx[i_cor[cor+1]]-x_cor[cor+1])-
(integrate_dx[i_cor[cor]]-x_cor[cor]))/(i_cor[cor+1]-i_cor[cor])
    delta_y = -((integrate_dy[i_cor[cor+1]]-y_cor[cor+1])-
(integrate_dy[i_cor[cor]]-y_cor[cor]))/(i_cor[cor+1]-i_cor[cor])
    for i in range(i_cor[cor+1]-i_cor[cor]):
        ddx.append(delta_x)
        ddy.append(delta_y)
# ---------------------------------------------------------------------

dx_new, dy_new, integrate_dx_new, integrate_dy_new = [], [], [], []
indx, indy = 0, 0
```

```
for i in range(nb_images):
    ndx = dx[i] + ddx[i]
    indx = indx + ndx
    dx_new.append(ndx)
    integrate_dx_new.append(indx)
    ndy = dy[i] + ddy[i]
    indy = indy + ndy
    dy_new.append(ndy)
    integrate_dy_new.append(indy)

plt.plot(integrate_dx)
plt.plot(integrate_dx_new)
plt.show()
plt.plot(integrate_dy)
plt.plot(integrate_dy_new)
plt.show()

output = open(output_file, "w")
output.write("MultiStackReg Transformation File\n")
output.write("File Version 1.0\n0\n")
for i in range(nb_images):
    x = x_ini + dx_new[i] if correct_x else x_ini + dx[i]
    y = y_ini + dy_new[i] if correct_y else y_ini + dy[i]
    output.write("TRANSLATION\n")
    output.write("Source img: %d Target img: 1\n" % (i+2,))
    output.write("%.13f\t%.13f\n" % (x, y))
    output.write("0.0\t0.0\n0.0\t0.0\n\n")
    output.write("%f\t%f\n" %(x_ini, y_ini))
    output.write("0.0\t0.0\n0.0\t0.0\n\n")
output.close()
```

Appendix B: REV code

```
import os
import csv
import matplotlib.pyplot as plt
import numpy as np
from scipy.signal import convolve
import tifffile

from common.image.fake_image import image_from_blobs
from common.execution.utils import progression_bar
from common import TEMP_LOCATION


def deterministic_rev(arr):
    r"""
    Parameters
    ----------
    arr: array
        3D array with value 1 as the phase of interest

    Returns
    -------
    porosity: list
        list of the porosity measurements
    cube_size: list
        kernel in which the porosity is measured
    """

    percent_old = -1

    # DEFINING CENTER OF THE STACK AND ITS SIZE
    stack_z, stack_y, stack_x = arr.shape
    mid_z = int(stack_z / 2)
    mid_y = int(stack_y / 2)
    mid_x = int(stack_x / 2)
    lowest_dim = min(mid_z, mid_y, mid_x)
    porosity = np.array([])
    cube_size = np.array([])

    # MEASUREMENT OF POROSITY ON DETERMINISTIC REV, GROWING CUBE AND ADD
    # RESULTS TO DATAFRAME
    for step in range(lowest_dim):
        percent_old = progression_bar(step, lowest_dim, percent_old)
        zmin = mid_z - step
        zmax = mid_z + step
        ymin = mid_y - step
        ymax = mid_y + step
        xmin = mid_x - step
        xmax = mid_x + step
        if step == 0:
            cube = arr[mid_z, mid_y, mid_x]
        else:
            cube = arr[zmin: zmax, ymin: ymax, xmin: xmax]
```

```
        porosity = np.append(porosity, (np.sum(cube) / cube.size) * 100)
        cube_size = np.append(cube_size, cube.size)

    return porosity, cube_size

def save_to_csv(porosity, cube_size, fname,
                save_dir=None):
    """
    Save the list generated by stat_rev and stat-rev into csv file

    Parameters
    ----------
    porosity: list
        porosity measurements for deterministic REV
    cube_size: list
        cube size in which the porosity is measured for deterministic REV
    fname: str
        file name to save the csv file
    save_dir: str
        path to represitory to save csv file

    """
    if save_dir is None:
        save_dir = os.path.join(TEMP_LOCATION, 'REV_Python')
    if not os.path.exists(save_dir):
        os.makedirs(save_dir)

    file = open(save_dir + fname + ' REV Data.csv', 'w+', newline='')
    with file:
        write = csv.writer(file)
        write.writerow(porosity)
        write.writerow(cube_size)
```

Abstract

The intrinsic limits of Li-ion technology are nearing, driven by rising demands for autonomy, performance, and safety. Solid-state batteries show promise due to non-flammable solid electrolytes, enabling the use of lithium metal anodes. However, challenges arise from the fixed nature of solid-solid interfaces combined with volume changes in active materials due to lithium-ion movement. Amorphous thiophosphate (a-Li_3PS_4) stands out among solid electrolytes as it presents a reasonable ionic conductivity at room temperature (≈ 0.3 $mS{\cdot}cm^{-1}$) and straightforward manufacturing by room-temperature sintering. In addition to proposing a three-dimensional characterization methodology aimed at extracting the important metrics for the operation of a battery, this PhD work was aimed to elucidate the relationship between morphology and electrochemical performances of solid-state systems using a-Li_3PS_4. Focus Ion Beam coupled to a Scanning Electron Microscopy (FIB-SEM) is used to monitor the morphology evolution while electrochemical techniques are used to assess the system performance. Finally, an *operando* cell is developed to monitor the dynamic of morphological evolution within a FIB-SEM. In the separator, pressure significantly impacts the amount of porosity while sintering time impacts the pores network. Despite reaching a plateau of ionic conductivity with roughly 10 % porosity, the pores guide the lithium metal as it creeps under the stack pressure, ultimately enhancing decomposition and dendrite formations. In the composite cathode, polycrystalline $LiNi_{0.6}Mn_{0.6}Co_{0.6}O_2$ active material (NMC) fractures both from sintering and cycling. Nonetheless, longer sintering time and keeping moderate pressure favours the contacts between NMC and LPS, improving the overall battery performance, while partially preserving NMC microstructures. Moreover, NMC volume changes lead to detrimental decohesion during delithiation that is only partially recovered during lithiation. The *operando* FIB-SEM experiments lead to similar observations such as the fracturing of NMC and decohesion between NMC-LPS. However, dynamics evolutions such as the front of the delithiation during discharge or heterogeneous displacements have been observed, highlighting the need for *operando* techniques.

Résumé

Les limites intrinsèques de la technologie Li-ion sont proches, poussées par une demande croissante d'autonomie, de performances et de sécurité. Les batteries tout solides présentent un grand potentiel grâce à leurs électrolytes solides non inflammables, permettant l'utilisation d'anodes en lithium métal. Cependant, des challenges surviennent de la nature fixe des interfaces solides-solides combinée aux changements volumiques des matériaux actifs due aux mouvements des ions lithium. Les électrolytes solides amorphe thiophosphate (a-Li_3PS_4) se distinguent de leur homologue car ils présentent une conductivité ionique raisonnable à température ambiante (≈ 0,3 $mS{\cdot}cm^{-1}$) ainsi qu'une mise en œuvre simple par frittage à température ambiante. En plus de proposer une méthodologie de caractérisation tridimensionnelle visant à extraire les paramètres importants pour le fonctionnement d'une batterie, ce travail de thèse vise à déterminer la relation entre la morphologie et les performances électrochimiques d'un système tout solide utilisant le a-Li_3PS_4. Un faisceau d'ions focalisés couplé à un microscope électronique à balayage (FIF-MEB) est utilisé pour suivre l'évolution de la morphologie tandis que des techniques électrochimiques sont utilisées pour évaluer les performances du système. Enfin, une cellule *operando* est développée pour suivre la dynamique des évolutions morphologiques au sein d'un FIF-MEB. Dans le séparateur, la pression impacte significativement la quantité de porosité, tandis que le temps de frittage affecte le réseau de pores. Malgré qu'un plateau de conductivité ionique soit atteint avec environ 10 % de porosité, les pores guident le lithium métal lorsqu'il flue sous la pression de la cellule, favorisant la décomposition et la formation de dendrites. Dans la cathode composite, le matériau actif $LiNi_{0,6}Mn_{0,6}Co_{0,6}O_2$ polycristallin (NMC) se fracture à la fois lors du frittage et du cyclage. Néanmoins, un temps de frittage plus long et le maintien d'une pression modérée favorisent les contacts entre NMC et a-Li_3PS_4, améliorant ainsi les performances globales de la batterie tout en préservant partiellement les microstructures du NMC. De plus, les changements de volume du NMC entraînent une décohésion néfaste lors de la délithiation, partiellement récupérée lors de la lithiation. Les expériences *operando* FIB-SEM conduisent à des observations similaires telles que la fracturation du NMC et la décohésion entre le NMC et le a-Li_3PS_4. Cependant, des évolutions dynamiques telles que le front de délithiation pendant la décharge ou des déplacements hétérogènes ont été observés, mettant en évidence la nécessité des techniques *operando*.